REPORT DOCUMENTATION PAGE

Form Approved OMB No. 0704-0188

Public reporting burden for this collection of information is estimated to average 1 hour per response, including the time for reviewing instructions, searching existing data sources, gathering and maintaining the data needed, and completing and reviewing the collection of information. Send comments regarding this burden estimate or any other aspect of this collection of information, including suggestions for reducing this burden to Washington Headquarters Services, Directorate for Information Operations and Reports, 1215 Jefferson Davis Highway, Suite 1204, Arlington, VA 22202-4302, and to the Office of Management and Budget, Paperwork Reduction Project (0704-0188), Washington, DC 20503.

1. AGENCY USE ONLY (Leave blank)	2. REPORT DATE November 2000	3. REPORT TYPE AND DATES COVERED Final November 2000

4. TITLE AND SUBTITLE Optical Breakdown in Water and Ocular Media and Its Use for Intraocular Photodisruption	5. FUNDING NUMBERS F61775-00-WE016
6. AUTHOR(S) Dr. Alfred Vogel	
7. PERFORMING ORGANIZATION NAME(S) AND ADDRESS(ES) Medical University of Lubeck Medical Laser Center Lubeck 23562 Germany	8. PERFORMING ORGANIZATION REPORT NUMBER
9. SPONSORING/MONITORING AGENCY NAME(S) AND ADDRESS(ES) EOARD PSC 802 Box 14 FPO 09499-0200	10. SPONSORING/MONITORING AGENCY REPORT NUMBER SPC 01-4016

11. SUPPLEMENTARY NOTES

Dissertation submitted November 1998; updated November 2000. Translated from German by Dr. Donald McNeill, American Institute of Physics.

12a. DISTRIBUTION/AVAILABILITY STATEMENT Public release. Government Rights License. All other rights reserved by the copyright owner.	12b. DISTRIBUTION CODE A

12. ABSTRACT (Maximum 200 words)

Since its introduction into ophthalmology by Krasnov (1977), Fankhauser, et al. (1981), and Aron-Rosa, et al. (1980), photodisruption by short, intense laser pulses has come into widespread use because it makes noninvasive, intraocular microsurgery possible. This dissertation is devoted to a study of the physical mechanisms of photodisruption in water and ocular media for the purpose of determining the optimum laser parameters for existing laser surgical procedures and opening up possible new areas of application by shortening the laser pulse duration from the nanosecond to the picosecond or femtosecond range.

14. SUBJECT TERMS EOARD, Dissertation, Translation, German language, Ophthalmology, Laser surgery	15. NUMBER OF PAGES 16. PRICE CODE

17. SECURITY CLASSIFICATION OF REPORT Unclassified	18. SECURITY CLASSIFICATION OF THIS PAGE Unclassified	19, SECURITY CLASSIFICATION OF ABSTRACT Unclassified	20. LIMITATION OF ABSTRACT Unlimited

NSN 7540-01-280-5500

Standard Form 298 (Rev. 2-89)
Prescribed by ANSI Std. 239-18
298-102

20010920 033

REPORT DOCUMENTATION PAGE

Form Approved OMB No. 0704-0188

Public reporting burden for this collection of information is estimated to average 1 hour per response, including the time for reviewing instructions, searching existing data sources, gathering and maintaining the data needed, and completing and reviewing the collection of information. Send comments regarding this burden estimate or any other aspect of this collection of information, including suggestions for reducing this burden to Washington Headquarters Services, Directorate for Information Operations and Reports, 1215 Jefferson Davis Highway, Suite 1204, Arlington, VA 22202-4302, and to the Office of Management and Budget, Paperwork Reduction Project (0704-0188), Washington, DC 20503.

1. AGENCY USE ONLY (Leave blank)

2. REPORT DATE

Nov 2000
~~12-April-2001~~

3. REPORT TYPE AND DATES COVERED

Final Report

4. TITLE AND SUBTITLE

~~Publication of~~ Optical Breakdown in Water and Ocular Media and its Use for Intraocular Photodisruption

5. FUNDING NUMBERS

F61775-01-WE016

6. AUTHOR(S)

Dr. Alfred Vogel

7. PERFORMING ORGANIZATION NAME(S) AND ADDRESS(ES)

Medical Laser Center Lubek
Peter Monnik Weg #4
Lubek 23562
Germany

8. PERFORMING ORGANIZATION REPORT NUMBER

N/A

9. SPONSORING/MONITORING AGENCY NAME(S) AND ADDRESS(ES)

EOARD
PSC 802 BOX 14
FPO 09499-0200

10. SPONSORING/MONITORING AGENCY REPORT NUMBER

SPC 01-4016

11. SUPPLEMENTARY NOTES

[illegible] by Dr. Donald McNeill, AIP

12a. DISTRIBUTION/AVAILABILITY STATEMENT

Approved for public release; distribution is unlimited.

German [illegible]

12b. DISTRIBUTION CODE

A

13. ABSTRACT (Maximum 200 words)

This report results from a contract tasking Medical Laser Center Lubek as follows: The contractor will publish an English translation of his work 'Optical Breakdown in Water and Ocular Media, and its Use for Intraocular Photodisruption' (as updated Nov 2000, translated into English by Dr Donald McNeill).

14. SUBJECT TERMS

EOARD, Medicine, Laser Safety, Biology [illegible] Translation
Germany

15. NUMBER OF PAGES

242

16. PRICE CODE

N/A

17. SECURITY CLASSIFICATION OF REPORT	18. SECURITY CLASSIFICATION OF THIS PAGE	19, SECURITY CLASSIFICATION OF ABSTRACT	20. LIMITATION OF ABSTRACT
UNCLASSIFIED	UNCLASSIFIED	UNCLASSIFIED	UL

Optical Breakdown in Water and Ocular Media, and its Use for Intraocular Photodisruption

Habilitation dissertation
for the Degree of Habilitated Doctor of Science
at the Medical University of Lübeck, Germany

Submitted November 1998 by

Dr. Alfred Vogel

Medical Laser Center, Lübeck

Updated November 2000

Translated by Dr. Donald McNeill
American Institute of Physics

AQ F01-12-2581

Table of Contents

Notation viii

1 **Introduction** 1

1.1 Optical breakdown in gases, solids, and liquids 1

1.2 Intraocular photodisruption 3

1.3 Studies of the mechanism of intraocular photodisruption 4

1.4 Strategies for optimizing photodisruption 5

2 **Plasma formation** 7

2.1 Theoretical background 9

2.1.1 Linear and nonlinear absorption 9

2.1.1.1 Linear absorption in ocular media 9

2.1.1.2 Nonlinear absorption 10

2.1.2 Self-phase modulation 11

2.1.2.1 Self-focussing 13

2.1.2.2 Formation of a continuum 14

2.1.2.3 Influence of self-focussing on nonlinear absorption 15

2.1.3 Thresholds for optical breakdown 15

2.1.4 Plasma formation at the breakdown threshold 16

2.1.4.1 Multiphoton ionization 17

2.1.4.2 Cascade ionization 18

2.1.4.3 Diffusion and recombination losses 20

2.1.4.4 Analytical calculation of the threshold 21

2.1.4.5 Solution of the rate equation for the electron density 23

2.1.5 Absorption coefficient of the plasma at the breakdown threshold 23

2.1.6 Plasma formation above the breakdown threshold 23

2.2 Experimental techniques 27

2.2.1 Plasma formation 27

2.2.2 Determination of the focal angle and focal spot diameter 28

2.2.3 Determination of the breakdown threshold 29

2.2.4 Determination of the plasma shape and length 29

2.2.5 Determination of the optical properties of the plasma 30

- *2.2.5.1 Total and time resolved transmission* 30
- *2.2.5.2 Scattering* 31
- *2.2.5.3 Reflection* 32
- *2.2.5.4 Absorption* 32
- *2.2.5.5 Plasma radiation* 32

2.2.6 An examination of the effect of aberrations on plasma formation 33

2.3 Results and discussion 34

2.3.1 Plasma formation at the breakdown threshold 34

- *2.3.1.1 Focal spot diameter and threshold values* 34
- *2.3.1.2 Self-focussing and the generation of a continuum* 35
- *2.3.1.3 Dependence of the breakdown threshold on focal spot size* 38
- *2.3.1.4 Dependence of the breakdown threshold on pulse duration* 38
- *2.3.1.5 Dependence of the breakdown threshold on wavelength* 39
- *2.3.1.6 Comparison with calculated threshold values* 40
- *2.3.1.7 Time evolution of the electron density* 43

2.3.2 Plasma formation above the breakdown threshold 45

- *2.3.2.1 Plasma shape* 45
- *2.3.2.2 Plasma front velocity* 46
- *2.3.2.3 Plasma length* 47
- *2.3.2.4 Inhomogeneities in the plasma* 50

2.3.3 Optical properties of the plasma 51

- *2.3.3.1 Time resolved transmission* 51
- *2.3.3.2 Scattering* 51
- *2.3.3.3 Reflection* 53
- *2.3.3.4 Absorption* 53
- *2.3.3.5 Total transmission* 54
- *2.3.3.6 Absorption coefficient* 60

2.3.4 Plasma radiation 62

2.3.5 Plasma energy density 63

2.3.6 Effect of aberrations on plasma formation 64

2.4 Summary and clinical consequences 69

2.4.1 Summary 69
2.4.2 Clinical consequences 71

3 Shock wave production and cavitation bubble formation 74

3.1 Theoretical background 79
3.1.1 Detachment of the shock wave and formation of a cavitation bubble 79
3.1.2 The Gilmore model for cavitation bubble dynamics 81
3.1.3 Modelling the formation of laser produced bubbles 83
3.1.4 Modelling shock wave generation 84
3.1.5 The physics of the shock front 85
3.1.6 The equation of state for water 86
3.1.7 Determination of the shock pressure from the shock velocity 87
3.1.8 Similarity theorem 87
3.1.9 Shock wave energy and energy dissipation in the shock front 88
3.2 Experimental Techniques 90
3.2.1 High speed photographic analysis of shock wave emission and bubble expansion 90
3.2.2 Hydrophone measurements of the shock pressure 91
3.2.3 Determination of the plasma volume, bubble radius, and bubble energy 91
3.3 Results 93
3.3.1 Pictures series of shock wave formation and bubble expansion 93
3.3.2 Evolution of the velocity and pressure during shock wave propagation and bubble expansion 95
3.3.3 Shock wave energy 99
3.3.4 Plasma size, cavitation bubble size, and bubble energy 100
3.3.5 Numerical calculations of bubble dynamics and shock wave generation 101
3.4 Discussion 106
3.4.1 Shock wave production 106
3.4.1.1 Formation of the shock front 109
3.4.1.2 Maximum pressure at the plasma boundary 109
3.4.1.3 Shock wave width and duration 109
3.4.1.4 Pressure drop during shock wave propagation 110
3.4.1.5 Shock wave energy and energy dissipation 113

3.4.2 Cavitation bubble expansion ... 114
3.4.2.1 Bubble wall velocity ... 114
3.4.2.2 Bubble energy ... 115
3.4.3 Possible effects of shock waves and bubble expansion on tissue ... 116
3.5 Summary and clinical consequences ... 119
3.5.1 Summary ... 119
3.5.2 Clinical consequences ... 120

4 **Energy balance** ... 122
4.1 Methods ... 123
4.1.1 Plasma transmission, scattering, and reflection ... 123
4.1.2 Energy of vaporization ... 123
4.1.3 Cavitation bubble energy ... 124
4.1.4 Acoustic energy ... 124
4.1.5 The energy radiated by the plasma ... 125
4.2 Results and discussion ... 126
4.2.1 Total energy balance for selected parameters ... 126
4.2.2 Parameter dependence of the energy deposition ... 128
4.2.3 Parameter dependence of the efficiency of conversion of laser energy into mechanical energy ... 128
4.3 Clinical consequences ... 131

5 **Cavitation bubble dynamics** ... 132
5.1 Theoretical background ... 133
5.1.1 Spherical bubble collapse ... 133
5.1.2 Aspherical bubble collapse ... 134
5.1.2.1 Jet formation ... 134
5.1.2.2 Causes of cavitation damage ... 136
5.2 Experimental methods ... 138
5.3 Results and discussion ... 140
5.3.1 Solid boundary ... 140
5.3.2 Tissue boundary ... 141
5.4 Summary and clinical consequences ... 144

6 **Multipulse interactions** 145

6.1 Theoretical background 147

6.1.1 Plasma formation by a series of laser pulses 147

6.1.2 Effect of optical breakdown on gas bubbles from previous pulses 147

6.1.2.1 Gas bubble formation 147

6.1.2.2 Shock induced bubble collapse 148

6.1.2.3 Jet formation 149

6.1.2.4 The contributions of shock and flow pressure to gas bubble collapse 150

6.2 Experimental methods 152

6.2.1 Plasma formation by a series of laser pulses 152

6.2.2 Effect of optical breakdown on gas bubbles from previous pulses 152

6.3 Results and discussion 154

6.3.1 Plasma formation by a series of laser pulses 154

6.3.2 Effect of optical breakdown on gas bubbles from previous pulses 155

6.3.2.1 Gas bubble formation 155

6.3.2.2 Bubble collapse and jet formation. 157

6.3.2.3 Scaling laws 159

6.4 Summary and clinical consequences 162

6.4.1 Plasma formation by a series of laser pulses 162

6.4.2 Effect of optical breakdown on gas bubbles from previous pulses 162

7 **Tissue effects** 164

7.1 Experimental techniques 166

7.1.1 Measurements with different irradiation geometries 166

7.1.2 Microscopic and histological studies 169

7.1.3 Photographic studies 170

7.2 Results and discussion 171

7.2.1 Laser focus at the tissue surface 171

7.2.2 Laser focus in fluid near tissue 174

7.2.3 Effects of shock-induced gas bubble collapse 177

7.2.4 Damage range for optical breakdown 177

7.2.5 Comparison of the effects of the different damage mechanisms 179

7.2.6 Incision of tissue with different laser pulse durations 181

7.2.7 Laser focus in tissue 183

7.2.7.1 Acoustic emission and bubble dynamics 183

7.2.7.2 Morphology and damage range 184

7.2.7.3 Vaporization of intrastromal tissue 186

7.3 Summary and clinical consequences 191

8 From nano- to femtosecond pulses 193

8.1 Experimental techniques 194

8.2 Results and Discussion 196

8.2.1 Plasma formation at the breakdown threshold 196

8.2.2 Plasma formation above the breakdown threshold 199

8.2.3 Energy deposition and absorption coefficient 200

8.2.4 Mechanical effects 201

8.2.4.1 Shock waves and cavitation 201

8.2.4.2 Energy density in the breakdown region 203

8.2.4.3 Factors controlling the dependence of the energy density on pulse duration 204

8.2.5 Self-focussing 207

8.3 Clinical consequences 209

9 Strategies for optimizing intraocular photodisruption 210

9.1 General considerations for parameter choices 210

9.1.1 Wavelength 210

9.1.2 Focal angle 210

9.1.3 Laser modes and aberration free focussing 210

9.1.4 Pulse duration 211

9.1.5 Repetition rate 212

9.2 Specific laser applications 214

9.2.1 Capsulotomies and membranotomies 214

9.2.2 Fistulating operations 215

9.2.3 Cataract emulsification 216

9.2.4 Vitreoretinal surgery 217

9.2.5 Intrastromal refractive corneal surgery 217

10 Summary 220

11 References 223

Acknowledgements 239

Curriculum vitae 241

Notation

A	Absorption
A_p	Plasma surface area
a_S	Shock width
b	Enthalpy of vaporization
B	Constant in the Tait equation (B=314 MPa)
c	Speed of light in vacuum, Pressure dependent speed of sound in compressed media
c_0	Speed of sound in an uncompressed medium at rest
c_i	Speed of sound in medium i
C	Speed of sound in the fluid at a bubble wall, Specific heat
d	Distance between the laser focus and the center of a neighboring gas bubble
D	Electron diffusion constant
e	Electronic charge
$\vec{E}$	Electric field vector
E_abs	Absorbed laser energy
E_B	Energy of a cavitation bubble
E_cont	Threshold energy for the appearance of continuum radiation
E_Diss	Energy dissipated at a shock front
E_in	Incident laser energy
E_L	Laser pulse energy
E_mech	Mechanical energy
E_out	Transmitted laser energy
E_rad	Energy radiated by a plasma
E_S	Energy in shock wave
$E_S^{Gilmore}$	Energy in the shock near the plasma calculated using the Gilmore model
$\mathrm{E}_{\mathrm{S/10mm}}$	Shock energy at a distance of 10 mm from the source
E_th	Experimental energy threshold for optical breakdown
$E\mathrm{v}$	Energy of vaporization of the fluid within the plasma volume
ΔE	Energy difference between the conduction and valence bands
$\Delta E\bullet$	Difference between the energies for 10% and 90% breakdown probability

f	Focal length of a lens
F	Bjerknes force
F_{th}	Experimental fluence threshold for optical breakdown
g	Rate of diffusion of electrons out of the focal volume
h	Enthalpy
H	Difference in enthalpy between the fluid at the edge of a bubble and in the fluid at a large distances
$\hbar$	Planck's constant
I	Irradiance, impulse
I_{c}	Calculated threshold for optical breakdown through cascade ionization if a minimum seed electron density is available
I_{m}	Calculated threshold for the minimum free electron density produced by multiphoton ionization required for optical breakdown through cascade ionization
I_{mc}	Calculated optical breakdown threshold if multiphoton ionization and cascade ionization contribute to plasma formation throughout the entire laser pulse
I_{mp}	Calculated threshold for optical breakdown through pure mulitphoton ionization
I_{rate}	Breakdown threshold calculated by numerical solution of the rate equation
I_{SF}	Optical breakdown threshold taking self-focussing into account
I_{th}	Experimental irradiance threshold for optical breakdown
k	Number of photons required for excitation of mulitphoton processes
l	Distance between the laser focus and the most distant part of a corneal lesion
L	Overall length of plasma
m_{e}	Mass of an electron
m'	Reduced exciton mass
M_{w}	Mass of a water molecule
M	Parameter for describing beam quality compared to a gaussian beam
n	Constant in the Tait equation (n=7)
n_0	Refractive index
n_2	Proportionality constant for the nonlinear part of the refractive index [esu]
$N_{0\mathrm{min}}$	Minimum number of electrons in the focal volume required for the onset of an ionization cascade
p	Fluid pressure

p_0	Hydrostatic pressure
p_S	Post-shock pressure
p_V	Vapor pressure
p_{dyn}	Dynamic flow pressure
p_{WH}	Water hammer pressure
P	Pressure in the interior of a bubble
P_{cr}	Critical power at which diffraction and self-focussing are equal
$P_{cr}^{'}$	Critical power for beam collapse through self-focussing
P_L	Laser power
P_{th}	Experimental power threshold for optical breakdown
r	Radial distance
r_a	Radius of an aperture
r_g	Radius of a laser beam at the $1/e^2$ level
r_m	Distance from the source of a shock wave at which the shock pressure is measured or calculated
r_L	Radius of a laser lesion
R	Reflection, Bubble radius, Damage range
R_0	Radius of a cavitation bubble whose volume corresponds to the plasma volume at the end of the laser pulse
R_{max}	Maximum radius of a cavitation bubble
R_n	Equilibrium radius of a cavitation bubble
R_{na}	Equilibrium radius of a cavitation bubble at the beginning of the laser pulse
R_{nb}	Equilibrium radius of a cavitation bubble at the end of the laser pulse
s	Distance between a bubble center and a neighboring boundary surface
S	Scattering
S	Steepness of the optical breakdown threshold
t	Time
t_L	Laser pulse duration
T	Transmission, temperature
T_c	Collapse time of a cavitation bubble
u	Particle velocity in a fluid

u_B	Experimentally determined bubble wall velocity
u_p	Post-shock particle velocity
u_s	Shock front velocity
U	Bubble wall velocity
v	Flow (stream) velocity
v_B	Average bubble wall velocity during collapse of a gas bubble
$\bar{\mathrm{v}}_e$	Average electron velocity
$\bar{\mathrm{v}}_p$	Average plasma front velocity
V_f	Focal volume
V_p	Plasma volume
ΔV_n	Increase in volume of a bubble with equilibrium radius R_n
W	Probability of multiphoton processes, Work
z_R	Rayleigh length
$z_{\max}$	Maximum plasma length from the beam waist in the direction of the laser
α	Absorption coefficient, Angle of observation
α_{LIB}	Plasma absorption coefficient
β	Laser pulse energy relative to the energy threshold for optical breakdown
γ	Proportionality constant for the nonlinear part of the refractive index [cm^2/W], Dimensional distance between the center of a cavitation bubble and a neighboring boundary surface $\gamma = s/R_{\max}$.
δ	Displacement of tissue during passage of a shock wave, Penetration depth of heat diffusion
$\bar{\varepsilon}$	Average electron energy
ε_0	Vacuum dielectric constant, Internal energy of the uncompressed fluid under normal conditions
ε_s	Post-shock internal energy of the fluid
$\Delta\varepsilon$	Increase in internal energy as a shock front passes
ε_{LIB}	Energy density in the breakdown volume
ζ	Plasma emissivity
η_{mp}	Multiphoton ionization rate
η_{casc}	Cascade ionization rate
η_{rec}	Recombination rate

η_{cr}	Cascade ionization rate that generates the critical electron density ρ_{cr} during a laser pulse
φ	Angle between the optical axis and the direction of emission of the light transmitted or scattered by the plasma
Φ	Aberration function of a lens
κ	Ratio of the specific heats at constant pressure and volume, Thermal diffusivity
λ	Wavelength of light
Λ	Characteristic diffusion length for electrons between two collisions
μ	Dynamic shear viscosity
ρ	Electron density in plasma, Density of a fluid
ρ_0	Electron density at the beginning of an ionization cascade, Density of fluid under normal conditions
$\rho_{0\,\mathrm{min}}$	Minimum electron density required for the onset of an ionization cascade
ρ_{cr}	Critical electron density, in terms of which optical breakdown is defined
ρ_{T+S}	Energy density per steradian of radiation transmitted through and scattered by a plasma
ρ_S	Post-shock fluid density
ρ_i	Density of medium i
σ	Surface tension
σ_a	Inverse bremsstrahlung absorption cross section
σ_B	Stefan-Boltzmann constant
τ	Average electron-heavy particle collision time
τ_S	Duration of shock wave
θ	Focal angle
ν_m	Maximum of the spectral energy distribution of a black body emitter
ω	Radius of a laser beam at the $1/e^2$ level
ω_0	Focal spot radius
ω_L	Angular frequency of light
ω_p	Plasma frequency
ξ	Geometric parameter

1 Introduction

Since its introduction into ophthalmology by Krasnov (1977), Fankhauser, et al. (1981), and Aron-Rosa, et al. (1980), photodisruption by short, intense laser pulses has come into widespread use because it makes noninvasive, intraocular microsurgery possible. Photodisruption depends on nonlinear absorption of light at a laser focus, by which a plasma with a temperature of a few thousand Kelvin [Bar68, Sto94] is produced. This nonlinear absorption process, which is also known as "optical breakdown," makes it possible to deposit the laser energy within spatially limited regions in transparent ocular structures, as well as in pigmented tissue [Vog88b, Vog97a]. This possibility opens up a wide field of intraocular laser applications [Ste85, Fan89]. This dissertation is devoted to a study of the physical mechanisms of photodisruption in water and ocular media for the purpose of determining the optimum laser parameters for existing laser surgical procedures and opening up possible new areas of application by shortening the laser pulse duration from the nanosecond to the picosecond or femtosecond range.

1.1 Optical breakdown in gases, solids, and liquids

By the early 1960's, shortly after the discovery of the laser, it was possible to obtain "giant" pulses with pulse lengths in the nanosecond range and peak powers in the megawatt range by Q-switching the laser cavity [Hel61, Koe88]. When these laser pulses were focussed, they could produce irradiations exceeding 10^{10} W/cm^2. In 1963, Maker, Terhune, and Savage reported at the International Conference on Quantum Electronics in Paris that these high irradiances would cause formation of a plasma in the focal region that would absorb most of the incident laser energy [Mak64]. The start of the avalanche ionization process leading to plasma formation [Rai66, Bas72] is facilitated by the presence of linear absorbing structures in the focus, but it also takes place at higher irradiances in optically transparent media, in gases [Mey63, DeM69, Gre75, Smi76, Wey89], as well as in solids [Blo74] and liquids [Sac91]. Since the absorption by the medium depends on the irradiance of the laser light, the absorption process is nonlinear. Because this dependence is very strong and is only observed above a threshold value, it leads to very localized energy deposition that is confined to the region of the linear focus, as long as other nonlinear processes, such as self-focussing [Akh72, Mar75, She75] do not enter and change the intensity distribution of the laser light.

The localized energy deposition causes a rapid temperature rise and, because of the short laser pulse duration, an equally rapid rise in the pressure in the laser plasma. Thus, plasma formation is followed by an explosive expansion of the heated matter with compression of the surrounding medium. This leads to the formation of a shock wave. The details of this process and, especially, the following events, differ greatly, depending on the character of the surrounding medium. In gases, the plasma can easily expand into the surrounding gas. The situation is entirely different in solids and liquids. In solids, the expansion of the plasma often leads to fracture of surrounding structures, which, for example, can cause massive damage in optical components [Rea71, Blo74, Koe88]. In fluids, the expansion of the plasma generates a radially outward flow that leads to the formation of a cavitation bubble [Lau72, Vog86, Vog96a]. In a free liquid, the expanding bubble expands beyond the equilibrium state and then collapses because of the static pressure in the liquid. The collapse compresses the contents of the bubble and creates a high pressure inside the bubble, which leads to another oscillation of the bubble and renewed shock formation [Vog86, Vog88a]. In the neighborhood of solid boundaries, the collapse is asymmetric and is associated with the formation of a water stream (jet) as the bubble reexpands [Vog89]. Plasma production, shock formation, the appearance of a cavitation bubble, and the collapse of the bubble in the neighborhood of a solid boundary are illustrated in Fig. 1.1 for the case of optical breakdown in water.

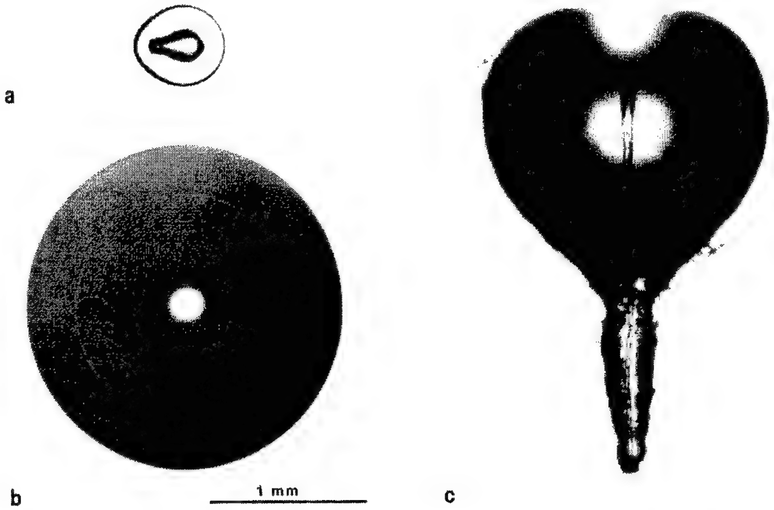

Fig. 1.1 Plasma, shock wave, and cavitation bubble produced by focussing a 5 mJ, 6 ns Nd:YAG laser pulse in water. The laser light was incident from the right. In (a) one can see the self-luminous plasma, the bubble in the beginning of its expansion phase, and the resulting shock wave 90 ns after the laser pulse. The picture in (b) was taken 130 μs after the laser pulse, when the cavitation bubble was at its maximum expansion. A solid boundary is located at the lower boundary of the picture in (c). Because of the asymmetric boundary conditions, a liquid jet develops during the collapse of the bubble and moves toward the boundary. It becomes visible during the rebound oscillation of the bubble following its collapse [Vog89]. The photograph was taken about 50 μs after the bubble had collapsed. Jet formation concentrates energy at some distance from the optical breakdown site. All pictures were taken with the same magnification.

Following the discovery of optical breakdown, laser induced plasma formation was mainly studied in gases and solids. In gases, the overall process is especially easy to study systematically and in solids, it is of great practical significance, since damage owing to plasma formation was often observed in optical components of high power laser systems. Optical breakdown in liquids drew much less attention. The first papers on optical breakdown in liquids in the 1960's [Bre64, Car66, Car67, Bel67, Bar68] were essentially limited to the study of plasma formation and the resulting acoustic effects. The approximately 1000 times slower cavitation effects (see Fig. 1.1) were either not observed or merely mentioned [Bre64]. Only in the beginning of the 1970's was attention turned to these cavitation effects [Fel72, Lau72]. Lauterborn, et al. subsequently used optical breakdown in water and silicone oil to generate spherical cavitation bubbles at specified places and at well defined times in order to investigate their dynamics in free liquids and near solid boundaries [Lau74, Lau75, Ebe78, Lau84, Vog88a, Vog89]. Greater interest in optical breakdown in liquids developed only toward the end of the 1970's and the beginning of the 1980's, when plasma mediated processes came into use in laser medicine [Git91, Vog97a], where they were used for intraocular microsurgery [Bir77, Ste84, Fan89], lithotripsy [Wat87], and angioplasty [Prin87].

1.2 Intraocular photodisruption

In the late 1970's, Krasnov introduced the use of focussed Q-switched ruby laser pulses for goniopuncture and iridotomy in glaucoma treatments [Kra77] and in 1980, Aron-Rosa et al. (1980) reported performing posterior capsulotomies following extracapsular cataract surgery employing picosecond pulse trains generated by a mode locked Nd:YAG laser. Shortly afterward, Fankhauser et al. published their first reports on laser surgery in the anterior and posterior sectors of the eye [Fan81, Fan82], which were conducted using pulses from a Q-switched Nd:YAG laser (pulse duration ≈10 ns) following extensive preliminary morphological studies [vdZ79]. The possibility of surgically operating by means of "photodisruption" on pigmented and unpigmented structures without opening the eye aroused great enthusiasm among ophthalmologists [Tro83, Ste85], as well as concerns about safety because of the explosive character of the laser effects and the fact that part of the laser light is transmitted through the laser plasma onto the retina [Mai83]. For this reason, a vigorous debate developed about the advantages and disadvantages of Q-switched lasers as opposed to mode locked lasers, which produce pulse trains of 7-10 picosecond pulses separated by 5-8 ns intervals [Koe88]. This debate initially relied primarily on the available literature about the fundamental physical effects [Tro83, Mai83, Tab83, Pul84], but specific studies were soon undertaken on the thresholds for optical breakdown [Loe83, Doc86a, Doc86b], on plasma transmission [Ste83a, Ste83b, Loe83, Cap88, Doc88c], and on mechanical laser effects [Fuj85, Vog86,Cap86, Mal87]. The major deficiency of these studies was that they dealt only with individual aspects of the complex laser-tissue interaction and it was not possible to develop a consistent overall picture on this basis. Thus, a systematic study was begun to examine the physical mechanisms of intraocular photodisruption (plasma formation, shock wave production, cavitation) and the resulting tissue effects as a research project of the DFG (Deutsche Forschungsgemeinschaft) [Bir88]. The results of these studies, which initially involved 6 ns and 30 ps laser pulse durations and were later extended to a larger range of pulse lengths, forms the basis of this dissertation.

1.3 Studies of the mechanism of intraocular photodisruption

Early efforts to explain the mechanism of photodisruption attributed the disruptive laser effects almost exclusively to the action of the plasma induced shock waves. Cavitation effects, also caused by the expansion of the plasma were, as previously in the physics literature of the 1960's, either completely ignored [Mai83, Tab83] or noted only marginally [vdZ79, Loe83, Pul84]. A different viewpoint has been raised in our papers [Vog86, Vog90], where it was found that, because of their short duration, shock waves can only produce effects on a cellular and subcellular level, while the longer lasting cavitation bubble dynamics causes tissue displacements on a macroscopic level, which are the decisive reason for the disruptive effects and unwanted side effects near the site where a laser pulse is applied. We have shown that, for a fundamental understanding of the mechanism of photodisruption, it is essential to analyze the *combined* process of plasma production, shock wave formation, and cavitation initiated by optical breakdown, including the role of boundary conditions which can decisively affect the expansion and collapse of bubbles and the interactions which may arise during repeated laser pulses [Vog90].

This dissertation is, therefore, organized in accordance with the physical processes that take place during photodisruption. *Chapter* 2 deals with various aspects of plasma production in aqueous media: the threshold for optical breakdown, the growth of the plasma size for energies above the breakdown threshold, the optical properties of the plasma, and the energy density in the plasma. In *Chapter* 3, shock wave formation and the expansion of cavitation bubbles owing to the expansion of the plasma are studied experimentally and numerically. In *Chapter* 4, the results of the previous chapters are used to develop an energy balance for the processes accompanying optical breakdown. The ratio of the fraction of energy expended in vaporization of the fluid within the plasma volume to the fraction which is converted into mechanical energy provides information on the character of the laser-tissue interaction for each laser pulse duration. *Chapter* 5 describes the cavitation bubble dynamics for different ambient conditions, including jet formation during the collapse of bubbles near boundaries, which leads to the concentration of energy at some distance from the treatment site and can, thereby, cause undesirable side effects. *Chapter* 6 is devoted to the interactions which take place during application of sequences of pulses between the bubbles created by earlier pulses and the subsequent laser pulses. These interactions can reduce the efficiency of the surgical process and also produce side effects at a relatively large distance from the treatment site. Tissue effects during intraocular photodisruption are studied in *Chapter* 7. The effects of the different physical mechanisms on the development of tissue effects are discussed and the differences in the effects of nano- and picosecond pulses are analyzed. Because femtosecond laser technology is currently developing very rapidly and studies of the potential for microscopic material processing with femtosecond pulses have begun, *Chapter* 8 provides an overview of the changes in optical breakdown that occur when the pulse duration is reduced from the nanosecond to the femtosecond range.

1.4 Strategies for optimizing photodisruption

In order to be able to optimize photodisruption with a view to minimal side effects at maximum efficiency, the dependence of the photodisruption process and tissue effects on the laser parameters is considered in each section of this dissertation. Here the important parameters are the laser wavelength, the pulse duration, the pulse energy, and the focal angle for the laser beam.

The clinically useful laser *wavelengths* are determined from the requirements that the laser light should be transmitted well through the refractive ocular media, be absorbed weakly in the ocular background, and not dazzle the patient, so these wavelengths are restricted to the near infrared. Thus, the breakdown thresholds and plasma transmission were measured at 1064 nm and 532 nm, but all the other studies were done with an Nd:YAG laser at 1064 nm.

The focal angle is an important design parameter for clinical laser systems and, depending on the position of the application site in the anterior or posterior portion of the eye, it can also be modified through the use of suitable contact lenses. In most of the studies discussed here, focal angles between 14° and 22°, which correspond to those in conventional clinical use, were employed. An extended range of angles, from 1.7° to 32°, was used in the studies of plasma formation in order to test the predictions of theoretical models and to permit an analysis of the effects of self-focussing, which mainly occur for small angles.

The *pulse duration* affects the optical breakdown threshold and, thereby, the minimum energy required for photodisruption. The energy threshold for breakdown clearly falls as the pulse duration is reduced [Doc86b], so that the damage range of the laser pulse decreases [Vog90, Zys89a] and the fineness of the single-shot effects is improved. Here the effect of single laser pulses with durations between 80 ns and 100 fs are compared. As noted above, in the early days of photodisruption, the characteristics of Q-switched laser pulses lasting a few nanoseconds were mainly compared with mode locked picosecond pulse trains. We showed in 1986, however, that the physical process initiated by a mode locked pulse train is very similar to that for a nanosecond pulse, because it depends on the combined effect of all the pulses in the pulse train [Vog86]. Therefore, a significant reduction in the threshold energy for optical breakdown and a corresponding increase in the precision of intraocular laser surgery can be attained only through the use of *single* pico- or femtosecond pulses.

In all of these studies, the *pulse energy* was varied over as wide a range as possible in order to clarify the fundamental physical behavior and provide reliable guidelines for clinical practice.

The results of the physical and tissue studies for different laser parameters are analyzed in *Chapter* 9 in order to optimize the parameters for intraocular photodisruption and the results of the first clinical trials employing picosecond pulses are reported. In addition, new applications of photodisruption with pico- or femtosecond pulses are discussed that go beyond the scope of current conventional clinical photodisruption.

2 Plasma formation

In order to be able to obtain precise and well localized tissue effects, it is important to know how the threshold for plasma formation depends on the laser pulse duration and focal angle and how these two parameters influence the length and optical properties (primarily absorption and transmission) of the plasma for pulse energies above the breakdown threshold. The threshold for optical breakdown determines the minimum energy required for intraocular laser surgery and, thereby, defines a lower bound for the fineness of the surgical effects. The plasma length or volume determine the localizability of the direct laser effects. The efficiency of the surgical procedure depends on the fraction of laser light absorbed in the plasma. The plasma transmission, along with the angular distributions of the transmitted and scattered light, determine the scale of possible side effects on sensitive tissue structures, such as the retina, behind the laser focus.

The studies of plasma formation presented here are divided into three areas: 1. First, the breakdown thresholds will be measured for different laser parameters and the experimental results compared with theoretical calculations of the thresholds based on Kennedy's (1995a) model. An extension of the model makes it possible to calculate the time evolution of the electron density before the threshold is reached. 2. For energies above the breakdown threshold, the plasma length will be studied as a function of the laser parameters and the results will be compared with the predictions of Docchio's (1988a) moving breakdown model. 3. Finally, the transmission, scattering, and reflection of the plasmas will be measured and the absorption coefficient of the plasmas will be determined from the plasma length and absorption. The experimental results will be compared with theoretical values calculated using the extended Kennedy model. The plasma energy density, which is the controlling parameter for the intensity of plasma induced mechanical effects, will also be estimated from the plasma volume and absorption.

Plasma formation was studied for pulse durations of 6 ns and 30 ps and focal angles between 1.7° and 32°. The parameters studied here cover the range of focal angles employed in clinical practice and also make it possible to understand self-focussing effects, which occur only for small angles. In order to permit a comparison of the measurements with the predictions of the theoretical model, great care has been taken to obtain well defined experimental relationships. For this purpose, the aberrations of the optical system have been minimized and, as opposed to previous studies by Loertscher (1983), Docchio, et al. (1986b), Zysset, et al (1989), and Vogel, et al. (1994), the analysis has not relied simply on diffraction limited focussing conditions, but the actual focal sizes have been measured. In order to study the effect of aberrations on plasma formation, some additional measurements were made with known aberrations in the optical system.

The influence of self-focussing effects on the breakdown threshold, the plasma shape, and plasma transmission was analyzed for small focal angles. The appearance of plasma filaments [Loy73] and continuum emission [Smi77] was invoked as a criterion for the detection of self-focussing. In order to clarify the wavelength dependence of optical breakdown phenomena, the breakdown thresholds and plasma transmission have been measured at 532 nm and 1064 nm. Most investigations have, however, been done at 1064 nm, since this wavelength is optimally suited for intraocular laser surgery (cf. 2.1.1.1).

2.1 Theoretical background

2.1.1 Linear and nonlinear absorption

The absorption properties of matter depend on the intensity of the incident light. The transmission of light to the application site for intraocular photodisruption will be determined by the linear absorption properties of the ocular medium. Only in the region of the laser focus will the intensity be high enough for nonlinear absorption processes to set in and lead to plasma formation.

2.1.1.1 Linear absorption in ocular media

During linear absorption single photons interact with atoms or molecules of the absorbing medium. Photons in the ultraviolet or visible portions of the spectrum cause electrons to be raised to higher energy levels or to be ionized, if the photon energy exceeds the binding energy of the electron. Photons in the infrared beyond about 1 μm induce rotation or vibration of the molecules. The probability of a single absorption event is proportional to the density of photons and, thereby, to the irradiance *I*.

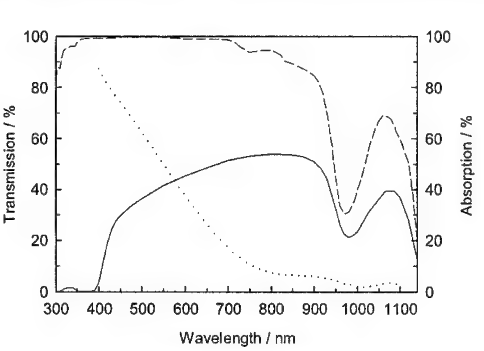

Fig. 2.1 Wavelength dependence of the direct transmission to the back of the eye (from [Boe62], smooth curve), of the transmission of pure water to the back of the eye (calculated for a Gullstrand standard eye with data from [Mah78], dashed curve), and the absorption of melanin in the retinal pigment epithelium (from [Gab78], dotted curve).

Figure 2.1 shows plots of the direct transmission of the ocular medium to the back of the eye, the transmission through a layer of water of thickness equal to the distance between the cornea and the retina, and the absorption by melanin in the retinal pigment epithelium (RPE). A comparison of these curves shows that the optical properties of the ocular media in the infrared are determined primarily by absorption in water. In the ultraviolet and blue, absorption in water only plays a subordinate role. The absorption properties of the biomolecules [Hil80] and the relatively strong scattering of light [Boe62, Sch92] are more important in this spectral region. Wavelengths in the near infrared between about 800 nm and 1150 nm are best suited for intraocular photodisruption, since here the refractive media transmit the laser light well and absorption by the melanin in the RPE, which could cause retinal damage, is low. The absorption by hemoglobin in the choroid is, likewise, low in the near infrared [Wel7, Vog92]. In addition, the laser light is invisible to the patient so there is no danger of dazzling and a sudden blinking reaction during treatment. The available equipment in this wavelength range for treatment with nanosecond and picosecond pulses includes compact Nd:YAG (1064 nm) and Nd:YLF lasers (1053 nm), and treatment with femtosecond pulses can employ Ti:Sapphire lasers [Cer94] (central wavelength 770 nm) or Nd:Glass lasers (1057 nm) [Aus98].

2.1.1.2 Nonlinear absorption

As the photon density increases, it becomes more probable that two or more photons will interact 'simultaneously' (within a time interval $\Delta t = 2\pi / \omega_L$) with a bound electron. If the sum of the photon energies equals the excitation energy of electronic, vibrational, or rotational states, then we have multiphoton absorption, and if it exceeds the binding energy of the electrons, we have multiphoton ionization [Kel65]. The probability W of multiphoton processes has a supralinear dependence on the intensity of the radiation., with

$$W = aI^k, \tag{2.1}$$

where k is the number of photons required for ionization [Nie93]. The limit $k=1$ corresponds to linear absorption. With increasing wavelength, as more photons are required to provide the corresponding excitation or ionization energy, the interaction process becomes more strongly nonlinear and, at the same time, the proportionality constant a and, thereby, the probability of multiphoton processes, decreases sharply (cf. 2.1.4.1).

In analyzing the role of multiphoton processes in optical breakdown, one must note that in solids or liquids there are no "free" electrons in the sense that there are in gases. Electrons are either bound to a particular molecule or in a lattice site, or they are "quasi-free", if they have sufficient kinetic energy to be able to move without being captured in local potential barriers. Transitions between bound and quasi-free states in condensed matter are the equivalent of ionization of molecules in gases. Sacchi (1991) has proposed, therefore, that water should be treated as an amorphous semiconductor [Wil76] and the excitation energy regarded as the energy required for a transition from the molecular $1b_1$ orbital into an exciton band (6.5 eV [Wil76, Gra79]). Six photons are necessary to produce an electron-hole pair at a wavelength of 1064 nm (photon energy 1.2 eV).

If (quasi-) free electrons exist in a medium, they can absorb photons in the non-resonant process known as *inverse Bremsstrahlung* in the course of collisions with heavy charged particles (ions or atomic nuclei) [Rea71, pp. 261-262]. A third particle (ion/atom) is necessary for energy and momentum to be conserved during the collision, as they cannot be conserved with only two particles (electron-photon). The electron gains kinetic energy during the absorption of a photon and, in a sequence of several such events, the energy gain can be so large that the electron can produce another free electron through collisional ionization. Two free electrons with low kinetic energies are now available and they can again gain energy through inverse Bremsstrahlung absorption. This process leads to an avalanche growth in number of free electrons (and, thereby, in the absorption coefficient), provided the irradiance is high enough to overcome the loss of free electrons through diffusion out of the focal volume and through recombination. The energy gain through inverse Bremsstrahlung must, moreover, be more rapid than the energy loss through collisions with heavy particles. (Electron-ion collisions are not entirely elastic, but a small part of the electron's energy, proportional to the ratio of the electron and ion masses, will be transferred to the ion.) At very high irradiance, such that the total losses can be neglected, the cascade ionization rate through inverse Bremsstrahlung will be proportional to the irradiance [She84].

While multiphoton ionization is "instantaneous," there are time constraints on cascade ionization because several consecutive inverse Bremsstrahlung absorption events are necessary for a free electron to pick up the kinetic energy required for impact ionization. When the ionization energy is 6.5 eV and the photon energy is, for example, 1.2 eV ($\lambda = 1064$ nm), an electron must undergo at least 6 inverse Bremsstrahlung events before impact ionization can occur. As mentioned above, these events can only occur during collisions of the electrons with heavy particles. Bloembergen (1974) estimates that in condensed matter the time τ between collisions is roughly 1 fs. The process thus requires at least 6 fs, even at extremely high irradiance such that almost every collision involves inverse Bremsstrahlung absorption.

Despite the time limits on inverse Bremsstrahlung absorption, it is the dominant absorption mechanism for plasma formation in condensed media (i.e., for high free electron collision rates) for pulse lengths > 40 fs [Stu96, Fen97]. This claim is based on the fact that the inverse Bremsstrahlung absorption coefficient is proportional to both the irradiance I and the free electron density, whereas multiphoton absorption depends only on I. As the free electron density increases during a laser pulse, cascade ionization becomes increasingly important compared to multiphoton ionization; within a picosecond it can lead to an increase in the charge carrier density by about a factor of 10^{12} or more [Yab72]. Nevertheless, multiphoton ionization is inevitable in linear nonabsorbing media as the source of the first free electrons for the ionization cascade.

2.1.2 Self-phase modulation

At high light intensities the refractive index of a medium changes, as well as its absorption coefficient. This leads to a modulation in the wave front within the laser beam, which depends on the intensity distribution over the beam cross section. This spatial phase modulation brings about a change in the intensity distribution (self-focussing or defocussing) that, in turn, has an effect on the nonlinear absorption process. Furthermore, during pulsed laser irradiation, the intensity dependent change in the refractive index leads to a temporal phase modulation and, since the frequency of the light is proportional to the time derivative of the phase, to a frequency modulation, as well. The pulse is, therefore, subjected to a frequency broadening, which, for sufficiently rapid variation in the refractive index can lead to the generation of a frequency "continuum," i.e., to the production of white light [She89, Nie93].

The change in the refractive index is a third order nonlinearity in connection with the electric field and the polarization induced in the medium by this field [Rie87, Nie93]. (Based on symmetry arguments, second order nonlinearities are unimportant in isotropic and point-symmetric media.) The change in the refractive index in transparent media is given by [Koe88]

$$\Delta n_0 = n_2 \left|\bar{E}\right|^2 = \gamma I \tag{2.2}$$

where n_2 or γ are the nonlinear part of the refractive index. The change in the refractive index is especially large in liquids with anisotropic molecules such as carbon disulfide (CS_2) and nitrobenzene (NB). The arbitrarily oriented molecules of the natural state reorient their polarization axes parallel to the external field in about 10 ps and, thus, acquire an intensity dependent anisotropic refractive index (molecular Kerr effect) [Rei87, She89]. The electronic Kerr effect, which is based on the deformation of the electron distribution in a medium induced by an external field, is about two orders of magnitude weaker, but has a shorter time constant of 1-10 fs [She89, Wan 89]. Since the time constant for the molecular Kerr effect is a few picoseconds, n_2 has a strong dependence on the pulse duration in "Kerr liquids" [Nie93, p. 952]. For water, on the other hand, the experimental values are roughly constant for pulse durations down to 150 fs (Table 2.1). Although, because of the polar nature of the water molecule, the molecular Kerr effect is probably also a contributing factor here, it is either weaker or its time constant is shorter than in the "Kerr liquids" owing to the smallness of the molecule.

Pulse Duration / ps	Wavelength / nm	n_2 / 10^{-13} esu	γ / 10^{-16} cm^2 W^{-1}
40000 [Pai69]	694	0.9	2.9
60 [Roc93]	532	1.3 ± 0.6	4.1 ± 1.9
30 [Smi77]	1064	1.7 ± 0.85	5.4 ± 2.7
10 [Ho79]	1064	1.3	4.1
3 [Roc97]	580	1.3	4.1
0.15 [Nib95]	808	1.8 ± 0.16	5.7 ± 0.5

Table 2.1 Nonlinear refractive index of water for different wavelengths and pulse durations.

2.1.2.1 Self-focussing

If a high intensity laser beam with a gaussian cross section propagates in water, then, according to Eq. (2.2), the refractive index in the center of the beam will be higher than at the edge. Therefore, the wave fronts move more slowly in the center than at the periphery, so that they will be deflected toward the axis as by a convex lens. This deflection is countered by the tendency of the beam to expand through diffraction. At a certain critical power

$$P_{cr} = \frac{c\lambda^2}{32\pi^2 n_2} \tag{2.3}$$

the diffraction and self-focussing for paraxial rays are exactly in balance [Mar75]. This effect depends solely on the laser power, but not on the intensity. If the beam cross section is reduced for a fixed power, the intensity and Δn are increased, but at the same time the diffraction induced beam divergence is enhanced, so that the overall result remains the same. If the laser power is raised above P_{cr} , the beam will be focussed and the radiation intensity on the optical axis will be increased, which causes the refractive index to rise further. Above a power threshold

$$P_{cr}' = 3.77\, P_{cr} \tag{2.4}$$

this self-amplifying effect leads to an extreme focussing to a small point with very high intensity [Mar75]. The factor of 3.77 is derived from a numerical solution of the nonlinear wave equation for a gaussian beam cross section. For water, the value of n_2 given in Table 2.1 for 1064 nm and 30 ps yields $P'_{cr} = 2.38 \pm 1.2$ MW.

In focussed beams, self-focussing causes a reduction of the "linear" focal diameter. For diffraction limited focussing of a gaussian beam with a power $P<P'_{cr}/4$, the reduction in the focal spot size is approximately [Soi89]

$$\omega_0' = \omega_0 / \sqrt{1 - P / P_{cr}'} \tag{2.5}$$

At higher powers, the reduction in the focal spot size must be calculated numerically [Mar75].

During laser pulses with a peak power $P>P'_{cr}$ and a pulse duration considerably longer than the time constant for the intensity dependent refractive index, the site of the focus produced by collapse of the beam moves toward the laser along the optical axis. This motion is quite complex: when $P_{cr}' < P < 2P_{cr}'$, for example, the focus splits into two foci immediately after collapse of the beam, with one propagating forward along the optical axis and the other at first moving opposite to the beam direction and then also travelling in the forward direction [Loy73, She84]. In cases where the radiant intensity at the focus results in plasma formation, the track of the focal spot movement shows up as a plasma filament in time integrated photographs.

If the pulse duration is of the same order of magnitude as the time constant for the change in the refractive index, then the dynamics of the focal spot movement will be different. The leading edge of the pulse only "sees" a small Δn and, therefore, diverges as a result of diffraction. The middle of the pulse encounters the larger Δn created by the leading edge and self-focussing takes place. Δn increases further and self-focussing is enhanced in the latter part of the pulse. In this way, a funnel shaped narrowing of the beam cross section takes place from the front to the back of the pulse. A picosecond pulse can propagate a substantial distance in this state ("dynamic self trapping"), and the time integrated trace of this motion is a filament formed in the "neck" of the funnel [Loy73, She 75]. In liquids, where the change in the refractive index is predominantly caused by the molecular Kerr effect, the time constant for the change in the refractive index amounts to a few picoseconds [She75, Nie93] and the mechanism for self-focussing differs for nano- and picosecond pulses. The constancy of n_2 for water between 60 ps and 150 fs (Table 2.1) indicates that the time constants for the mechanisms relevant to the changes in the refractive index are shorter than 150 fs. The phenomenon of dynamic self-trapping should, therefore, be less pronounced in water for pulses lasting >150 fs than for Kerr liquids.

The detection of plasma filaments with a diameter smaller than the diffraction limited diameter of the linear beam waist is good evidence of the appearance of self-focussing during laser-induced plasma formation. The diameter of the plasma filaments cannot, however, be arbitrarily small, for the high density of free electrons in the plasma makes a negative contribution to the real part of the refractive index, which opposes the original change in the refractive index and, therefore, has a self defocussing effect [Yab72, Mar75]. Assuming that the power in a filament is of order $P\bullet_{cr}$ and that the radiant power is on the order of the threshold for optical breakdown, I_{th}, (so that the laser induced free electron density is high enough to compensate the original Δn), we obtain a minimum filament diameter of 3-10 μm [Yab72].

2.1.2.2 Formation of a continuum

In addition to filament formation, the appearance of continuum radiation is a criterion for self-focussing. Smith et al. [Smi77] observed that the threshold for the appearance of a visible continuum during focussing of 30 ps Nd:YAG laser pulses in water always lies *above* the thresholds for optical breakdown and filament formation. They attributed this to the fact that the extraordinarily rapid time variation in the nonlinear refractive index during the motion of the focus produced by beam collapse (a rise in the refractive index during the self-focussing phase and a drop during plasma formation) produces an especially marked spectral broadening of the laser light through self phase modulation [She89]. The spectral components, which have been broadened through rapid phase modulation, will then be further amplified [Smi77] by means of stimulated Raman processes and parametric four-photon interactions [Pen77] and can be detected easily by visual observation or photographically.

2.1.2.3 Influence of self-focussing on nonlinear absorption

If self-focussing effects lead to beam collapse, the local irradiance will increase suddenly, causing an increase of the nonlinear absorption which usually leads to optical breakdown. The pulse energy required for breakdown decreases owing to the beam collapse and the plasma shape is modified because of filament formation. The narrowing of the laser light cone changes the irradiance distribution up to a large distance behind the linear focus. It is, therefore, of great significance for intraocular photodisruption to establish the conditions under which plasma formation would be modified by self-focussing. The fact that self-focussing depends on the laser power, while optical breakdown depends on the irradiance, means that the relative importance of the two processes varies with the focusing angle. For small focal angles, higher laser powers are required to attain radiation powers sufficient for optical breakdown because of the large focal spot diameter. Self-focussing, therefore, becomes more important for smaller focal angles. It, likewise, becomes more significant as the laser pulse duration is reduced, since higher irradiances and, consequently, higher laser powers are then needed to produce breakdown [Fen97].

2.1.3 Thresholds for optical breakdown

For sufficiently high irradiance, a combination of the nonlinear processes described above lead to an "optical breakdown," during which the material at the focus of the laser becomes partially or fully ionized. The expression is based on an analogy with electrostatic breakdown, which occurs when very high dc fields are applied to electrical insulators [Blo74]. A critical free electron density of $\rho_{cr} = 10^{18}$ cm^{-3}, which already produces a measurable diminution in the transmission through the laser focus, is customarily taken as the optical breakdown threshold [Bar68, Yab72, Blo74]. For breakdown in condensed matter, however, a distinctly higher electron density on the order of 10^{20} cm^{-3} or above is necessary [Bar68]. An electron density of this magnitude represents a degree of ionization of 1.5×10^{-3} in water [Bar68, Ken95a].

When nano- and picosecond pulses are employed, optical breakdown is accompanied by the formation of a luminous plasma [Bar68, Vog96c] that is well suited to experimental detection of its optical flash. With shorter laser pulses, on the contrary, there is no plasma emission in the visible region of the spectrum, and breakdown can only be detected by observing the formation of a cavitation bubble [Ham96, Noa98a].

In order for an ionization cascade leading to plasma formation to occur, a few free electrons must be available in the focal volume at the beginning of the laser pulse. They can be produced either by heating of linearly absorbing impurities in the fluid or by multiphoton ionization. Because of the uncertainty as to whether a given irradiance will produce a sufficient number of initiating electrons for development of a cascade, the breakdown process is statistical in character. The breakdown threshold is, therefore, defined as the irradiance at which plasma formation will be observed with a 50% probability.

2.1.4 Plasma formation at the breakdown threshold

In order to determine theoretically the irradiance I_{th} required to achieve a critical electron density, the time evolution of the electron density ρ under the influence of the laser light must be calculated. The time evolution of the electron plasma and its energy distribution are described exactly by the Fokker-Planck equation [Spa81, Jon89, Stua96]. However, the scattering rates for electrons, which are required to solve this equation, depend on the state of the matter and are unknown for water. Therefore, a simplified model must be invoked for describing the development of a plasma. For this purpose a rate equation of the form

$$\frac{d\rho}{dt} = \eta_{\mathrm{mp}} + \eta_{\mathrm{casc}}\,\rho - g\,\rho - \eta_{\mathrm{rec}}\,\rho^2 , \tag{2.6}$$

applies, where the first two terms represent the production of free electrons through multiphoton and cascade ionization, and the last two the losses through diffusion of electrons out of the focal volume and recombination. A similar approach has been followed by previous authors [Smi76, She84, Ken95a, Niem95, Stua96, Noa98a], however, only Stuart (1996) and Noack (1998a, Noa99) have considered all the terms. The cascade ionization rate and the diffusion loss rate are proportional to the number of already produced free electrons, while the recombination rate is proportional to ρ^2, as it involves an interaction between two charged particles.

Equation (2.6) is based on the assumption that the ionization and loss rates do not vary during breakdown. This seems to be correct for ultrashort pulses, as the lattice temperature can barely change during a pulse [Stu96]. For nano- and picosecond pulses, however, such a simplification is too crude, as the increase in the free electron density is accompanied by a rise in the temperature and pressure, which leads to a transition from a fluid state of aggregation to a supercritical state in which the "amorphous semiconductor" band structure (cf. 2.1.1.2) is lost and the water molecules dissociate [Rob96]. Obviously, in the end phase of the ionization avalanche, one can no longer assume an energy of 6.5 eV for the production of quasi-free electrons, but must rely on the ionization energy for the water molecule, 12.6 eV, or its dissociation products (13.6 eV for both hydrogen and oxygen). This trend is opposed by the fact that the gain in temperature and pressure in the focal volume leads to a change in the Boltzmann distribution of the electrons and, thereby, on the average, to a simpler ionization process.

If the free electron density ρ is high enough that the plasma frequency

$$\omega_p^2 = \frac{\rho e^2}{m_e \varepsilon_0} \tag{2.7}$$

equals or exceeds the angular frequency ω_L of the incident light, the bulk of the light will be reflected and further energy coupling is prevented [Hug75]. (m_e is the mass of an electron, e is the charge on an electron, and ε_0 is the vacuum dielectric permittivity.) The "plasma frequency" is the frequency at which displaced electrons oscillate about their equilibrium position. If the plasma frequency exceeds that of the light, then the electron motion can follow the laser frequency. The medium is then highly reflective and has a high absorption coefficient. The critical electron density for the case $\omega_p = \omega_L$ is

$$\rho_{cr} = \omega_L^2 \frac{m_e \varepsilon_0}{e^2} \tag{2.8}$$

For λ = 1064 nm it amounts to 1.0×10^{21} cm^{-3}, i.e., it lies about an order of magnitude above the threshold for plasma formation.

Any change of the ionization rate because of a disintegration of the band structure, a change of the Boltzmann distribution, or an increase of the reflection from the plasma happens at the end of the ionization avalanche. It does, indeed, modify the attainable electron density, but probably has little influence on the threshold for optical breakdown.

In the following the individual terms in the rate equation (2.6) will be discussed in the form presented by Kennedy [1995a].

2.1.4.1 Multiphoton ionization

The dependence of the transition rate for electrons between the conduction and valence bands on the irradiance I was first calculated quantum mechanically by Keldysh [Kel65]. The radiation field was described classically as a plane wave. The transition rate (for simplicity, referred to as the "ionization rate" below) is calculated from the wave functions for the free and bound ground states of the electron. It is a function of the frequency of the electromagnetic radiation. The transition can take place through a multiphoton interaction, as well as through tunneling of the band gap for sufficiently high electric fields. If the period of the applied field is shorter than the time for the electrons to cross the barrier, then multiphoton ionization will predominate. This is the case for the irradiances considered by Keldysh [Kel65] and in the present work. The multiphoton ionization rate per unit volume and time can then be written approximately as [Ken95a]

$$\eta_{\mathrm{mp}} \approx A(BI)^k , \tag{2.9}$$

where

$$A = \frac{2\omega_L}{9\pi}\left(\frac{m'\omega_L}{\hbar}\right)^{3/2} e^{2K}\Phi\left(2k - \frac{2\Delta E}{\hbar\omega_L}\right)^{1/2}$$

and

$$B = \frac{e^2}{16m'\Delta E\omega_L^2 c\varepsilon_0 n_0}.$$

$\Phi(z)$ is the Dawson integral

$$\Phi(z) = e^{-z^2}\int_0^z e^{y^2}dy \;=\; e^{-z^2}\sum_{n=0,\infty}\left[z^{2n+1}/n!(2n+1)\right].$$

Here k is the minimum number of absorbed photons required to surmount a band gap of width ΔE, ω_L is the angular frequency of the incident light, e is the electronic charge, $m' \approx m_e/2$ is the reduced exciton mass, c is the speed of light in vacuum, ε_0 is the vacuum dielectric permittivity, and n_0 is the refractive index at frequency ω_L.

If the laser light interacts with the medium for a time Δt, a free charge carrier density

$$\rho = \Delta t W = \Delta t A(BI)^k \tag{2.10}$$

will be produced. Equation (2.10) yields the *threshold I_{mp} for optical breakdown through pure multiphoton ionization*, and if ρ is set equal to the critical electron density ρ_{cr}, then

$$I_{mp} = \frac{1}{B}\left(\frac{\rho_{cr}}{A\Delta t}\right)^{1/k} \tag{2.11}$$

The *threshold I_m for production of the minimum free electron density ρ_{0min} required for initiation of cascade ionization* is, accordingly,

$$I_m = \frac{2}{B}\left(\frac{\rho_{0min}}{A\Delta t'}\right)^{1/k} \tag{2.12}$$

2.1.4.2 Cascade ionization

If quasi-free electrons are already present in the focal volume of the laser beam, they can absorb electrons in the course of collisions with heavy particles (inverse Bremsstrahlung, cf. 2.1.1.2). The quasi-free electrons can produce more free electrons through impact ionization as soon as their kinetic energy has reached the band gap energy of the water molecule in the course of a series of collisions. As the new free electrons created in this way are also accelerated in the conduction band, avalanche multiplication of the charge carriers takes place. If an electron does not absorb a photon during a collision with the much heavier molecules, it loses energy, rather than gaining it, in this collision.

Following Shen (1984), Kennedy described the average electron energy $\bar{\varepsilon}$ in terms of a classical model for the electron, which moves freely among the atoms until collisions occur. The average electron energy obeys the following equation:

$$\frac{d\bar{\varepsilon}}{dt}=\left(\frac{e^2\tau}{m_e c\, n_0 \varepsilon_0(\omega_L^2\,\tau^2+1)}I-\frac{2m_e\,\omega_L^2\,\tau\bar{\varepsilon}}{M_W(\omega_L^2\,\tau^2+1)}\right) \tag{2.13}$$

Here m_e and M_W are the masses of the electron and water molecule, respectively, and τ is the mean time between collisions. The first term represents the energy gain through inverse Bremsstrahlung and the second, the collisional energy loss. Assuming that every electron whose energy exceeds the band gap energy ΔE immediately produces another free electron through collisional ionization, we obtain the cascade ionization rate η_{casc} per electron by dividing Eq. (2.13) by ΔE:

$$\eta_{\text{casc}}=\left(\frac{e^2\tau}{m_e\; c\; n_0\,\varepsilon_0\,(\omega_L^2\,\tau^2+1)\Delta E}I-\frac{m_e\omega_L^2\,\tau}{M_W\,(\omega_L^2\,\tau^2+1)}\right) \tag{2.14}$$

Here we have assumed for simplicity that the average energy $\bar{\varepsilon}$ of all the quasi-free electrons equals $\Delta E/2$.

Using Eq. (2.14), Kennedy (1995a) derived an expression for the intensity I_C required to attain the critical electron density ρ_{cr} when thermal ionization or multiphoton ionization have already produced an initial electron density ρ_0 and cascade ionization predominates as breakdown evolves further. Kennedy started with a simplified form

$$\frac{d\rho}{dt}=(\eta_{\text{casc}}-g)\rho \tag{2.15}$$

of the rate equation (2.6). Equation (2.15) has the solution

$$\rho(t)=\rho_0\,e^{(\eta_{casc}-g)t} \tag{2.16}$$

Attainment of the critical electron density ρ_{cr} during a breakdown time Δt requires a critical ionization rate η_{cr}. Equation (2.16) yields

$$\eta_{cr}=g+\frac{1}{\Delta t}\ln\left(\frac{\rho_{cr}}{\rho_0}\right). \tag{2.17}$$

Setting $I=I_C$ in Eq. (2.14) yields a second relationship for η_{cr}. On substituting Eq. (2.17) in Eq. (2.14), we obtain the cascade ionization threshold I_C,

$$I_c = \left(\frac{m_e c n_0 \varepsilon_0 \Delta E(\omega_L^2 \tau^2 + 1)}{e^2 \tau} \right) \left[g + \frac{1}{\Delta t} \ln\left(\frac{\rho_{cr}}{\rho_0} \right) \right] + \frac{m_e^2 \omega_L^2 c \, n_0 \varepsilon_0 \Delta E}{M_W e^2} \tag{2.18}$$

Here it is assumed for simplicity that the intensity of the light is unchanged during the time interval Δt.

2.1.4.3 Diffusion and recombination losses

A portion of the free electrons produced by multiphoton or cascade ionization will diffuse out of the focal volume during the laser pulse and no longer contribute to the ionization cascade. The rate g at which electrons diffuse out of the focal volume is

$$g = D / \Lambda^2, \tag{2.19}$$

where D is the diffusion coefficient and Λ is the characteristic diffusion length. The diffusion constant $D = \overline{v}_e l / 3$ [Zel66] is determined by the average electron velocity $\overline{v}_e = \sqrt{2\overline{\varepsilon} / m_e}$ and their mean free path length $l = \tau \overline{v}_e$:

$$D = 2\overline{\varepsilon}\tau / 3m_e \approx \Delta E \tau / 3m_e . \tag{2.20}$$

Assuming a cylindrical focal volume with a diameter equal to the focal diameter 2 ω_0 of a gaussian beam and a length equal to the Rayleigh length $z_R = \pi\omega_0^2 / \lambda$, the diffusion length is [Smi76]

$$\frac{1}{\Lambda^2} = \left(\frac{2{,}4}{\omega_0} \right)^2 + \left(\frac{1}{z_R} \right)^2 \tag{2.21}$$

The significance of the electron losses through diffusion out of the focal volume can be evaluated by comparing the values of g and $\Delta t^{-1} \ln(\rho_{cr} / \rho_0)$ in Eq. (2.18). For a 10 ns laser pulse duration, a 10 µm focal spot diameter, an average time $t = 10^{-15}$ s between two collisions [Blo74], and $\rho_{cr} = 10^{20}$ cm^{-3}, electron diffusion changes I_C by less than two percent. Thus, diffusion losses begin to play a significant role in the optical breakdown of condensed media only for pulse lengths well over 10 ns.

Electron losses through recombination, i.e., through transitions from the conduction into the valence band, were completely neglected by Kennedy. The neglect of recombination losses is, however, only permissible for low electron densities. Because they are proportional to ρ^2, recombination losses play an increasingly important role as the electron density increases. The main effect of these losses is a limitation on the maximum electron density that can be attained during breakdown, but they have little influence on the threshold value (cf. 2.3.1.6).

I am unaware of any theoretical derivation of the recombination rate η_{rec} in water. Docchio [88d] obtained a value of $\eta_{rec} \approx 2 \times 10^{-9}$ cm^3/s from an analysis of the duration of the plasma light emission during optical breakdown with picosecond pulses.

2.1.4.4 Analytical calculation of the threshold

Kennedy (1995a) was the first to calculate the threshold intensity I_{th} for producing the critical electron density for optical breakdown. In order to avoid having to solve the rate equation (2.6) numerically and to obtain analytic formulas for calculating the threshold intensity, he made a few simplifying assumptions:

1. Kennedy assumed that the intensity of the light is constant during the laser pulse. The ionization rate is, therefore, time independent.

2. Charge carrier production was divided into two steps that follow one another in time. In the first step an initial electron density ρ_0 is produced by multiphoton ionization. It is then raised to the critical electron density by pure cascade ionization over the rest of the pulse. Dividing the breakdown process into two phases makes it possible to determine the threshold I_m for production of seed electrons using Eq. (2.12) and the threshold I_C for attainment of the critical electron density through an ionization cascade using Eq. (2.18). The radiation intensity I_{mp}, above which the critical electron density for optical breakdown can be reached through multiphoton ionization alone, can be calculated using (Eq. (2.11)).

3. It was assumed that a tenth of the laser pulse duration t_L is available for production of the initial electrons through multiphoton ionization. A time of $0.9t_L$ was assumed for completion of the ionization cascade in the case of femtosecond pulses and a time $\Delta t = 0.5\ t_L$ for picosecond and nanosecond pulses. (This quite arbitrary distinction was justified by the assumption that, in long pulses, the critical electron density is reached right at the time of the intensity peak of the pulse.)

4. The initial density ρ_{0min} of free electrons required for onset of the ionization cascade was calculated assuming that a constant number N_{0min} of initial electrons ($N_{0min} = 1$ for ns-pulses and $N_{0min} = 10$ for ps-pulses) are required for initiation of the ionization cascade, regardless of the focal volume. ρ_{0min} is then given by $\rho_{0min} = N_{0min}/V_f$ in terms of the focal volume V_f, which is approximated by a cylinder with diameter $2\ \omega_0$ and length $z_R = \pi\omega_0^2 / \lambda$.

5. For pulse durations in the nanosecond and picosecond range, the attainment of a critical electron density $\rho_{cr} = 10^{20}\ \text{cm}^{-3}$ was used as a breakdown criterion based on the estimate of Barnes and Rieckhoff (1968) for the plasma electron densities obtained with ns-pulses. For pulse lengths ≤ 3 ps, it was assumed that $\rho_{cr} = 10^{18}\ \text{cm}^{-3}$. The lower value of ρ_{cr} for ultrashort laser pulses was motivated by the absence of visible plasma light. The average time τ between collisions of free electrons with heavy particles was taken to be $\tau = 10^{-15}$ s following Bloembergen's estimate for condensed matter [Blo74].

Which of the calculated threshold intensities I_m, I_C, or I_{mp} represents the actual threshold I_{th} for a given laser pulse duration depends on the importance of multiphoton and cascade ionization in the case at hand, which, in turn, depends on the pulse length and wavelength of the laser. Three scenarios can be distinguished:

1. *Long pulses.* Long laser pulses imply that a relatively long time is available for charge carrier multiplication through cascade ionization. Thus, the threshold I_C is lower than the threshold I_m for initial charge carrier production through multiphoton ionization. In pure media, I_m corresponds to the measured threshold, since multiphoton ionization is necessary for production of the initial electrons. In media with linear absorption or impurities, where enough initial electrons can be formed by thermal ionization, the measured threshold is given by I_C.

2. *Short pulses.* The time available for the ionization avalanche is reduced, so that a higher light intensity is required to reach the critical electron density. As the dependence of the multiphoton ionization rate on the intensity ($\eta_{mp} \propto I^k$, Eq. (2.9)) is much stronger than that of the cascade ionization rate ($\eta_{casc} \propto I$ if losses are neglected, (Eq. 2.14)), multiphoton ionization contributes increasingly to the production of free electrons throughout the whole laser pulse. Thus, we now have $I_c > I_m$ and the measured threshold lies between I_C and I_m. Impurities now scarcely cause a drop in the measured threshold, since the decisive barrier to breakdown is no longer the production of initial electrons, but completion of the ionization cascade during the laser pulse.

3. *Ultrashort pulses.* For pulse durations of <<1 ps, cascade ionization alone cannot cause optical breakdown no matter how high the radiation intensity, since every doubling of the electron density in the cascade requires a time of at least 6 fs (cf. 2.1.1.2). In the limiting case of extremely short pulses with $\tau < 40$ fs, the number of electrons produced by multiphoton processes ultimately outweighs the contribution from cascade ionization [Stua96, Fen97]. The measured threshold is now given by the intensity I_{mp} which is necessary for production of the critical electron density ρ_{cr} *predominantly* through multiphoton processes.

Despite a few somewhat arbitrary assumptions, Kennedy's attempt at calculating the threshold was an important contribution to understanding the mechanisms for optical breakdown, because the separate specification of the thresholds I_m, I_C, and I_{mp} facilitated the identification discussion of the roles of multiphoton and cascade ionization for different laser pulse lengths. Kennedy's approach will be followed here for a first analysis of the experimental data. Afterwards, the solutions of the rate equation (2.6) will be presented in order to reduce the number of arbitrary assumptions in calculating the breakdown threshold I_{th}, to account for the interplay between multiphoton and cascade ionization during the entire laser pulse, and to be able to follow the evolution of the electron density during breakdown.

2.1.4.5 Solution of the rate equation for the electron density

The time evolution of the electron density, $\rho(t)$, is calculated for laser pulses with a gaussian time variation [Noa98a,Noa99]. Since free electrons must exist in the interaction volume for cascade ionization to occur, the term for cascade ionization is first included when the free electron density owing to multiphoton ionization has increased to the point where a statistical average of 0.5 electrons exist within the focal volume V_f. Optical breakdown should follow with 50% probability. In order to account for the time $\tau_{ion} = \tau k$ required for an electron to acquire the band gap energy ΔE through inverse Bremsstrahlung absorption and produce another free electron (cf. 2.1.1.2), the contribution of cascade ionization is evaluated using the electron density that was present at time $(t - \tau k)$, with $\tau = 10^{-15}$ s [Blo74]. In order to determine the breakdown threshold, the laser pulse intensity that yields a critical electron density of 10^{20} cm^{-3} is calculated iteratively.

2.1.5 Absorption coefficient of the plasma at the breakdown threshold

The time evolution $\rho(t)$ of the electron density calculated from Eq. (2.6) and the inverse Bremsstrahlung cross section σ_a can be used to calculate the time averaged absorption coefficient α_{LIB} of the plasma for energies near the breakdown threshold,

$$\alpha_{\mathrm{LIB}} = \sigma_a \frac{\int I(t)\rho(t)dt}{\int I(t)dt}. \tag{2.22}$$

Here *I(t)* is the time variation of the laser pulse. The inverse Bremsstrahlung cross section corresponds to the first term in Eq. (2.13),

$$\sigma_a = \frac{e^2\tau}{m_e c n_0 \varepsilon_0 (\omega_L^2 \tau^2 + 1)}, \tag{2.23}$$

which gives a cross section of $1{,}934\times10^{-17}$ cm^2 for $\lambda = 1064$ nm.

2.1.6 Plasma formation above the breakdown threshold

Plasma assisted laser surgery will always be performed at radiation intensities above the breakdown threshold, i.e., under conditions such that plasma formation begins at the laser focus and the plasma grows backward into the laser beam cone [Ram64a]. Because of the strong absorption of the laser light in the plasma, the plasma growth is largely limited to the side from which the laser beam is incident. An understanding of the mechanisms for the plasma growth and of the behavior which regulates the overall length of the plasma is essential for optimizing plasma assisted surgical procedures. This need is especially important for intraocular microsurgery, in which the application site is often adjacent to sensitive tissue structures that must not be affected.

The expansion of plasmas in gases has been interpreted as a radiation driven detonation wave [Ram64b, Dai67]. After plasma is first formed at the beam waist, a shock wave develops which compresses the surrounding medium and partially ionizes it within the shock front. The resulting free electrons cause increased absorption of the light and, thereby, the formation of more plasma. The advance of the plasma front, in turn, drives the shock front. This model can provide a correct description for plasma formation in gases by nanosecond pulses, where high shock speeds are attained, along with high temperatures in the shock front [Rai66], but it breaks down for short pulse durations, when the velocity of the plasma front exceeds the shock velocity. It is entirely unsuitable for describing the plasma growth in liquids. This failure can be illustrated by the following example: plasma formation in water by a 10 mJ, 6 ns Nd:YAG laser pulse creates a shock front in the water with a shock pressure at the plasma boundary of about 7000 MPa [Vog96a]. This corresponds to a temperature rise at the shock front of about 350 K [Duv63]. which is far too low to cause significant ionization. In addition, the shock speed near the plasma is only 4.5 km/s [Vog96a]. This is much lower than the experimentally observed average plasma front velocities, which lay between 12 km/s and 76000 km/s, depending on the focussing angle and pulse duration (cf. Section 2.3.2.2).

A realistic explanation for the expansion of the plasma is provided by the "moving breakdown" model originally proposed by Ambartsumyan [Amb65] and Raizer [Rai65] and further developed by Docchio, et al. [Doc88a]. In this model, it is assumed that optical breakdown is independent of the preceding plasma formation and occurs wherever the radiation intensity exceeds the breakdown threshold I_{th}. As the intensity in the laser pulse increases, the plasma front moves along the optical axis at the same velocity as the site where the breakdown threshold is exceeded at any given time. This model can explain the high plasma front velocities observed experimentally and, therefore, will serve as a basis for interpreting the following experimental results.

The original moving breakdown model was based on a conical shape of the laser beam and a triangular laser pulse shape with a linear rise in the laser power [Rai65]. This yielded a constant plasma front velocity during the rising portion of the laser pulse, contrary to experimental observations with a streak camera [Ram64ab, Dai67]. Docchio applied the concept of a moving breakdown front to pulses with a gaussian time variation and took the shape of the beam waist of the laser focus into account, assuming a gaussian beam cross section. In this way, he obtained substantially better agreement between the predicted and measured motion of the plasma front [Doc88a].

The form of the moving breakdown model presented by Docchio is based on a few simplifying assumptions: 1. The time for the completion of breakdown is negligibly short. 2. The breakdown threshold is independent of the laser beam diameter. 3. The breakdown threshold does not vary during the laser pulse, i.e., plasma formation during the pulse does not influence the breakdown threshold in the immediate neighborhood of the plasma. These assumptions yield the motion of the plasma front and the maximum extent of the plasma in the direction of the laser directly from the motion of the $I=I_{th}$ intensity contour during the pulse. The incident laser power is given by

$$P(t) = P_{\max} e^{-2(t/2A)^2} \tag{2.24}$$

for a gaussian pulse with a maximum at $t=0$, where $A = t_L / 2\sqrt{2\ln 2}$ is a measure of the laser pulse duration (FWHM) t_L. For diffraction limited focussing, where the beam cross section is also gaussian, the intensity along the optical axis is

$$I(z,t) = \frac{P_{max}}{\pi\omega^2(z)} e^{-2(t/2A)^2} \tag{2.25}$$

where

$$\omega(z) = \omega_0 \left[1 + (z/z_R)^2\right]^{1/2}, \tag{2.26}$$

and $z_R = \pi\omega_0^2/\lambda$ is the Rayleigh focal distance.

The peak intensity in the pulse compared to the threshold for optical breakdown is defined in terms of the dimensionless parameter $\beta = I_{max}/I_{th} = P_{max}/P_{th}$. P_{max} can thus be written in the form

$$P_{max} = \beta\pi\omega_0^2 I_{th}. \tag{2.27}$$

Setting $I(z,t) = I_{th}$ in Eq. (2.25), substituting Eqs. (2.26) and (2.27), and solving for t, we obtain the time for plasma formation as a function of position z along the optical axis,

$$t(z) = -A\sqrt{2\ln\frac{\beta}{1+(z/z_R)^2}}. \tag{2.28}$$

The time at which plasma formation begins in the beam waist is then given by $t_0 = t_{z=0} = -A\sqrt{2\ln\beta}$. The inverse of Eq. (2.28) is

$$z(t) = z_R\sqrt{\beta e^{-2(t/2A)^2} - 1}. \tag{2.29}$$

For $t = 0$ this gives the *maximum plasma length* attained at the intensity maximum of the laser pulse,

$$z_{max} = z_R\sqrt{\beta - 1}. \tag{2.30}$$

The laser light incident on the plasma after the intensity peak of the laser pulse only heats the plasma and does not elongate it further.

Equation (2.30) also yields the *relationship between the length of the plasma and the focal angle* θ upon substituting $z_R = \pi\omega_0^2/\lambda$ and $\omega_0 = \lambda/\pi\tan(\theta/2)$:

$$z_{max} = \frac{\lambda}{\pi\tan^2(\theta/2)}\sqrt{\beta-1}. \tag{2.31}$$

The *dependence of the plasma length on the laser pulse duration* is only implicit in Eqs. (2.30) and (2.31). Evaluation of these dependencies requires knowledge of the threshold energy E_{th} for optical breakdown for the given pulse length. Since $\beta \equiv I_{max} / I_{th} = E / E_{th}$ for constant focal conditions, the value of β corresponding to each pulse energy can then be determined from E_{th} and, from that, z_{max} can be calculated.

At this point it should be emphasized that Eqs. (2.30) and (2.31) only give the length of the plasma from the beam waist in the direction of the laser. The actual plasma length is, as a rule, somewhat greater, for there is also some expansion of the plasma in the direction opposite the laser. Of course, this expansion is greatly limited by the high absorption of laser light in the plasma. As will be shown in 2.3.2.4 and 8.2.5, only when self-focussing and defocussing occur will plasma filaments develop in the region behind the laser focus.

The moving breakdown model is no longer applicable for long laser pulse durations and large focal angles, when the expansion velocity of the heated plasma volume becomes comparable to the propagation velocity of the breakdown front. For very short laser pulse durations, where the spatial extent of the laser pulse is shorter than the observed plasma length, the assumptions of the model are, likewise, not satisfied. In this case, for pulse lengths under about 1 ps [Ken97, Noa97], the breakdown front moves in the propagation direction of the laser pulse. This movement will be affected in a complicated way by self-focussing, which will modify the focal region intensity distribution of Eq. (2.25) (cf. Section 8.2.5 and [Fen87, Noa87]). In the following, the predictions of the model for different focal angles will be experimentally checked for 30 ps and 6 ns pulse lengths.

2.2 Experimental techniques

2.2.1 Plasma formation

The experimental setup for studying plasma formation is shown in Fig. 2.2. A Nd:YAG laser system (Continuum YG 671-10), which produced single pulses lasting 6 ns or 30 ps at wavelengths of 1064 nm or 532 nm, was used. The beam profile of the ps-pulse was gaussian (TEM_{00}) and the shot-to-shot variation in the energy was within ±10%. The ns-pulses were produced in an unstable cavity in which the reflectivity of the output mirror decreased continuously from the inside outward [Mag89]. This cavity yielded a roughly gaussian beam profile with a weak ring structure (Fig. 2.3a). The shot-to-shot reproducibility of the energy was better than ±2%. The average pulse shape of the ns-pulses is shown in Fig. 2.3c. The relative height of the two intensity maxima fluctuated slightly from shot to shot. The pulse energy could be varied without affecting the beam profile using a rotatable $\lambda/2$-plate between two polarizers [Vog94a].

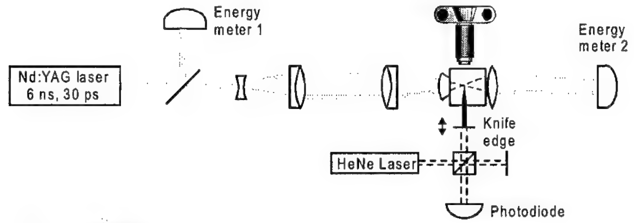

Fig. 2.2 The experimental arrangement for studying breakdown thresholds and plasma lengths.

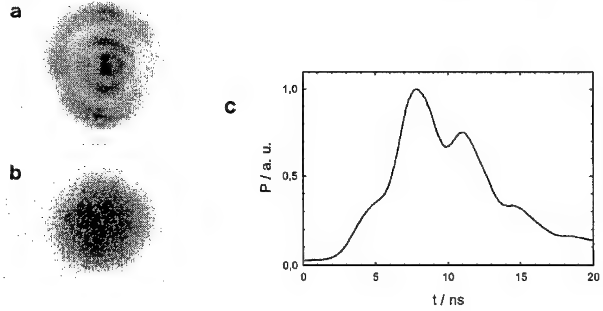

Fig. 2.3 Near-field burn spots from (a) a 6-ns pulse and (b) a 30-ps pulse on thermal print paper and (c) the pulse shape of the 6-ns pulse averaged over 500 pulses.

The laser beams were focussed into a glass cell containing distilled water. The focal angles ($1/e^2$ drop in the light intensity) were varied between 1.8° and 32° for the ns-pulses and between 1.7° and 28° for the ps-pulses. The laser beam was expanded before focussing in order to ensure a large distance between the focus and the cell wall even for large focal angles. In this way, damage to the cell could be avoided at high pulse energies. Nd:YAG laser achromats (f = 120 mm) were used to collimate and focus the laser beam and an ophthalmological contact lens (Rodenstock RYM) was installed in the cell wall in order to minimize spherical aberration. The laser focus lay at the aplanatic point of the contact lens. Different focal angles could be obtained by varying the beam expansion before focussing. The upper limit of the beam expansion is determined by the requirement that the beam profile should not be changed by vignetting at the lens mount. In order to achieve the largest focal angles (28° and 32°), suitable aplanatic meniscus lenses had to be installed between the focussing achromats and the contact lens. In order to obtain the smallest focal angles, the beam expansion was removed.

The energy was measured by deflecting part of the beam with a beam splitter and directing it onto a pyroelectric detector (Laser Precision Rj 7100). The detector was first calibrated by comparison with the readout from a second instrument installed right in front of the cell. In order to determine the energy at the laser focus, the measured energies were corrected for the absorption of the light in the water between the contact lens and the laser focus. (The optical path length was 9 mm and the absorption coefficient of water at 1064 nm is $\alpha = 0.165\ \mathrm{cm}^{-1}$ [Mah78].)

In order to obtain reproducible experimental conditions we used distilled water as the medium for optical breakdown. The water was additionally purified prior to the measurements using a 0.22 μm filter (Millipore Sterfil-D-GS). The results, however, are transferable to ocular media, as it has been established in previous studies that the thresholds for plasma formation with ns- and ps-pulses in ocular media and distilled water are very similar [Doc86a, Vog94b].

2.2.2 Determination of the focal angle and focal spot diameter

The focal angle θ was determined by measuring the diameter of the parallel beam in front of the focussing lens and calculating the further propagation of the light using a ray tracing program. The beam diameter was determined by measuring the transmission through a sequence of successively smaller apertures. For a gaussian beam profile, the transmission of the apertures is given by [Koe88]

$$T = 1 - e^{-2(r_a/\omega)^2} \tag{2.32}$$

where r_a is the aperture radius and ω is the beam radius at the $1/e^2$ intensity points. In order to determine ω, the function (2.32) was fit to the measured $T(r_a)$ data with ω as the fitting parameter.

The focal spot diameter was determined using the knife edge technique [Nah96, Sie91]. The knife edge was moved by a piezoelectric translator whose position was measured with a Michelson interferometer (Fig. 2.2). The laser pulse energies used for these measurements were kept small enough to avoid plasma formation and the resulting damage to the knife edge. The laser beam diameter was measured in different planes in the beam waist region. The shape of the beam waist is given by [Sas89]

$$\omega(z) = \omega_0 \sqrt{1 + \left(\frac{M^2 \lambda z}{\pi \omega_0^2} \right)^2} \; . \tag{2.33}$$

Here $\omega(z)$ denotes the beam cross section at position z along the optical axis, where $z = 0$ is the position of the beam waist, ω_0 is the focal spot radius, and M^2 is a parameter which describes the "quality" of the beam compared to a purely gaussian beam ($M^2 = 1$). Equation (2.33) was fit to the measured $\omega(z)$- data in order to determine ω_0.

2.2.3 Determination of the breakdown threshold

The breakdown thresholds were determined from the frequency of plasma formation as the energy was raised in steps from subthreshold to above threshold levels. 20 to 50 laser shots were evaluated for each value of the energy. The pulses were spaced 30 s apart in order to prevent plasma production on the gas bubbles which remain near the laser focus for several seconds after each laser shot. Optical breakdown was detected through the visible plasma radiation in the darkened laboratory. For this purpose, the region of the laser focus was observed with a microscope at a 20-time magnification. In order to determine the energy E_{th} for a 50% breakdown probability, the measured relative breakdown frequencies were plotted as a function of the incident energy E_{in} and fit to a gaussian error function. The slope of the breakdown threshold, $S' = E_{th}/\Delta E'$, was also determined. Here $\Delta E'$ is the energy interval between 10% and 90% breakdown probabilities.

2.2.4 Determination of the plasma shape and length

The plasma shape and length were studied by photographing the plasmas at a 7 times magnification with a Leitz-Photar macro-objective (F = 3.5). This objective provided a spatial resolution of about 4 µm. Depending on the brightness of the plasma light, Kodak T Max 400 (for ps-plasmas), Kodak T Max 100, or Agfapan APX 25 (for ns-plasmas) films were used. In order to indicate the position of the beam waist on the plasma photographs, a needle tip was positioned above the spot where plasma would form at the breakdown threshold. The plasma length z_{max} from the beam waist in the direction of the laser was measured on the photographic negatives with the aid of a microscope. In order to detect self-focussing, the negatives were searched for signs of filament formation. In addition, observations were made to see if continuum radiation appeared on a white screen mounted behind the cell. Continuum radiation is indicative of self-focussing effects (Section 2.1.2.2). The radiation was recorded using a 35 mm camera body in the path of the beam behind the cell.

2.2.5 Determination of the optical properties of the plasma

2.2.5.1 Total and time resolved transmission

The total and time resolved plasma transmission were measured using the setup of Fig. 2.4.

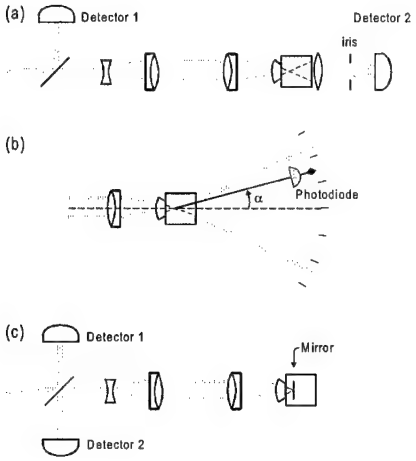

Fig. 2.4 Experimental setup for the determination of the transmission, scattering, and reflection by the plasma. (a) Total time integrated transmission (detector 2 = energy meter) and time resolved transmission (detector 2 = photodiode); (b) angular dependence of the transmission and scattering by the plasma; (c) back reflection into the focal angle.

The transmitted light was collected by a large aperture biconvex lens (N.A. = 0.55) onto a detector behind the cell. For any focal angle of the incident laser light, only transmitted light within the same angle would be collected. Stray light outside this angle was blocked by an iris diaphragm. In order to determine the energy E_{in} incident on the laser focus, detector 1 (Laser Precision Rj 7100) was calibrated against a second energy meter directly in front of the cell and the measured value was corrected for absorption in the water between the contact lens and the focus. The transmitted energy E_{out} was measured by detector 2 (Digi Rad R-752/P-444). In order to account for the light lost through absorption in the water and reflection on optical surfaces, detector 2 was calibrated against detector 1. Here it was assumed that well below the breakdown threshold, 100% of the incident light would be transmitted through the laser focus so that the losses will be caused exclusively by absorption in the water and reflection. In determining the plasma transmission for the 6-ns pulses, measurement data were recorded for 20 pulses at each energy setting (shot-to-shot variation 2%) and the transmission was calculated from the averaged values of E_{in} and E_{out}. In the case of the 30-ps pulses, for which the variation in the pulse energy was much greater (±10%), another strategy was followed. A large number of (E_{in} , E_{out}) data in various energy ranges were recorded and grouped, using a computer program, into intervals of E_{in} with a maximum width of 3%. Each interval contains at least 10 (E_{in} , E_{out}) pairs, which were then used to calculate the average transmission for the respective energy interval. Special attention was devoted to the energies near the breakdown threshold. Here it was noted whether plasma was formed or not in each laser shot, and the transmission data with and without plasma formation were evaluated separately.

The time resolved transmission was measured by means of a fast photodiode (Motorola MRD 500) with a risetime of 1.2 ns. The plasma light was blocked with an Schott LG 840 filter in front of the photodiode. The diode signal was recorded with a digital oscilloscope (Tektronix TDS 540; risetime 0.7 ns) and 1000 laser pulses were averaged for each energy setting. The laser was run at a repetition rate of 2 Hz, in order to avoid, as much as possible, any interaction of the laser pulses with the gas bubbles generated during previous pulses, which remained in the focal region for a while after each pulse.

2.2.5.2 Scattering

The forward scattering by the plasma was determined using the goniometric apparatus of Fig. 2.4b for measuring the angular dependence of the plasma transmission and scattering above and below the breakdown threshold. The photodiode was rotated around the plasma in steps of 2° for $\alpha \leq 10°$ and in steps of 5° for $\alpha > 10°$. The measurement region was limited to a maximum of 45° by the dimensions of the cell. The angular resolution was 0.2°, determined by the diameter of the detector area of the diode (1 mm) and the distance between the diode and the plasma (300 mm). The angle γ at which the light left the focal region was calculated by deducting the refraction at the cell wall from the angle α in the goniometric apparatus. For each angle, the diode signal was averaged over 1000 laser pulses on a PC. The angular dependence of the transmission and scattering were measured for normalized energies of $\beta = 0.5$ and $\beta = 15$.

The time integrated diode signal for each angle γ is proportional to the energy per steradian, ρ_{T+S}. The radiation dE_{T+S} transmitted and scattered into the element of solid angle $\mathrm{d}\Omega = 2\pi \sin\gamma \,\mathrm{d}\gamma$ is

$$\mathrm{d}E_{T+S} = 2\pi \rho_{T+S}(\gamma) \sin\gamma \,\mathrm{d}\gamma, \tag{2.34}$$

and the total transmitted and scattered energy is given by

$$E_{T+S} = 2\pi \int \rho_{T+S}(\gamma) \sin\gamma \mathrm{d}\gamma. \tag{2.35}$$

When a plasma is produced in the focal volume, it reduces the transmitted energy through plasma absorption and the angular distribution $\mathrm{d}E_{T+S}(\gamma)$ of the radiant energy behind the focus is broadened by scattering in the plasma. In order to determine the extent of forward scattering for $\beta = 15$, it is necessary to compare the angular distribution for this value of β with the distribution obtained without a plasma. This can be done by measuring the energy distribution below the breakdown threshold, for example, for $\beta = 0.5$. The distributions are normalized relative to one another by introducing the measured value of

$T(\beta = 15)$ for the total transmission within the focal angle θ, which is obtained in a separate measurement, as described in Section 2.2.5.1. The normalized $\tilde{\rho}_{T+S}(\gamma)$ and $\mathrm{d}\tilde{E}_{T+S}(\gamma)$ curves must satisfy the condition

$$\frac{\int_{-\theta/2}^{\theta/2} \tilde{\rho}_{T+S}(\gamma)_{super} \sin\gamma \, \mathrm{d}\gamma}{\int_{-\theta/2}^{\theta/2} \tilde{\rho}_{T+S}(\gamma)_{sub} \sin\gamma \, \mathrm{d}\gamma} = T(\beta)\,, \tag{2.36}$$

where the subscripts *super* and *sub* denote the cases with and without plasma formation. The forward scattering through the plasma can be estimated by comparing of the area under the normalized curves inside and outside the laser beam cone.

2.2.5.3 *Reflection*

The experimental apparatus in Fig. 2.4c was used to measure the amount of light that is back reflected from the plasma into the cone angle of the focussing optics. First, an aluminum mirror was placed in the laser focus and a measurement was made at an energy low enough that no plasma was produced on the mirror. In this way, the calibration factor between the two energy monitors could be determined from the known reflection of the aluminum mirror (about 80%). The mirror was then removed and the plasma reflection for a 6-ns pulse was measured for normalized energies in the range $3.5 \leq \beta \leq 5.5$ and for 30-ps pulses for energies in the range $1.5 \leq \beta \leq 4.3$. Data from 100 laser shots were averaged for each measurement.

2.2.5.4 *Absorption*

A direct determination of the plasma absorption would require measurements using a water filled integrating sphere. Measurements of this sort are barely feasible, since at 1064 nm water is a relatively strong absorber (the absorption coefficient is 0.165 cm^{-1}), so that the distribution of the light is no longer uniform even in a small sphere with a diameter of just a few centimeters. The plasma absorption A was, therefore, calculated from the measured values of the transmission T, scattering S, and reflection R, i.e., $A=1-T-S-R$.

2.2.5.5 *Plasma radiation*

The duration of the plasma radiation was measured by imaging the plasma with a photographic objective (Pentax 50 mm/1.8) onto the detector plane of a fast, amplified photodiode (Opto-Electronics AD 110) with a risetime of 380 ps. The signal from the diode was recorded on an analog storage oscilloscope (Tektronix 7934) with a 700 ps risetime. Stray light from the laser was blocked with an Nd:YAG blocking filter. For a comparison, the corresponding laser pulse shape was recorded using a photodiode (Antel AR-S1 with a 90 ps risetime).

2.2.6 Examination of the effect of aberrations on plasma formation

A study of the influence of aberrations on plasma formation was made for 6 ns pulses at a wavelength of 1064 nm. Spherical aberrations of known magnitude were produced in the optical system of Fig. 2.2 by replacing the achromats L_1 and L_2 with planoconvex lenses (the achromats reduce spherical, as well as chromatic, aberrations) and a larger beam expansion was used (f = -30 mm instead of f = -40 mm). The extent of aberrations can be described in terms of an aberration function F, which gives the displacement of the disturbed wave front relative to a perfect spherical wave front. For a planoconvex lens with a focal length f, radius r_a, and refractive index n_0, we have [Aar74]

$$\Phi(\rho) = -\frac{(r_a \rho)^4}{32 f^3}\left[\frac{n_0^2}{(n_0-1)^2} - \frac{n_0}{n_0+2} + \frac{\left(2n_0^{\,2} - n_0 - 4\right)^2}{n_0(n_0+2)(n_0-2)^2}\right], \tag{2.37}$$

where $\rho = r / r_a$ and r denotes the distance to the optical axis. The maximum $\Phi_{\max}$ of the aberration function is determined by the size of the lens aperture, r_a. For a ray bundle with a gaussian intensity distribution, the focal quality depends not only on $\Phi_{\max}$, but also on the position r_g of the $1/e^2$ intensity point. Therefore, $\Phi(r_g)$ will be used to characterize the magnitude of the aberrations of an optical system.

After the achromat L_1 (f = 200 mm) was replaced with a planoconvex lens with a 200 mm focal length, $\Phi(r_g)$ was 5.5 λ, and when the achromat L_2 (f = 120 mm) was, additionally, replaced by a planoconvex lens with a 150 mm focal length, $\Phi(r_g)$ rose to 18.5. (As the optical path between the two achromats is parallel, the aberration function of the combined system can be approximated by the sum of the aberration functions of the two achromats.) Relatively strong aberrations were produced so that the aberration dependent changes of the focal quality could be clearly distinguished. Such changes have played a role in earlier studies of optical breakdown [Eva69, Aar74] and may show up in intraocular photodisruption when unsuitable contact lenses are used [Rol86], when the contact lens is tilted, or when the application site lies in the periphery of the fundus (in the last two cases, primarily as coma and astigmatism).

For $\Phi(r_g) = 5{,}5\ \lambda$ and $\Phi(r_g) = 18{,}5\ \lambda$ the optical breakdown thresholds, the plasma shape and length, and the plasma transmission were determined and compared with the corresponding values for aberration minimized focussing.

2.3 Results and discussion

2.3.1 Plasma formation at the breakdown threshold

2.3.1.1 Focal spot diameter and threshold values

The measured focal spot diameters and energy thresholds E_{th} for optical breakdown, along with the corresponding intensity (irradiance) thresholds I_{th}, radiant exposure thresholds F_{th}, and power thresholds P_{th} are presented in Tables 2.2 and 2.3. For comparison, the diffraction limited focal spot sizes and the corresponding values of I_{th} and F_{th} are also listed there.

					Diffraction Limited			Measured		
λ nm	θ °	E_{th} μJ	P_{th} kW	S′	$2\omega_o$ μm	F_{th} Jcm^{-2}	I_{th} 10^{11}Wcm^{-2}	$2\omega_o$ μm	F_{th} Jcm^{-2}	I_{th} 10^{11}Wcm^{-2}
1064	32.0	90	15	2.5	2.4	2055	3.42	5.4	394	0.66
1064	22.0	141	23	2.1	3.5	1477	2.46	7.7	305	0.51
1064	8.0	493	82	2.1	9.7	669	1.12	11.5	472	0.79
1064	5.4	1082	180	2.2	14.4	668	1.11	14.6	648	1.08
1064	1.8	8023	1337	0.9	45.7	489	0.82	47.8	447	0.75
			Average:	2.0				Average:	453	0.76
532	22.0	38.5	6.4	1.5	1.7	1615	2.69	5.3	174	0.29

Table 2.2 Focal spot diameter and breakdown thresholds for 6 ns pulse duration.

					Diffraction Limited			Measured		
λ nm	θ °	E_{th} μJ	P_{th} kW	S′	$2\omega_o$ μm	F_{th} Jcm^{-2}	I_{th} 10^{11}Wcm^{-2}	$2\omega_o$ μm	F_{th} Jcm^{-2}	I_{th} 10^{11}Wcm^{-2}
1064	28.0	2.3	76	2.9	2.7	39.6	13.2	4.6	13.8	4.61
1064	22.0	2.4	79	4.9	3.5	25.0	8.34	4.7	13.6	4.53
1064	14.0	5.0	167	3.2	5.5	20.1	6.99	5.8	18.9	6.31
1064	8.5	9.9	328	3.6	9.1	15.1	5.04	9.6	13.6	4.53
1064	4.0	33.3	1110	2.9	19.4	11.3	3.76	19.6	11.1	3.70
1064	1.7	178.5	5951	3.8	45.7	10.9	3.32	47.7	10.0	3.32
			Average:	3.6				Average:	13.5	4.5
532	22.0	1.0	33.7	4.2	1.74	42.4	14.1	3.4	11.3	3.75

Table 2.3 Focal spot diameter and breakdown thresholds for 30 ps pulse duration.

For small focal angles, the measured and diffraction limited focal diameters are very similar; however, for large angles, when increased aberration sets in, the measured and diffraction limited values for the focal diameter diverge by a factor of about 2.3 for the nanosecond pulses and by a factor of 1.7 for the picosecond pulses. The divergence is smaller for the ps-pulses, since they have a pure gaussian beam profile. Before the dependence of the breakdown thresholds on the various laser parameters is discussed, we must first analyze self-focussing effects, since they can influence the threshold variations.

2.3.1.2 Self-focussing and the generation of a continuum

In order for self-focussing to occur, a critical laser power P_{cr} that is independent of the focal spot size must be exceeded. The occurrence of optical breakdown is, in contrast, coupled to the crossing of a certain irradiance threshold. As the focal diameter increases (i.e., the focal angle decreases), higher laser powers will be required in order to reach the irradiance threshold for optical breakdown. Below a certain focal angle, the laser power required for breakdown finally exceeds the critical power P_{cr} for self-focussing, and at still smaller angles it also exceeds the critical power P'_{cr} beyond which the laser beam collapses and filament formation takes place (cf. Section 2.1.2.1). We observed plasma filaments at θ = 1.8° for the 6 ns pulses and at θ = 1.7° for the 30 ps pulses (Fig. 2.5). For these focal angles, plasma formation was always accompanied by filament formation indicating self-focussing, even at the breakdown threshold.

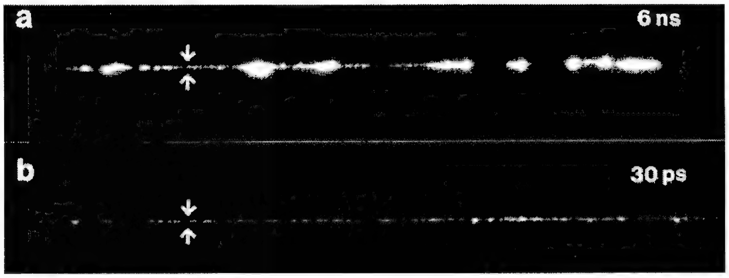

Fig. 2.5 Filament formation for small focal angles: (a) 6 ns pulse duration, 1.8° focal angle, and (b) 30 ps pulse duration, 1.7° focal angle. The arrows indicate the diameter of the beam waist measured at low laser powers.

The diameter of the filaments in Figs. 2.5a and 2.5b is about 5 μm, compared to a diffraction limited focal spot diameter of 48 μm. The filaments produced by the 30 ps pulses are uniformly thin, while those produced by the 6 ns pulses are interspersed with thick plasma spots with diameters of up to 45 μm. With ps pulses, filament formation 'downstream' of the 'linear' laser focus was also observed at larger focal angles (4° and 8.5°), but only for pulse energies well above the breakdown threshold (cf. Fig. 2.7b in Section 2.3.2.4).

The theoretical threshold for filament formation through self-focussing of gaussian beams is $P'_{cr} =$ 2.38 ± 1.2 MW (cf. Section 2.1.2.1). This value is well below the power required for optical breakdown with 30 ps pulses ($P_{th} = 5.9$ MW for $\theta = 1.7°$) and slightly above the power at which breakdown would be attained with 6 ns pulses ($P_{th} = 1.34$ MW for $\theta = 1.8°$). It lies, however, within the range of error in determining P'_{cr}. This implies that optical breakdown at a wavelength of 1064 nm for small focal angles for both ps and ns pulses will be affected by self-focussing at the threshold. This result is in accord with the data of Soileau, et al. [Soi89] on optical breakdown in solids.

The reduction in the laser beam diameter owing to self-focussing raises the irradiance and, thereby, the probability of plasma formation. The values of I_{th} given in Tables 2.2 and 2.3 refer to the focal spot size measured at low irradiances and, therefore, merely represent an estimate of lower bound for the irradiance at which breakdown has actually taken place. The beam cross section begins to decrease through self-focussing at laser powers below the threshold for radiation collapse and filament formation [Mar75]. Equation (2.5) implies that the actual breakdown threshold I_{th}^{SF} for $P_{th} \le P'_{cr}/4$ owing to the reduced beam diameter can be approximated by

$$I_{th}^{SF} = \frac{I_{th}}{1 - P_{th}/P'_{cr}}. \tag{2.38}$$

The calculated values of I_{SF} from the measurements of Tables 2.2 and 2.3 are listed in Table 2.4. No values are given for $P_{th} > P'_{cr}/4$.

6 ns				30ps			
$\frac{\theta}{°}$	$\frac{P_{th}}{\text{MW}}$	$(1-\frac{P_{th}}{P'_{cr}})^{-1}$	$\frac{I_{th}^{SF}}{10^{11}\,\text{Wcm}^{-2}}$	$\frac{\theta}{°}$	$\frac{P_{th}}{\text{MW}}$	$(1-\frac{P_{th}}{P'_{cr}})^{-1}$	$\frac{I_{th}^{SF}}{10^{11}\,\text{Wcm}^{-2}}$
32.0	0.015	1.006	0.66	28.0	0.076	1.033	4.76
22.0	0.023	1.010	0.51	22.0	0.079	1.034	4.69
8.0	0.082	1.036	0.82	14.0	0.167	1.075	6.78
5.4	0.180	1.082	1.17	8.5	0.328	1.160	5.25
1.8	1.337			4.0	1.110		
				1.7	5.961		

Table 2.4 Thresholds I_{th}^{SF} for optical breakdown at 1064 nm calculated from I_{th} using Eq. (2.38) for $P_{th} < P'_{cr}/4$.

With 30-ps pulses and a focal angle of 1.7°, visible continuum emission was observed (Fig. 2.6). Similar ring patterns from continuum radiation have been reported by Smith, et al. [Smi77] in the beam path behind a cell. The threshold for 50% probability of continuum radiation was $E_{cont} = 1.02 \pm 0.02$ mJ, or $P_{cont} = 33.9 \pm 0.6$ MW. It was a factor of 5 times higher than the threshold for optical breakdown.

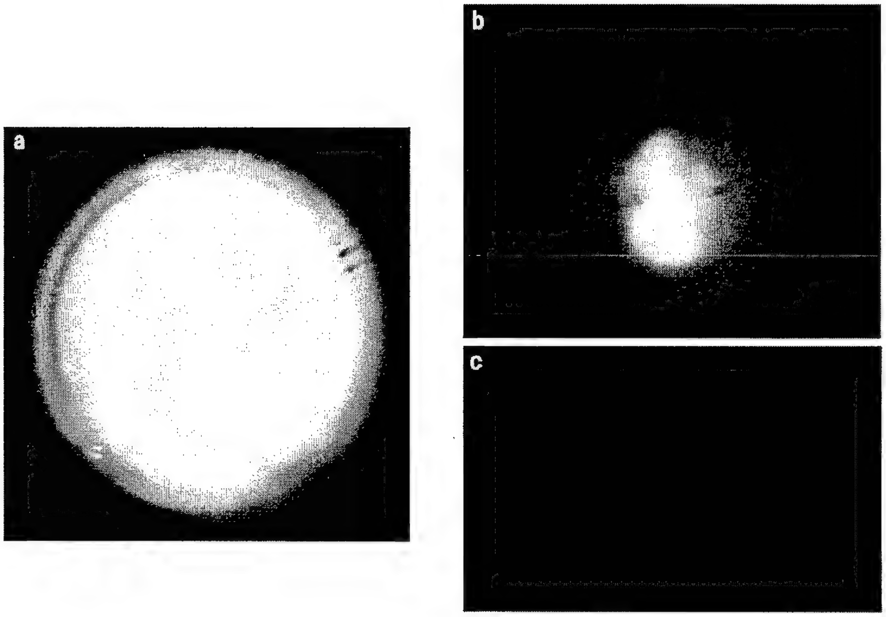

Fig. 2.6 Continuum radiation behind a water filled cell produced by a 30 ps pulse with an energy of 2.32 mJ focussed at an angle of 1.7°. This energy was a factor of 1.8 higher than the threshold for visible continuum production. The pictures in (a)-(c) were obtained using neutral density filters with different densities: (a) OD = 0.3, (b) OD = 1.0, (c) OD = 1.3. In this way it is possible to recognize a structure of rings with different colors which would be lost in a single print from a slide because the contrast range of photographic paper is much smaller than that of photographic film. The ring pattern proceeds outward with blue rings which are likewise only recognizable on the slide.

Continuum radiation was also often observed for a 4° focal angle, but only for pulse energies above 2.5 mJ. The observation of continuum emission is, along with filament formation, further confirmation of self-focussing effects (cf. 2.1.2.2).

It is worth noting that Docchio, et al. [Doc86b] observed no self-focussing or continuum emission, although they were studying plasma formation at very small focal angles between 0.2 and 1.7°. (These values were calculated from the focal spot areas given by Docchio.) This may be because they were observing plasma formation only with the naked eye for the purpose of measuring the breakdown threshold and did not photograph the plasmas. In the present report (cf. also [Vog97b]) self-focussing effects were first detected through analysis of photographs of the plasma. Kennedy, et al. [Ken97] have speculated that the discrepancy between the results of Docchio, et al. and Vogel, et al. [Vog 97b] may originate in the fact that in Docchio's experiments the optical path through the nonlinear medium is shorter so that self-focussing effects are suppressed. In fact, the path length of the light through water was about the same in both studies and about 10 mm.

2.3.1.3 Dependence of the breakdown threshold on focal spot size

We observed no systematic dependence of the irradiance I_{th} required for optical breakdown and the focal spot size (Tables 2.2-2.4). In particular, no increase in the threshold value for small focal spot diameters was found, as had been expected if the diffusion of free electrons from the focal volume during the laser pulse were to play a large role. The lack of a focal size dependence justifies the assumption in the moving breakdown model that the breakdown threshold I_{th} is independent of the laser beam diameter (cf. Section 2.1.6).

Our results are in contrast with those of Loertscher [Loe83] and Docchio, et al. [Doc86b], who report that the breakdown threshold rises with decreasing focal spot diameter. They interpreted this as a consequence of higher electron losses through diffusion out of the focal volume. Loertscher studied large focal angles between 8° and 16°, for which it is very difficult to eliminate optical aberrations. Nevertheless, he did not determine the actual focal spot diameter, but calculated I_{th} assuming a diffraction limited focal spot size. Evans and Grey Morgan [Eva69] pointed out that this can lead to an apparent dependence of the breakdown threshold on the focal spot diameter, since the scale of the aberrations increases normally with increasing focal angle. This circumstance is also illustrated by the spot size dependence of the thresholds calculated for a diffraction limited focal diameter in Tables 2.2 and 2.3.

Docchio, et al. investigated very small focal angles $\leq 1.7°$, at which according to our results the optical breakdown would be affected by self-focussing of the laser beam. The dependence of the breakdown threshold on focal spot size reported by Docchio is clearly stronger for picosecond pulses than for nanosecond pulses. Therefore, it cannot depend on the diffusion of electrons out of the focal volume, since that is negligible for the picosecond pulses. The observed spot size dependence is probably an artefact of self-focussing effects: the reduction in the beam diameter owing to self-focussing [Ham97b] leads to a drop in the energy threshold for optical breakdown and, if I_{th} is calculated assuming a diffraction limited focal spot size, to an apparent decrease in I_{th}. This effect becomes more pronounced as the focal angle is reduced when self-focussing effects increase further, and this leads to an apparent dependence of the intensity threshold on the focal spot size.

2.3.1.4 Dependence of the breakdown threshold on pulse duration

The irradiance I_{th} required for optical breakdown with 30 ps pulses is 5.9 times higher on the average than for 6 ns pulses (cf. Tables 2.2 and 2.3) and the fluence F_{th} is a factor of about 34 lower. The weak effect of pulse duration on I_{th} (or the strong effect on F_{th}) would be surprising if cascade ionization were the only breakdown mechanism. In this case, neglecting losses, the ionization rate would be proportional to the irradiance I (cf. Eq. (2.14)) and it would require a substantial increase in the irradiance to compensate for a shortening of the pulse duration by a factor of 200. The weak influence of the pulse duration on I_{th} indicates that multiphoton ionization, with its strong intensity dependence (cf. Eq. (2.9)) must play a significant role, at least in the production of seed electrons for the ionization cascade.

If we assume a dependence on pulse duration of the form $I_{th} \propto t_L^n$, then the data from the present experiments give $n = 0.33 \pm 0.035$, in good agreement with the experimental data of Zysset, et al. [Zys89] ($n = 0.29$) and Docchio, et al. [Doc86b] ($n = 0.3$, averaged over data for different focal spot sizes). The relatively small value of n confirms the importance of multiphoton ionization for the initiation of optical breakdown. Experimental studies of breakdown in solids have, on the contrary, predominantly yielded $n \approx 0.5$ [Koe88]. The discrepancy between the data for distilled water and for solids can be explained by assuming that the solids that were studied had more impurities than the distilled water. Van Stryland, et al. [Str81] found $n = 0.5$ for NaCl and SiO_2 only with large focal volumes, for which is it probable that the seed electrons for the ionization cascade would be provided by thermal ionization of impurities. In this case, the dependence of the cascade ionization threshold on the pulse duration is decisive in the pulse length dependence for optical breakdown. For small focal volumes a weaker interrelation between I_{th} and t_L was observed. This has been interpreted as evidence that now multiphoton ionization is necessary for initiating optical breakdown. The probability that impurities exist in the focal volume decreases for smaller focal volumes, and the medium acts more and more as a pure substance, in which the initial free electrons can only be produced through multiphoton ionization. Given the low impurity content of the distilled water, it behaves as a pure medium for all the focal volumes that were studied.

The average slope S of the breakdown threshold is $3{,}6 \pm 0{,}8$ for 30-ps pulses and $2{,}0 \pm 0{,}6$ for 6-ns pulses. The steeper threshold for the ps pulses can be explained in terms of an increasing influence of multiphoton ionization for shorter pulse durations, which implies a stronger dependence of the ionization rate on the irradiance.

2.3.1.5 Dependence of the breakdown threshold on wavelength

At a wavelength of 532 nm the breakdown threshold for a 6-ns pulse is 43% lower than the corresponding value for 1064 nm, and the threshold for a 30-ps pulse is about 17% lower. A similar trend was observed by Kennedy, et al. [Ken95b] for water and by Soileau, et al. [Soi89] for NaCl and SiO_2. The decrease in the thresholds at short wavelengths indicates that the measured breakdown threshold is not determined by the threshold I_C for cascade ionization, but by the multiphoton process which supplies the seed electrons for the cascade. I_C increases with decreasing wavelength (cf. Eq. (2.18) and [Spa81]), while the threshold I_m for multiphoton ionization of seed electrons decreases, since fewer photons will be required for ionization at shorter wavelengths [Whe84]. Although the observed wavelength dependence has the direction expected for multiphoton processes, it is much weaker than would be the case for a pure multiphoton process [Soi89, Whe84]. Within the range of pulse durations studied here, during optical breakdown multiphoton and cascade ionization processes work together in such a way that their opposite wavelength dependences largely compensate one another.

2.3.1.6 Comparison with calculated threshold values

The threshold I_{mp} for pure multiphoton ionization calculated using Eq. (2.11) is 2.3×10^{13} W cm^{-2} for 6-ns pulses and 5.7×10^{12} W cm^{-2} for 30-ps pulses at 1064 nm ($\rho_{cr} = 10^{20}\,\mathrm{cm}^{-3}$). These values are 31 and 13 times, respectively, higher than the measured breakdown thresholds I_{th} for these pulse lengths. These factors indicate that optical breakdown with nanosecond and picosecond pulses cannot be produced primarily by multiphoton processes, but that the dominant process is cascade ionization. Multiphoton processes are, nevertheless, necessary for the generation of seed electrons. Table 2.5 is a comparison of the measured breakdown threshold I_{th} and the calculated thresholds I_m for multiphoton production of initial electrons and I_c for the continuation of the ionization cascade. The calculations were done under the assumptions of Kennedy described in Section 2.1.4.4. It turns out that for both laser pulse lengths I_{th} is substantially higher than I_c (especially for large focal angles), but is close to I_m. The measured breakdown threshold, therefore, depends on the irradiance I_m required to prepare the seed electrons.

	6 ns					30 ps				
$\frac{\lambda}{\mathrm{nm}}$	$\frac{\theta}{\circ}$	$\frac{I_{th}}{10^{11}\,\mathrm{Wcm^{-2}}}$	$\frac{I_c}{10^{11}\,\mathrm{Wcm^{-2}}}$	$\frac{I_m}{10^{11}\,\mathrm{Wcm^{-2}}}$	$\frac{I_{rate}}{10^{11}\,\mathrm{Wcm^{-2}}}$	$\frac{\theta}{\circ}$	$\frac{I_{th}}{10^{11}\,\mathrm{Wcm^{-2}}}$	$\frac{I_c}{10^{11}\,\mathrm{Wcm^{-2}}}$	$\frac{I_m}{10^{11}\,\mathrm{Wcm^{-2}}}$	$\frac{I_{rate}}{10^{11}\,\mathrm{Wcm^{-2}}}$
1064	32.0	0.66	0.017	1.02	0.74	28.0	4.61	0.79	4.01	1.1
1064	22.0	0.51	0.017	0.80	0.59	22.0	4.53	0.79	3.94	1.1
1064	8.0	0.79	0.017	0.61	0.45	14.0	6.31	0.82	3.44	0.98
1064	5.4	1.08	0.017	0.52	0.38	8.5	4.53	0.89	2.46	0.81
1064	1.8	0.75	0.018	0.24	0.17	4.0	3.70	0.99	1.53	0.71
1064						1.7	3.32	1.07	1.07	0.67
532	22	0.29	0.065	0.0022	0.41	22	3.75	2.52	0.0506	0.94
			$I_{mc} = 0.059$					$I_{mc} = 1.37$		

Table 2.5 Comparison of the measured breakdown thresholds I_{th} with the values I_m and I_c, calculated using Eqs. (2.12) and (2.18), along with the value I_{rate} obtained by solving the rate equation (2.6) numerically. The thresholds I_c and I_{rate} refer to a critical electron density of $\rho_{cr} = 10^{20}\,\mathrm{cm}^{-3}$.

The calculated values of I_m in Table 2.5 have a clear dependence on the focal angle θ, as opposed to the experimental observation that I_{th} is independent of θ. The relationship between I_m and θ is a direct consequence of the assumption that the ionization cascade is started by a constant *number* N_{0min} of initial electrons, regardless of the focal spot size (cf. 2.1.4.4). This assumption is, however, brought into question by the fact that, for all the focal sizes studied, the plasmas at the breakdown threshold fill, or are even larger than, the entire focal volume (cf. 2.3.2.3). For small focal angles the focal depths are so long (Rayleigh lengths >150 µm) that the ionization cascade must begin at many positions that are independent of one another, so that the critical electron density can be reached in the overall focal volume during the laser pulse. Therefore, it seems reasonable to assume a constant initial *density* ρ_{0min} of free electrons. ρ_{0min} can be estimated by using Eq. (2.12) to calculate the electron density and number of electrons in the focal volume for which I_m is simply equal to the measured threshold value I_{th}. Here, for the 30-ps pulse, we adopt Kennedy's assumption that the time available for the production of the seed electrons by multi-photon ionization equals $t_L/10$. For the 6-ns pulse, on the other hand, it will be assumed that $\Delta t = t_L/2$, since the ionization avalanche sets in at the breakdown threshold shortly before the intensity peak of the laser pulse is reached (cf. Fig. 2.7). The results of these calculations are presented in Table 2.6.

6 ns			30 ps		
$\frac{\theta}{^\circ}$	$\frac{\rho_{0\min}}{10^9\,\mathrm{cm}^{-3}}$	N_{0min}	$\frac{\theta}{^\circ}$	$\frac{\rho_{0\min}}{10^{10}\,\mathrm{cm}^{-3}}$	N_{0min}
32.0	0.77	0.37	28.0	8.91	23
22.0	0.16	0.32	22.0	8.02	23
8.0	2.26	23	14.0	58.59	384
5.4	14.78	387	8.5	8.02	394
1.8	1.66	5010	4.0	2.38	2012
			1.7	1.24	37414
Average:	3.9		Average:	14.5	

Table 2.6 Initial electron densities ρ_{0min} and numbers N_{0min} for which the calculated threshold value I_m for the production of seed electrons equals the measured breakdown threshold I_{th} at 1064 nm. (At 1064 nm the production of seed electrons is the decisive condition for optical breakdown.)

The calculations show that the number N_{0min} of seed electrons varies by almost four orders of magnitude, depending on the focal spot size. For ns-pulses and large focal angles the calculated value of N_{0min} is somewhat less than 1. This value is physically impossible, but the deviations lie within the range determined by the uncertainty in the measurement of I_{th} and by the probabilistic character of the threshold values. The data in Table 2.6 suggest that the initial electron density ρ_{0min}, which must be created by multiphoton ionization, is roughly the same for all focal angles (with a scatter of about an order of magnitude). The average values of ρ_{0min} are 3.9×10^{9} cm^{-3} for 6-ns pulses and 14.5×10^{10} cm^{-3} for 30-ps pulses, i.e., the initial electron density must be about a factor of 40 higher for the shorter pulses. With shorter pulses, the diffusion radius encompassed by the ionization cascade that moves out from a seed electron is smaller than for the longer pulses, so a that a higher density of seed electrons is necessary for the breakdown process to proceed everywhere within the focal volume.

Kennedy, et al. [Ken95b] obtained a deceptive agreement between their results based on the unrealistic assumption that N_{0min} = const, which suggests a dependence of the breakdown threshold on the focal spot size, and Docchio's data which also appear to demonstrate a dependence of the breakdown threshold on the focal spot size. The results of the present study indicate, however, that the focal size dependence in Docchio's studies can probably be attributed to an inadequate treatment of self-focussing effects (cf. 2.3.1.3) and that the assumption ρ_{0min} = const offers a realistic basis for the threshold calculations.

At 532 nm multiphoton processes play a substantially greater role than at 1064 nm, since only 3 photons are needed to surmount the band gap, rather than 6. The calculated thresholds I_m are, therefore, lower than I_c (Table 2.5). In this case, the actual threshold value according to Kennedy (1995a) should lie between I_m and I_c. It is obtained by stepwise increasing the electron density ρ_0 at the beginning of the ionization cascade. This leads to a rise in I_m and a fall in I_c, until they both meet at the value I_{mc} corresponding to an initial electron density of ρ_{mc}. The notation I_{mc} was chosen in order to stress that not only multiphoton ionization, but also cascade ionization makes a substantial contribution to plasma formation. The agreement between the calculated thresholds I_{mc} and the measured values I_{th} is not as good as at 1064 nm. In the analytic threshold calculations, optical breakdown was treated as if initially only mulitphoton ionization and later only cascade ionization contribute to the formation of free electrons. In this way, the contribution of multiphoton ionization appears as a "catapult start" for the electron avalanche [Ken95a]. Actually, however, both processes contribute throughout the duration of laser pulse. A more exact treatment of the problem involves solving the rate equation (2.6) (cf. Section 2.1.4.5). In fact, the agreement between I_{rate} and I_{th} at 532 nm is, altogether, much better than that between I_{mc} and I_{th}.

The thresholds I_{rate} in Table 2.5 calculated with the aid of the rate equation also depend, just as I_m does, on the focal angle, because (for purposes of a better comparison with the analytically calculated threshold values) a constant number of seed electrons has been assumed as the initial condition for the start of the ionization cascade. This deficiency is not fundamental in nature, but can be corrected by assuming a constant seed electron density ρ_{0min}.

For λ = 1064 and a 6 ns pulse duration the agreement between I_{rate} and the experimental values is very good. For a pulse duration of 30 ps, however, the values of I_{rate} lie clearly below I_{th}. Here the agreement is substantially better if a critical electron density of $\rho_{cr} = 10^{21}\,\text{cm}^{-3}$ for optical breakdown is assumed instead of $\rho_{cr} = 10^{20}\,\text{cm}^{-3}$ (the values of I_{rate} are then doubled).

The existence of different thresholds for the start and for the advance of an ionization cascade during optical breakdown in pure materials has consequences for the statistics of the breakdown process. In earlier papers [Bas72, Doc86a, Sch89], the probabilistic nature of optical breakdown has been attributed to the statistics of cascade ionization. When, however, $I_m > I_c$, as happens at 1064 nm for the range of pulse durations considered here, the statistics of the multiphoton process will determine the threshold, while the ionization cascade will proceed with certainty, as long as seed electrons are generated. When $I_m < I_c$, the barrier to the creation of seed electrons disappears and then the breakdown statistics will probably be mainly determined by the advance of cascade ionization. This is the case at a wavelength of 532 nm for the pulse durations considered here.

2.3.1.7 Time evolution of the electron density

The time evolution of the electron density calculated using the rate equation (2.6) provides more information on the alternation of the mechanisms involved in optical breakdown when the pulse duration and wavelength are varied (Fig. 2.7).

At 1064 nm the production of seed electrons through multiphoton ionization is the decisive prerequisite for completion of the breakdown process. The ionization avalanche first sets in when the maximum intensity is reached in the laser pulse, because multiphoton ionization is very strongly dependent on the intensity. The late onset of the ionization avalanche was confirmed by the time-resolved measurements of the plasma transmission at 1.7 times the threshold energy described in Section 2.3.3.1, which show that a significant change in the transmission first occurrs only shortly before the peak of the pulse. Once the ionization cascade begins, it proceeds very rapidly, as I is significantly higher than I_C. (For the 6-ns pulses I_{th} is, on average, 45 times greater than I_C, and for the 30-ps pulses, 6 times greater.) At high electron densities, the cascade is abruptly slowed by the increasing effect of recombination which is proportional to ρ^2. The fall in the electron density after the end of the laser pulse is both for ns- and ps- pulses mainly determined by the recombination rate.

At 532 nm, $I_m < I_c$ (Table 2.5); that is, there is no lack of seed electrons for the ionization avalanche. The cascade, therefore, sets in relatively early in the laser pulse and proceeds more slowly than at 1064 nm. At high electron densities, a dynamic equilibrium develops between the production of

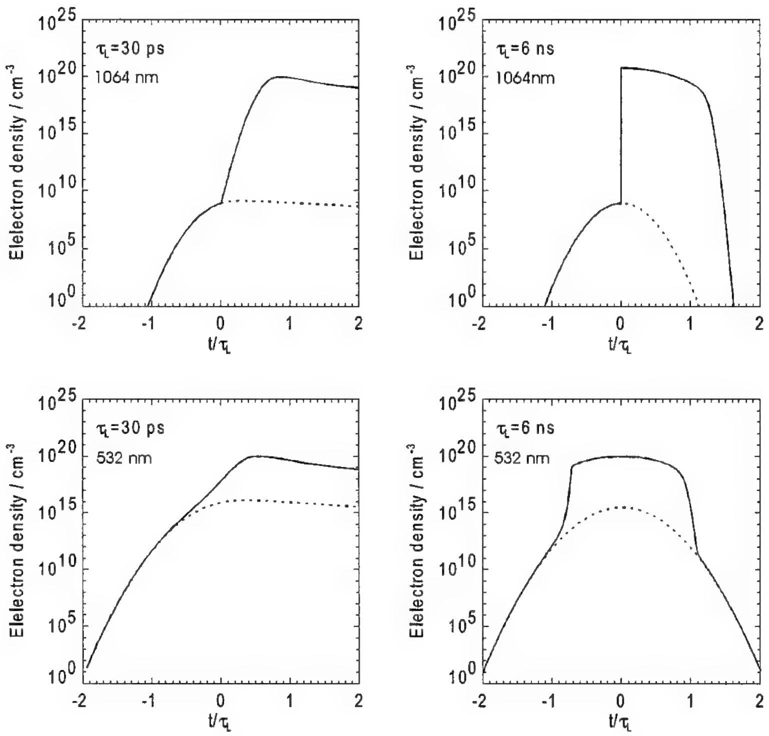

Fig. 2.7 Time evolution of the electron density at the threshold for optical breakdown. The calculations were done for a critical electron density of 10^{20} cm^{-3} and a focal spot diameter of 6 μm. The time axis has been normalized by the laser pulse duration (FWHM). The pulse duration and wavelength are given on the graphs. The dashed curve denotes the time variation in the electron density owing to multiphoton processes.

free electrons and their recombination, for which the rate is dependent on intensity. The maximum electron density coincides, therefore, with the intensity maximum of the laser pulse. The contribution of multiphoton ionization to the total number of free electrons is 7-8 orders of magnitude higher than at 1064 nm. Nevertheless, as before, cascade ionization predominates. Its contribution is roughly 1000 times greater than that of the multiphoton process.

In all calculations for Fig. 2.7, it has been assumed that $\rho_{cr} = 10^{20}$ cm^{-3}, based on Barnes and Rieckhoff's (1968) estimate using experimental data from 30-ns pulses. Whether the electron density attained is actually the same for all laser parameters, is not yet known. The calculations of the threshold values in the preceding section suggest that the critical electron density for ps-pulses lies in the range of 10^{21} cm^{-3} rather than 10^{20} cm^{-3}. One possible explanation for a lower electron density in the ns-plasmas might be that the maximum electron density is limited by the recombination effects occurring during the laser pulse. For ps pulses, the irradiation must be higher to complete the breakdown cascade during the shorter time available. The cascade ionization rate is, therefore, so high that recombination is not a limiting factor for the maximum electron density reached. While an electron density of 10^{21} cm^{-3} in ps-pulses is physically possible (the corresponding degree of ionization is 1.5%), it is unlikely that the electron density will significantly exceed 10^{21} cm^{-3}. Above this limit the plasma frequency will be above that of the light frequency, so a large part of the laser light would be reflected by the plasma (cf. 2.1.4).

2.3.2 Plasma formation above the breakdown threshold

2.3.2.1 Plasma shape

Figures 2.8 and 2.9 show plasmas produced by 30 ps and 6 ns pulses with different energies and focal angles.

In all cases a plasma appears in the laser beam cone in front of the laser focus. The region behind the laser focus is "shielded" by absorption of the laser light. The shapes of the plasmas produced by the ns and ps pulses are different, probably owing to the different beam profiles (cf. Fig. 2.3). The ns-plasmas are conical in shape; they fill the laser beam cone completely out to a large distance from the

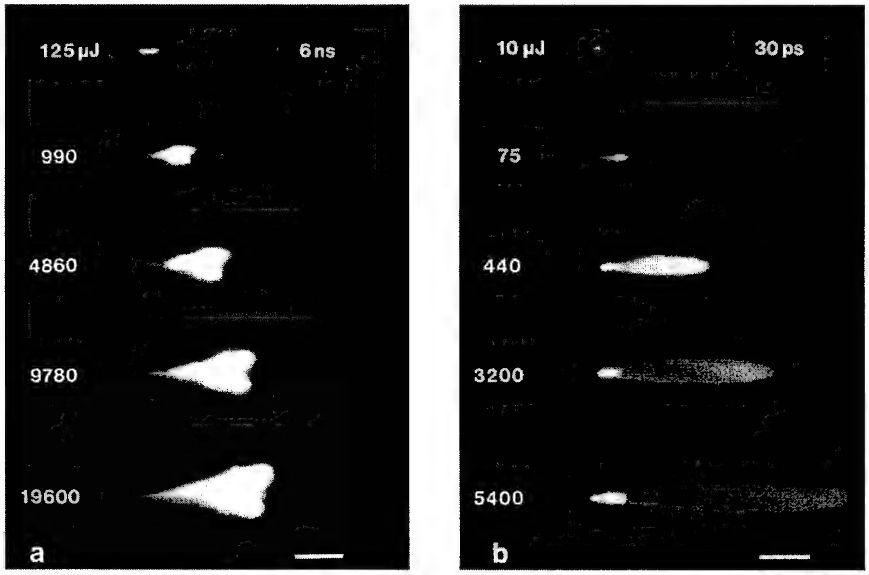

Fig. 2.8 Plasma shape for different pulse energies: (a) 6 ns pulse duration, (b) 30 ps pulse duration. The focal angle is 22°. The pulse energies are indicated in the frames. The laser light is incident from the right. The scale represents a length of 100 µm.

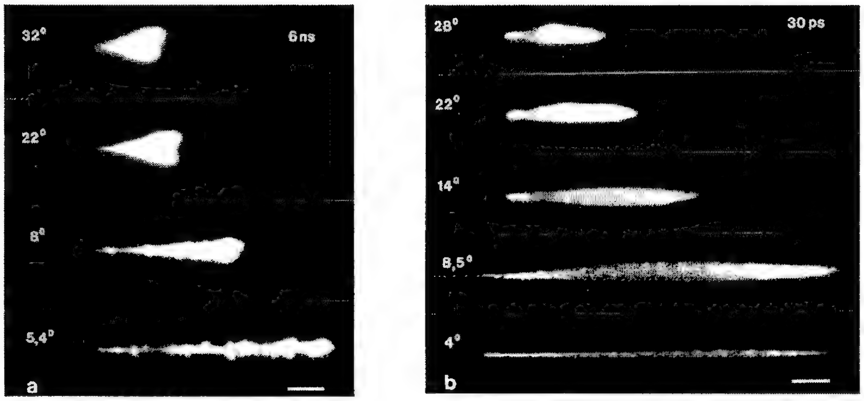

Fig. 2.9 Plasma shape for different focal angles: (a) 6 ns pulse duration,10 mJ pulse energy; (b) 30 ps pulse duration, 3 mJ pulse energy. The focal angles are indicated in the frames. The laser light is incident from the right. The scale represents a length of 100 μm.

focus, since the beam profile contains a peripheral ring of high intensity. The ps-plasmas are spindle shaped; their shape conforms to the laser beam cone only in the neighborhood of the beam waist and becomes ever thinner at larger distances (cf. Fig. 2.9b, $\theta = 28°$, for example). The beam profile of the ps-pulses is gaussian, so that at a certain distance from the beam waist, the threshold intensity I_{th} will be exceeded only in the neighborhood of the beam axis. For both pulse lengths, the plasma shape apparently conforms to an approximate intensity contour with $I = I_{th}$. This conformance is an indicator of the validity of the moving breakdown model, in which it was assumed that plasma is formed wherever I_{th} is exceeded.

2.3.2.2 Plasma front velocity

A further indication of the validity of the moving breakdown model is the high velocity at which the plasma front moves back into the beam cone during the laser pulse. The average velocity of the plasma front is given by the ratio of the plasma length to the pulse duration: $\bar{v}_p = z_{max} / t_L$. Table 2.7

6 ns			30 ps		
	$\beta = 10$	$\beta = 100$		$\beta = 100$	$\beta = 1000$
$\frac{\theta}{°}$	$\frac{\bar{v}_p}{\mathrm{kms}^{-1}}$	$\frac{\bar{v}_p}{\mathrm{kms}^{-1}}$	$\frac{\theta}{°}$	$\frac{\bar{v}_p}{\mathrm{kms}^{-1}}$	$\frac{\bar{v}_p}{\mathrm{kms}^{-1}}$
32.0	12.5	23.3	28.0	2500	8670
22.0	16.7	38.3	22.0	3330	11.300
8.0	50.0		14.0	7.330	26.300
5.4	133.3		8.5	19.000	
			4.0	76.000	

Table 2.7 Average plasma front velocity for different focal angles and normalized pulse energies β.

shows that $\overline{v}_p$ varies between 12 km/s and 76000 km/s, depending on the focal angle, pulse duration, and normalized pulse energy β. The peak velocity of the plasma front, which, based on the shape of the beam waist, is attained in the beginning stage of plasma formation, is considerably higher than the corresponding average value [Doc88a]. It has already been mentioned in Section 2.1.6. that a radiation driven detonation wave [Ram65, Dai67] cannot account for the high plasma front velocity, since the experimentally observed velocity of the shock front produced in water by optical breakdown is at most only about 4.5 km/s [Vog96a]. The motion of the plasma front can, therefore, only be interpreted as the migration of the site where optical breakdown is taking place. As opposed to the propagation of a detonation wave, this migration is not associated with material motion, but is a sort of phase velocity. Hence, the plasma front velocity can become extremely high.

2.3.2.3 Plasma length

The length of the plasma from the beam waist towards the laser is plotted in Fig. 2.10 as a function of the laser pulse energy for different focal angles. There is obviously a strong relationship between the plasma length and the focal angle, which is even more marked for ps-pulses than for ns-pulses. For equal energies and equal focal angles, ps-plasmas are always longer than ns-plasmas. This elongation occurs because the energy threshold for optical breakdown with ps-pulses is substantially lower than for ns-pulses, and the ps-plasmas will thus be produced much further above the threshold.

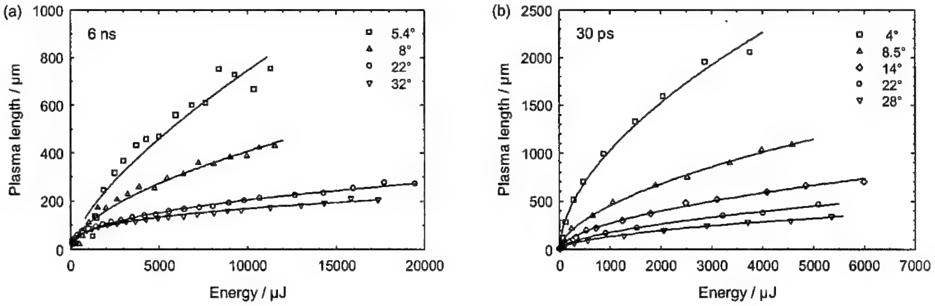

Fig. 2.10 The length of the plasma from the beam waist towards the laser, z_{max}, as a function of the laser pulse energy for different focal angles. Pulse length (a) 6 ns, (b) 30 ps.

In order to compare the measurement data with the moving breakdown model, the length of the plasma on the laser side is plotted as a function of $(\beta-1)$ on a log-log scale in Fig. 2.11. If Eq. (2.30), which predicts a proportionality between z_{max} and $\sqrt{\beta-1}$, is valid, then the measurement data in Fig. 2.11 should be fit by straight lines with a slope of 0.5. This fit is possible for the ps-pulses (Fig. 2.11a). The

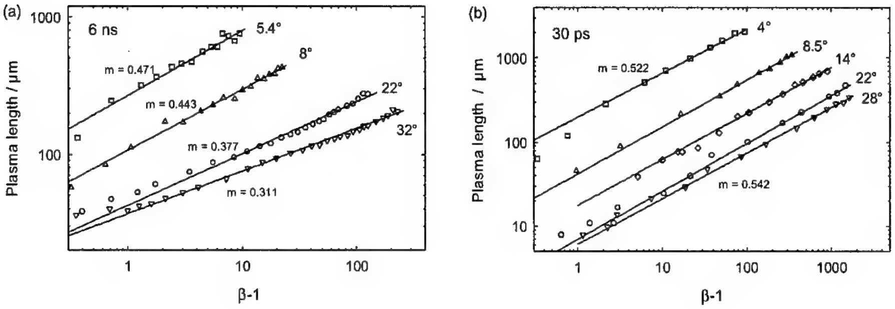

Fig. 2.11 The length of the plasma on the laser side, zmax, as a function of $(\beta\text{-}1)$ for different focal angles. Pulse length (a) 6 ns, (b) 30 ps.

slopes for the different focal angles lie between 0.52 and 0.56, the measured plasma lengths differ by no more than ±30% from the values predicted by Eq. (2.30), and the $z_{max}(\theta)$- dependence is described by Eq. (2.31). For ns-pulses agreement with the predictions of the model is not as good (Fig. 2.11b), in terms of either the slopes, which range between 0.31 and 0.47, or the absolute magnitudes of the plasma lengths and the $z_{max}(\theta)$- dependence. According to the model, the ns-plasmas should be just as long asthe ps-plasmas for the same β, but, as Fig. 2.12 shows, they are considerably longer. For $\beta = 10$ and $\theta = 22°$, for example, the ns-plasma is 100 µm long, while the length of the ps-plasma only reaches 25 µm. (The model predicts $z_{max} = 27$ µm.) The relative deviation of the measured values for the ns-plasmas from the predicted plasma lengths on the laser side is greatest for large focal angles and energies near the breakdown threshold.

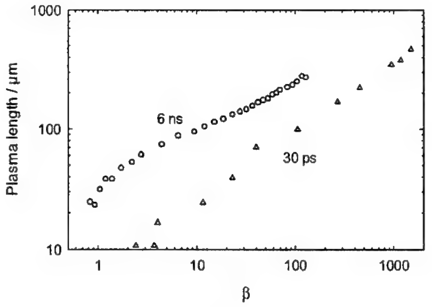

Fig. 2.12 A comparison of the plasma lengths on the laser side observed with 6 ns and 30 ps pulse durations for a focal angle of 22°. The plasma lengths are plotted as a function of β. Docchio's moving breakdown model predicts that the plasma length is independent of the pulse duration for constant β. In fact, the ns-plasmas are considerably longer than the ps-plasmas.

A large part of the discrepancy between the plasma length for the ns-pulses and the predictions of the model is probably attributable to the UV radiation emitted by the plasma. It provides seed electrons for the ionization cascade near the previously formed plasma [Alc68]. Figure 2.7 implies that a high electron density will be reached right after the intensity maximum of the pulse is reached. Hence, this leads to emission of bremsstrahlung and recombination radiation in the UV as long as the intensity of the incident laser light is high. Since UV radiation can excite electrons from the valence band into the conduction band, the breakdown process becomes independent of the production of seed electrons through multiphoton ionization and the threshold I_{th} falls from I_m to I_c. Because of this reduction in I_{th} during the laser pulse, the plasma expands further into the laser beam cone than predicted by the moving breakdown model, which assumes a constant threshold. For ps-pulses, where I_m is substantially closer to I_c, the breakdown threshold will be affected much less by the plasma radiation and remains roughly constant throughout the breakdown process, as assumed in the model. The wavelength and penetration depth of the plasma radiation are compatible with this interpretation. Stolarski, et al. (1995) have established that the spectrum of the radiation from ps-plasmas corresponds to that from a black body at about 10,000 K. At these temperatures, the black body radiation contains substantial energy at wavelengths under 190 nm, for which the photon energy exceeds 6.5 eV and is, therefore, sufficient to produce quasi-free electrons in the conduction band [Gra79]. The recombination radiation likewise contains photons with energies equal to the band gap of 6.5 eV. The optical penetration depth for 6.5-7 eV photons lies between 4 cm (for 6.5 eV, i.e., 190 nm) and 110 μm (for 7 eV, 177 nm) [Wil76, Pai69]. This penetration depth is long enough to explain why the observed plasma lengths are between 30 μm and 800 μm longer than the predictions of the moving breakdown model, depending on the focal angle and pulse energy.

A second cause of the discrepancy between the model predictions and the experimental data is the deterioration of the laser focus owing to aberrations and deviations from a gaussian beam profile that were not taken into account in the model. All theoretical calculations of the plasma length were based on diffraction limited focal spot sizes, which were calculated from the focal angle measured a long distance from the beam waist. This is a good assumption for large values of β-, for which the plasma expands back into a portion of the laser beam cone, where the idealized $\omega(z)$ - curve for a gaussian beam is very close to the actual form of $\omega(z)$. For energies near the breakdown threshold, however, plasma will be formed only in the region of the beam waist, where deformations in the intensity distribution caused by aberrations and a bad beam profile have the greatest effect. For example, if the measured focal spot diameter is twice the diffraction limited value, then the corresponding Rayleigh length $z_R = \pi\omega_0^2 / \lambda$ will be four times that for the diffraction limited case and the plasma length, calculated from the measured focal spot diameter, will be longer by the same factor. The deviations of the measured focus from the diffraction limited focus were greater for ns-pulses than for ps-pulses and were the greatest for large focal angles (cf. Tables 2.2 and 2.3). This coincides with the cases where the discrepancies between the measured plasma lengths and the model predictions were largest.

2.3.2.4 Inhomogeneities in the plasma

In general, the ps- and ns-plasmas both appear to be homogeneous (Figs. 2.8 and 2.9) and no multiple plasma formation of the type reported by others [Loe83, Cap86] was observed. This is because of the use of distilled and filtered water as the medium for optical breakdown and the minimization of optical aberrations, so that local intensity maxima ("hot spots") could be avoided in the focal region of the laser beam [Eva69, Vog97c]. The free electrons produced by UV radiation during the laser pulse can also contribute to the formation of a homogeneous plasma, especially for nanosecond pulses, where the production of seed electrons for the ionization cascade is the limiting factor in the breakdown process. Because of the UV radiation, free electrons are always available in the region surrounding the previously formed plasma after plasma formation has begun, so that optical breakdown then loses much of its statistical character. Only for the smallest focal angles of 5.4° is the plasma boundary no longer smooth and the plasma structure "grainy." In this case the plasma expansion is presumably too fast and the penetration depth or intensity of the UV radiation too small to guarantee a homogeneous plasma structure.

For pulse energies well above the breakdown threshold, the ps-plasmas feature a bright spot near the beam waist (Fig. 2.8b, 2.9b). Although the plasma partly shields the focal region as it propagates back into the beam cone during the pulses, the transmitted light is always sufficient to produce an irradiance at the focal region in excess of the optical breakdown threshold. (Even well above the threshold, 10-30% of the laser light is transmitted; cf. Fig. 2.20.) If a constant transmission fraction for the plasma during the overall laser pulse is assumed and possible changes in the focal spot size through self-focussing are neglected, we can conclude from the transmission data of Section 2.3.3.5 that a bright spot appears when the irradiance in the focal region exceeds $1.7 \pm 0.5 \times 10^{13}$ W/cm^2. This value is 43 times higher than I_{th}. A very high electron density can, therefore, be achieved in the focal region, which explains the bright plasma radiation. Nanosecond plasmas, as opposed to the ps-plasmas, are brightest on the laser side at high pulse energies. This indicates that the absorption coefficient in the ns-plasmas is higher than in the ps-plasmas. The energy incident during the second half of the laser pulse will, therefore, mainly be absorbed on the side of the plasma facing the laser and cause further heating of this portion of the plasma.

For focal angles of 14° or less ps-plasmas feature a spike in the region beyond the beamwaist (cf. Fig. 2.9 and [Vog94a]). This observation can be explained by the combined effect of self-induced defocussing in the plasma (cf. Section 2.1.2.1) and self-focussing in the medium behind the plasma. Optical breakdown begins at the beam waist and the plasma front expands toward the laser as the laser power rises. The light transmitted through the plasma then passes through a region with a negative nonlinear refractive index (because of the high density of free electrons) and is defocussed [Fei74]. As soon as it enters the medium behind the plasma, it creates a positive nonlinear refractive index there. If the remaining laser power is still greater than P'_{cr}, self-focussing sets in and leads to a beam collapse followed by optical breakdown and a lengthening of the plasma. The defocussing region thus becomes longer and the location of the beam collapse migrates further downstream. The process ends when P falls below the critical power P'_{cr}. The shape of the plasma behind the beam waist is similar to the spikes created by spherical aberrations (cf. Section 2.3.6), but this similarity is largely coincidental.

2.3.3 Optical properties of the plasma

2.3.3.1 Time resolved transmission

Figure 2.13 shows the time resolved transmission through the focal region for energies below (β = 0.3) and above ($\beta > 1$) the breakdown threshold for 6 ns pulse duration and a 22° focal angle. *T(t)* could not be measured for the ps-pulses. All curves have been normalized so that the peak amplitudes of the incident pulses are equal.

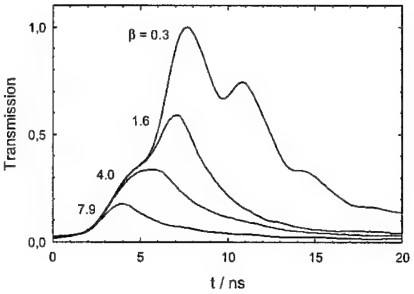

Fig. 2.13 Time resolved transmission through the focal region for energies below (β = 0.3) and above ($\beta > 1$) the breakdown threshold. The curves are all averaged over 1000 laser pulses. t_L = 6 ns and θ = 22°.

For β = 1.6, the drop in transmission caused by optical breakdown begins shortly before the peak intensity of the laser pulse is reached. With increasing β, it begins earlier and the area under the transmitted pulse, which represents the total transmission, decreases. The parameter dependence for the total transmission is described in Sections 2.3.3.5 and 2.3.3.6.

2.3.3.2 Scattering

The angular distributions $\rho_{T+S}(\gamma)$ of the energy per steradian behind the laser focus with and without plasma formation are compared in Fig. 2.14a for 6-ns pulses at 1064 nm. Figure 2.14b shows the corresponding energy distributions $dE_{T+S}(\gamma)$ calculated from the $\rho_{T+S}(\gamma)$- curves using Eq. (2.34). Both angular distributions are given in arbitrary units, but the curves for the cases with and without plasma formation are normalized to one another in accordance with Eq. (2.36). The area A under the upper curve in Fig. 2.14b corresponds to the energy incident on the focus, while the total area under the lower curve represents the energy transmitted through the plasma and scattered on it. The area B represents the fraction of the energy which is scattered in the forward direction out of the laser beam cone.

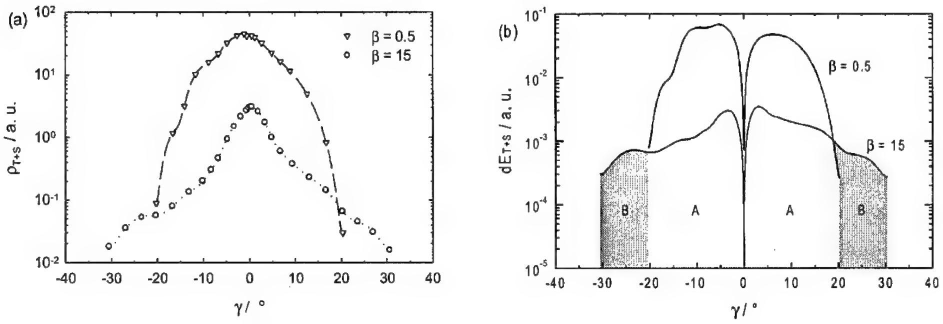

Fig. 2.14 The angular dependence of the time integrated plasma transmission and scattering (t_L = 6 ns, θ = 22°). (a) The energy per steradian ρ as function of the angle γ between the detector and the optical axis. (b) The energy distribution $dE_{T+S}(\gamma)$ with $dE_{T+S} = 2\pi\rho_{T+S}(\gamma)\sin\gamma\, d\gamma$. $\beta = 0.5$ and $\beta = 15$ represent cases without and with plasma formation, respectively.

Relative to the incident energy, this fraction is given by

$$S = \frac{B}{A}. \tag{2.39}$$

Equation (2.39) only provides a lower bound estimate for the light scattered from the plasma, since scattering in the intervals outside the e^{-2} points on the laser beam (±11°) but still within the angular interval covered by area A (about ±20°) were not included. Light scattered into angles greater than ±30° could also not be included, since the scattered light intensity at large angles was below the sensitivity threshold of the photodetector.

The scattered light fraction was S=0.5% for the 6-ns pulses and S=7.6% for the 30-ps pulses. At first glance it is surprising that the scattering is so much stronger for the ps- than for the ns-pulses. It should be noted, however, that the plasma transmission is also much higher for ps-pulses: when $\beta = 15$ it is 28.4% for the 30-ps pulse, but only 4.6% for the 6-ns pulse. The ratio of scattering to transmission is thus similar for both pulses. At both pulse durations, 4-9 times more light is transmitted within the cone angle than is scattered out of the cone angle. This result is consistent with the (qualitative) results of Meyerand and Haught [Mey64] for light scattering on plasmas in argon gas. Light scattering on plasmas in liquids is examined here for the first time.

2.3.3.3 Reflection

For a focal angle of 22° and 6 ns pulse duration, 0.8±0.02% of the incident laser light was reflected back from the plasma into the focal angle, and for a 30 ps pulse duration, 1.7±0.9%. Within the energy range that was studied ($3.5 \leq \beta \leq 5.5$ for 6 ns pulses and $1.5 \leq \beta \leq 4.3$ for 30 ps pulses), no energy dependence of the reflectivity was observed. The low plasma reflection leads to the conclusion that the maximum electron density in the plasma remains below the critical density of 10^{21} cm^{-3} at which the plasma frequency becomes greater than the frequency of the light (cf. 2.1.3). Going above the critical electron density would lead to a sharp rise in the reflection factor [Hug75]. This effect has been observed during plasma production on the surfaces of condensed media surrounded by a medium with a very high breakdown threshold (e.g., dry gases or a vacuum). Then plasma formation is limited to the surface, and, for sufficiently high irradiances, a very high free electron density can be attained, such that the reflection rises to about 0.5 [God77]. In homogeneous media, in contrast, plasma formation spreads out into new regions as the power in the pulse rises. In this way, the previously formed plasma will be shielded and an extended zone with a low electron density is always available at the plasma edge, which guarantees good laser-plasma coupling (though at the cost of spatial precision in the energy deposition).

2.3.3.4 Absorption

It has been pointed out in the previous sections that only a small fraction of the incident laser light is reflected by the plasma or scattered from it. This means that the absorption is given roughly by $A \approx (1-T)$. The relationships of the optical parameters for plasma production in liquids are utterly different from those for plasma production at solid surfaces, where reflection is a major factor (see above) [Rea71, Hug75, God95].

Since $A \approx (1-T)$, the plasma transmission is the decisive measurement for determining the efficiency of energy input to the plasma and, therefore, the efficiency of plasma aided surgical processes. The transmission also determines the extent of possible hazards to sensitive tissue structures located behind the laser focus. The parameter dependence of the plasma transmission will, therefore, be discussed in detail in the next two sections.

2.3.3.5 *Total transmission*

Dependence of the transmission on pulse duration. Figures 2.15 and 2.16 contain plots of the energy transmitted through the plasma, E_{out}, and the plasma transmission, $T = E_{out}/E_{in}$, for 6-ns and 30-ps pulses as functions of the laser pulse energy. Both figures show the entire range of E_{in} plus an enlarged scale in the threshold region. The E_{in}, E_{out} data above the breakdown threshold have been fitted to curves of the form $E_{out} = a + bE_{in}^{c}$, and these fits transferred to the graphs of T (E_{in}). The small bump in the beginning of the E_{in}, E_{out} curve in Fig. 2.15a is attributable to the shoulder in the rising portion of the laser pulse (cf. Fig. 2.3c). It was not included in the fit. The straight lines in Figs. 2.15b and 2.16b represent 100% transmission through the laser focus.

The threshold behavior for both pulse lengths is extraordinarily different: for 6-ns pulses, the transmission drops suddenly by about 50% as soon as a plasma is formed, while for 30-ps pulses, more than 90% of the laser light is still transmitted through the plasma. The transmission for the ps-pulses remains also substantially higher when β is well above the breakdown threshold: for β = 50 the transmission only amounts to 2.8±0.2% for 6-ns pulses, while it is 17.5±0.4% for 30-ps pulses. Even for β = 300, the transmission for the ps-pulses is still 9.5%. If, however, the transmission is compared for equal absolute magnitudes of the incident energy, there is little difference between the two pulse durations: with E_{in} = 500 μJ, for example, E_{out} is 68 μJ for 6-ns pulses and 52 μJ for 30 ps-pulses, and with E_{in} = 800 μJ, E_{out} is the same (70 μJ) for both pulse durations.

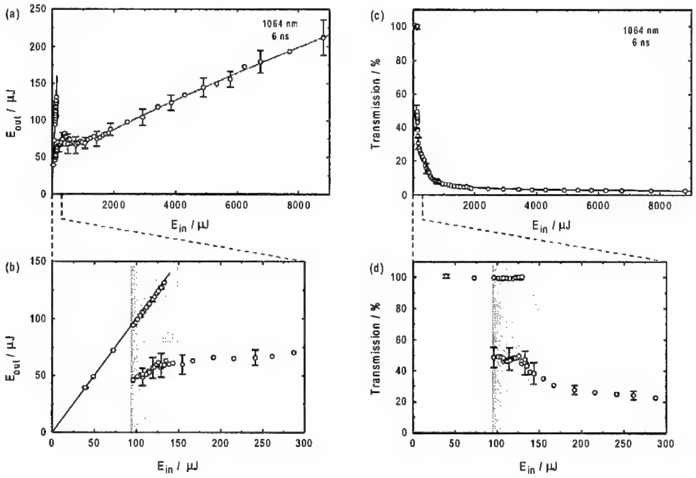

Fig. 2.15 (a), (b) Transmitted energy as a function of incident energy for 6-ns pulses at a wavelength of 1064 nm with a 22° focal angle. (c), (d) Transmission as a function of incident energy. (b) and (d) are expanded scales within the threshold region, with the shaded areas indicating the region between 10% and 90% breakdown probability. E_{th} (50% breakdown probability) lies in the center of the shaded area.

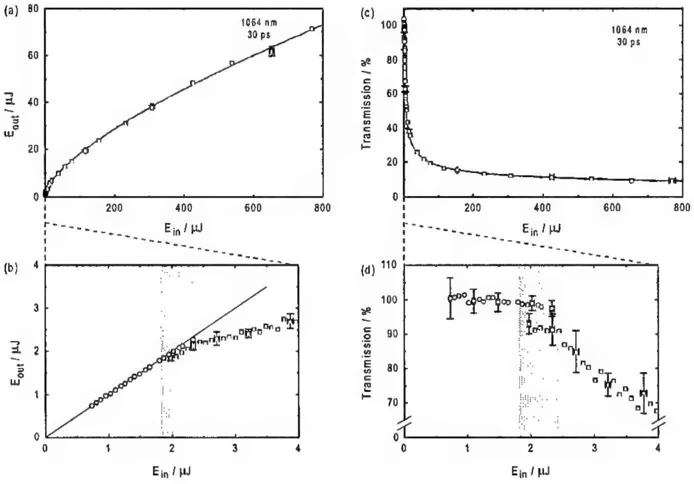

Fig. 2.16 (a), (b) Transmitted energy as a function of incident energy for 30-ps pulses at a wavelength of 1064 nm with a 22° focal angle. (c), (d) Transmission $T = E_{out}/E_{in}$ as a function of incident energy. (b) and (d) are expanded scales within the threshold region, with the shaded areas indicating the region between 10% and 90% breakdown probability. E_{th} (50% breakdown probability) lies in the center of the shaded area.

The different threshold behaviors of the transmission for 6-ns and 30-ps pulses can mostly be attributed to the different plasma lengths: ns-plasmas are substantially longer at the threshold (Fig. 2.12) and, therefore, absorb substantially more light for the same electron density. Because of the fall in the breakdown threshold during the laser pulse (cf. 2.3.2.3), the ns-plasmas are probably also larger in the lateral direction than the ps-plasmas. For that reason and because the heated fluid volume is beginning to expand, less light can be transmitted to the plasma through the focal region. The rapid rise in the electron density during the laser pulse (cf. Fig. 2.7) is an additional reason for the low transmission of the ns-plasmas.

Dependence of the transmission on wavelength. Figures 2.17 and 2.18 show the transmission data for 532 nm. At this wavelength the transmission is somewhat higher than at 1064 nm, especially at energies well above the breakdown threshold: for $\beta = 20$ and a 6 ns pulse duration, it amounts to 7.4% at 532 nm, compared to 4.1% at 1064 nm. The corresponding values for 30-ps pulses are 35% at 532 nm and 25% at 1064 nm. The higher transmission at the shorter wavelength can be explained by the fact that multiphoton ionization plays a much greater role than at 1064 nm. Thus, I_m is lower than I_c (cf. 2.3.1.6), the ionization avalanche proceeds relatively slowly (cf. Fig. 2.7), and there is no plasma growth beyond the focal region because the breakdown threshold remains constant during the laser pulse. By contrast, at

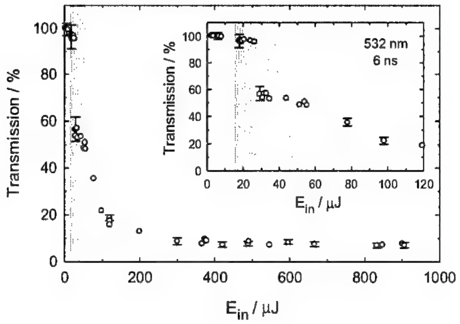

Fig. 2.17 Transmission as a function of incident energy for 6-ns pulses at a wavelength of 532 nm. The inset shows the threshold region on a magnified scale. The shaded areas indicate the region between 10% and 90% breakdown probability.

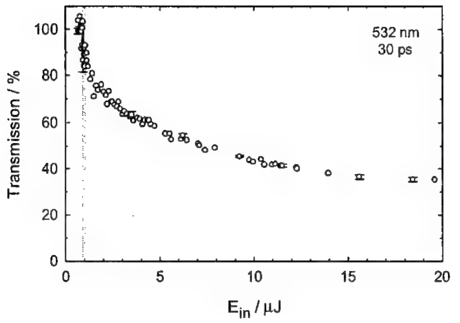

Fig. 2.18 Transmission as a function of incident energy for 30-ps pulses at 532 nm with a 22° focal angle.

1064 nm, where I_m is higher than I_c, the breakdown threshold decreases during the pulse, and this leads to a lengthening of the plasma and a reduction in the transmission.

In the threshold region the transmission for 6-ns pulses at 532 nm is slightly reduced (to about 95%), even when no visible plasma has been formed (Fig. 2.17). This observation can also be explained in terms of a greater contribution from multiphoton absorption. Slightly below the breakdown threshold, so many free electrons will probably already be produced by multiphoton ionization that an ionization cascade can begin. In this way, by the end of the laser pulse a free electron density $\rho < \rho_{cr}$ will be reached which is enough to reduce the transmission but not to produce perceptible plasma light.

Dependence of the transmission on focal angle. The dependence of the transmission on the focal angle is presented in Figs. 2.19 and 2.20. In order to facilitate the comparison between different angles, the transmission is shown as a function of the normalized pulse energy. The transmission increases with decreasing focal angle for both pulse lengths, and most markedly well above the threshold. The rise in the transmission is very surprising at first glance, because for constant β a decreasing focal angle is accompanied by a strong (roughly quadratic) rise in the plasma length (cf. 2.3.2.3). The experimental results can only be understood if the increased plasma length is compensated, or overcompensated, by a

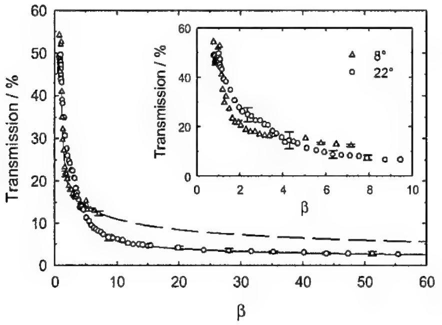

Fig. 2.19 Plasma transmission for different focal angles plotted as a function of the normalized laser pulse energy β. $t_L = 6$ ns and λ = 1064 nm. Because of the high breakdown threshold energy for θ = 8°, only low values of β could be studied. In order to make the trend clearer, the curves fitted to the measured data have been extrapolated to higher values of β.

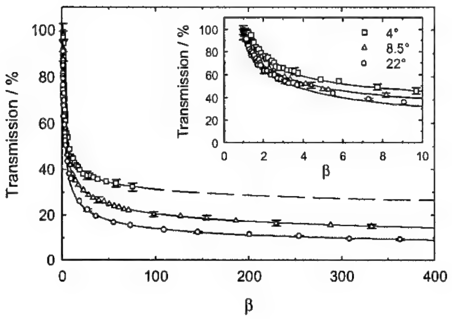

Fig. 2.20 Plasma transmission for different focal angles plotted as a function of the normalized laser pulse energy β. $t_L = 30$ ps and λ = 1064 nm. The inset shows the breakdown threshold region on a magnified scale.

decline in the absorption coefficient inside the plasma. In the following, an explanation will be presented according to which the small absorption coefficient at small angles is attributable to a reduced energy density in the plasma.

Figure 2.21 makes it clear that, for constant pulse energy, the energy density falls off with decreasing focal angle. The plasma expands into the laser beam cone until it reaches a beam cross section at which the irradiance has fallen to the threshold for optical breakdown. This beam cross section is always the same, independently of the focal angle for a constant pulse energy, but the distance between the plane of this cross section and the laser focus is greater for smaller focal angles. Thus, the enclosed volume of the beam cone (the plasma volume) is also greater and the energy density in this volume is smaller. The reduced energy density in the plasma results in a lower absorption coefficient, since the dominant absorption mechanism in the plasma is inverse bremsstrahlung (for all the pulse durations studied here). Given the requirements of energy and momentum conservation, an electron can absorb photons by an inverse bremsstrahlung mechanism only when it lies in the field of an ion or collides with an atom. The absorption probability for the photons, therefore, depends not only on their pathlength

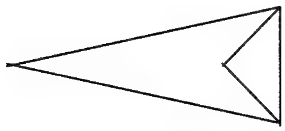

Fig. 2.21 Illustration of the dependence of the plasma volume on the focal angle for a constant pulse energy.

through the plasma and the density ρ of the free electrons, but also on the frequency ν_{coll} of collisions between electrons and heavy particles (Eq. (2.13)). Both ρ and ν_{coll} decrease as the plasma energy density is reduced.

Dependence of transmission on pulse energy. It is striking that the transmission of ns-pulses falls off at moderate values of β (especially for large focal angles; cf. Fig. 2.19), while the transmission of ps-plasmas remains quite high, even for very high values of β (Fig. 2.20). These parameter dependences can, as will be shown in the following, also be attributed to changes in the plasma energy density.

For ps-pulses the plasma length z_{max} is roughly proportional to $(\beta-1)^{1/2}$ (cf. Fig. 2.11b) and the plasma volume is, accordingly, proportional to $(\beta-1)^{3/2}$ (provided that the shape of the plasma remains the same, which is the case well above the threshold). The dependence of the energy density ε_{LIB} on the pulse energy is then given by

$$\varepsilon_{LIB} = \frac{AE_{in}}{V_p} \propto \frac{A\beta E_{th}}{(\beta-1)^{3/2}} \approx \frac{AE_{th}}{\sqrt{\beta}} \quad \text{for } \beta >> 1. \tag{2.40}$$

Here $A \approx (1-T)$ is the coupling coefficient of the laser energy into the plasma and V_{p} is the plasma volume. For high β, A is roughly constant, since the transmission T barely changes as the pulse energy is varied (cf. Figs. 2.19 and 2.20). With Eq. (2.40) this weak dependence gives the interesting result that the average energy density in the plasma decreases with rising pulse energy. Because of the smaller collision frequency of the electrons at lower plasma energy density, the cross section for inverse bremsstrahlung will decrease and, accordingly, the absorption coefficient (cf. Table 2.8 in the following section). This effect could explain why the transmission of ps-plasmas remains relatively high as the pulse energy is raised, despite the increasing plasma length.

For ns-pulses with a 22° focal angle, the plasma length is approximately proportional to $(\beta-1)^{1/3}$ (cf. Fig. 2.11a). Pursuing the argument given above, this implies that the energy density and thus the absorption coefficient of the plasma remain approximately constant as β is increased. This occurs with a marked decrease in the plasma transmission because of the increasing plasma length. For ns-pulses with an 8° focal angle, however, the measurements yielded $z_{max} \propto (\beta - 1)^{0.45}$ (Fig. 2.11a), similar to the case of ps-pulses. Consequently, the transmission remains at a relatively high level as β increases (Fig. 2.19).

Influence of self-focussing effects. As stated above, the transmission increases as the focal angle is reduced. Figure 2.22 shows that this increase becomes even more pronounced for a focal angle of under 2°, for which plasma formation will be accompanied by self-focussing effects. The measurements for 6-ns pulses (Fig. 2.22a) must be interpreted with a certain amount of caution, since they may be distorted by small bubbles in the focal volume owing to the high energy threshold for breakdown. These bubbles have not completely disintegrated even where there is a 30 s interval between laser shots. (The bubbles develop through diffusion of dissolved gas into expanded cavitation bubbles; cf. Section 6.1.2.) Thus, in the breakdown threshold region and above it, the actual transmission values with and without optical breakdown are yet higher than implied by the figure. With 30-ps pulses (Fig. 2.22b), a continuum was observed above 500 μJ, but this did not change the transmission.

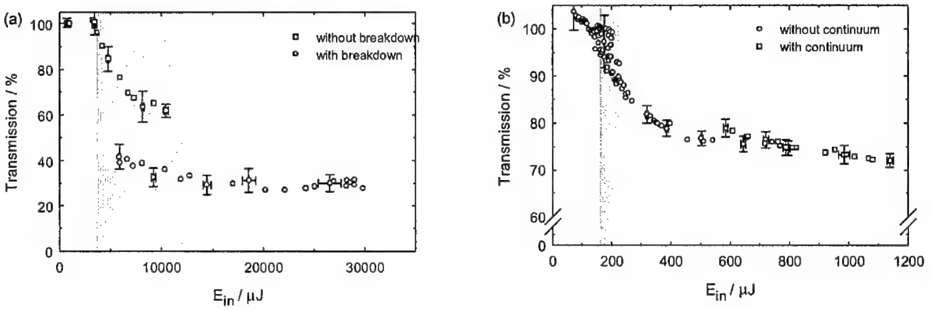

Fig. 2.22 Plasma transmission under self-focussing conditions at 1064 nm. (a) t_L = 6 ns and θ = 1,8°, (b) t_L = 30 ps and θ = 1,7°. The shaded areas indicate the region between breakdown probabilities of 10% and 90%.

The increased transmission under self-focussing conditions is probably attributable to changes in the beam profile during filament formation. An extended region with a low light intensity develops in the neighborhood of the filament [Loy73, Bro97, Mar75 p. 45] and the energy in this part of the beam cross section can presumably be at least partially transmitted through the focal region without contributing to plasma formation.

Comparison with the data of other authors. The preceding sections have shown that the plasma transmission depends on the pulse duration, laser wavelength, focal angle, and self-focussing effects, and Section 2.3.6 will demonstrate that it is influenced by aberrations of the focussing optics. (Aberrations lead to increased transmission.) This multiparameter dependence makes it difficult to compare the present results with previous studies [Loe83, Ste83a, Ste83b, Doc88, Cap88, Doc91, Bop93, Ham97]. Such comparison is often even impossible, because several of the relevant parameters were not given by the authors. Before the present investigations, the most thorough studies of plasma transmission with single laser pulses of different durations have been conducted by Docchio and Sacchi [Doc88c] and Hammer, et al. [Ham97]. Our observation that the transmission increases with decreasing pulse duration is in agreement with Hammer's results but contradicts those of Docchio and Sacchi. No convincing explanation for this discrepancy has been found. In any case, a comparison with Docchio's results is difficult because his experiments were limited to energies near the threshold and neither the focal angle nor the focal spot diameter was given.

2.3.3.6 Absorption coefficient

The measured plasma transmission and plasma length can be used to calculate the absorption coefficient of the plasma using Beer's law. Streak photographs of the plasma radiation from 12-ns pulses showed that the plasma in the focal region already dies out as the front moves into the laser beam cone [Doc88b]. The lengths of the ns-plasmas at each time point during the laser pulse were, on the average, about half as long as the total plasma lengths L observed on the time integrated photographs [Doc88b]. Thus, for ns-pulses, we have

$$\alpha_{\mathrm{LIB}} \approx -\frac{2 \ln T}{L}. \tag{2.41}$$

For ps-pulses, the spatially integrated plasma radiation lasts considerably longer than the laser pulse (cf. 2.3.4). It was therefore assumed that the plasma does not die out locally anywhere during the laser pulse. During the first half of the laser pulse the plasma front expands into the laser beam cone, so the time averaged plasma length is $\approx L/2$. During the second half of the laser pulse the plasma length equals L, so that the average length during the entire laser pulse duration is estimated to be $3L/4$. For ps-pulses, therefore,

$$\alpha_{\mathrm{LIB}} \approx -\frac{4 \ln T}{3L}. \tag{2.42}$$

The absorption coefficients calculated using Eqs. (2.41) and (2.42) are summarized in Table 2.8.

At the breakdown threshold ($\beta = 1$) the average absorption coefficient is lower than for higher pulse energies. This lowering is a result of the fact that, in the determination of the absorption coefficient, it has been ignored that part of the laser light passes the focal region before plasma formation and another part passes by the edge of the plasma. Thus, one obtains low values for α_{LIB}, especially near the threshold and for the ps-plasmas, which are smaller axially and laterally than the ns-plasmas.

β	6 ns			30 ps		
	T	L [μm]	α_{LIB} [cm^{-1}]	T	L [μm]	α_{LIB} [cm^{-1}]
1	0.49	60	238	0.91	17	73
2	0.28	80	318	0.63	20	307
5	0.11	120	367	0.43	30	375
20	0.045	170	365	0.245	60	313
50	0.028	225	319	0.175	90	258
400				0.09	230	140

Table 2.8 Absorption coefficients of ns- and ps-plasmas for different pulse energies β calculated using Eqs. (2.41) and (2.42) with the measured data on the transmission T and plasma length L (λ = 1064 nm, θ= 22°).

The absorption coefficient is, in general, somewhat higher for the ns- than the ps-pulses. This is probably a consequence of the rapid rise in the electron density during the longer laser pulse (Fig. 2.7).

While the absorption coefficient for the ns-plasmas remains almost constant as the pulse energy is raised, in the case of the ps-plasmas it reaches a peak at $\beta = 5$ and then falls to less than half that value by $\beta = 400$. This phenomenon can be explained by the reduction in the energy density in ps-plasmas as β increases which was discussed in the preceding section (Eq. (2.40)).

The values of the average plasma absorption coefficient in Table 2.8 rely on a crude estimate of the average plasma length. Docchio wanted to achieve better accuracy, so he used the plasma length $z(t)$ from Eq. (2.29) for the first half of the laser pulse and the length z_{max} from Eq. (2.30) for the second half [Doc91]. This procedure, however, is even more inaccurate than the estimate proposed here. First, because it considers only the plasma length on the laser side and not the overall plasma length, second, it ignores the fact that the ns-plasmas decay in the focal region during the laser pulse, and third, it is not based on measurements of the plasma length, but instead assumes the validity of the theoretically derived Eqs. (2.29) and (2.30). It was shown, however, in Section 2.3.2.3 that the ns-plasmas can be several times longer than predicted by the moving breakdown model. The values obtained by Nahen and Vogel (1996) for the absorption coefficient of ns-plasmas on the basis of Docchio's moving breakdown distributed shielding model are, therefore, too high. Depending on β, they are 2.5-5 times greater than the values obtained here. The values for ps-plasmas, whose lengths predicted by the moving breakdown model are approximately correct, are 1.3-1.6 times the present results.

The absorption coefficients at the breakdown threshold calculated using the rate equation model for the electron density and Eq. (2.22) with $\rho_{cr} = 10^{20}\,\text{cm}^{-3}$ are α_{LIB} = 1200 cm^{-1} for a 6 ns pulse and

$\alpha_{LIB} = 400\ cm^{-1}$ for a 30 ps pulse [Noa99]. The ratio of the values for the ns- and ps-pulses is similar to that for the two experimental values of $\beta = 1$ in Table 2.8, but the calculated absolute values are evidently higher. The difference is partly a result of the fact that the experimental values also include the light transmitted around the plasma and are, therefore, lower than the actual absorption coefficient of the plasma. Perhaps the actual electron density in the plasma is also somewhat lower than assumed in the calculation of α_{LIB}.

2.3.4 Plasma radiation

Figure 2.23 shows oscilloscope traces of the spatially integrated plasma radiation from 30-ps and 6-ns pulses. The plasma light clearly outlasts the laser pulse in both cases, but the afterglow is longer following the ns-pulses.

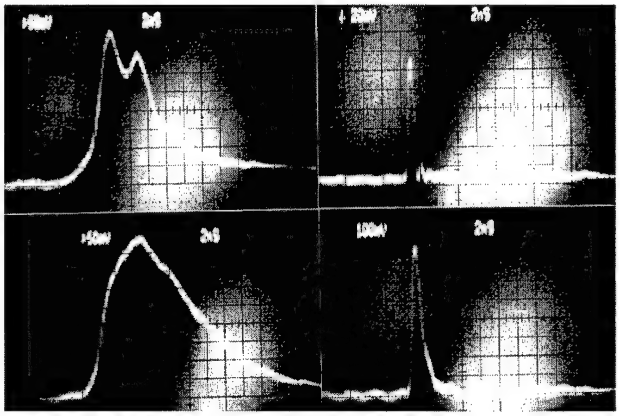

Fig. 2.23 Oscilloscope traces of the laser light intensity (above) and plasma radiation (below) from a 6-ns, 1 mJ pulse (left) and a 30-ps, 2.2 mJ pulse (right). The duration of the plasma radiation after the end of the laser pulse is less than 1 ns for the ps-pulse and about 4 ns for the ns-pulse. The duration (FWHM) of the radiation from the ns-plasmas rises from 9 ns with a 200 μJ pulse energy to 11 ns for 10 mJ.

The duration of the afterglow following the ps-pulses can provide information on the rate of recombination in the plasma. Since the plasma radiation is mostly attributable to free electron bremsstrahlung and recombination radiation [Bek66], its disappearance is evidence of a drop in the free electron density through recombination [Doc88d]. The diffusion of the electrons certainly plays no role in the light lasting less than 1 ns. The photodiode signal from the plasma radiation consists mainly of the pulse response of the detection system, although the slow decrease in the last third of the signal probably reflects the actual duration of the plasma radiation. A deconvolution assuming an exponential decay of the plasma light intensity yielded a duration of about 500 ps (FWHM). Using streak photography, Docchio obtained a half width of 240 ps [Doc88d] and Thomas et al. (1996) obtained 500 ps. The duration of the recombination process is, therefore, substantially longer than the laser pulse duration for the 30-ps pulses and the free electron density falls off correspondingly slowly (cf. Fig. 2.7).

For ns-pulses, the laser pulse is longer than the recombination time. One might then expect that the free electron density would fall off rapidly after the end of the laser pulse (Fig. 2.7) and the plasma light would barely last longer than the laser pulse. This argument, however, neglects the fact that energy will be transferred from the electrons to the molecules throughout the entire laser pulse, so that the average plasma temperature will rise continuously. The energy transfer, as well as the temperature rise, is greater for the ns-pulses because they last longer than ps-pulses. Therefore, recombination is taking place at the end of an ns-pulse, but at the same time free electrons are being produced as a result of the high plasma temperature. The plasma radiation dies out primarily as a result of the cooling caused by the explosive expansion of the entire heated plasma volume (Chapter 3). For this reason, the plasma emits light for a few nanoseconds after the laser pulse and the edge of the rapidly expanding ns-plasma always looks slightly blurred in the photographs (cf. Figs. 2.8 and 2.9).

The above discussion implies that the spectral distribution of the plasma radiation for the ns-plasmas can yield information about the average plasma temperature, because an approximate thermodynamic equilibrium sets in during the laser pulse. For a 5 ns pulse at 1064 nm, Stolarski, et al. (1995) found temperatures of about 10000 K. At the end of the 30 ps pulses, on the other hand, the electron temperature is still considerably higher than the average plasma temperature, as equilibrium is reached only after the energy transfer through recombination and inelastic collisions between free electrons and molecules has ended. The plasma radiation from the ps-pulses, thus, consists primarily of bremsstrahlung and recombination radiation and contains a very low fraction attributable to thermally excited electrons. The plasma radiation, therefore, reflects only the electron temperature and permits no inference regarding the average plasma temperature. This is the reason why the spectroscopically determined "temperature" of ps-plasmas (6000-7000 K [Sto95]) is much higher than the temperature calculated from the input energy and the equation of state of water (2160 K [Cha 97]).

2.3.5 Plasma energy density

The energy density within the breakdown volume is the controlling parameter for the importance of mechanical effects during optical breakdown. The spatially averaged energy density was determined by estimating the absorbed energy according to $E_{abs} \approx E_{in}\ (1\text{-}T)$ and ascertaining the plasma volume from photographs of the plasmas.

For the 6-ns pulses this yielded 33.2 kJ/cm^3 for a pulse energy of 1 mJ and 40.3 kJ/cm^3 for 10 mJ ($\theta = 22°$). The values for the 30-ps pulses were 11.1 kJ/cm^3 for a pulse energy of 50 µJ, 10.7 kJ/cm^3 for 1 mJ, and 6.5 kJ/cm^3 for 6 mJ ($\theta = 14°$). The energy density in the plasma is, hence, more than three times higher for the ns-pulses than for the ps-pulses. It increases with rising pulse energy in the ns-pulses, while it decreases at high energies in the ps-pulses, in accordance with Eq. (2.41). Locally, deviations from the average energy densities given here can occur for both pulse durations. Pronounced "hot spots" develop at the plasma tip with increasing β in the ps-plasmas, and the energy density on the laser side of the plasma is higher than in the rest of the plasma in the ns-plasmas (cf. 2.3.2.4).

The energy deposited in the focal volume consists of the kinetic energy of the quasi-free electrons and the electron energy transferred to the fluid through nonradiative recombination and collisions. As the kinetic energy of the electrons exceeding thermal equilibrium will, after some time, also be transferred to the molecules, the total energy density $\varepsilon_{\mathrm{LIB}}$ reached in the focal volume can be estimated integrating the losses through collisions (second term in Eq. (2.13)) and recombination (fourth term in Eq. (2.6)) with respect to time:

$$\varepsilon_{\mathrm{LIB}} = \Delta E \int_{-\infty}^{\infty} \left(\frac{m_e \omega_L^2 \tau}{M(\omega_L^2 \tau^2 + 1)} \rho(t) + \eta_{rec} \rho^2(t) \right) dt . \tag{2.43}$$

Here, as in Section 2.1.4.2, it is assumed that the average kinetic energy of all the quasi-free electrons equals ΔE/2. One can see from Eq. (2.4.3) that the energy density in the breakdown zone will be greater, the higher the peak electron density is and the longer a high electron density exists. The energy density thus increases with increasing laser pulse duration. However, we are not dealing with a direct proportionality, rather it is determined by the respective time evolution of $\rho(t)$. The time evolution of $\rho(t)$ for 30-ps and 6-ns pulses is displayed in Fig. 2.7, the evolution for fs-pulses in Fig. 8.2 (see below).

The energy density in the plasma is well above the vaporization enthalpy of water, which is 2.59 kJ/cm^3 at room temperature. It also exceeds the stored energy density of an explosive, such as TNT (≈5 kJ/cm^3 [Col48]). In the ns-pulses only 6.4-7.8% of the deposited energy is required for vaporization and in the ps-pulses, 23.3-39.8%. One consequence of the high energy density is the strong mechanical effect in plasma aided laser surgery, which will be described in more detail in Chapters 3 and 4.

2.3.6 Effect of aberrations on plasma formation

All the results on plasma formation described so far were obtained in the laboratory using an optical delivery system with minimal aberrations. Aberrations are much less easy to avoid during intraocular photodisruption. They change the breakdown threshold and the plasma shape and length, as well as the transmission properties of the plasma and, therefore, have a major influence on the precision and side effects of laser surgery. Table 2.9 compares the breakdown parameters for 6-ns pulses focussed with minimized aberrations and with spherical aberrations of different strengths [Vog98a, Vog99c].

	Spherical aberrations		
	minimized	$\Phi(r_g) = 5.5\,\lambda$	$\Phi(r_g) = 18.5\,\lambda$
Focal angle θ	22°	28°	24°
Focal spot diameter (μm), diffraction limited	3.5	2.7	3.2
Focal spot diameter (μm), measured	7.6 ± 0.6	96.6 ± 3.6	130.2 ± 5.9
E_{th} (μJ)	141 ± 1.3	371 ± 3	1202 ± 9
I_{th} ($10^{11}\,Wcm^{-2}$) diffraction limited	2.44	10.8	24.9
I_{th} ($10^{11}\,Wcm^{-2}$), measured	0.52	0.0084	0.015
Steepness of threshold, S	2.05	1.88	1.48

Table 2.9 Breakdown parameters during focussing of 6-ns pulses with minimized aberrations and spherical aberrations of different strengths. $\Phi(r_g)$ is the phase difference between the paraxial ray and the ray at the $1/e^2$ intensity point of a gaussian beam.

For the strongest aberrations considered here ($\Phi(r_g) = 18.5\,\lambda$.), the energy threshold for optical breakdown is 8.5 times that for the minimized aberrations. The steepness of the breakdown threshold decreases as the aberrations increase.

The most precise value of the threshold irradiance is obtained when the threshold energy and the spot size measured for the case of minimized aberrations are used for the calculation of I_{th}. For simplicity, we call this value ($I_{\mathrm{th}} = 0.52\times10^{11}$ Wcm^{-2}) the actual breakdown threshold. Use of the *diffraction limited spot size* for the calculation of I_{th} leads to erroneously large values, particularly for strong aberrations. The value obtained for $\Phi(r_g) = 18.5\,\lambda$ is 48 times larger than the actual threshold value. Even in the case of an optimized delivery system, the threshold obtained with a diffraction limited spot is still 4.7 times larger than the actual value, because residual aberrations are hard to avoid at large focusing angles.

When the *measured focal spot size* is used to calculate the irradiance threshold for an aberrated beam, one obtains values for I_{th} that are substantially lower than the actual threshold. For $\Phi(r_g) = 18.5\,\lambda$ the I_{th} - value is now 35 times lower than the value obtained with minimum aberrations. This presumably happens because marked intensity peaks ("hot spots") are present in the focal region of the aberrated beam (see Fig. 2.24) where plasma formation can start before the breakdown threshold is surpassed in the

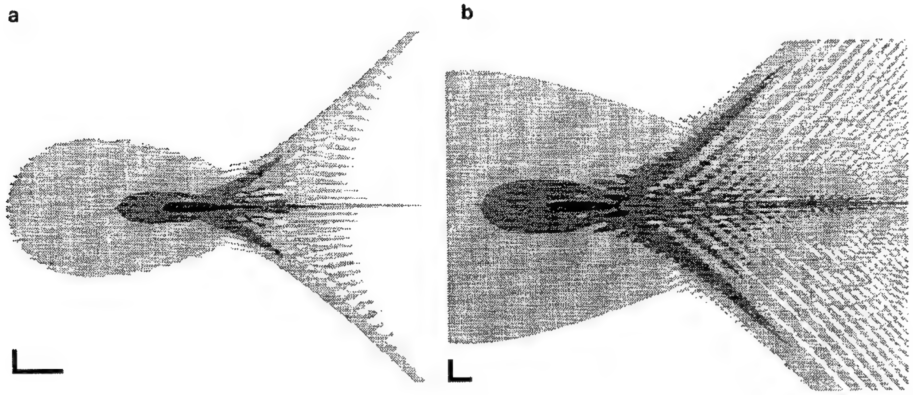

Fig. 2.24 Calculated intensity distribution in the focal region for (a) $\Phi(r_g) = 5{,}5\ \lambda$ and (b) $\Phi(r_g) = 18{,}5\ \lambda$ (from [Vog99c]). The laser light is incident from the right and the focal angle is 22°. The vertical and horizontal scales represent lengths of 10 µm and 100 µm, respectively. The three gray levels represent a total irradiance range of 100:1.

entire focal volume. In these hot spots, the threshold irradiance is probably the same as in the optimized system. The calculation based on the measured focal spot diameter yields a significantly lower value, because it averages over the maxima and the low-intensity regions lying between them. We can conclude that the presence of aberrations leads to erroneous values for the optical-breakdown threshold even if the measured focal spot size is used for its determination.

Figure 2.25 shows how the plasma shape changes owing to spherical aberrations. The plasmas produced with the optimized system are compact and fill the laser beam cone. Aberration affected plasmas are longer and often consist of several parts. They have a sharp spike behind the beam waist and also form "wings" at the edge of the beam cone when the pulse energy is high. These plasma shapes develop because a convex lens with spherical aberrations focuses the peripheral rays more strongly than the paraxial region of the laser beam. Thus, peripheral rays and paraxial rays intersect in front of the beam waist and a hollow cone shaped zone with a high intensity develops, within which the plasma "wings" are formed (cf. Fig. 2.24). The plasma spike develops along the paraxial rays of the laser beam, which are focussed behind the beam waist. Interference between the intersecting parts of the beam causes a modulation in this intensity distribution and leads to the formation of "hot spots" [Eva69, Vog99c].

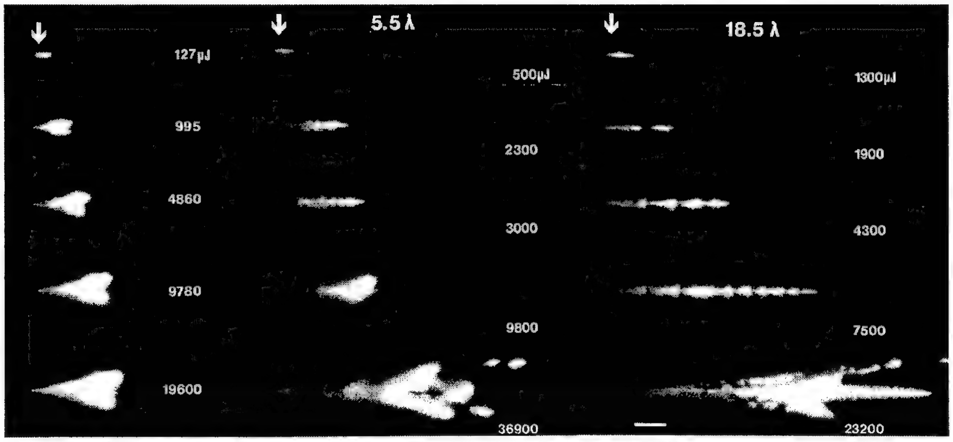

Fig. 2.25 Shape of the plasma for aberrations of different strengths. (a) Minimal aberrations, $\theta = 22°$, (b) $\Phi(r_g) = 5.5\ \lambda$, $\theta = 28°$, (c) $\Phi(r_g) = 18.5\ \lambda$, $\theta = 24°$. The laser light is incident from the right and the position of the beam waist is marked by an arrow. The corresponding pulse energies are indicated on the frames. The scale represents a length of 100 μm.

For pulse energies above the breakdown threshold the plasmas affected by aberrations are up to three times longer than in optimized systems and the plasma length at the breakdown threshold also increases as the degree of aberration increases (Fig. 2.26). The greater plasma length is attributable to the distortion of the plasma shape illustrated in Fig. 2.25 and to the formation of plasma islands outside the main plasma. In this way, aberrations make localized energy deposition into a medium more difficult.

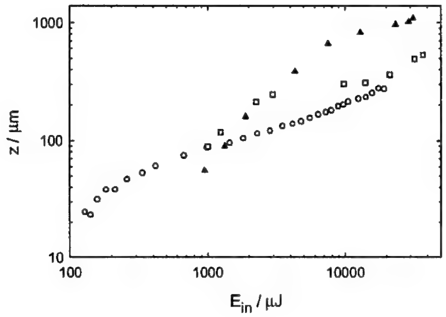

Fig. 2.26 Plasma length for minimum aberrations (o), for $\Phi(r_g) = 5.5\ \lambda$ (□), and for $\Phi(r_g) = 18.5\ \lambda$ (Δ).

Aberrations lead to a considerable increase in the plasma transmission. The laser energy transmitted through the plasma is, in the entire energy range studied here, for $\Phi(r_g) = 18.5\lambda$ 17-20 times greater than in the case of minimized aberrations (Fig. 2.27). The rise in the transmitted energy is partly

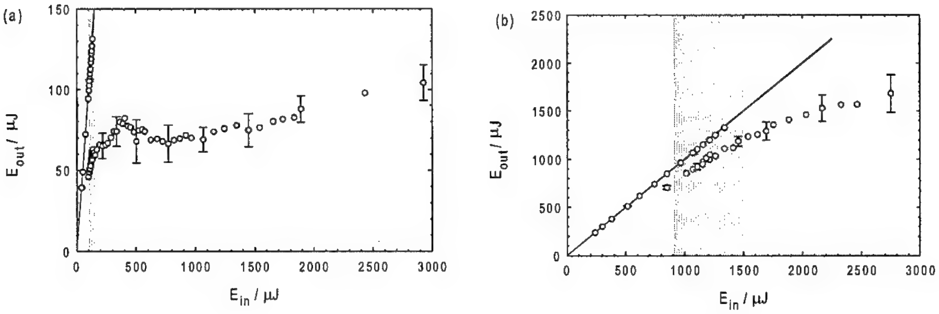

Fig. 2.27 Transmitted energy as a function of the incident energy (a) for minimized aberrations and (b) for $\Phi(r_g) = 18.5\ \lambda$. The shaded areas indicate the region between 10% and 90% breakdown probabilities. E_{th} (the 50% breakdown probability) lies in the middle of the shaded region.

attributable to the higher breakdown threshold and is partly a consequence of the irregular intensity distribution in the focal region. The incident laser light is mainly absorbed at the intensity maxima and partially transmitted between or next to the maxima. Therefore, a larger percentage of the laser light is transmitted (Fig. 2.28). At the threshold, the transmission is 50% in the optimized case but 85% with strong aberrations.

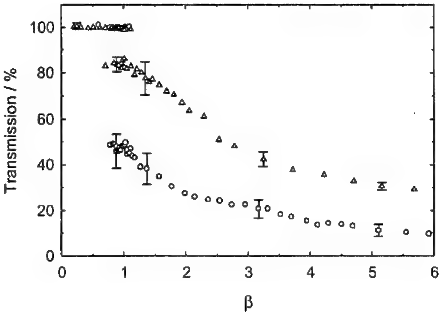

Fig. 2.28 Transmission as a function of the normalized pulse energy β for minimal aberrations (o) and for $\Phi(r_g) = 18.5\ \lambda$ (Δ).

2.4 Summary and clinical consequences

2.4.1 Summary

The thresholds for optical breakdown in water, the plasma formation at irradiances above the breakdown threshold, the optical properties of laser plasmas, and the energy density in the plasmas have been studied for 30-ps and 6-ns Nd:YAG laser pulses with different focal angles and wavelengths (532 nm and 1064 nm).

Plasma formation at the breakdown threshold. The irradiance I_{th} required for optical breakdown increases with decreasing pulse duration, while the fluence threshold F_{th} decreases. The average value of I_{th} for the 30-ps pulses (4.5×10^{11} W/cm^2) was 5.9 times higher than for the 6-ns pulses (0.76×10^{11} W/cm^2), and the average value of F_{th} for the ps-pulses (13.5 J/cm^2) was 34 times lower than for the ns-pulses (453 J/cm^2).

For the focal spot sizes between 5 µm and 50 µm studied here, no systematic dependence of the breakdown threshold on the focal spot diameter was observed. This result is in contrast to the assertions of previous authors who calculated the threshold values with diffraction limited, instead of measured, focal diameters and neglected optical aberrations and self-focussing effects. Aberrations show up primarily for large focal angles and self-focussing plays a role for angles under 2° within the range of pulse durations studied here.

The experimental data have been analyzed with the aid of Kennedy's model for optical breakdown [Ken95a] and by solving the complete rate equation for the time evolution of the electron density. At 1064 nm, the measured thresholds I_{th} were roughly equal to the calculated thresholds I_m for the production of seed electrons for the ionization cascade through multiphoton ionization, but they were substantially higher than the thresholds I_C for completion of a cascade during the laser pulse. Hence, optical breakdown in distilled water for 30 ps and 6 ns pulse lengths proceeds through multiphoton-initiated avalanche ionization. The initial electron density required to initiate an ionization avalanche was about 4×10^9 cm^{-3} for 6-ns pulses and 1.4×10^{11} cm^{-3} for 30-ps pulses. At 532 nm, multiphoton ionization provides not only the seed electrons for cascade ionization, but also contributes significantly to the production of free electrons throughout plasma formation.

The statistics of optical breakdown in distilled water are strongly influenced by multiphoton processes at both wavelengths and cannot be completely described if only the cascade ionization is considered.

Plasma formation above the breakdown threshold. Plasma formation for irradiation levels above the breakdown threshold can be described as a "breakdown wave," in which an optical breakdown takes place everywhere the threshold I_{th} is exceeded ("moving breakdown" [Doc88a]).

For equal pulse energies, ns-plasmas were always shorter than ps-plasmas, since they could not expand as far back into the laser beam cone because of the higher breakdown threshold F_{th}. For equal *normalized* energies β the ns-plasmas were, nevertheless, significantly longer, especially for pulse energies near the breakdown threshold and for large focal angles. This observation is in contrast to the Docchio's moving breakdown model [Doc88a] according to which the plasma length is independent of the laser pulse duration for constant β. In the ns-pulses the breakdown threshold presumably decreases during a pulse, because the plasma formed in the beam waist toward the beginning of the pulse emits UV radiation that produces the free electrons in the neighborhood of the plasma required for initiation of cascade ionization. In this way, the plasma can become larger than predicted by the model assuming a temporally and spatially constant breakdown threshold throughout the plasma formation process.

The plasma length on the laser side, z_{max}, as a function of the normalized pulse energy β could, for the ps-pulses, be described by $z_{max} \propto (\beta - 1)^{n}$ with $n = 0.54 \pm 0.02$, in good agreement with the moving breakdown model, which yields $n = 0.5$. For the ns-pulses, there were deviations from the model for the reasons given above: for large focal angles $n = 0.31$ and only for very small angles did the exponent increase to $n = 0.47$. The plasma length depends strongly on the focal angle θ. For ps-pulses and constant β, $z_{\max} \propto [\tan(\theta/2)]^{-2}$. The dependence on θ was not so marked for the ns-pulses.

Optical properties of the plasma. Scattering and reflection from the plasma only involved a few percent of the incident laser energy, so that the plasma absorption could be approximated by $A \approx (1\text{-}T)$. The reflection factor for the plasma is low, because the site of the optical breakdown moves toward the incident laser beam as the power in the laser pulse rises. As the plasma grows, a new absorber is continually produced with a relatively lower electron density and, accordingly, a lower plasma frequency, so that good energy coupling is guaranteed [Hug75]. Absorption of the light in the newly formed plasma lowers the energy input to the previous produced plasma further downstream and, thereby, limits the attainable electron and energy density in the overall breakdown volume.

The transmission was substantially higher for ps-pulses than for ns-pulses, regardless of the focal angle. For the 6-ns pulses, the transmission at the threshold fell immediately to about 50% for all the focal angles studied here ($\theta = 22°$, 8.5°, 4°), and for a normalized energy of $\beta = 50$ (attainable only for $\theta = 22°$) it was less than 3%. For the 30-ps pulses, on the other hand, the transmission at threshold was 91% for focal angles of 22° and 8.5° and was 98% for an angle of 4°. As the energy was raised to $\beta = 50$, the transmission fell (depending on the focal angle) to just 17.5-42%. The transmission of the ns-plasmas is lower primarily because they are longer for equal β than the ps-plasmas. In addition, the absorption coefficient for the ns-plasmas is higher ($a_{LIB} \approx 240$ cm^{-1}) at the breakdown threshold than for the ps-plasmas ($a_{LIB} \approx 75$ cm^{-1}). Above threshold, for $2 < \beta < 50$, the absorption coefficient of the ns-plasmas (320-370 cm^{-1}) was only slightly higher than that of the ps-plasmas (260-375 cm^{-1}).

The plasma transmission rose with decreasing focal angle, probably because the energy density in the plasma is lower for small angles which leads to a lower electron collision frequency and, thereby, to a lower interaction cross section for inverse bremsstrahlung absorption. Self-focussing effects for focal angles below 2° caused a further rise in the transmission. This phenomenon presumably happens because, as the central filament develops with higher irradiance, an extended region arises in the surroundings of the filament where the irradiance remains below the breakdown threshold [Loy73, Mar75].

Energy density in the plasma. The energy density in the ns-plasmas (33-40 kJ/cm^3 for $\theta = 22°$) is more than three times higher than in the ps-plasmas (6.4-11.1 kJ/cm^3 for $\theta = 14°$). For both plasma durations the energy density is substantially higher than the enthalpy of vaporization of water at room temperature (2.6 kJ/cm^3). Strong shock waves and cavitation effects during intraocular photodisruption are consequences of the high plasma energy density.

The role of aberrations. Spherical aberrations lead to an increase in the energy threshold for optical breakdown (by a factor of 8.5 for $\Phi(r_g) = 18.5\ \lambda$), to a breakup of a compact plasma into isolated plasmas, to a total plasma length that is as much as three times longer than in an optimized system, and to higher transmission. At the threshold, the transmission increases from 0.5 to 0.85, and the transmitted energy within the total energy range was 17-20 higher when $\Phi(r_g) = 18.5\ \lambda$ than when aberrations were minimized.

2.4.2 Clinical consequences

Nonlinear absorption permits spatially limited energy deposition *inside* linear transparent media and allows, therefore, noninvasive intraocular laser surgery. The absorption coefficient, at about 300 cm^{-1}, is, however, substantially lower than the linear absorption at selected wavelengths in the UV and IR. For example, the absorption coefficient of the cornea is about 40000 cm^{-1} at 193 nm [Pet96] and about 13500 cm^{-1} at 2940 nm (for 77% water content in the cornea [Mau94] and an absorption coefficient for water of 17700 cm^{-1} [Mah78]). Thus, photodisruption *within* tissue cannot attain as high a spatial precision as ablation at a tissue *surface* on the basis of linear absorption.

The characteristics of plasmas on tissue surfaces differ from those inside tissue [Rea71, God77, Kim98], so that when subnanosecond pulses are applied, thin tissue layers with thicknesses on the order of 1 μm or less can be removed using plasma aided ablation [Ste89, Nie91].

The *optimum wavelength* for intraocular laser surgery lies between about 800 and 1150 nm, since in this range light is transmitted well in the eye, linear absorption by melanin and blood in the background of the eye is low, and the light is invisible to the patient.

The primary effect of the laser pulse in plasma aided intraocular laser surgery involves *vaporization of tissue within the plasma volume* [Vog90]. This primary effect can be created with greater precision by ps-pulses than by ns-pulses, since ps-pulses permit plasma formation at lower pulse energies and the plasmas are smaller than the ns-plasmas near the breakdown threshold (for equal β).

The *efficiency of energy transfer* from laser light to plasma is substantially higher for 6-ns pulses than for 30-ps pulses, since approximately 50% of the pulse energy will be absorbed at the breakdown threshold for the ns-pulses. With ps-pulses, this percentage is first reached at $\beta = 6$ and at the threshold, absorption is less than 8%. The low percentage of energy deposition, together with the low threshold energy for optical breakdown, can, therefore, be used to produce very small scale tissue effects even on a cellular level (Section 7.2.6 and [Vog94b]).

In intraocular microsurgery, sensitive structures behind the laser focus (e.g., the retina) will be protected from damage by absorption and scattering of the laser light in the plasma. This *plasma shielding* effect is most effective for ns-pulses: E_{out}/E_{in} is 2-6 times lower for 6-ns pulses than for 30-ps pulses. For equal values of β the transmitted energy E_{out} is, nevertheless, always at least a factor of 8 smaller for ps-pulses than for ns-pulses, since the threshold energy for the formation of ps-plasmas is very much smaller.

Large focal angles produce a low breakdown energy (at 22° roughly 1/4 of the value at 8°), short and compact laser plasmas, and a maximal absorption of the laser energy in the plasma. Because of the large divergence angle behind the laser focus the irradiance at the retina and at other structures located behind the application site will be low. Thus, the maximum possible focal angle should be applied for each application site in the eye. The optimum focal angle can be realized by using appropriate contact lenses placed on the corneal surface of the eye.

The breakdown energy can be further minimized by using an optimum laser mode with a gaussian intensity distribution and by the *elimination of aberrations* in the optical system. Elimination of aberrations involves choosing a contact lens whose aplanatic point coincides with the plane of the application site in the eye and avoiding tilting of the contact lens. If the laser light is focussed behind the aplanatic point of the contact lens, there is a dramatic rise in the spherical aberrations [Rol86] causing an increase of the breakdown threshold, a drop in the plasma absorption, and a deterioration in plasma shielding. Tilting of the contact lens leads to similar negative consequences through coma and astigmatism.

Self-focussing plays no role in intraocular microsurgery within the range of pulse durations considered here. It has been observed in the neighborhood of the breakdown threshold only for very small focal angles < 2°. For clinically relevant focal angles, it was observed only for ps-pulses and only for energies very far above the breakdown threshold. Self-focussing appears at clinically relevant focal angles and near the breakdown threshold only when the pulse duration is shortened into the femtosecond range (cf. Chapter 8).

3 Shock wave production and cavitation bubble formation

During laser induced plasma formation, an extraordinarily high energy density of about 10-40 kJ/cm^3 develops in the focal volume within a very short time (cf. Section 2.3.5). Temperature and pressure rise rapidly to very high values, causing an explosive expansion of the laser plasma. The expansion of the plasma leads to the production of a shock wave and, if the application site is in a fluid environment, to the formation of a cavitation bubble. These mechanical effects form the basis of laser lithotripsy [Teng87a,b, Rin95, Vog97a] and, in many intraocular laser applications, e.g., posterior capsulotomy [Ste85, Fan89], they contribute to the desired surgical effect. More often, however, they are the source of undesirable side effects, which limit the spatial precision of laser surgery. This comment also applies to plasma aided intraocular microsurgery near sensitive tissue structures (retina or corneal endothelium) [Vog86, Mel87, Vog90, Vog94a,b, Vog96a], and to short pulse laser ablation in fluid environments, as during angioplasty [Leu93, Vog96b] or arthroscopic surgery [Sie92]. Whether the mechanical effects are desirable or not, shock wave production and cavitation effects must be characterized in order to be able to estimate the dependence of tissue effects on the laser parameters and to find an optimum compromise between efficiency and precision.

In order to *characterize the propagation of shock waves*, one studies the pressure amplitude p_S at the shock front and the shock wave profile as a function of the distance r from the emission center of the shock wave. The peak pressure and the risetime of the shock front determine the pressure gradient to which the tissue and cells will be exposed. The shape of the shock wave (the complete pressure profile) determines the energy content of the shock wave and the tissue displacement caused by the shock wave. The possible range over which damage occurs will be affected by how rapidly the shock pressure decays with distance. For spherical shock waves, this pressure drop is determined by the geometric decrease in the pressure amplitude, as well as by energy dissipation at the shock front [Duv63] and the increase in the shock wave duration owing to nonlinearities in the propagation of sound [Col48]. The determination of $p_S(r)$ and of the increase of the shock wave duration make it possible to estimate the spatial distribution of the shock wave energy dissipation. This way, the energy transfer from the shock wave to the tissue can be assessed. Knowledge of the scaling laws for the shock pressure with increasing distance from the emission center also forms the basis for calculating the pressure in the neighborhood of the emission center from measurements in the far field, which are generally much simpler than measurements near the plasma.

In order to *characterize cavitation effects*, one studies the initial expansion velocity and maximum size of the cavitation bubble. These parameters determine the maximum tissue displacement that can be caused by expansion of the laser plasma and, thus, define the potential for structural tissue deformation and rupture on a macroscopic scale.

The maximum size of the cavitation bubble can be easily determined by optical or acoustic methods (Section 3.2.3 and [Vog86]) and the shock pressure in the far field can also be simply measured with piezoelectric pressure probes, assuming that its risetime is short compared to the duration of the shock wave [Vog88]. The initial phase of bubble expansion and shock propagation in the neighborhood of the emission center are, however, difficult to assess experimentally. Earlier studies of optical breakdown at clinically relevant laser pulse energies have shown that the shock speed falls to near the normal sound speed within a few hundred nanoseconds and over a distance of a few hundred micrometers [Fuj85, Zys89, Dou91]. Characterization of the shock wave parameters thus requires a detailed study of events taking place within a volume of less than a cubic millimeter over a time of about 100 ns. This situation imposes very high requirements on the measurement accuracy: the spatial and temporal resolution must be within a few micrometers or nanoseconds.

The *shock pressure in the vicinity of the plasma* cannot be measured with a hydrophone. The active element of piezoelectric pressure sensors is usually flat and no smaller than 1 mm^2. If they are used to detect a spherical shock wave with a small radius of curvature, then at any time only a part of the plane sensor element will be struck by the shock and this leads to an error in the measurement data. In addition, a hydrophone can easily be damaged by strong pressure transients or cavitation events. Fiber optic hydrophones [Sta93] provide better spatial resolution, down to about 100 μm, but this limit is still far coarser than required for shock wave measurements in the vicinity of the plasma and, as before, the danger of damage to the sensor during optical breakdown remains. Noninvasive optical diagnostics offer a method by which the shock waves may be recorded by a focussed probe laser beam or photographically. Here the spatial resolution is determined by the size of the probe laser beam focus and the resolution of the imaging optics, and can be a few micrometers.

In general, the optical techniques use the fact that the refractive index of a fluid increases with rising pressure [Scr90, Ved75, Tho85]. If a shock wave is illuminated by a laser beam, the pressure dependence of the refractive index will lead to a phase shift of the light and to a change in direction of the light that is proportional to the pressure gradient [Sul84]. The first group of optical techniques is based on a quantitative determination of the phase shift or of the deflection of the light. The phase shift can be determined by interferometric techniques [War91, All94] or from the far field diffraction pattern [Hin76].

The beam deflection can be measured by converting the deviation in direction by means of schlieren or aperture stops into an intensity modulation that can be detected by a photodiode [Hin76, Dav80, Sul84, Sig86, Vog88]. All of these procedures yield the complete shock profile including the peak amplitude of the pressure pulse. They are, however, complicated and can only be used at distances over 200 µm from the laser plasma [All94]. At shorter distances, the path of the light through the spherical shock can no longer be described in a simple way [Dav80], so that the determination of the shock profile and, with it, the peak pressure, will be too inexact. A further difficulty arises because the shock front is considerably thinner than 1 µm [Eis64, Har82] and, therefore, considerably smaller than the optical resolution. Thus, only the trailing edge of the shock wave will actually be detected. The pressure at the shock front can only be determined if the "base pressure" far behind the shock is known. This, however, is not the case for shock waves in the vicinity of the plasma, where the pressure between the shock front and plasma is everywhere far higher than the hydrostatic pressure.

The second group of optical techniques, in which the deflection of light through the shock wave is only used qualitatively for detecting the location of the shock, is suitable for measurements of shock front pressure in the immediate vicinity of the plasma. In these techniques, the shock speed is measured, and the pressure jump at the shock front is then determined with the aid of the equation of state of the fluid [Fuj85, Zys89, Dou91, Vog94a, Juh94, Noa95, Vog96a, Juh96, Noa97]. In the first version of this method, which has been used by Fujimoto, et al. [Fuj85] and Zysset, et al. [Zys89], the shock passes through the focus of a single probe laser beam and deflects the light. This produces an intensity modulation that is determined by a photodiode. By varying the distance r between the laser plasma and the probe beam focus in successive laser shots and measuring the time t between plasma formation and the diode signal, the $r(t)$ curve for the shock wave can be obtained. The shock speed u_S and, from that the pressure jump p_S at the shock front, can be determined as a function of t or r from the slope of the $r(t)$ curve. A systematic study of the shock pressure as a function of distance was, however, not made by Fujimoto and Zysset. Here Doukas, et al. [Dou91] have done the pioneering work. They used a somewhat different measurement technique, in which the shock wave passed through two laser foci that are separated by a known distance. It was possible to determine the velocity directly from the distance between the foci (about 35 µm) and the time for the shock to pass, without having to first make further measurements for determining the $r(t)$ curve. This success was achieved, however, at the cost of a substantial limitation on the spatial resolution, which is set by the distance between the two laser foci.

Both pump-probe techniques have the disadvantage of only providing a one-dimensional picture of the shock propagation. The position of the measurement site relative to the plasma is hard to control, and fluctuations in the location where the plasma is produced lead to inaccuracies in the determination of the distance r moved by the shock waves. In the following study, the shock wave and bubble wall velocities will, therefore, be determined from a series of photographs, which were taken with increasing delays between the times of optical breakdown and the exposure [Vog94a, Vog96a]. For these pictures, part of the Nd:YAG laser light used to produce the plasma was separated by a beam splitter, frequency doubled, passed through an optical delay line, and used for illumination. The advantage of this method is that it provides two-dimensional information, while the reproducibility and plasma formation site can be checked in the photographs. The spatial resolution is set by the resolution of the photographic objective (about 4 μm) and is, therefore, just as high as in the methods employed by Zysset and Fujimoto. The time resolution is determined by the duration of the illumination pulse and the intervals over which the time separation between plasma formation and the illumination pulse is increased. The time resolution was better than 6 ns in all measurements. For the time immediately after breakdown, the step size was reduced to only 1 ns. A further improvement in time resolution to the subnanosecond range is possible by recording the shock wave propagation with the aid of streak photography (cf. Chapter 8) [All94, Noa95, Noa97]. Streak photography can also be used to record the complete *r(t)* curve in a single shot.

The experiments were done for 30 ps and 6 ns pulse durations with the same laser system and the same focussing optics used in the study of plasma formation (Chapter 2). The events following ps-pulses with energies of 50 μJ and 1 mJ and ns-pulses with energies of 1 mJ and 10 mJ were studied in special detail. For both pulse durations, the lower energy value is about 5 times the breakdown threshold and the higher energy is close to the upper limit of the clinically suitable energy range. The common energy of 1 mJ permits a direct comparison of the effects for the two pulse lengths.

Since measurements of the initial phase of the shock wave emission and bubble expansion are very tedious, it would be desirable to have a method to deduce the respective pressure and velocity values from other measurements which are easier to perform. Such a *calculation of the shock and bubble dynamics* is possible when the deposited laser energy, plasma volume, and laser pulse duration are specified [Lo90, Ait96, Cha97, Coo97]. The accuracy of the calculated peak pressure in the plasma depends thereby very strongly on the quality of the equation of state for the material in the plasma volume, which must be known for a temperature range of a few thousand degrees and a pressure range of at least 10000 MPa. The system of equations of Harr et al. (1981) and tabulated equations of state data such as SESAME [Lyp92] are available for this purpose. A weakness of most numerical studies is that instantaneous energy deposition is assumed and the time variation of the laser pulse is neglected. This weakness is not fundamental in nature, but can be overcome with more computing time [Coo97]. Finite element hydrodynamic codes offer the possibility of taking the spatial variation in the energy deposition, i.e., the motion of the plasma front during the laser pulse, into account [Sca98] and of estimating the zone where damage is done to tissue in the neighborhood of an expanding cavitation bubble [Gli97].

Here an alternative, less computationally expensive, approach is followed [Ebe78, Vog96a] in which bubble formation and shock emission are described using the Gilmore model for cavitation bubble dynamics [Gil52, Kna71]. It begins with a nucleation bubble equal in size to the plasma volume. The deposited energy is introduced into the calculation "retrospectively" over the dimensions of the resulting cavitation bubble: the initial conditions are varied iteratively until the calculation gives the experimentally observed cavitation bubble size. The model permits calculation of quantities that are difficult of access, by using easily determined experimental measurement data (both the maximum cavitation bubble size and the plasma volume are easy to determine). The advantage of this method is that few demands are placed on knowledge of the equation of state of the material in the plasma volume. Certainly, in order to obtain a realistic description of shock propagation near the plasma or of bubble expansion, the equation of state of the liquid in the neighborhood of the bubble must be known as accurately as possible. Inasmuch as the temperatures in the liquid are substantially lower than in the plasma or in the interior of the bubble, one can, however, rely on relatively simple analytic equations of state.

The numerical calculations were done for the same laser parameters as in the experimental studies. The experimental and numerical results are partially complementary, as they provide access to different shock wave parameters. For example, a determination of the complete shock wave profile in the vicinity of the plasma is almost impossible experimentally but can be done numerically. Conversely, when the propagation of the shock is followed numerically into the far field with the model, inadequacies of the theoretical model show up ever more strongly, so that here the experimental data are given priority. The pressure decrease $p_S(r)$ and the velocity of the bubble wall in the neighborhood of the plasma can, on the other hand, be determined both experimentally and numerically. Comparison of the experimental and numerical results for these parameters allows an assessment of the accuracy of the model predictions. In order to obtain a coherent overall picture of shock propagation and bubble formation, the experimental and numerical results will be presented separately but discussed together.

3.1 Theoretical background

3.1.1 Detachment of the shock wave and formation of a cavitation bubble

The input of energy by laser light leads primarily to a rise in the free-electron density and an increase in the energy of the free electrons within the breakdown volume. The energy of the electrons is then transferred to molecules through inelastic collisions of the electrons and recombination and an equilibrium temperature sets in within the plasma volume. For ps-pulses, this equilibration process takes place mainly after the end of the laser pulse, while for nanosecond pulses a dynamic equilibrium between the production of free electrons and their recombination develops during the pulse (Fig. 2.7). In this way, for equal maximum free-electron densities (10^{20} cm^{-3}) a higher energy density develops in the plasma volume for ns-pulses than for ps-pulses. The resulting temperatures are about 10000 K for 6-ns pulses and about 2200 K for 30-ps pulses, both for a wavelength of 1064 nm (cf. 2.3.4). The rapid temperature rise causes an equally rapid pressure rise to between 1 and 10 GPa [Vog96a]. As a result, the water in the plasma volume enters a highly supercritical state with $T \gg T_{crit} = 374$ °C, $P \gg P_{crit} = 22.5$ MPa). The high pressure leads to an explosive expansion of the plasma volume, which proceeds with a pressure drop and an adiabatic fall in the temperature. Because of the pressure drop, the supercritical water becomes steam and a phase boundary develops between the material in the breakdown volume and the surrounding fluid. From then on, one can speak of the existence of a cavitation bubble and treat the further dynamics as the expansion of a bubble. For simplicity of terminology, in the following reference will be made to "bubble expansion" even in the early stage of plasma expansion, with the bubble wall being identified with the boundary between the plasma and the fluid or with the boundary between supercritical water and water under normal conditions.

The elevated pressure, P, in the interior of the bubble compresses the surrounding fluid and accelerates it to a particle velocity u. The compression wave propagates in accordance with the Kirkwood-Bethe hypothesis [Kir42] at a velocity $c+u$ into the surrounding fluid, where c is the local speed of sound in the stationary medium at pressure p. Since the propagation velocity; $c+u$, is greater than the particle velocity, the leading edge of the compression wave detaches immediately from the bubble wall. Both the sound speed and the particle velocity increase with rising pressure. Parts of the pressure pulse with a higher amplitude move, therefore, faster than those with a smaller amplitude. As a result, the front of the pressure pulse steepens as it propagates (Fig. 3.1) and a shock front forms, i.e. a discintinuity develops in the pressure, density, and particle velocity (Fig. 3.2).

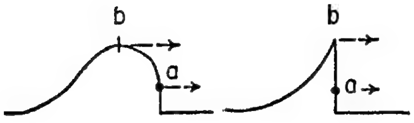

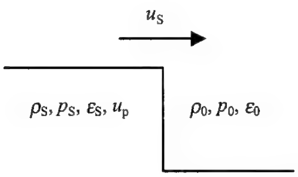
u_S
$\rho_S, p_S, \varepsilon_S, u_p$
$\rho_0, p_0, \varepsilon_0$

Fig. 3.1 Formation of a shock front in a pressure pulse with very high amplitude. Since the pressure is higher at b than at a, the sound speed and the particle velocity are higher at b, so that the perturbation at b moves faster than at a. Hence, regions with higher pressure catch up with regions with lower pressure moving ahead of them, and a front with a very steep density gradient develops.

Fig. 3.2 Parameters for describing a shock front: ρ_0 and ρ_S are the density, p_0 and p_s are the pressure, and ε_0 and ε_S are the internal energy before and after compression; u_S is the shock speed and u_p denotes the particle velocity behind the shock front. The particle velocity in the medium at rest ahead of the shock front is zero.

The medium at the shock front is suddenly compressed and must be accelerated to the particle velocity u, which involves the dissipation of energy (3.1.9). Therefore, the shock front moves at a velocity u_S that is higher than the sound speed c_0 in the stationary, uncompressed medium, but lower than the local sound speed $(c+u)$ immediately behind the shock front [Kir42, Col48]. Because of the higher sound speed behind the shock front, the tendency of the shock front to flatten owing to dissipative effects is constantly compensated and the shock front remains stable over long distances out to pressures below 0.1 MPa [Flo55, Eis64, Rog77]. Since $(c+u)$ decreases on the decaying side of the shock front and is lower than the shock front velocity at a sufficient distance from the shock front, the shock wave broadens as it propagates [Col48].

The pressure pulse emitted into the fluid does not develop into a shock wave under all circumstances, because a spherical geometry implies a rapid diminution in the amplitude of the pressure pulse and, thereby, a weakening of the nonlinear effect which is responsible for the steepening of the rising front of the pulse. With long laser pulse durations, the initial risetime of the pressure pulse may be so long that the amount of steepening in the high pressure phase is not sufficient to create a shock front [Ben58].

Between the shock front and the cavity wall, a radial, outwardly directed flow develops into which ever more fluid will be drawn as the shock propagates. The flow is driven by the interior pressure of the bubble which falls rapidly because of the bubble expansion. This causes a drop of the pressure in the fluid at the bubble wall to a value smaller than that at the shock front. When the pressure at the bubble wall has fallen to the hydrostatic pressure, one can say that the shock wave has detached. At this point in time, the kinetic energy of the fluid in the neighborhood of the bubble is maximal. Owing to inertia, the fluid continues to expand radially. This expansion leads to a drop in the pressure inside the bubble and in the fluid adjacent to the bubble to levels below the hydrostatic pressure. The increasing difference between the hydrostatic pressure and the pressure inside the bubble finally brings the expansion of the bubble to a halt and leads to the collapse of the bubble (Chapter 4).

In order for a cavitation bubble model to adequately describe bubble formation and shock wave emission, it must satisfy a few minimum requirements: (i) It must take into account the gas content of the bubble, since the driving force for the expansion of the bubble will be modeled by an elevated pressure inside the bubble. (ii) It must account for the energy of compression, which will be stored in the fluid through pressure induced density changes. (iii) It must reproduce the finite propagation velocity of the pressure wave as correctly as possible. The Rayleigh bubble model [Ray17, Kna71] for the collapse of an empty cavity in an incompressible fluid ($c = \infty$) satisfies none of these requirements. It does, indeed, provide good estimates for the collapse time of real bubbles that contain fixed amounts of water vapor and gas, but it is completely unsuitable for the analysis of processes in the end phase of collapse or during bubble generation. Similarly, Plesset's modification of the Rayleigh equation [Ple49, Kna71], which does take the gas content of the bubble and surface tension into account, but still treats the fluid as incompressible, is also inadequate for analyzing acoustic emission. The acoustic approximation for the compressibility, which is based on a constant sound speed c_0, goes a step further. A good summary of the 'acoustic' first order models has been given by Prosperetti and Lezzi (1986). They are suitable for the description of the bubble dynamics, as long as the maximum bubble wall velocity remains clearly below the sound speed in the fluid [Lez87]. This velocity restriction, however, is not satisfied for bubble production from laser induced plasmas, as will be shown below. The pressure dependence of the sound speed must, therefore, be taken into account. A second order model of this sort, first presented by Gilmore [Gil52, Kna71], will be used in the following for modeling bubble formation.

3.1.2 The Gilmore model for cavitation bubble dynamics

Gilmore's model for cavitation bubble dynamics takes the compressibility of the fluid, viscosity, and surface tension into account. The gas content of the bubble is assumed constant, and vaporization and condensation, as well as the diffusion of gas through the bubble wall, are neglected. Heat conduction between the interior of the bubble and the surrounding fluid is, likewise, neglected. Heat conduction and condensation have an obvious effect on the pressures attained as the bubble collapses [Fuj85], but for the initial phase of laser-induced bubble expansion they are presumably of secondary importance. The compressibility is not modeled directly as a relationship between the pressure and density, but through the variation in the enthalpy of the fluid. A compression corresponds to a rise in the "elastic" energy of the fluid and, thereby, to a rise in the enthalpy. This rise results in a radial compression wave owing to the expansion of the heated and pressurized fluid, which can be described as the propagation of kinetic enthalpy $(h + u^2/2)$. During the expansion, the elastic energy is partially conserved as a compression zone behind the shock front, partially converted into kinetic energy of the radial fluid flow, and partially converted into potential energy of the growing bubble [Pro86].

The bubble dynamics obey the equation

$$\dot{U} = \left[-\frac{3}{2}\left(1-\frac{U}{3C}\right)U^2 + \left(1+\frac{U}{C}\right)H + \frac{U}{C}\left(1-\frac{U}{C}\right)R\frac{dH}{dR}\right]\cdot\left[R\left(1-\frac{U}{C}\right)\right]^{-1}. \tag{3.1}$$

Here R is the bubble radius, $U = dR/dt$ is the velocity of the bubble wall, C is the sound speed in the fluid at the bubble wall, and

$$H = \int_{p_0}^{P(R)} \frac{dp}{\rho} \tag{3.2}$$

is the difference between the enthalpy of the fluid at the boundary of the bubble and that of the fluid at large distances, where the hydrostatic pressure p_0 predominates; p and ρ denote the pressure and density in the fluid.

In deriving Eq. (3.1) from the Navier-Stokes equations [Gil52, Kna71], Gilmore used the Kirkwood-Bethe hypothesis to describe the pressure dependence of the sound speed. It states that the quantity $y = r\,(u^2/2 + h)$ propagates in the fluid with a velocity $c+u$ [Kir42]. Here h is the enthalpy difference per unit mass between the fluid at pressures p and p_0 and $u^2/2$ represents the kinetic energy per unit mass of the fluid. It is known that perturbations propagate in flowing media at a velocity c_0+u, i.e., the sum of the sound speed and the flow velocity, when the pressure amplitude is small [Lig78]. It seems reasonable, therefore, that the propagation velocity for perturbations with a higher amplitude should also approach the (now pressure dependent) sum $(c+u)$ of the local sound speed and flow velocity.

The enthalpy H and the sound speed C at the bubble wall can be calculated from Eq. (3.2) and

$$C = \sqrt{\frac{dp}{d\rho}}, \tag{3.3}$$

if the relation between pressure and density, i.e., the equation of state of the medium, is known. Gilmore used the isentropic Tate equation,

$$\frac{P+B}{p_0+B} = \left(\frac{\rho}{\rho_0}\right)^n, \tag{3.4}$$

which neglects the effect of temperature on the pressure-density relationship (cf. 3.1.6) and, thereby, allows an especially simple analytic representation of the pressure dependence of the enthalpy and sound speed. The constants B and n for water are given by B =314 MPa and n=7 [Rid 88]. The Tait equation yields [Gil52, Kna71]

$$H = \frac{n(p_0 + B)}{(n-1)\rho_0}\left[\left(\frac{P+B}{p_0+B}\right)^{(n-1)/n} - 1\right] \tag{3.5}$$

and

$$C = c_0\left(\frac{P+B}{p_0+B}\right)^{(n-1)/2n} . \tag{3.6}$$

The pressure P in the bubble obtained under the assumption of an ideal gas in the bubble is [Kna71],

$$P = \left(p_0 + \frac{2\sigma}{R_n}\right)\left(\frac{R_n}{R}\right)^{3\kappa} - \frac{2\sigma}{R} - \frac{4\mu}{R}U , \tag{3.7}$$

where σ is the surface tension, μ is the dynamic shear viscosity and κ is the ratio of the specific heats at constant pressure and volume; R_n indicates the equilibrium radius of the bubble, i.e. the radius at which the pressure of the gas contained in the bubble corresponds exactly to the hydrostatic pressure.

3.1.3 Modeling the formation of laser produced bubbles

The Gilmore model was used to calculate the time evolution of the bubble radius, the pressure inside the bubble, and the pressure distribution in the surrounding fluid based on the laser pulse duration, the size of the plasma at the end of the laser pulse, and the size of the resulting cavitation bubble. The plasma size corresponds to the volume in which the laser energy has been deposited and the size of the expanding bubble is a measure for the deposited energy. The calculation begins with a seed bubble, whose interior pressure is in equilibrium with the ambient hydrostatic pressure. The radius R_0 of the seed bubble is chosen so that the bubble volume is the same as the photographically determined plasma volume. The energy input during the laser pulse is simulated by raising the equilibrium radius R_n of the seed bubble from its small initial value $R_{na}=R_0$ to a very much larger final value R_{nb} [Ebe78]. Inasmuch as R_n is a measure for the amount of gas contained in the cavitation bubble, its enlargement implies that the internal pressure in the bubble rises to a level above the hydrostatic pressure so that the bubble expands. R_{nb} was determined by iteration and chosen so that the calculated maximum radius R_{max} of the expanded bubble is as big as the experimentally determined value.

The time evolution of the laser power P_L during the pulse is modeled as a $\sin^2$ function with a half width τ and overall length 2τ:

$$P_L = P_{L0}\sin^2\left(\frac{\pi}{2\tau}t\right) \qquad 0 \le t \le 2\tau. \tag{3.8}$$

It is assumed that the volume increase ΔV_n of the "equilibrium" bubble with radius R_n up to time t during the laser pulse is proportional to the already absorbed laser energy E_{abs}, i.e.,

$$\Delta V_n(t) = (4\pi/3)\left[R_n^3(t) - R_{na}^3\right] = k E_{abs}(t)\,, \tag{3.9}$$

where

$$E_{abs}(t) = \int_0^t P_{L0} \sin^2\left(\frac{\pi}{2\tau} t\right) dt = P_{L0}\left[\frac{t}{2} - \frac{\tau}{2\pi}\sin\left(\frac{\pi}{\tau} t\right)\right]. \tag{3.10}$$

By analogy with Eqs. (3.9) and (3.10), the total energy of the laser pulse is given by

$$E_{abs}^{tot} = \frac{\Delta V_n^{tot}}{k} = \frac{4\pi}{3k}\left(R_{nb}^3 - R_{na}^3\right) \tag{3.11}$$

or

$$E_{abs}^{tot} = \int_0^{2\tau} P_{L0} \sin^2\left(\frac{\pi}{2\tau} t\right) dt = P_{L0}\tau\,. \tag{3.12}$$

Combining Eqs. (3.11) and (3.12) yields $P_{L0} = (4\pi/3k\tau)\left(R_{nb}^3 - R_{na}^3\right)$. Substituting this expression for P_{L0} in Eq. (3.10) and combining Eqs. (3.9) and (3.10) gives

$$\frac{4\pi}{3}\left[R_n^3(t) - R_{na}^3\right] = \frac{4\pi}{3\tau}\left(R_{nb}^3 - R_{na}^3\right)\left[\frac{t}{2} - \frac{\tau}{2\pi}\sin\left(\frac{\pi}{\tau} t\right)\right]. \tag{3.13}$$

Solving for $R_n(t)$ gives an equation for the time evolution of the equilibrium radius during the laser pulse:

$$R_n(t) = \left\{R_{na}^3 + \frac{R_{nb}^3 - R_{na}^3}{2\tau}\left[t - \frac{\tau}{\pi}\sin\left(\frac{\pi}{\tau} t\right)\right]\right\}^{\frac{1}{3}}. \tag{3.14}$$

In order to calculate the dynamics of the laser produced cavitation bubble, the differential equation (3.1) was integrated numerically with the aid of Eqs. (3.5), (3.6), (3.7), and (3.14) using a predictor-corrector procedure [Sha75]. The following constants for water at 20°C were used: density ρ_0 = 998 kg/m^3, surface tension σ = 0.072583 N/m, polytropic index κ = 4/3, dynamic shear viscosity μ = 0.001046 Ns/m^3, sound speed c_0 = 1483 m/s, and static ambient pressure p_0 = 100 kPa.

3.1.4 Modeling shock wave generation

The solution of Eq. (3.1) can be used to calculate the pressure distribution in the fluid surrounding the bubble with the help of the method of outward propagating characteristics [Gil52, Kna71]. This method is based on the Kirkwood-Bethe hypothesis that the quantity $y = r(u^2/2 + h)$ propagates at a velocity equal to the sum $u+c$ of the fluid velocity and the local sound speed. This yields the differential equations

$$\dot{u} = -\frac{1}{c-u}\left[(c+u)\frac{y}{r^2} - \frac{2c^2u}{r}\right], \qquad \dot{r} = c+u \tag{3.15}$$

for the velocity distribution in the fluid [Kna71, Ebe78] with

$$c = c_0\left(\frac{p+B}{p_0+B}\right)^{(n-1)/2n} \qquad \text{and} \qquad y = r\left(\frac{u^2}{2}+h\right). \tag{3.16}$$

The pressure p at the position $r = r(t)$ is given by

$$p = (p_0+B)\left[\left(\frac{y}{r}-\frac{u^2}{2}\right)\cdot\frac{(n-1)\rho_0}{n(p_0+B)}+1\right]^{n/(n-1)}. \tag{3.17}$$

In order to determine the pressure distribution in the fluid, the time evolution of the quantity y at the bubble wall is first determined using the Gilmore model Eq. (3.1). Finally, the velocity distribution in the fluid is calculated by integrating Eq. (3.15) and reduced into pressures using Eq. (3.17). In order to obtain the pressure distribution at a given time, the points with t = const. must be chosen from the family of $p(r,t)$ curves.

3.1.5 The physics of the shock front

Although it is very difficult to describe the nonlinear acoustic propagation and calculate the shock profile in the vicinity of the plasma, it is relatively easy to formulate the physics of an idealized shock front and that offers a comparatively simple approach to the experimental determination of the pressure at the shock front.

Because of its small thickness of less than 1 µm [Eis64, Har82], the shock front essentially represents a discontinuity surface in the fluid, at which the pressure, the particle velocity, the density, and the internal energy of the fluid change suddenly. Quantities in front of and behind the shock front are linked by the conservation laws for mass, momentum, and energy. For the case of a medium at rest in front of the shock front ($u_p = 0$), the following "jump conditions" apply [Duv63]:

$$u_s\rho_0 = (u_s - u_p)\rho_s, \tag{3.18}$$

$$p_s - p_0 = u_s u_p \rho_0, \tag{3.19}$$

and

$$p_s u_p = \frac{1}{2}\rho_0 u_s u_p^2 + \rho_0 u_s(\varepsilon_s - \varepsilon_0). \tag{3.20}$$

Here ρ_0 and ρ_s are the densities and p_0 and p_s are the pressures in front of and behind the compression, u_s is the shock speed, u_p is the particle velocity behind the shock front, and $(\varepsilon_s - \varepsilon_0)$ is the increase in the specific internal energy of the fluid as it crosses the shock front. Combining Eqs. (3.18) and (3.19) makes it possible to eliminate u_s and u_p in Eq. (3.20) and obtain the Rankine-Hugoniot equation

$$\varepsilon_s - \varepsilon_0 = \frac{1}{2}\left(\frac{1}{\rho_0} - \frac{1}{\rho_s}\right)(p_s + p_0)\,. \tag{3.21}$$

Together with an additional material-specific equation, the jump conditions (3.18)-(3.20) provide a complete description of the mutual relationships among all the shock front parameters (p_s, ρ_s, u_s, u_p). Given this equation, it is sufficient to measure a single parameter in order to determine the others and one can, for example, determine the shock pressure by measuring the shock speed (cf. 3.1.7). The material-specific equation can either be the equation of state of the medium, which couples p_s and ρ_s, or the Hugoniot curve for the medium, which describes the relationship between u_s and u_p.

3.1.6 The equation of state for water

The equation of state of a substance describes the relationship between pressure, density, and temperature. Describing the changes of state within the breakdown volume requires very complicated equations, since not only the pressure and density, but also the temperature, change substantially during plasma formation. Semi-empirical equations for a large number of thermodynamic variables have been published by Tödheide (1972), Haar, et al. (1981), and in the SESAME Tables [Lyo92]. Roberts, et al. (1996) and Cook, et al. (1997) have also considered the dissociation and ionization of the water molecule. The temperature changes outside the breakdown volume produced by heat conduction and energy dissipation at the shock front are much smaller than the plasma-induced temperature rise in the breakdown volume itself (cf. 3.1.9). Thus, simpler equations suffice for describing the changes in state of the fluid at the shock front.

The isentropic Tait equation (3.4)

$$\frac{P + B}{p_0 + B} = \left(\frac{\rho}{\rho_0}\right)^n$$

is one such simplified form for the equation of state. In it, the effect of temperature on the relationship between pressure and density is neglected, as it is assumed that $B(T)$ = const. Experimental studies show that B varies by less than 3% from its average of 304 MPa within the temperature range from 20-80°C [Mül87]. B can, therefore, be assumed constant, so long as the temperature change at the shock front, which propagates through water at room temperature, is not significantly higher than 60°C. This is the case for pressure jumps up to about 1 GPa (cf. 3.1.9). The isentropic Tait equation, thus, provides very good results only for moderate shock pressures [Col48, Mül87]. It has the advantage, however, that it is well suited to providing an analytical representation of the relationship between the pressure and other variables, such as density, sound speed, or enthalpy (cf. 3.1.2), and, for that reason, is often used for theoretical modeling of cavitation bubble dynamics.

For the interpretation of the present experimental results, the Hugoniot curve determined by Rice and Walsh (1957),

$$u_p = c_1\left(10^{(u_s - c_0)/c_2} - 1\right), \tag{3.22}$$

will be used, since it relies on measurements over a very wide pressure range from 0 to 25 GPa. Here c_0 is the normal sound speed in water, $c_1 = 5190$ m/s, and $c_2 = 25306$ m/s.

3.1.7 Determination of the shock pressure from the shock velocity

The jump condition (3.19) and Eq. (3.22) yield a relationship between the shock front velocity and the pressure at the shock front:

$$p_s = c_1 \rho_0 u_s \left(10^{u_s - c_0 / c_2} - 1\right) + p_0 \,. \tag{3.23}$$

The Tait equation (3.4), likewise, yields a relationship between the pressure and velocity at the shock front [Mül87]:

$$p_s = (p_0 + B)\left(\frac{2nu_s^2}{(n+1)c_0^2} - \frac{n-1}{n+1}\right) - B \,. \tag{3.24}$$

If Eq. (3.24) is used to determine the shock pressure from the experimentally obtained shock speeds, the values of the pressure for high u_S lie clearly below the values calculated with Eq. (3.23). For $u_S = 3000$ m/s Eq. (3.24) yields a pressure of 1.62 GPa, while Eq. (3.23) yields 2.3 GPa. The corresponding values for $u_S = 4500$ m/s are 4.52 GPa and 7.36 GPa. The discrepancies are a consequence of the inaccuracy of the Tait equation at high shock pressures.

Equations (3.23) and (3.24) are both exact only for an instantaneous pressure jump and will become more imprecise as the pressure gradients at the leading and trailing edge of the pressure transient become more similar [Duv63].

3.1.8 Similarity theorem

If the pressure distribution $p\,(r,t)$ in the neighborhood of a spherical plasma with radius r_0 is known, then the pressure distribution $p(r, t)$ in the neighborhood of a plasma with radius ξr_0 is given by a similarity theorem [Col48], provided that the initial pressure in both plasmas is the same:

$$p(r,t) = p_0\left(\frac{r}{\xi}, \frac{t}{\xi}\right). \tag{3.25}$$

The similarity theorem implies that the pressure depends only on the relative distance r/r_0 from the source.

3.1.9 Shock wave energy and energy dissipation in the shock front

The energy in a spherical shock wave passing a point a distance r_m from the central source is given by [Col48, Chapter 4.8]

$$E_s = \frac{4\pi r_m^2}{\rho_0 c_0} \int p^2 dt \,. \tag{3.26}$$

Determining the shock wave energy with Eq. (3.26) assumes knowledge of the shock *p(t)* profile at the point r_m. Since the shock wave loses energy at its front by viscous damping as it propagates [Zel66], the shock profile immediately adjacent to the plasma must be invoked in order to determine the total acoustic energy produced by optical breakdown. As noted in the introduction to this chapter, *p(t)* can be measured without error by a hydrophone only in the far field of the source. Immediately adjacent to the plasma, the shock profile is difficult to determine experimentally and, thus far, has been obtained only through numerical calculation (cf. 3.1.4).

In the following, an indirect experimental way to determine the shock energy in the neighborhood of the plasma will be proposed. The energy originally contained in the shock wave will be determined by integrating the energy dissipated in the shock front [Vog98c].

The Rankine-Hugoniot equation (3.21) relates the gain in specific internal energy per unit mass of fluid as a shock front passes to the pressure jump $p_0 \rightarrow p_S$ and the density jump $\rho_0 \rightarrow \rho_S$ [Duv63],

$$\Delta\varepsilon(r) = \frac{1}{2}\left[\frac{1}{\rho_0} - \frac{1}{\rho_s(r)}\right]\left(p_s(r) + p_0\right) \approx \frac{1}{2}\left[\frac{1}{\rho_0} - \frac{1}{\rho_s(r)}\right]p_s(r) \,. \tag{3.27}$$

The pressure p_S and density ρ_S behind the shock can be obtained experimentally from a measurement of the shock velocity u_S. One obtains the pressure from u_S via Eq. (3.23), and combination of Eqs. (3.18) and (3.19) gives the density

$$\rho_s = \frac{\rho_0}{1 - \dfrac{p_s}{u_s^2 \rho_0}} \,. \tag{3.28}$$

The total internal energy deposited as a spherical shock moves from r_0 to r_1 is obtained by integrating Eq. (3.27):

$$E_{Diss} = \int_{r_0}^{r_1} 4\pi r^2 \rho_s(r) \Delta\varepsilon(r) dr \,. \tag{3.29}$$

Since a large part of the shock wave energy will be dissipated right in the vicinity of the plasma [Vog96a], the summation of the energy losses according to Eq. (3.29) can be used as a lower bound estimate for the energy content of the shock wave. The total energy of the shock wave can be obtained if data are available on u_S(r) up to a position where an error free hydrophone measurement is possible. The shock wave energy is then given by the sum of E_{Diss} and the residual energy determined from the hydrophone measurements using Eq. (3.26).

The assumed equality of the dissipated energy and the internal energy deposited in the shock front holds exactly only for a pressure step, i.e., for an infinitely long "shock wave." In real shock waves, part of the energy deposited in the shock front returns to the shock wave during the pressure drop in the trailing part of the wave [Col48]. The return flow of energy decreases as the ratio of the shock duration to the shock front rise time becomes larger. Since the shock waves produced in the neighborhood of the plasma during optical breakdown in water last 20-60 ns (cf. Table 3.3) and their risetimes are about 20 ps [Har82], the ratio exceeds 1000. Therefore, we neglect here the return flow of energy in a first approximation.

Viscous damping in the shock front leads to a rise in entropy and to a lasting temperature rise in the medium [Zel66]. Up to now, semi-empirical approaches have been available for calculating the temperature rise in water [Cow70], but no self-consistent theory. The measurements of Justus, et al. (1985) yielded a temperature rise of 33 °C for an 840 MPa shock pressure. According to Duvall and Fowles (1963), the temperature rises were 257 °C for 5.5 GPa and 690 °C for 12 GPa shock pressures. Holmes, et al. (1986) have obtained temperature jumps of 347 °C for 7.5 GPa and 547 °C for 11.7 GPa by Raman spectroscopy.

According to the above data, the critical point of water (374.2 °C) will be crossed for a shock pressure of about 7.5 GPa with a 20°C initial temperature. If pressures of this magnitude occur during laser-induced plasma formation, shock wave propagation leads to a "vaporization" of the water in the vicinity of the plasma and, thereby, to an enlargement of the cavitation bubble that was originally generated by the "vaporization" of the fluid within the plasma volume. ("Vaporization" is written in inverted commas, because the liquid in the plasma volume and the liquid heated by the shock are initially supercritical water. They will, however, be converted to vapor as the pressure drops below the critical point during expansion of the bubble.) The enlargement of the bubble by shock-induced vaporization causes a drop in the average pressure and temperature in the interior of the bubble, because the temperatures attained during shock-induced vaporization are considerably lower than the temperatures in the plasma [Rob96]. We can conclude that shock wave production and bubble formation during optical breakdown are not only related to one another through a common driving force (the expansion of the plasma), but are, as a whole, very closely intertwined with one another.

3.2 Experimental Techniques

3.2.1 High speed photographic analysis of shock wave emission and bubble expansion

The experimental apparatus for studying shock wave emission and the expansion of cavitation bubbles is sketched in Fig. 3.3.

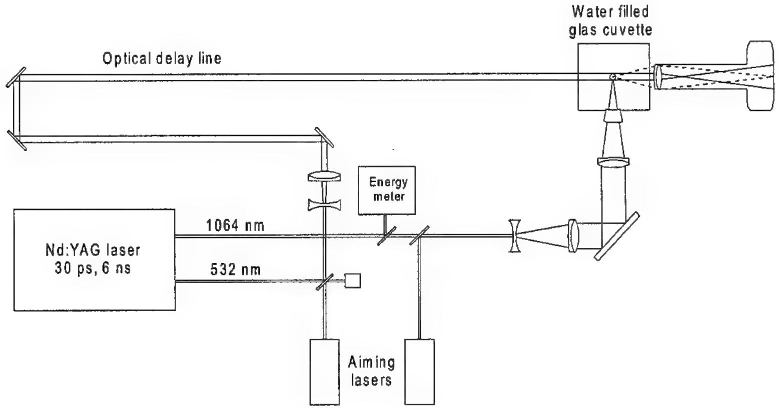

Fig. 3.3 Apparatus for studying shock wave emission and the expansion of cavitation bubbles.

Nd:YAG laser pulses of 6 ns or 30 ps duration at 1064 nm were generated using the system previously described in Section 2.2.1. The laser pulses were focussed into a glass cell containing distilled water. The convergence angle in the water was 14° for the ps-pulses and 22° for the ns-pulses, and the corresponding focal spot diameters ($1/e^2$ intensity, measured with the knife edge technique described in Section 2.2.2) were 5.8 µm or 7.6 µm, respectively. The threshold for plasma production (50% breakdown probability) was 7 µJ for the ps-pulses and 150 µJ for the ns-pulses.

Shock wave emission and bubble expansion were tracked using a series of photographs taken with an increasing delay between the time of optical breakdown and the exposure time for the individual pictures. The photographs were taken with a Leitz Photar objective (F = 3.5) with 7× magnification on Agfapan APX25 film. The spatial resolution was better than 4 µm. For illumination, part of the Nd:YAG laser output was frequency doubled and optically delayed by 2-136 ns relative to the 1064 nm pulse which produced the optical breakdown [Bel67]. The time delay between the optical breakdown and the photographic exposure was increased in 1 ns steps up to 10 ns, in 2 ns steps up to 20 ns, and afterward in steps of 4 ns. The illumination time for the pictures corresponds to that of the main laser pulse, i.e., 30 ps or 6 ns, respectively.

The events following 50 μJ and 1 mJ, 30-ps pulses and 1 mJ and 10 mJ, 6-ns pulses were studied. The pulse energy in each shot was measured with a pyroelectric energy detector (Laser Precision Rj 7100). In order to ensure good reproducibility of the individual breakdown events, only those pictures in which the pulse energy deviated by less than ±7% from the above energies for the ps-pulses and less than ±2%, for the ns-pulses were interpreted. The radii of the shock wave and bubble were determined by measuring the corresponding diameters through the plasma center and dividing by two. For each delay time, the measurements from 6 breakdown events were averaged.

The corresponding distances r between the optical axis and shock front or bubble wall were plotted as a function of the delay time t and analytic functions were fit to these data using a curve fitting program (Table Curve, Jandel Scientific). The shock velocity $u_S(t)$ or $u_S(r)$ and the bubble velocity $u_B(t)$ were deduced from the slope of the $r(t)$ curves obtained in this way. Then Eq. (3.23) was used to calculate the pressure $p_S(r)$ at the shock front from the values of u_S, and the internal energy input at the shock front was determined using Eq. (3.28).

3.2.2 Hydrophone measurements of the shock pressure

The determination of the shock pressure from a measurement of the shock velocity requires that the difference between the shock velocity and the normal sound speed can be measured with sufficient accuracy. This measurement is possible only in the vicinity of the plasma within a zone of less than 1 mm^3. The measurement uncertainty in u_S for velocities near the sound speed is about 20 m/s, which corresponds to a pressure of approximately 15 MPa. The pressure measurements in the far field were, therefore, made with a hydrophone. Reliable pressure values are obtained as long as the distance between the source center and the hydrophone is large enough that the shock waves striking the sensor element can be approximated as plane waves. A PVDF hydrophone (Ceram) with a 1 mm^2 detector area, 12 ns risetime (28 μm layer thickness), and a sensitivity of 280 mV/MPa was used. The calibration factor applies over a frequency range out to 10 MHz (Manufacturer's data). When the output of the hydrophone is terminated in a high impedance, the voltage signal on an oscilloscope is proportional to the pressure amplitude [Sch87]. The hydrophone signal was, therefore, recorded on a fast oscilloscope (Tektronix TDS 540 with a 0.7 ns risetime) with a 1 MΩ input impedance.

3.2.3 Determination of the plasma volume, bubble radius, and bubble energy

The calculations of shock wave emission and bubble expansion require information on the plasma size and the radius of maximum expansion of the cavitation bubble. The plasma size was determined from photographs of the plasma radiation taken without background illumination by the frequency doubled Nd:YAG laser. The bubble size was determined by measuring the time interval between the shock waves produced by optical breakdown and by collapse of the bubble. Lauterborn [Lau74] has shown that the expansion and collapse of the bubble are very symmetrical if the laser pulse duration is substantially shorter than the oscillation period of the bubble and the fluid's viscosity is low. This is true for optical breakdown in water with ns- and ps-laser pulses. The time interval between the pressure pulses from optical breakdown and bubble collapse is then twice the Rayleigh collapse time T_C, which is related to the maximum bubble radius by [Ray17]

$$R_{max} = T_c / 0.915 \left(\frac{\rho_0}{p_0 - p_v} \right)^{0.5}, \tag{3.30}$$

where p_v is the vapor pressure inside the bubble (p_v = 2330 Pa for 20 °C). R_{max} can be used to calculate the bubble energy [Col48],

$$E_B = (4/3)\pi R_{max}^3 (p_0 - p_v). \tag{3.31}$$

Although Eq. (3.30) was derived for spherical bubbles, it is approximately valid for elongated bubbles of the sort which develop with small focal angles. A comparison of the bubble volumes determined from a series of high-speed photographs with the values predicted by Eq. (3.30) yielded discrepancies of less than 10% even for bubbles with an axis ratio as large as 5:1 [Noa98a].

3.3 Results

3.3.1 Photographs of shock wave formation and bubble expansion

Figure 3.4 shows the events associated with optical breakdown for all the pulse durations and energies studied here at a fixed time (44 ns after the laser pulse) and Fig. 3.5 shows the complete sequences of events following 1 mJ, 30 ps and 10 mJ, 6 ns pulses. The laser light is incident from the right. The location of the beam waist is indicated by arrows in Fig. 3.5. The shock wave and cavitation bubble appear dark against a light background, since they deflect the illuminating light out of the imaging lens. Although each picture was taken for a separate breakdown event, shock wave emission and bubble expansion can be tracked very well, since the shot-to-shot reproducibility is very good. The arrow heads in Fig. 3.5 mark the location at which the bubble radius and the distance traveled by the shock were measured.

The shock front detaches from the plasma immediately after the plasma is formed, since the velocity of the shock front is always substantially higher than the post-shock particle velocity (cf. 3.1.1). Since the ps-plasmas are created within a time substantially shorter than the time between frames, the detachment of the shock wave seems to occur everywhere on the plasma at the same time (Fig. 3.5a). By contrast, in the series of pictures in Fig. 3.5b the expansion of the ns-plasma and the detachment of the shock wave can be tracked during the laser pulse. Plasma formation begins in the beam waist and

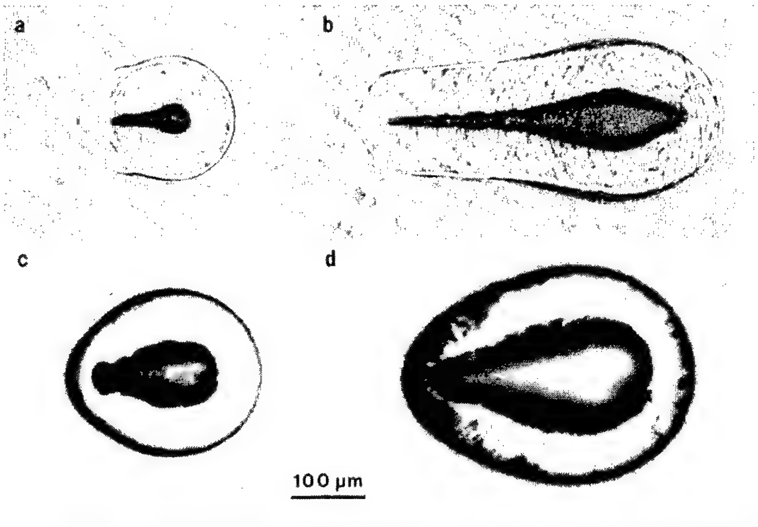

Fig. 3.4 Plasma, shock wave, and cavitation bubble produced by Nd:YAG laser pulses with different durations and energies: (a) 30 ps, 50 μJ; (b) 30 ps, 1 mJ; (c) 6 ns, 1 mJ; (d) 6 ns, 10 mJ. All pictures were taken 44 ns after optical breakdown.

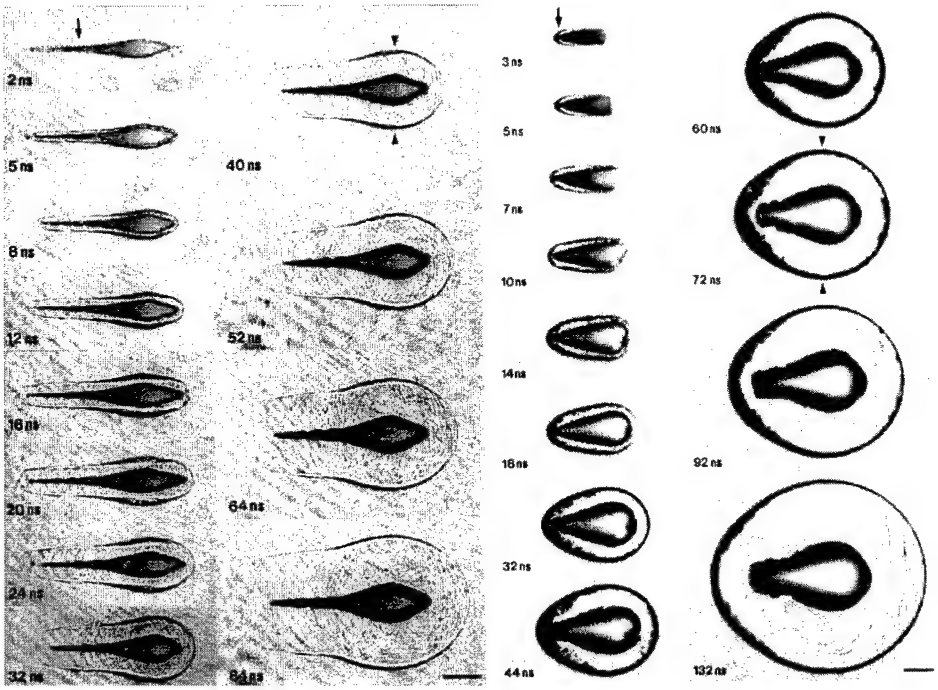

(a) (b)

Fig. 3.5 Shock wave emission and cavitation bubble expansion in the initial phase following optical breakdown with (a) a 1 mJ, 30 ps pulse and (b) a 10 mJ, 6 ns pulse. The laser light is incident from the right. The position of the beam waist is indicated by an arrow. The delay of the illumination pulse relative to the pulse which produced the plasma is indicated in each picture. Plasma light is visible in all of the pictures, regardless of the time at which the shock wave and cavitation bubble were illuminated, since the pictures were taken in a dark room with the camera shutter open. The arrow heads indicate the location at which the bubble radius and the distance traveled by the shock were measured. The scale represents a length of about 100 μm.

the plasma expands into the cone of incident laser light, as long as the laser intensity is rising (Section 2.1.5). Detachment of the shock wave, accordingly, also begins in the beam waist and occurs at the end of the plasma facing the laser only after about 10 ns, i.e., after the expansion of the plasma has terminated.

In pictures of optical breakdown with ns-pulses taken more than 20 ns after breakdown, it appears as if detachment of the shock wave has begun on the laser beam side, although it actually begins at the plasma tip. This observation has been documented previously [Dai67, Ebe78, Lau77], but, because of poor time resolution, it could not be explained. The false impression is a result of the fact that the energy density and pressure are higher on the end of the plasma toward the laser than near the focus. This, in turn, is a consequence of the fact that the laser energy will be deposited on the end of the plasma toward the laser after the intensity peak of the laser pulse has been reached. The high pressure in this part of the plasma generates a strong shock on the laser side and compression waves on the side toward the focus which move with a velocity *u+c* higher than the velocity u_S of the shock front at the plasma tip. (cf. 3.1.1). The compression waves eventually catch up with the shock front after about 130 ns. Before that they cause a broadening of the image of the shock wave in the neighborhood of the plasma tip and, thereby, create the illusion, until about 60 ns after breakdown, that the shock wave has not yet detached on this side.

3.3.2 Evolution of the velocity and pressure during shock wave propagation and bubble expansion

A quantitative evaluation of the photographic series is presented in Figs. 3.6-3.8.

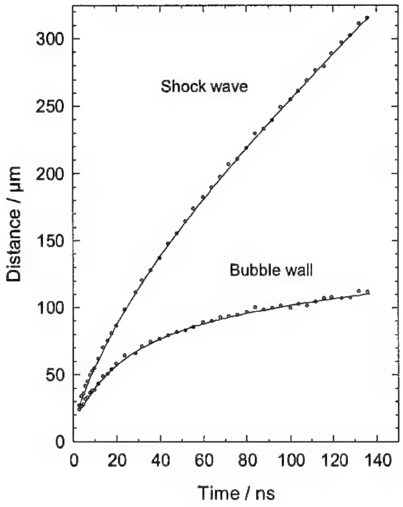

Fig. 3.6 Time evolution of the distance from the shock front and bubble wall to the optical axis after a 10 mJ, 6 ns Nd:YAG laser pulse. The distances are plotted as a function of the time delay between the main laser pulse and the illumination pulse. Each data point is the average of 6 measurements. The standard deviation is less than ±1.0 µm for times up to 30 ns, and for longer delay times ≤ 2.4 µm for the shock wave and ≤2.8 µm for the bubble wall. The standard deviation between the data points and the fit curve is 1.25 µm for the position of the shock and 1.15 µm for the position of the bubble wall.

The distances from the shock front and the bubble wall to the optical axis are plotted as a function of time for 10 mJ, 6 ns laser pulses in Fig. 3.6. The *r(t)* data for the other laser parameters are similar and are, therefore, not shown here. The *r(t)* curves were fit to the measured data using a curve fitting program, and the shock velocity $u_S(t)$ and bubble velocity $u_B(t)$ were deduced from the slope of these curves. These are plotted in Fig. 3.7, along with the post-shock particle velocity $u_p(t)$ calculated using Eq. (3.22). The maximum shock velocity is 2500 m/s for 50 µJ, 30 ps pulses, 2750 m/s for 1 mJ, 30 ps pulses, 3050 m/s for 1 mJ, 6 ns pulses, and 4450 m/s for 10 mJ, 6 ns pulses. These values are somewhat higher than the 2600 m/s for 1 mJ picosecond pulses and 2400 m/s for 1 mJ nanosecond pulses obtained by Zysset, et al. [Zys89]. The maximum bubble wall velocity is slower than the sound speed in water (1483 m/s) for the picosecond pulses (u_B = 390 m/s and 780 m/s) and faster for the nanosecond pulses (u_B = 1850 m/s and 2450 m/s). For all laser parameters, the particle velocity during detachment of the shock front is roughly the same as the initial bubble wall velocity because shock wave formation and bubble expansion are both driven by the expanding laser plasma. After the shock front has detached, the post-shock particle velocity and the bubble wall velocity refer to different positions and are, therefore, no longer comparable.

Figure 3.8 shows the shock pressure calculated with Eq. (3.23) as a function of the distance r from the optical axis. The maximum pressure amplitude for each $p_S(r)$ curve corresponds to the pressure at the plasma rim. It is, in general, higher for ns-pulses (2400 MPa and 7150 MPa for 1 mJ and 10 mJ pulse energies, respectively) than for ps-pulses (1300 MPa and 1700 MPa for 50 µJ and 1 mJ pulse ener-

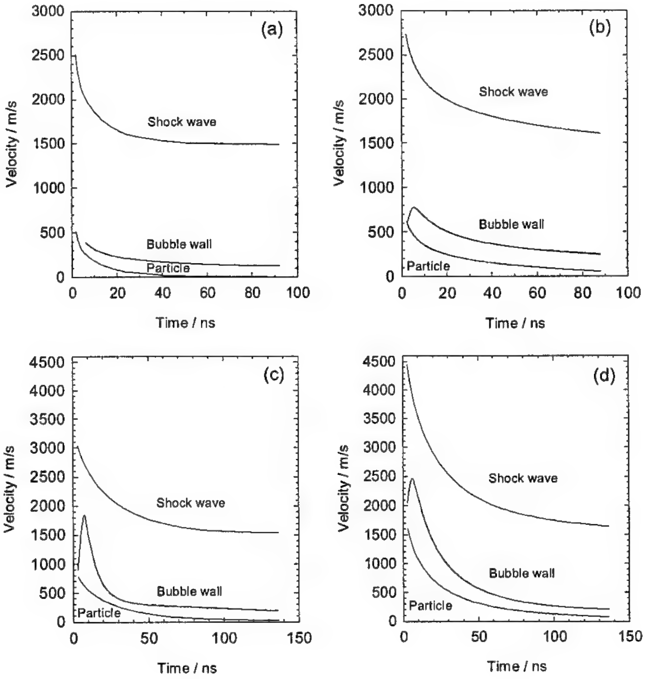

Fig. 3.7 Experimentally determined velocities of the shock wave, u_S, bubble wall, u_B, and particles behind the shock front, u_p, as functions of the time delay between the main laser pulse and the illumination pulse. The laser parameters are: (a) 30 ps, 50 µJ; (b) 30 ps, 1 mJ; (c) 6 ns, 1 mJ; (d) 6 ns, 10 mJ. $u_p(t)$ was calculated from $u_S(t)$ with the aid of Eq. (3.3).

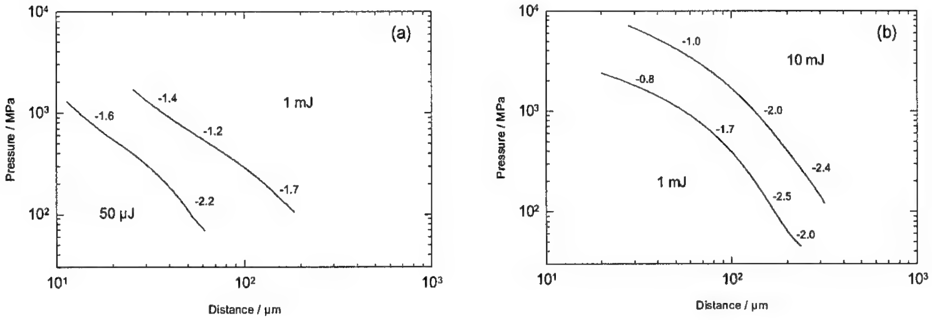

Fig. 3.8 Experimentally determined near field shock pressure $p_S(r)$ after (a) 30 ps pulses of 50 µJ and 1 mJ energy and (b) 6 ns pulses of 1 mJ and 10 mJ energy. The pressures were calculated using Eq. (3.1) from the shock velocities in Fig. 3.7. They are plotted as a function of the time delay between the main laser pulse and the illumination pulse. Some local values of the slopes of the curves are indicated next to the p_S(r) curves.

gies, respectively). The pressures increase with rising pulse energy, and this energy dependence is most marked for the ns-pulses. The maximum pressures obtained in the present study are 4-9 times higher than the values observed by Doukas et al. [Dou 91], since the measurements were made significantly closer to the plasma boundary and with better spatial resolution. The slope of the $p_S(r)$ curves in the log-log plots for the ns-pulses is initially around -1 and then reaches a maximum of -2.5. For the ps-pulses the slope is steeper than -1 from the beginning onward, but the maximum slope is less than for the ns-pulses.

Figure 3.9 shows plots of the far field pressure measurements together with the $p_S(r)$ curves for the near field. The pressure drop in the far field is slower than in the near field. The transition between

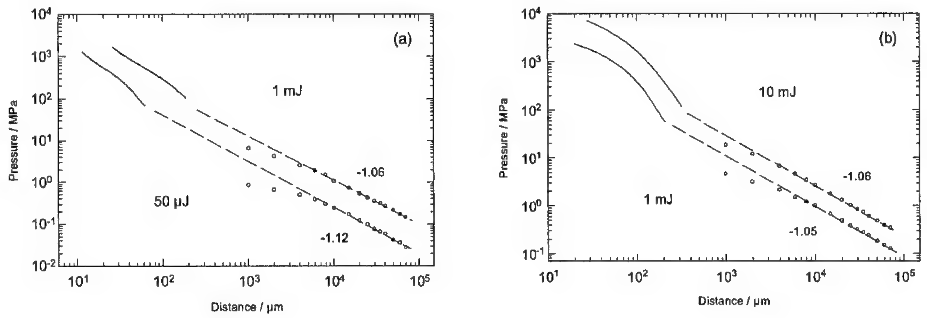

Fig. 3.9 Shock pressure $p_S(r)$ in the near and far fields after (a) 30 ps pulses with energies of 50 µJ and 1 mJ and (b) 6 ns pulses with 1 mJ and 10 mJ energies. The data points represent the results of the hydrophone measurements in the far field. The dashed lines are fits to the pressures at distances ≥ 5 mm from the shock source. The numbers indicate the local slopes of the $p_S(r)$ curves.

the two regions occurs at about 100 MPa for all laser parameters. The data points obtained from the hydrophone measurements for $r \leq 5$ mm lie below the lines obtained from a fit to the measurement points for $r \geq 5$ mm. This deviation is an artifact arising from the detection of a spherical shock wave with a plane sensor element. The greater the curvature of the shock, the smaller the surface in which the sensor and shock wave overlap and the greater the distortion in the pressure signal. Schoeffmann, et al. [Sch87] have observed a similar bending of the $p_S(r)$ curve and attributed the lower slope of the curve for small r to near field effects in cylindrical shock formation. This interpretation turns is incorrect in the present case, since the shock is spherical by 100-200 μm from the source, except for the 1 mJ picosecond pulse (Fig. 3.4). Even with the 1 mJ picosecond plasma, after about 0.5 mm the shock attains a roughly spherical shape (Fig. 3.5a). The low pressure values for $r \leq 5$ mm are, hence, a detection artifact. The hydrophone data for $r \leq 5$ mm are, therefore, ignored and the fit for $r \geq 5$ mm is extrapolated into the region $r \leq 1$ mm, as shown in Fig. 3.9. The extrapolated fit lines are in very good agreement with the optical near field measurements.

Figures 3.10 show the shock wave profiles obtained at a distance of 10 mm from the shock source. At this distance, the hydrophone signals are no longer distorted by geometric effects. The risetime of the detected pressure signal does not represent the actual risetime of the shock front, which is less than

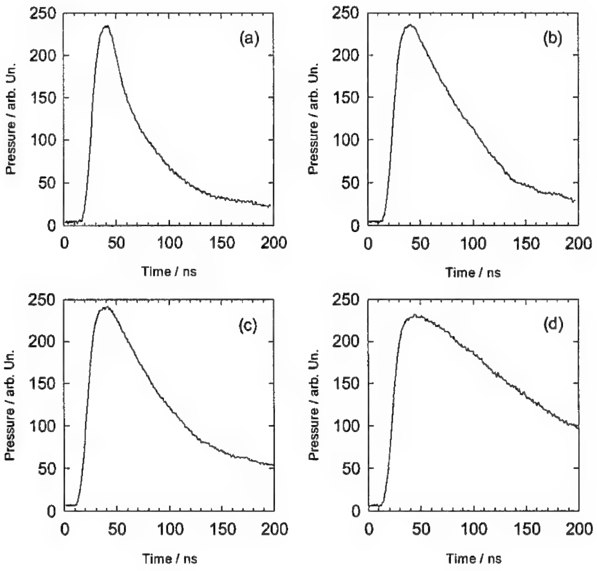

Fig. 3.10 Hydrophone signals obtained a distance of 10 mm from the shock wave source. The corresponding laser pulse lengths and energies are (a) 30 ps, 50 μJ; (b) 30 ps, 1 mJ; (c) 6 ns, 1 mJ; (d) 6 ns, 10 mJ.

1 ns [Flo55, Eis64, Har81, Har82], but is the risetime of the detector (12 ns). The duration of the shock wave increases with rising pulse energy. For equal pulse energies (1 mJ) the duration is roughly the same for ns- and ps-pulses.

3.3.3 Shock wave energy

The acoustic energy dissipated in the shock front was calculated from the measured spatial dependence $u_S(r)$ of the shock velocity using Eqs. (3.26) and (3.28). In Fig. 3.11, the integrated energy loss is plotted as a function of the distance traveled by the shock. For most laser parameters, the loss rate has clearly slowed down by the end of the near field measurement region. The integrated energy loss E_{Diss} can, therefore, be treated as a lower bound estimate for the energy content of the shock (Table 3.1). Only for the 1 mJ, 30 ps pulse, where the pressure in the neighborhood of the plasma falls off more slowly than for the other laser parameters owing to the cylindrical plasma shape (cf. Fig. 3.4), does the energy loss rate remain relatively high at large distances.

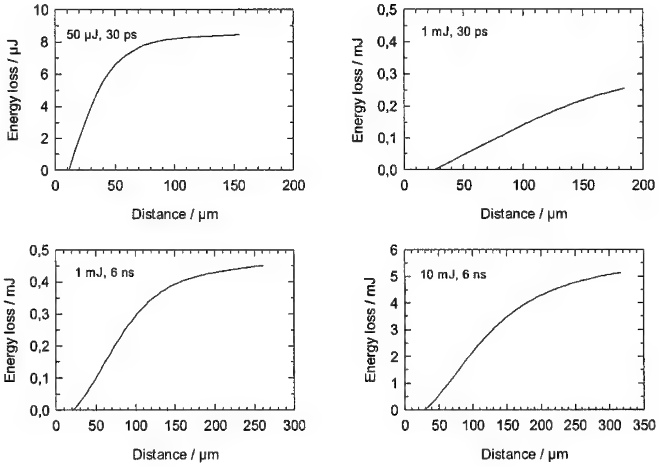

Fig. 3.11 The cumulative energy loss E_{Diss} at the shock front as a function of the distance r traveled by the shock.

The shock energy at 10 mm from the source was calculated from the hydrophone signals of Fig. 3.10 using Eq. (3.25). The data for the peak pressure and shock duration at a distance of 10 mm and the corresponding shock energies $E_{S/10mm}$ are compiled in Table 3.1.

The total acoustic energy produced during optical breakdown can be estimated by adding the energy E_{Diss} dissipated in the near field to the energy $E_{S/10mm}$ remaining in the far field. This procedure still gives a lower bound estimate, since damping in the region $0.3 < r < 10$ mm was not taken into account. This error is, however, at least partially compensated since E_{Diss} was calculated ignoring the fact that part of the acoustic energy deposited in the shock front as internal energy returns to the shock wave as mechanical energy during decompression in the post shock region (cf. 3.1.9).

The degree of conversion of the light energy E_{abs} absorbed at the focus into shock energy $(E_{Diss} + E_{S/10mm})$ ranges from 40% for 30 ps, 50 µJ pulses to 71% for 6 ns, 10 mJ pulses (Table 3.1). Most of the shock energy (85-89%) is already dissipated in the near field.

	30 ps		6 ns	
	50 µJ (25 µJ)	1 mJ (0.64 mJ)	1 mJ (0.77 mJ)	10 mJ (8.2 mJ)
Shock wave energy E_{Diss} dissipated in the vicinity of the plasma (µJ)	8.4	250	450	5200
Shock pressure p_S (MPa) at r=10 mm	0.24	1.06	0.99	2.62
Shock wave duration τ_s [ns] at r = 10 mm	43	70	77	148
Shock wave energy $E_{S/10mm}$ [µJ] at r = 10 mm	1.52	48	46.2	622
Degree of conversion of absorbed energy into shock energy $(E_{Diss} + E_{S/10mm})/E_{abs}$ [%]	39.6	46.6	64.4	71.0

Table 3.1 Shock wave energy in the vicinity of the plasma and at a distance of 10 mm from the plasma. The data on the laser pulse energy refer to the energy incident in front of the cell and the energy absorbed at the laser focus (in parentheses). The latter is calculated from the plasma transmission data of section 2.3.3 considering the absorption and reflection losses along the optical path to the laser focus.

3.3.4 Plasma size, cavitation bubble size, and bubble energy

The experimentally determined plasma volume enters as the seed bubble size in the numerical calculations of bubble formation and shock wave generation. The values of the seed bubble radius are listed in Table 3.2. They refer to bubbles with a volume equal to that of the nonspherical plasmas. The acoustically determined radii of the maximum cavitation bubble and the bubble energy calculated from them using Eq. (3.30) are listed as well.

	30 ps		6 ns	
	50 μJ (25 μJ)	1 mJ (0.64 mJ)	1 mJ (0.77 mJ)	10 mJ (8.2 mJ)
Seed bubble radius R_0 [μm] representing the plasma volume	8.5	26	18	37
Maximum bubble radius R_{max} [μm]	225	780	800	1820
Bubble energy E_B [μJ]	4.7	197	212	2500
Degree of conversion of absorbed energy E_{abs} into bubble energy E_B [%]	18.8	30.8	27.5	30.5

Table 3.2 Experimental results on the expansion of cavitation bubbles. The data on the laser pulse energy refer to the energy in front of the cell and to the energy deposited in the laser focus (in parentheses). The calculated degree of conversion from light energy into bubble energy is based on the absorbed energy.

3.3.5 Numerical calculations of bubble dynamics and shock wave generation

Figures 3.12 and 3.13 show the calculated evolution of the bubble wall velocity and the pressure inside the bubble during the initial phase of bubble expansion following optical breakdown with 30 ps and 6 ns pulses. The calculations were performed using the data of Table 3.2.

Figures 3.14 and 3.15 present the calculated pressure distributions *p(r)* in the fluid surrounding the bubble at different times *t* after the start of the laser pulse. For each time *t*, the position *R* of the bubble wall and the corresponding pressure *P(R)* are indicated by a dot. The pressure profiles *P(R)* in the liquid become steeper with time until a shock front forms. Afterwards, the pressure profiles begin to become double valued. This ambiguity is physically impossible and can, therefore, only be interpreted as an indicator of the existence of a physical discontinuity, i.e., of a shock front [Lan91]. The position of the shock front can be obtained from the calculated double-valued pressure profile using the conservation laws for mass, momentum, and energy flux through the shock front. It is defined by a vertical line in the *u(r)* plots cutting off an area of the overhanging part of the *u(r)* curve that is a big as the area added under the lower section of the curve [Lan91, Rud77]. The position of the shock front was thus determined in the *u(r)* plots (not shown here) and then transferred to the *p(r)* plots, where it is shown as a dashed line. The reduction of the peak pressure values resulting from this procedure corresponds to a dissipation of energy at the shock front.

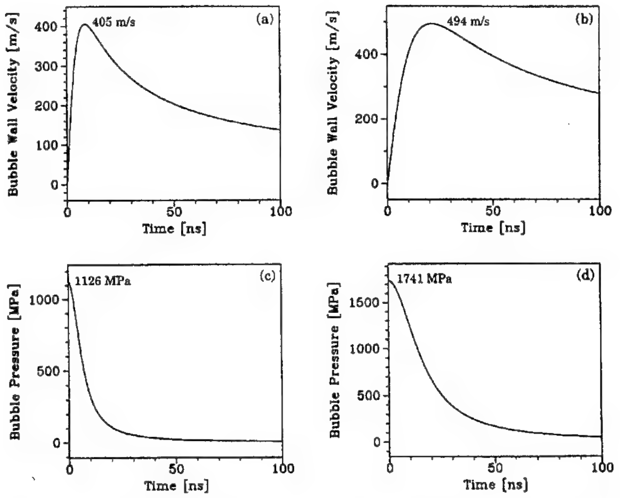

Fig. 3.12 Results of the numerical calculations for 30 ps pulses: bubble wall velocity *U(t)* and pressure *P(t)* inside the bubble during the initial phase of bubble expansion, where *t* is the time following the start of the laser pulse. The parameters used in the calculations were R_{na} = 8.5 μm and R_{nb} = 87.2 μm for the 50 μJ pulse and R_{na} = 26 μm and R_{nb} = 298.3 μm for the 1 mJ pulse. R_{na} is the radius of a sphere with the same volume as the laser plasma and R_{nb} was chosen so that the calculation yields the experimentally observed maximum radius of the cavitation bubble (225 μm for the 50 μJ pulse and 780 μm for the 1 mJ pulse).

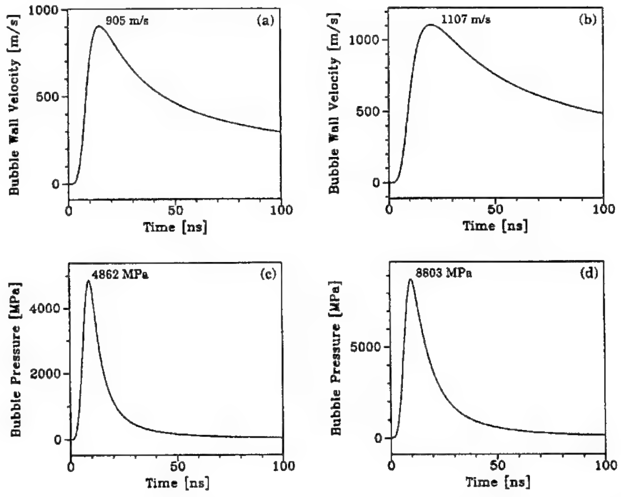

Fig. 3.13 Results of the numerical calculations for 6 ns pulses: bubble wall velocity *U(t)* and pressure *P(t)* inside the bubble during the initial phase of bubble expansion, where *t* is the time following the start of the laser pulse. The parameters used in the calculations were R_{na} = 18 μm and R_{nb} = 297 μm for the 1 mJ pulse and R_{na} = 37 μm and R_{nb} = 671 μm for the 10 mJ pulse. R_{na} is the radius of a sphere with the same volume as the laser plasma and R_{nb} was chosen so that the calculation yields the experimentally observed maximum radius of the cavitation bubble (800 μm for the 1 mJ pulse and 1820 μm for the 10 mJ pulse).

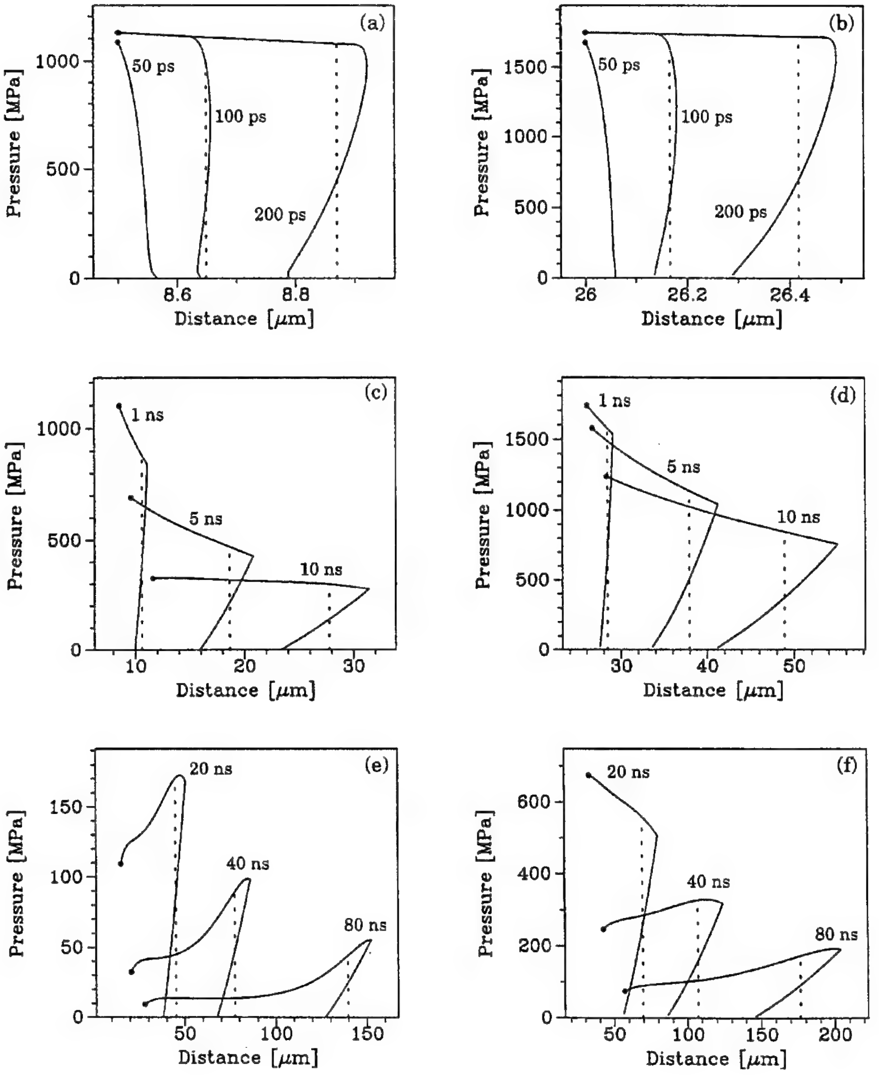

Fig. 3.14 Calculated pressure distribution in the liquid surrounding the cavitation bubble after a 30 ps laser pulse with an energy of 50 μJ (left column) and 1 mJ (right column). The pressure is plotted as a function of the distance r from the emission center for different times t after the start of the laser pulse. The same parameters were used for the calculations as for Fig. 3.12. The dots indicate the position R of the bubble wall and the corresponding pressure P. The position of the shock front is indicated by the dashed lines.

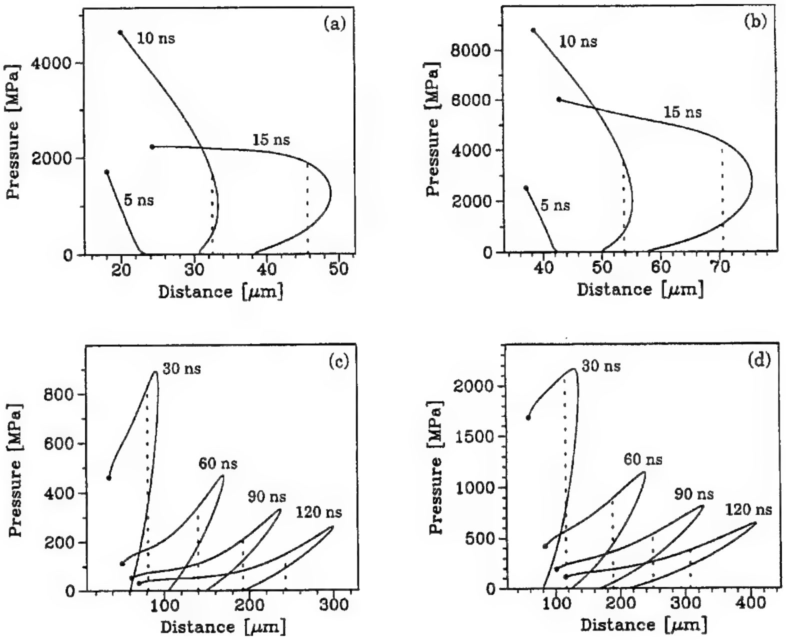

Fig. 3.15 Calculated pressure distribution in the liquid surrounding the cavitation bubble after a 6 ns laser pulse with an energy of 1 mJ (left column) and 10 mJ (right column). The pressure is plotted as a function of the distance r from the shock emission center for different times t after the start of the laser pulse. The same parameters were used for the calculations as for Fig. 3.13. The dots indicate the position R of the bubble wall and the corresponding pressure P. The position of the shock front is indicated by a dashed line.

The pressures, p_S, at the shock front of the pressure profiles in Figs. 3.14 and 3.15 are plotted as a function of distance from the shock source in Fig. 3.16. The form of the $p_S(r)$ curves obtained this way is in good agreement with that of the experimentally determined $p_S(r)$ curves in Fig. 3.6. The slope of the calculated curves is, however, somewhat lower than that of the measured curves.

The shock wave energy in the vicinity of the plasma was also obtained from the calculated pressure profiles (Figs. 3.14 and 3.15) using Eq. (3.26). The calculations were done for a distance r_m from the shock source at which $r_m/R_0 = 6$ [Vog96a]. Here an approximately exponential shock wave shape has already developed. Since the distance r_m is considerably greater than the shock wave width, it can in Eq. (3.26) be approximated as constant for the whole shock wave; r_m is identified with the center of the shock wave. The calculation provides a lower bound estimate of the energy in the shock wave, since during the propagation up to the distance $r_m/R_0 = 6$ a part of the acoustic energy is already dissipated at the shock front. The resulting conversion rate of absorbed laser energy into acoustic energy lies between 17.8% for the 50 µJ, 30 ps pulse and 51.1% for the 10 mJ, 6 ns pulse (cf. Table 3.3).

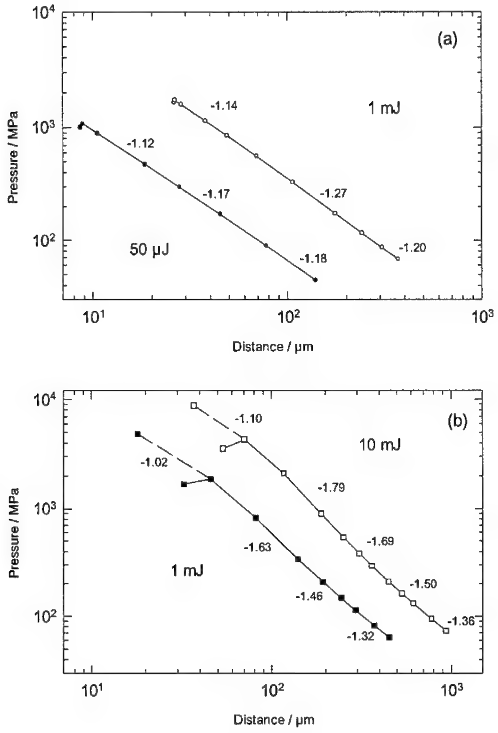

Fig. 3.16 Numerically determined shock front pressure p_s as a function of the distance r from the shock source after (a) 30 ps pulses with energies of 50 µJ and 1 mJ and (b) 6 ns pulses with energies of 1 mJ and 10 mJ. For the ns-pulses, where the shock front pressure is lower than the peak pressure at early times, the maximum pressure at the bubble wall is also indicated. It is connected by a dashed line to the data points for which the peak pressure lies at the shock front. The numbers give the local slopes of the $p_s(r)$ curves.

3.4 Discussion

3.4.1 Shock wave production

The most important results of the experimental and numerical investigations on shock wave production are summarized in Table 3.3 for a combined discussion.

	30 ps		**6 ns**	
	50 μJ (25 μJ)	1 mJ (0.64 mJ)	1 mJ (0.77 mJ)	10 mJ (8.2 mJ)
Plasma boundary				
Measured pressure p_S at the plasma boundary (MPa)	1300	1700	2400	7150
Calculated maximum bubble pressure P [MPa]	1126	1741	4861	8801
Calculated shock wave data for $r_m/R_0 = 6$				
Width a_s (μm)	32	93	54	114
a_s/R_0	3.8	3.6	3.0	3.1
Duration τ_S (ns)	20	53	33	58
Energy $E_S^{Gilmore}$ (μJ)	4.44	214	309	4190
Degree of conversion of absorbed energy E_{abs} into shock wave energy E_S (%)	17.8	33.4	40.1	51.1
Data for $r = 10$ mm				
Pressure p_S (MPa)	0.24	1.06	0.99	2.62
Duration τ_S (ns)	43	70	77	148
Energy $E_{S/10mm}$ (μJ)	1.5	48	46.2	622
Measured shock wave energy				
Shock energy E_{Diss} dissipated in the vicinity of the plasma (μJ)	8.4	250	450	5200
$(E_{Diss} + E_{S/10mm})$ [μJ]	9.9	298	496	5822
Degree of conversion of absorbed energy E_{abs} into shock wave energy $(E_{Diss}+E_{S/10mm})$ (%)	39.6	46.6	64.4	71.0

Table 3.3 Summary of the experimental and numerical results on shock wave generation. The data on the laser pulse energy refer to the energy in front of the cell and the energy deposited in the laser focus (in parentheses).

3.4.1.1 Formation of the shock front

The initial pressure distribution for optical breakdown depends in a complicated way on the intensity profile of the laser beam, the intensity dependence of the absorption coefficients, the laser pulse shape, and the migration of the plasma front toward the pulse. The pressure wave emitted as the plasma expands initially has a finite risetime, so the shock front, with its pressure discontinuity, first develops after the wave has traveled a certain distance. Numerical calculations of the shock wave propagation make it possible to estimate this distance. Here it will be assumed for simplicity that the pressure in the plasma (or in a seed bubble of the same size as the laser plasma) is homogeneous and falls off suddenly at the plasma boundary.

The pressure rise inside the seed bubble occurring during the laser pulse causes a compression of the surrounding liquid, whereby the leading edge of the compression wave corresponds approximately to the leading edge of the laser pulse. The pressure transients created by the picosecond pulses thus have an initial risetime of only 30 ps, which leads to the formation of a shock front within about 100 ps following the start of the laser pulse (Fig. 3.14). The transients created by the nanosecond pulses initially have a longer risetime of about 6 ns, so a shock front is formed over a much longer period of about 10 ns (Fig. 3.15), which corresponds to a path length of about 20 μm.

If the plasma boundary is not as sharp as assumed in the calculations, then shock front formation may require a somewhat longer time. Conversely, the time to form the shock front is shorter if the movement of the plasma front during the first half of the laser pulse is also taken into account. The plasma front velocity is about 15-40 km/s for a focal angle of 22° and a 6 ns laser pulse (Table 2.7). The penetration depth of the light in the plasma is about 30 μm, since the average absorption coefficient in the plasma is about 330 cm^{-1} (Table 2.8). The plasma front, therefore, will travel a distance corresponding to the optical penetration depth in about 1 ns. Thus, in the first half of the laser pulse, the pressure rise at every point in the breakdown volume occurs within 1 ns, and is therefore substantially faster than implied by the calculations which assume that the pressure rise follows the laser pulse shape. During the second half of the pulse, on the other hand, when the plasma length remains constant, a slower pressure rise occurs in the side of the plasma facing the laser.

3.4.1.2 Maximum pressure at the plasma boundary

The maximum shock pressure at the plasma boundary depends on the energy density in the plasma volume which is determined by the absorbed laser pulse energy, the original plasma volume and the extent of the plasma expansion during the laser pulse. The shock pressure is generally higher after ns-pulses than after ps-pulses (Table 3.3). This pressure difference is a consequence of the fact that the fluence threshold F_{th} for optical breakdown is lower for the ps-pulses than for the ns-pulses, so that the threshold can be exceeded within a greater volume for equal pulse energies. The volume increase results in a lower energy density in the ps-plasmas and, thereby, a lower pressure.

With both pulse lengths, the pressure at the plasma boundary is higher at pulse energies well above the threshold than near the threshold. For a 10 mJ pulse it is almost three times higher than for a 1 mJ pulse. Similar results were obtained by Noack (1998a) in detailed studies of the energy dependence of the shock pressure. A possible explanation is that after passing the intensity peak of the laser pulse the plasma growth ceases, and most of the laser energy will be deposited in a region on the laser side of the plasma that is only about 30 µm thick (determined by the optical penetration depth in the plasma, see Table 2.8). The energy density attained this way at the laser end of the plasma is substantially higher at high pulse energies than for low energies.

For the ps-pulses the calculated maximum internal bubble pressure agrees well (±13%) consistent with the experimentally determined pressure at the plasma boundary. For the 1 mJ nanosecond pulse, on the other hand, the calculated value is roughly twice the experimental value and for the 10 mJ pulse it is slightly higher. One possible explanation for the discrepancy observed with the ns pulses is the blurring of the picture of the shock wave during the roughly 6 ns illumination time for the photographs. Because of the blurring, the location of the shock front is detected too far away from the source, and this effect is strongest close to the plasma boundary where the shock speed is highest. In this way, the slope of the measured $r_S(t)$ curves diminishes, especially in the neighborhood of the plasma, as do the resulting shock velocities and pressures. This measurement artifact can be avoided if the $r_S(t)$ curve is detected by streak photography with an effective illumination time shorter than 200 ps [Noa98a,b]. The pressure amplitudes at the plasma boundary determined by streak photography are clearly higher than those determined here by framing camera photography (8400 MPa *vs.* 2400 MPa for 1 mJ pulses and 11800 MPa *vs.* 7200 MPa for 10 mJ pulses) [Noa98b]. Doukas, et al. (1991), on the other hand, obtained substantially lower peak pressures than found here (under 700 MPa for all pulse energies up to 14 mJ), because the limited spatial resolution of this measurement technique did not allow them to measure up to the plasma boundary.

A comparison between the experimental data and numerical calculations is made difficult by the use of two different material specific equations for the calculations and the evaluation of the experimental data, respectively. For equal shock velocities, the Hugoniot curves of Rice and Walsh (Eq. (3.22)) yield higher pressures than the Tait equation (3.4) employed in the Gilmore model and are, in particular, more exact for p>2 GPa (cf. 3.1.6 and 3.1.7). It would be desirable to use the Rice and Walsh equation for the numerical calculations. The combination of Eq. (3.22) and the jump conditions (3.18)-(3.20) leads to transcendental equations for the pressure and density as functions of the particle velocity. As opposed to the isentropic Tait equation, there, hence, is no explicit relationship between the pressure and density, so that the sound speed and enthalpy required for integrating Eq. (3.1) must be determined numerically. The effort required to do this is beyond the scope of the present work.

Calculations with the Los Alamos MESA-2D code employing the tabulated SESAME equation of state gave a peak pressure of 4300 MPa for a 1 mJ, 30 ps pulse under the present experimental conditions [Cha97]. This value is a factor of 2.5 higher than the measured pressure and that calculated using the Gilmore model (Table 3.3). For 6 ns, 10 mJ pulses, calculations yielded a peak plasma pressure of 9500 MPa, likewise somewhat higher than the 8800 MPa given by the Gilmore model [Sca98].

3.4.1.3 Shock wave width and duration

The shock waves appear in the photographs as dark stripes (Figs. 3.4 and 3.5) since the gradient in the refractive index created by the pressure wave causes the illumination light to be deflected out of the photographic objective. The width of the shock wave image is, thus, determined both by the gradient in the refractive index and the numerical aperture of the objective lens. The half width of the shock wave image may therefore, not simply be identified with the half width of the shock wave. As the shock wave detaches from the plasma, the gradient behind the shock front is not very steep (Figs. 3.14 and 3.15), so this region does not appear dark on the photograph. However, because of compression waves behind the shock front owing to plasma inhomogeneities and vortices initiated as the shock front passes [Lan91], additional refractive index gradients can develop and appear as darkening.

The values of the shock wave width and duration in the neighborhood of the plasma obtained by numerical calculation and the shock wave durations at 10 mm from the source determined from the hydrophone measurements are summarized in Table 3.3. The shock wave width near the plasma at a distance r_m/R_0 = 6) was obtained from the calculated *p*(*r*) profiles in Figs. 3.14 and 3.15 and the corresponding shock wave duration τ_S was determined considering the local shock wave velocity. The shock wave durations measured at a distance of 10 mm range from 43 ns for a 50 μJ, 30 ps pulse to 148 ns for a 10 mJ, 6 ns pulse. These values lie in the same range as the data of Ebeling (1978), Dunina, et al. (1982), Vogel, et al. (1988), Ward and Emmony (1991), and Alloncle (1994), but they are lower than the 200-400 ns obtained by Teslenko (1977) and Schöffmann, et al. (1987) with higher laser energies. Results by other authors for the shock wave width in the immediate vicinity of the plasma are available for the 1 mJ picosecond pulse and 10 mJ nanosecond pulse. Chapyak, et al. (1997) obtained a width of 36 μm for 30-ps pulses, which is to be compared with 93 μm in Table 3.3, and Scammon, et al. (1998) calculated a width of 41 μm for 6-ns pulses, which is to be compared with 114 μm in the present study.

The initial shock wave duration is longer for ps pulses than for ns pulses with the same energy. It is, therefore, *not* proportional to the laser pulse duration in the range of pulse durations studied here. Shock wave production and bubble expansion after picosecond pulses are an "impulse response" to a quasi-instantaneous energy input, and the situation is similar for nanosecond pulses, since the bubble wall moves insignificantly during the laser pulse. Under these circumstances, the shock wave duration does not depend on the laser pulse duration, but only on the pressure in the plasma and the plasma size [Col48]. Since the pressure is higher in the ns plasmas than in the ps plasmas, the cavitation bubble expands more rapidly, so that the pressure inside the bubble also falls more rapidly, and this leads to a shorter shock duration or width. The pulse duration dependence becomes evident if the shock width a_S is normalized to the initial radius R_0 of the cavitation bubble corresponding to the plasma radius: a_s/R_0 is 3.6-3.8 for ps pulses, but only 3.0-3.1 for ns pulses (Table 3.3). The normalized shock wave width is nearly independent of the laser pulse energy, in accord with the similarity principle formulated by Cole (see Section 3.1.8). The width of the energy range over which the similarity principle is valid is remarkable: the normalized width of laser induced shock waves is approximately the same as the value $a_s/R_0 = 2.5$ calculated by Penney and Dasgupta for the detonation of a 900 kg TNT charge [Col48, p. 132]. The similarity of the normalized shock wave widths in both cases is based on the similarity of the energy density in TNT (about 5 J/mm^3) and laser plasmas (about 10 J/mm^3 in ps plasmas and 40 J/mm^3 in ns plasmas; cf. Section 2.3.5).

The shock wave duration at a distance of 10 mm from the source is longer for all laser parameters than the initial shock wave duration in the vicinity of the plasma, owing to the nonlinearity of sound propagation at high pressure [Col48]. The pressure dependence of the sound speed means that the parts of the trailing edge of the shock wave for which $c+u$ is smaller than u_S will fall ever further behind the shock front and this, in turn, leads to a lengthening of the shock duration. The nonlinearity of the sound propagation has a stronger effect at higher initial pressures; thus, the increase in the shock duration for the 1 mJ ns pulse is more marked than for ps pulses with the same energy.

3.4.1.4 Pressure drop during shock wave propagation

For spherical acoustic transients for which dissipation and lengthening of the pulse can be neglected as they propagate, one can expect the pressure to drop as r^{-1}. The corresponding slope of the log-log plots of $p_S(r)$ curves is -1. For cylindrical acoustic sources, the pressure decreases as $r^{-0.5}$. In the case of *shock* propagation, where the dissipation of acoustic energy and the broadening of the pressure pulse with distance cannot be neglected [Col48], the pressure decay is significantly greater.

Experimental observations. For the shocks generated by nanosecond pulses, a pressure drop proportional to $r^{-(2-2.5)}$ was observed at a distance of 100-200 µm from the emission source (Fig. 3.8b). This decay rate agrees well with the results of Noack (1998a,b), who obtained a dependence of the form $p_S \propto r^{-2.7}$ using streak photography.

In the immediate vicinity of the ns-plasma, the slope of the $p_S(r)$ curves is lower than at somewhat greater distances. Initially, it has a value near -1 and then decreases continuously over a distance of about 60 µm (i.e., a time of about 25 ns) to a value near -2.5. (Figs. 3.8b and 3.16b). This decrease may reflect the relative increase in the dissipation of acoustic energy as the shock front develops. The measurement artifacts owing to the blurring of the motion in shock wave photography described in Section 3.4.1.2 are a further cause of the slower pressure decay at the beginning of the $p(r)$ curve. In the $p(r)$ curves for pico-second pulses (Figs. 3.8a, 3.16a), no such pronounced change of the slope was observed, since the shock front already exists after about 100 ps and the shock wave pictures exhibit no blurring of the motion.

The pressure decay is slower for picosecond than for nanosecond pulses, probably because the normalized shock width a_s/R_0 is greater for ps pulses (Table 3.3) and, thereby, provides a larger energy reservoir for compensating the dissipation at the shock front. After the 1 mJ picosecond pulse, the $p_S(r)$-curve initially has a slope between -1.2 and -1.4 (Fig. 3.8a), which falls to -1.7 at a somewhat greater distance from the source. The initially slower pressure drop is probably attributable to the elongated shape of the ps plasmas at high pulse energies, which produce almost cylindrical shocks. The shocks after 50 µJ pulses are spherical, so that their pressure falls more rapidly.

Doukas, et al. (1991) have found that the pressure falls, on the average, as r^{-2} for spherical shocks propagating over 200 µm $< r <$ 1.5 mm. They presented a theoretical validation of their results by deriving an r^{-2} dependence from momentum conservation in the shock *front*. This argument, however, neglects the broadening of the shock profile, which is especially marked near the source, where it leads to a more rapid drop in the shock pressure.

If one considers the near and far field data together (cf. Fig. 3.9), a distinct decrease in the slope of the $p_S(r)$- curves is observed at about 100 MPa. A similar observation has been made by Alloncle, et al. [All94]. In the far field the slope lies between -1.05 and -1.12 (Fig. 3.9). These values are in good agreement with the observations of Schöffmann, et al. and Arons, who found -1.12 [Sch87] and -1.13 [Aro54] for laser-induced breakdown and underwater explosions, respectively. Arons found the same constant for the pressure drop in a pressure range of over 4 orders of magnitude, from 140 MPa to 0.01 MPa. Once a shock front develops as a result of nonlinear acoustic propagation, it remains over a large pressure range, even down to pressures where the shock speed approaches the normal sound speed [Rog77]. Correspondingly, shock front risetimes in the sub-nanosecond range have been measured even for pressure jumps below 1 MPa [Flo55, Eis64]. It is, therefore, misleading when some authors speak of a "shock wave region" of only 200-500 µm surrounding the plasma [Fuj85, Zys89, Dou91]. The only characteristic feature of this range is, in fact, that the shock speed is easily distinguishable from the normal sound speed. For pressure values below 15 MPa, the difference in velocities is very difficult to measure, but the shock front still exists.

Numerical solutions. At pressures below 100 MPa, the experimental data for shock propagation ($p_s \propto r^{-1.05...-1.12}$) can be described quite well by the approximate analytical solution for weak shocks [Poc71, Rog77]. However, the approximate solution cannot model the large slopes of the measured $p_s(r)$- curves at higher pressures. At those pressures, the numerical solutions based on Eqs. (3.15) and (3.17) provide significantly better results.

The general form of the numerically calculated $p_s(r)$- curves (Fig. 3.16) resembles that of the experimental $p_s(r)$- curves: the curves for nanosecond pulses have a slope somewhat smaller than -1 near the shock source, where the shock front is still developing. The slope then decreases (for the 10 mJ pulse) to -1.79 and below 100 MPa again rises to -1.4. For the picosecond pulses, the slope of the $p_s(r)$- curves changes less strongly than for the nanosecond pulses, as in the experiments, since here the shock front develops within the first 100 ps.

A shape of the $p_s(r)$- curves similar to that found here was obtained by Akulichev, et al. (1968) in their calculations of the propagation of pressure waves generated during the collapse of cavitation bubbles. In the numerical studies of bubble collapse by Hickling and Plesset (1964) and Fujikawa and Akamatsu (1980), on the other hand, the calculations were brought to an end just when the shock front had developed. Thus, no decay constant smaller than -1 was obtained even when the pressure in the collapsed bubble was greater than 2000 MPa [Hic64].

Although the shape of the calculated $p_s(r)$- curves is similar to the experimental $p_s(r)$- curves, the pressure drop is, in general, not as fast as in the measured curves. The main cause of this deviation is probably the use of different equations of state. If the relation (3.24) derived from the Tait equation was used to interpret the experimental data, then at high shock velocities the resulting pressures were clearly lower than those obtained on the basis of the equation of state of Walsh and Rice (cf. Section 3.1.7). In this way, the maximum slope of the p_S (r)- curve would approach the prediction of the Gilmore model. A reason for the deviation between calculated and experimental $p_s(r)$- curves might be that the bubble wall velocity calculated with the Gilmore model in the initial phase is always lower than the experimental value (cf. Section 3.4.2.1). The bubble wall velocity equals the fluid velocity u next to the bubble wall. The velocity $c+u$ at which the quantity $r(u^2/2 + h)$ propagates in the fluid according to the Kirkwood-Bethe hypothesis is, hence, too low, so that the nonlinearity in the propagation of sound and the energy dissipation in the shock front will be underestimated.

3.4.1.5 Shock wave energy and energy dissipation

The shock wave energy was obtained in two ways: (i) by integrating the energy dissipated in the near field and adding the energy that remains at $r = 10$ mm (Section 3.3.3) and (ii) from the shock profiles calculated for $r_m/R_0 = 6$ (Section 3.3.5). The results of both approaches are generally in good agreement with one another (Table 3.3). It is, however, noteworthy that the second approach yields lower values for all the laser parameters. This result can be explained by the fact that during the passage of the pressure pulse to the position $r_m/R_0 = 6$, part of the acoustic energy is dissipated.

The degree of conversion of the light energy absorbed at the laser focus into acoustic energy lies between 40% for a 50 µJ, 30 ps pulse and 71% for a 10 mJ, 6 ns pulse. The degree of conversion is greater for ns than ps pulses, since they produce more compact plasmas with a higher energy density (cf. 2.3.5). The degree of conversion is also higher for pulse energies well above the breakdown threshold, probably because of a higher energy density in the plasma.

By the time the shock is 10 mm from the source, 85-89% of the acoustic energy has been dissipated as heat in the fluid. The percentage of dissipated energy is highest for 10 mJ, 6 ns pulses (89%), although at a distance of 10 mm from the source the dimensionless path r/R_0 is much lower than for 50 µJ, 30 ps pulses, where 85% of the initial energy is lost. The stronger dissipation in the 10 mJ pulses is probably attributable to the higher initial pressure of the shock wave.

Fig. 3.9 indicates that the bulk of the dissipation takes place within a range of a few hundred micrometers. This result shows that the shock energy will be greatly underestimated if one tries to determine it from the far field measurements, as was done previously [Tes77, Vog88].

The dissipation of acoustic energy in the neighborhood of the plasma leads to a rise in the fluid temperature. For shocks stronger than about 7500 MPa, the temperature rise is so large that the critical temperature of water is exceeded (cf. Section 3.1.9). Pressures of this magnitude will be attained during optical breakdown with nanosecond pulses for pulse energies above about 10 mJ (cf. Table 3.3). At these pulse energies, the bubble wall dynamics is modified in the initial phase following optical breakdown. In a region where a pressure of 7500 MPa is exceeded, water vapor is formed, as soon as the pressure in the passing shock wave falls below the critical pressure of 22 MPa. Detailed documentation on bubble growth during shock-induced vaporization has been provided by Vogel and Noack (1998c).

3.4.2 Cavitation bubble expansion

Table 3.4. summarizes the most important findings on bubble expansion for a unified discussion of the experimental and numerical results.

	30 ps		6 ns	
	50 μJ (25 μJ)	1 mJ (0.64 mJ)	1 mJ (0.77 mJ)	10 mJ (8.2 mJ)
Seed bubble radius $R_0 = R_{na}$ (seed bubble volume = plasma volume) (μm)	8.5	26	18	37
Maximum bubble radius R_{max} (μm)	225	780	800	1820
Measured max. bubble wall velocity u_{Bmax} (m/s)	390	780	1850	2450
Calculated max. bubble wall velocity U_{max} (m/s)	405	494	905	1106
Bubble energy E_B (μJ)	4.7	197	212	2500
Degree of conversion of absorbed energy E_{abs} into bubble energy E_B (%)	18.8	30.8	27.5	30.5

Table 3.4 Summary of the experimental and numerical results on bubble expansion. The data on the laser pulse energy indicate the energy in front of the cell and the energy deposited at the laser focus (in parentheses).

3.4.2.1 Bubble wall velocity

The initial bubble wall velocity approximately equals the initial post-shock particle velocity calculated from the experimentally determined shock velocities (Fig. 3.7), in good agreement with theoretical predictions where $u_B(t = 0) = u_p(t = 0)$ [Pet87]. Afterwards, the measured bubble wall velocity increases for a few nanoseconds (except in Fig. 3.7a, where u_B data are only available for $t \geq 6$ ns) and then decreases again. The maximum bubble wall velocities are on the order of the normal sound speed in water, and for ns pulses they are even greater than the sound speed (Table 3.4).

These observations lead to the following picture of the early phase of bubble expansion: as soon as a plasma with a high pressure within its volume is produced, the surrounding fluid will be compressed and begin to flow radially outward. The compression wave propagates in the fluid and draws ever more fluid into the radial flow. This flow always begins with a rapid acceleration of the stationary fluid in front of the shock to the (pressure dependent) post-shock particle velocity. Near the plasma, the acceleration of the surrounding fluid lasts until after the shock front has detached, since the pressure inside the bubble is, as before, very high. The radial flow at the bubble wall, thus, reaches a higher peak velocity than the initial particle velocity at the shock front. With time, however, the kinetic energy imparted to the fluid is distributed over an ever larger fluid volume between the bubble and shock radius, so that the bubble wall velocity falls again after about 10 ns. At this time, the pressure inside the bubble is still well above the hydrostatic pressure (cf. Fig. 3.12 and 3.13) and, as before, drives the expansion of the bubble.

The numerical calculations of the bubble wall velocity using the Gilmore model provide a somewhat different picture (Figs. 3.12 and 3.13), according to which the bubble wall is accelerated *continuously* from an initial velocity of zero for 10-20 ns, during which time the bubble wall velocity is lower than the post-shock particle velocity (cf. Fig. 3.7). The inconsistency is especially clear in the case of a 1 mJ, 30 ps pulse, where the experimental u_S data imply that a particle velocity of 630 m/s is reached at the plasma or bubble wall at the end of the laser pulse (Fig. 3.7b). The bubble wall velocity calculated with the Gilmore model was less than 500 m/s and does not reach this maximum until 20 ns after the pulse (Fig. 3.12b). For all the other laser parameters, the calculated peak bubble wall velocity is also lower and reached later than the experimentally observed maximum; 100 ns after the laser pulse, however, the calculated velocities are higher than the measured velocities.

The deviation from experimental data and the inconsistency with the above theoretical arguments probably occur because, in deriving the Gilmore equation (3.1) for the bubble dynamics, it was assumed that the pressure, density, and enthalpy in the surrounding fluid are constant. The effect of the fluid on the motion of the bubble wall was taken into account in an integral fashion. In reality, however, an instability in the form of a shock front develops within the fluid which is responsible for the initial jump in the bubble wall velocity from zero to u_p but which was not taken into account in the derivation. Calculations using finite element hydrodynamic codes based on the local states of the bubble content and the fluid yield a correct representation of the sudden rise in the bubble wall velocity [Sca98].

3.4.2.2 Bubble energy

The bubble energies (Table 3.4) are, for all laser parameters, about half the total shock energy (Table 3.3), but 3-4 times the acoustic energy measured at a distance of 10 mm from the plasma. If the bubble energy were compared only with the acoustic energy determined from far field measurements as in Vogel, et al. (1988), this would lead to an overestimate of the relative significance of the bubble dynamics in the events associated with optical breakdown.

3.4.3 Possible effects of shock waves and bubble expansion on tissue

The energy in the shock wave and bubble are of similar magnitudes, but the two forms of mechanical energy act on very different time scales and produce different effects in tissue.

Shock waves. After plasma formation, tissue is first exposed to the shock wave, which, depending on the laser parameters and the distance from the plasma, passes over a given site in the tissue within 20-150 ns (Table 3.3). The important changes in state happen in the shock front over a time that is about 1000 times shorter than the total duration of the shock wave. The thickness of the shock depends on the pressure jump at the shock front [Eis64, Lan91 pp448-452]. Harris and Presles (1981) obtained a shock thickness of 2.4-5 nm for pressures of 2000-10000 MPa, which corresponds to a rise time of a few picoseconds; for a pressure of 580 MPa they found a risetime of 20 ps (corresponding to a thickness of about 40 nm) [Har82]. A risetime of 700 ps (corresponding to a shock thickness of 1 μm) was observed for a pressure jump of 10 MPa [Eis64].

The present data show that the shock front from a 1 mJ nanosecond pulse is fully developed after a distance of 50-60 μm from the source (Figs. 3.8 and 3.13). The pressure jump is then about 1000 MPa and the pressure gradient is 2.5×10^7 MPa/mm. The pressure jump is associated with a 1.22 times compression of tissue, as well as with an acceleration of the medium to a particle velocity of 430 m/s, both within only 20 ps. Thus, for 20 ps the acceleration reaches 2.15×10^{13} m/s^2 or 10^7 times that in an ultracentrifuge. The rapid compression in the region of the shock front is accompanied by the conversion of kinetic energy into heat and leads to a temperature rise of about 35° [Duv63, Jus85]. Despite the high post-shock particle velocity, the displacement *d* of the tissue as the entire shock wave passes is relatively small. It can be estimated as $d = \tau_S u_p$ and is 14 μm right behind the shock front at $p_S = 1000$ MPa. At a distance of 0.8 mm, which corresponds to the maximum cavitation bubble radius in water, the displacement of tissue by the shock is only 0.5 μm and at a distance of 15 mm (a typical distance between the application site and the retina in posterior capsulotomy), only 40 nm. Viscous damping at the shock front is accompanied by shear forces over molecular dimensions, which are proportional to the pressure gradient [Zel66]. They can become extremely high, but last only a very short time.

In general, the above discussion implies that the passage of shock waves leads to strong changes of state and to strong forces, but these are limited to very small dimensions. They can cause the breaking of chemical bonds [Ham69, Smi75, Gra79, Sus88], damage to cell organelles and membranes [Dou93, Del94, Dou95], or fragmentation of DNA [Tes95]. The destructive effect of monopolar pressure pulses is often attributed to the high pressure gradients in the rising portion of the pressure pulse [Dou95] or shock front [Gra79]. Other studies attribute it to the shock wave impulse [Kod00]. The damaging effect of thermoelastically induced bipolar transients, on the other hand, is ascribed to the trailing edge of the pulse [Ham69, Smi75, Cle77, Zhi98]. The tension produced by a 10 MPa bipolar pressure pulse is about 1/6 the strength of a C-C bond [Ham69, Cle77]. Bipolar transients arise not only through thermoelastic acoustic sources, but also during optical breakdown, when this takes place in tissue with a sufficiently high viscosity or elasticity (cf. Section 7.2.7.1 and [Vog99]). Tensile stresses can also be produced by reflection at acoustic impedance discontinuities in tissue (e.g., at the interfaces between cell nucleus and cytoplasm, between collagen fibers and background material, cornea and aqueous humor, lenses and vitreous humor, etc.) during the propagation of initially monopolar pressure pulses. Even though the amplitude of these tensile stresses is not very high because of the relatively small impedance difference in the tissue (the density varies by about 10%), they can still lead to cellular damage since tissue is much more sensitive to tensile stress than to pressure [Cum93, Par79]. Besides leading to tensile stresses, the density variations in various tissue or cell constituents can also lead to the appearance of shear forces, since the acceleration of an individual cell constituent is inversely proportional to its density. Shear forces are manifested primarily in damage to cell membranes [Roo74].

Bubble expansion. In contrast to the effect of shock waves, the expansion of cavitation bubbles is associated with a macroscopic motion of the surrounding medium: the maximum bubble wall velocity after a 1 mJ, 6 ns pulse is 1850 m/s and it stays above 200 m/s for the first 100 ns. The bubble radius increases from 18 μm to 60 μm within this time interval. The maximum bubble radius of 800 μm is reached after 73 μs. The expansion of a cavitation bubble thus leads to a large, and initially very rapid, displacement of the material surrounding the plasma. This displacement can lead to rupture of tissue on a macroscopic level, especially if the tissue matrix is already weakened owing to microscopic changes caused by the shock wave.

In clinical practice the application site usually lies in the vicinity of some tissue boundary, so that the bubble dynamics is not entirely spherical. During the collapse phase this asymmetry can result in motion of the cavitation bubble and to the formation of a liquid jet in the direction of the boundary, which can in turn lead to a strong concentration of energy at some distance from the application site [Vog89, Vog90]. As will be shown in the next chapter, this concentration mechanism contributes to the damage potential of the cavitation bubble dynamics.

The different scales of the mechanical motion in the shock front and around the cavitation bubble suggest that the morphology of the macroscopically observable mechanical tissue effects is dominated by the cavitation bubble dynamics. This will be confirmed by the histologic studies of Chapter 7. Weakening of tissue by a shock wave probably occurs mostly within the first 100-300 μm of the shock propagation, where the bulk of the acoustic energy is dissipated (cf. Fig. 3.9). This region is clearly smaller than the maximum cavitation bubble radius (800 μm for a 1 mJ pulse energy). The shock wave effects are, therefore, concealed by the consequences of bubble expansion, although they can certainly contribute to weakening of tissue structures and, thereby, to the disruptive effect of optical breakdown.

Similar conclusions can be reached by considering the zone in which the pressure is high enough to cause functional cell damage. Doukas et al. found that monopolar laser-induced pressure pulses caused cell damage when their amplitude exceeded 50-100 MPa [Dou93] and the pressure gradients exceeded 2 MPa/μm [Dou95]. After a 1 mJ, nanosecond pulse, a pressure of 50 MPa will be reached only to a distance of 250 μm from the source which is much less than the maximum bubble radius of 800 μm.

The possible range of the shock wave effects can extend beyond the maximum cavitation bubble radius only if the shock wave energy is concentrated and converted into a macroscopic fluid flow. If the shock encounters a gas bubble produced by a previous laser pulse, then this bubble will be collapsed by the shock and a liquid jet will be produced in the propagation direction of the shock wave (cf. [Vog90] and Section 5.2). This liquid jet can cause tissue damage at a distance from the plasma more than four times the maximum cavitation bubble radius ([Vog90] and Section 7.2.4).

3.5 Summary and clinical consequences

3.5.1 Summary

Shock wave formation and cavitation bubble expansion after optical breakdown with 30 ps and 6 ns Nd:YAG laser pulses with energies between 50 µJ and 10 mJ have been studied by time resolved photography, hydrophone measurements, and numerical calculations based on the Gilmore model for cavitation bubble dynamics. The calculations relied on the experimentally determined laser pulse durations, plasma size, and maximum cavitation bubble radius, i.e., on simply measurable parameters. Calculated and experimental values for the maximum shock pressure and the maximum bubble wall velocity differed by less than a factor of 2 from one another for all laser parameters investigated. Given the simplifying assumptions for the calculations and the required high temporal and spatial resolution of the measurements, this agreement is very good.

The experimental and numerical results are complementary. They provide the following picture of the events following optical breakdown with ps and ns pulses:

Conversion of light energy into mechanical energy. During expansion of a laser produced plasma, a large percentage of the absorbed laser energy (48-71% for picosecond pulses and 80-92% for nanosecond pulses) is converted into the mechanical energy of the shock wave and the cavitation bubble. About 2/3 goes into the shock and 1/3 into the bubble. The efficiency of the conversion into mechanical energy is lower for ps pulses than for ns pulses, since the energy density in ps plasmas is lower, so that a larger percentage of the energy is required in order to vaporize the fluid in the plasma volume.

Shock wave production. The measured pressures at the plasma boundary range from 1300 MPa (50 µJ, 30 ps) to 7150 MPa (10 mJ, 6 ns). During the formation phase for the shock front, in the first 10 ns, the $p_S(r)$- curves for ns pulses have an initial region with relatively lower energy dissipation, where the pressure falls off roughly proportional to r^{-1}. Next an intermediate region with stronger dissipation and $p_S \propto r^{-2...-2.5}$ follows. Below about 100 MPa a region with lower dissipation and $p_S \propto r^{-1.05...-1.06}$ sets in. This region of "weak shock propagation" extends to a distance of some centimeters from the shock source region and to pressures below 0.1 MPa. For ps pulses, the shock front forms within about 100 ps after the laser pulse, and the $p_S(r)$- curve already manifests a relatively strong dissipation from the very beginning. The pressure drop in the near field is, however, smaller than for ns pulses, since the initial pressure is lower and the relative shock width is greater and since the ps-plasmas have a more strongly cylindrical shape at higher pulse energies than ns-plasmas. In the far field the pressure falls off as $\propto r^{-1.06...-1.12}$, as with the ns pulses.

Within the first 10 mm of shock wave propagation, 85% (50 µJ, 30 ps) to 89% (10 mJ, 6 ns) of the shock energy will be dissipated, mostly in the immediate vicinity of the plasma ($r < 0.1$-0.3 mm). At high laser-pulse energies the energy dissipation at the shock front in the immediate vicinity of the plasma leads to vaporization of the fluid and, thereby, to an increase in the bubble volume.

The calculated shock wave duration τ_S in the vicinity of the plasma (at $r_m/R_0 = 6$) ranges from 20 to 58 ns, and the measured duration at $r = 10$ mm from 43 to 143 ns. The increase in τ_S with increasing distance originates in the pressure dependence of the sound speed. Within the parameter range studied here, τ_S is not correlated with the laser pulse length, but with the plasma size and the energy density in the plasma. The ratio of the shock wave width and plasma radius is roughly constant when the laser pulse energy is varied, in agreement with the similarity principle formulated by Cole [Col48]. Limitations on the validity of the similarity principle arise from the energy dependence of the pressure within the ns-plasmas.

Cavitation bubble expansion. The initial cavitation bubble volume corresponds to the plasma volume. The initial bubble contents are not gaseous, but supercritical, water. Steam forms only as the temperature and pressure inside the bubble decrease below the critical values. From then on a distinct phase boundary exists between the bubble and the surrounding fluid. Since the bubble expansion and shock wave production are both driven by the expanding plasma, the initial bubble wall velocity equals the initial post-shock particle velocity as the shock detaches from the plasma. The bubble wall velocity then increases for a few nanoseconds more, because of the high pressure in the bubble interior, and reaches a maximum about 10 ns later. The maximum is 390-780 m/s for ps pulses and 1850-2450 m/s for the ns pulses, higher than the normal sound speed in water. The rapid expansion leads to a maximum bubble radius of 225 µm for 50 µJ, 30 ps pulses and 1.8 mm for 10 mJ, 6 ns pulses.

3.5.2 Clinical consequences

The desired primary surgical effect of the laser pulses in intraocular microsurgery is the vaporization of the tissue within the plasma volume. This effect can be aided by the disruptive mechanical effects resulting from shock production and bubble expansion, but the latter can also cause undesired side effects in the neighborhood of the application site. The ratio of the vaporization energy and mechanical energy for the ps pulses is about 5 times higher than for the ns pulses. Ps pulses are, therefore, especially suited to all laser applications in which tissue effects with minor disruptive side effects are desired.

Shock wave induced tissue effects occur primarily on a cellular and subcellular level, while cavitation leads to macroscopic tissue rupture. The mechanical effects during plasma aided surgery are, therefore, dominated by cavitation and the range of the effects from a single laser pulse is on the order of the cavitation bubble radius. Close to the plasma, in a region with about 1/3 the maximum cavitation bubble radius, the shock waves can, however, cause a weakening of the tissue matrix that greatly facilitates the destructive action of the oscillations of the cavitation bubble.

For the laser pulse energies used clinically, the pressures at a distance of 15 mm (the typical distance from the posterior lens capsule to the retina) are on the order of 1 MPa. Even though this pressure is 10 times atmospheric pressure, it produces a tissue displacement of only about 40 nm and has, therefore, a low potential for side effects.

Numerical modeling of the bubble dynamics and shock formation with the aid of the Gilmore model can be used as a method for optimizing the parameters for medical laser applications, since it can easily cover a very wide parameter range. At the same time, the validity of the model is not limited to plasma-induced effects, and it can be used in a similar form to study tissue ablation by short laser pulses. Vogel, et al. (1996b) have used it to develop a strategy for minimizing cavitation-induced disruptive effects during short-pulse laser ablation in a liquid environment.

4 Energy balance

The type and extent of plasma-induced tissue effects depend on the threshold for optical breakdown and on the distribution of the laser energy over the various channels shown in Fig. 4.1. Only the absorbed portion of the laser energy can be effective. The transmission of light through the plasma, together with scattering and reflection on the plasma, lower the efficiency of the surgical process. The absorbed energy is divided further into the energy expended in vaporizing tissue, the energy of plasma radiation, and the mechanical energy of the shock wave and cavitation. The portion of the energy that goes into vaporization contributes to the primary cutting effect of the laser pulse and the portion that is converted into shock and bubble energy causes supplementary mechanical rupture. Knowledge of the parameter dependence of the energy balance in optical breakdown is, therefore, an important prerequisite for adapting the laser parameters to different surgical applications, depending on whether disruptive effects or cutting effects with minimum possible side effects are preferred.

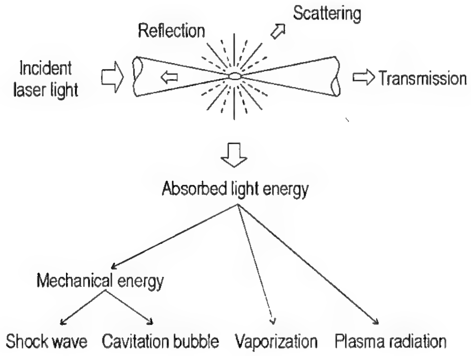

Fig. 4.1 Channels for energy partition during optical breakdown.

In this chapter, the results presented in Chapters 2 and 3 will be used to derive the energy balance for optical breakdown in water [Vog98b]. First, a total energy balance will be established for selected laser parameters. This balance shows that scattering and reflection on the plasma are small compared to absorption and transmission and that the ratio of the shock and bubble energies is roughly constant. These results make it possible to conduct a more comprehensive investigation of the influence of pulse duration, focal angle, and pulse energy on the energy balance when only the plasma transmission and the cavitation bubble energy will be measured. The bubble energy is here used as a standard for measuring the conversion of laser energy into mechanical energy.

4.1 Methods

4.1.1 Plasma transmission, scattering, and reflection

The plasma transmission was determined using the apparatus shown in Fig. 2.6a in Section 2.2.5.1. Only the light transmitted in the focal angle was measured; scattered light was blocked. In order to estimate the extent of forward scattering on the plasma, the angular distributions of the transmitted light above and below the threshold for plasma formation were compared (Fig. 2.6b). Back reflection from the plasma into the cone angle of the focussed laser beam was determined using the apparatus shown in Fig. 2.6c. First, the measurement system was calibrated at energies below the threshold for plasma formation by measuring the reflection of an aluminum mirror with known reflectivity. Based on this standard, the reflection by the plasma could then be determined. Since direct measurements of the plasma absorption with an integrating sphere were not possible because of the strong absorption at 1064 nm in water (cf. 2.2.5.4), the absorption was calculated from the measured transmission, scattering, and reflection: $A=1-T-S-R$.

4.1.2 Energy of vaporization

The energy spent on vaporization was estimated assuming that all the water in the plasma volume is vaporized and that heat conduction into the surrounding liquid can be neglected. Heat conduction can be neglected in a first approximation, because the laser pulse is very short (≤ 6 ns) and the content of the bubble formed by the expanding plasma cools to room temperature within a few microseconds [Fuj80]. The penetration depth δ of heat diffusion is [Wel95]

$$\delta = (4\kappa\tau_R)^{1/2}, \tag{4.1}$$

where τ_R is the thermal relaxation time and $\kappa = 0.15$ mm^2/s is the thermal diffusivity of water at 37°C. For a thermal relaxation time of a few µs, δ is in the order of 1-2 µm which is small compared to the plasma size at the laser parameters investigated. Almost no laser energy will be deposited outside the plasma volume because of the extreme nonlinearity of the absorption during optical breakdown. The plasma volume, V_P, was determined from photographs of the plasma radiation (cf. 2.2.4). The heat of vaporization is given by

$$E_v = \rho V_p [C(T_2 - T_1) + b] \tag{4.2}$$

Here $\rho = 998$ kg m^{-3} is the density of water, V_p is the plasma volume, $C = 4.18$ kJ (kg K)$^{-1}$ is the specific heat, $T_2 = 100$°C, $T_1 = 20$°C, and $b = 2256$ kJ kg^{-1} is the latent heat of vaporization. The latent heat of vaporization and specific heat at constant pressure are used, since the initially very high pressure inside the bubble falls off to values within the range of the hydrostatic pressure within a small fraction of the bubble's oscillation cycle.

4.1.3 Cavitation bubble energy

The energy of a spherical cavitation bubble is

$$E_B = \frac{4\pi}{3}(p_0 - p_v)R_{\max}^3 , \tag{4.3}$$

where R_{max} is the radius of the bubble at its maximum expansion and p_0-p_v is the difference between the hydrostatic pressure and the vapor pressure inside the bubble. The bubble radius was, as described in Section 3.2.3, determined from an acoustic measurement of its oscillation period.

4.1.4 Acoustic energy

The energy of a shock wave with profile $p(t)$ is [Col48, Chapter 4.8]

$$E_s = \frac{4\pi r_m^2}{\rho_0 c_0}\int p^2 dt , \tag{4.4}$$

where r_m denotes the distance from the source at which the pressure p is measured. Since the shock wave profile could not be determined experimentally immediately adjacent to the plasma, it was calculated using the Gilmore model. Measured parameters used for the calculation were the plasma volume, the laser pulse duration, and the maximum cavitation bubble radius (cf. 3.1.2 - 3.1.4). The shock profile at the dimensionless distance $r_m/R_0 = 6$ was then used to calculate the shock energy $E_S^{Gilmore}$ with the aid of Eq. (4.4) (cf. 3.3.5).

In a second approach, the energy dissipated in the shock front was integrated to estimate the initial energy content of the shock wave (cf. 3.1.9). The energy deposited as a spherical shock wave moves from r_0 to r_1 is

$$E_{Diss} = \int_{r_0}^{r_1} 4\pi r^2 \rho_s(r)\Delta\varepsilon(r)dr , \tag{4.5}$$

where

$$\Delta\varepsilon(r) \approx \frac{1}{2}\left[\frac{1}{\rho_0} - \frac{1}{\rho_s(r)}\right]p_s(r) . \tag{4.6}$$

The post-shock pressure p_S and density ρ_s can be determined indirectly by measuring the shock front velocity u_S. The pressure is obtained from u_S using Eq. (3.23) and the density can then be calculated from Eq. (3.28). The total acoustic energy was estimated by summing the energy E_{Diss} dissipated in the near field ($r \leq 300$ µm) and the energy $E_{S/10mm}$ remaining at a distance of 10 mm from the source. Using Eq. (4.4), $E_{S/10mm}$ was determined from the hydrophone measurements of the pressure profile.

4.1.5 The energy radiated by the plasma

Barnes and Rieckhoff (1968) and Stolarski, et al. (1995) have determined the spectral energy distribution of the plasma radiation emitted during optical breakdown in water over the wavelength interval 300 nm < λ < 900 nm and found that it resembles the spectral distribution of a black body radiator. According to the Stefan-Boltzmann radiation law, the energy of the black body radiation depends on the temperature T and area A_p, of the black body, and on the duration τ_{rad} of the emission:

$$E_{rad} = \sigma_B A_p \tau_{rad} T^4 , \tag{4.7}$$

where σ_B = 5,670 10^{-8} W m^{-2} K^{-4}. The temperature T of the black body radiator can be determined by using Wien's displacement law

$$T = 1{,}70 \times 10^{-9} \nu_{\max} \qquad \text{or:} \qquad T\lambda_{\max} = 2.88 \times 10^{-3} \text{ mK} \tag{4.8}$$

from the maximum $\lambda_{\max}$ of the spectral energy distribution.

For a given temperature, Eq. (4.7) provides an upper estimate of the energy in the plasma radiation, as it presupposes a perfect black body. More refined models that include the emissivity $\zeta(\lambda)$ $(0 \leq \zeta \leq 1)$ of the plasma as a function of the pressure and temperature of the plasma components and its size have been put forward by Weyl and Tucker (1989b) and Roberts, et al. (1996). However, the simple estimate of Eq. (4.7) is sufficient to demonstrate that the energy of the plasma radiation is negligibly low for the laser parameters studied here. Values for the plasma temperature were taken from the literature [Sto95], the plasma surface area was obtained from photographs, and the duration of the plasma radiation was determined by a fast photodiode (cf. 2.3.4).

4.2 Results and discussion

4.2.1 Total energy balance for selected parameters

Figure 4.2 presents the total energy balance for optical breakdown with selected laser parameters [Vog99b].

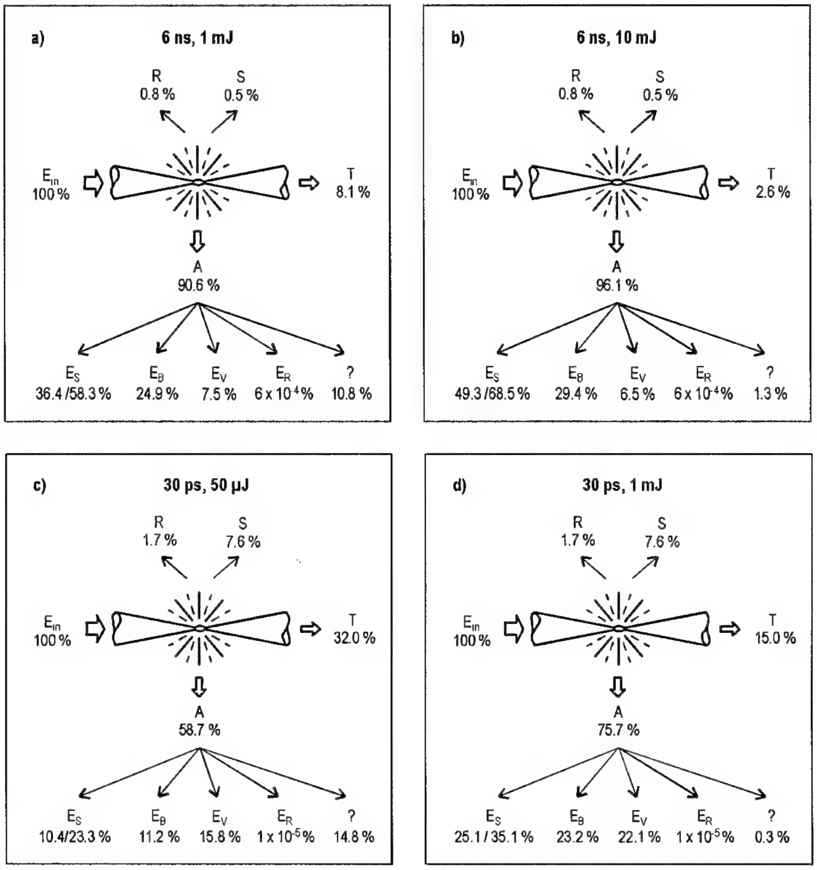
a)
6 ns, 1 mJ
R 0.8 %
S 0.5 %
E_in 100 %
T 8.1 %
A 90.6 %
E_S 36.4 /58.3 %
E_B 24.9 %
E_V 7.5 %
E_R 6 x 10^-4 %
? 10.8 %
b)
6 ns, 10 mJ
R 0.8 %
S 0.5 %
E_in 100 %
T 2.6 %
A 96.1 %
E_S 49.3 /68.5 %
E_B 29.4 %
E_V 6.5 %
E_R 6 x 10^-4 %
? 1.3 %
c)
30 ps, 50 µJ
R 1.7 %
S 7.6 %
E_in 100 %
T 32.0 %
A 58.7 %
E_S 10.4/23.3 %
E_B 11.2 %
E_V 15.8 %
E_R 1 x 10^-5 %
? 14.8 %
d)
30 ps, 1 mJ
R 1.7 %
S 7.6 %
E_in 100 %
T 15.0 %
A 75.7 %
E_S 25.1 / 35.1 %
E_B 23.2 %
E_V 22.1 %
E_R 1 x 10^-5 %
? 0.3 %

Fig. 4.2 The energy balance for selected laser parameters. The focal angle was 22° for the ns pulses and 14° for the ps pulses. For the shock wave energy, two values $E_S^{Gilmore}$ and $(E_{Diss} + E_{S/10mm})$ are given which were determined in different ways; "?" denotes the difference of the complete energy balance from 100%. It refers to the average of the two values for the shock wave energy.

Near threshold (50 μJ, 30 ps or 1 mJ, 6 ns) considerably more light is transmitted through the plasma than scattered on it. Well above threshold (1 mJ, 30 ps or 10 mJ, 6 ns), the relative importance of the transmission decreases. For all laser parameters, considerably less light is reflected or scattered than absorbed. The plasma absorption can thus be approximated by $A \approx 1\text{-}T$. This result differs from the energy partition during plasma formation at solid surfaces where the reflection plays a much larger role, because plasma is formed only in a thin layer in which the electron density tends to exceed the plasma frequency [God77] which, in turn, is the precondition for a large plasma reflectivity. When plasma is formed in water, however, the breakdown front moves during the rising part of the laser pulse towards the incoming laser beam, because the breakdown threshold is surpassed ever further upstream (see Section 2.1.6). The light absorbed upstream limits the electron density further downstream, and the plasma frequency remains therefore smaller than the frequency of the laser light. The laser-plasma coupling is thus not impaired, and little light is reflected.

The energy of the plasma radiation was calculated with the help of Eqs. (4.6) and (4.7). We used the plasma temperatures determined by Stolarski, et al. (1995) for 1064 nm Nd:YAG laser pulses (9860 K for 5 ns, 4 mJ pulses, and 6230 K for 80 ps, 1 mJ pulses). The measured duration of the plasma emission was 10 ns after a 5 mJ, 6 ns pulse and 0.5 ns after a 2 mJ, 30 ps pulse (see Section 2.3.4). The energy loss through plasma radiation is negligible ($\leq 10^{-3}$%) for all laser parameters studied here. This finding agrees qualitatively with the result of previous theoretical investigations of the plasma radiation during laser lithotripsy [Wey89b] showing that the energy carried away by plasma radiation remains below 0.1 % of the incident laser light energy of a 1-μs pulse, when the plasma temperature is 8000 K.

The main channels into which the absorbed laser energy is partitioned are vaporization, shock wave formation, and cavitation. During the expansion of the bubble, the vapor inside the bubble cools rapidly and condenses, mainly on the bubble walls. The energy of vaporization of the fluid in the plasma volume is thereby dissipated as heat in the surrounding fluid. Only that part of the absorbed energy that exceeds the energy of vaporization is available for conversion into the mechanical energy of the shock wave and the bubble motion. As very high temperatures are attained during plasma formation, for all the parameters studied here, considerably more laser energy is converted into mechanical energy than into energy of vaporization. The high conversion ratio is especially marked for the 6 ns pulses, where the mechanical energy is 10 to 14 times the energy of vaporization. For the 30 ps pulses, the mechanical enrgy is still 1.8 to 2.4 greater.

The mechanical energy is divided into a ratio of shock wave energy to bubble energy of 2:1 for the ns pulses and of 1.5:1 for the ps pulses. These ratios were calculated using the average of the two values of the shock energy obtained by the different methods.

The deviation of the total energy balance from 100% was on average -6.8% and at maximum -14.8% (for 50-µJ, 30-ps pulses). In view of the large number of channels in the energy balance and the relatively large uncertainty in the determination of the shock wave energy, this result is very satisfactory. One possible explanation for the deficit is that light lost by scattering in a sideward direction was not taken into account. Furthermore, the amount of thermally dissipated energy may have been underestimated. We considered only the energy required to transform the liquid in the breakdown volume into vapor of 100°C, neglecting losses by heat conduction. Losses by heat conduction are most important for the 50-µJ, 30-ps pulses where the largest deficit was observed, because the penetration depth of heat diffusion (1-2 µm, cf. Section 4.1.2) is here not very much smaller than the photographically determined plasma radius of 8.5 µm. For the other laser parameters, the radius of a sphere of equivalent size to the plasma volume ranges between 18 µm and 37 µm, and heat conduction thus hardly enlarges the evaporated liquid volume.

4.2.2 Parameter dependence of the energy deposition

The total energy balance for selected parameters showed that the plasma absorption is approximately given by $A \approx 1-T$. Therefore, the parameter dependence of the energy deposition at the optical breakdown site can be derived from the parameter dependence of the transmission. The plasma transmission was discussed in detail in Chapter 2. Thus, here the results will only be summarized and the corresponding sections of Chapter 2 cited.

The efficiency of energy deposition increases with increasing focal angle, since the transmission decreases for large angles (cf. 2.3.3.5 and 2.3.3.6).

The efficiency of energy deposition decreases as the laser pulse duration is shortened. The decrease is most pronounced near the breakdown threshold. This trend, which was described in sections 2.3.3.5 and 2.3.3.6 for 6 ns and 30 ps pulses, continues when the pulses are shortened to 3 ps, but is reversed in the femtosecond range (cf. Chapter 8).

4.2.3 Parameter dependence of the efficiency of conversion of laser energy into mechanical energy

Since the ratio of the shock wave energy to the cavitation bubble energy varies only between 1.5:1 and 2:1 for all the laser parameters studied in Section 4.2, one can use the bubble energy as a "measure" of the total mechanical energy in a study of the conversion of laser energy into mechanical energy over a wider range of parameters.

Figure 4.3 presents the degree of conversion of laser energy into bubble energy for 6 ns and 30 ps pulses with different focal angles as a function of pulse energy.

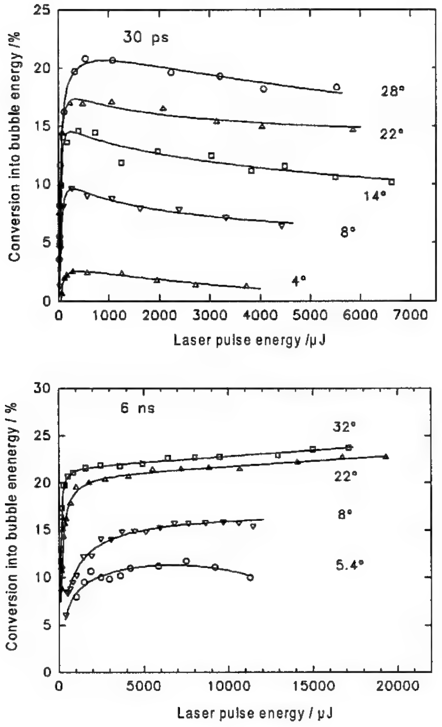

Fig. 4.3 The degree of conversion of laser energy into bubble energy for different focal angles and laser pulse energies with 30 ps and 6 ns pulses.

Dependence on focal angle. The degree of conversion into bubble energy rises with increasing focal angle, since the energy density in the plasma is highest for large focal angles. Because of the higher energy density, a smaller portion of the laser pulse energy is needed for vaporization of the fluid in the plasma volume and a larger portion is available for producing mechanical effects. The reason for the dependence of the energy density on the focal angle can be explained using Fig. 2.21 of Section 2.3.3.5. The plasma expands into the cone angle of the laser beam until it reaches the cross section where the irradiance has fallen to the threshold for optical breakdown. For equal pulse energies, this cross section is independent of the focal angle, but the distance between the plane of the beam cross section and the laser focus is shorter for large angles. Thus, the plasma volume is smaller and the energy density in the plasma is higher.

Dependence on pulse energy. As the pulse energy is raised above the threshold value for optical breakdown, the degree of conversion into bubble energy increases rapidly at first (Fig. 4.3). With ns-pulses, it saturates, while with ps pulses, it falls off after reaching a maximum as the pulse energy is raised further. This behavior depends on the fact that the energy density ε_{LIB} in ps plasmas decreases at high pulse energies, as has already been noted in Section 2.3.3.5. With ps pulses, the plasma length z_{max} is approximately proportional to $(\beta-1)^{1/2}$ and the plasma volume V_p is, therefore, proportional to $(\beta-1)^{3/2}$. Thus,

$$\varepsilon_{LIB} = \frac{AE_{in}}{V_p} \propto \frac{A\beta E_{th}}{(\beta-1)^{3/2}} \approx \frac{AE_{th}}{\sqrt{\beta}} \quad \text{for b} >> 1 \tag{4.8}$$

Here *A»(1-T)* is the plasma absorption. For large β, A is roughly constant, since the transmission T hardly changes as the pulse energy is varied (cf. 2.3.3.5). Hence, $\varepsilon_{LIB} \propto 1/\sqrt{\beta}$, i.e., the average energy density in the plasma falls off with increasing pulse energy.

With ns pulses and large focal angles, the plasma length is roughly proportional to $(\beta-1)^{1/3}$ (cf. 2.3.2.3). This scaling implies that the energy density ε_{LIB} remains nearly constant as β is increased, which explains the constant degree of conversion into bubble energy. For a 5.4° focal angle, however, the plasma length is proportional to $(\beta-1)^{0.47}$, similar to the case of ps pulses. Hence, a slight falling off of the degree of conversion is also observed here for large β.

Dependence on pulse duration. Figure 4.4 implies that the degree of conversion of laser energy into bubble energy falls off with decreasing laser pulse duration for all focal angles. This trend can also be explained in terms of the parameter dependence of the plasma energy density. It was shown in Section 2.3.5 that the energy density falls from 33-40 kJ/cm^3 for 6 ns plasmas ($\theta = 22°$) to 6-11 kJ/cm^3 for 30 ps plasmas ($\theta = 14°$).

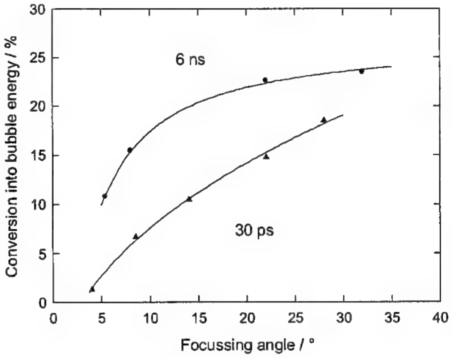

Fig. 4.4 The degree of conversion of laser energy into bubble energy for energies well above the breakdown threshold (β > 10).

The energy density continues to decrease as the pulse duration is shortened into the femtosecond range, and, as a consequence, the transformation of laser energy into bubble energy is also reduced (cf. Chapter 8).

4.3 Clinical consequences

The degree of conversion of laser energy into mechanical energy during optical breakdown (Table 4.1) is as high as 90% for ns pulses, more than for any other laser-tissue interaction [Tes77, Lya81]. The high conversion is the reason for the disruptive character of plasma-mediated laser surgery. When cutting-effects with little disruptive side effects are desired, the laser parameters must be chosen so as to ensure as small a ratio of the mechanical energy E_{mech} and vaporization energy E_{v} as possible.

	30 ps		6 ns	
	50 µJ	1 mJ	1 mJ	10 mJ
Degree of conversion of *incident* laser energy into mechanical energy E_{mech} (%)	28.1	53.3	72.3	88.3
Degree of conversion of *absorbed* laser energy into mechanical energy E_{mech} (%)	47.5	70.8	79.8	91.6
Degree of conversion of *incident* laser energy into energy of vaporization E_{v} (%)	15.8	22.1	7.5	6.5
Degree of conversion of *absorbed* laser energy into energy of vaporization E_{v} (%)	26.8	30.0	8.2	6.7
$E_{\mathrm{mech}}/E_{\mathrm{v}}$	1.8	2.4	9.7	13.6

Table 4.1 Comparison of the conversion of laser energy into mechanical energy and energy of vaporization for the laser parameters of Fig. 4.2. The mechanical energy consists of the bubble and shock energies. The shock energy was taken to be the average of the values obtained by the two methods described in Section 4.1.4.

The degree of conversion into mechanical energy falls when small focal angles are used (Figs. 4.3 and 4.4). However, this is not a practical way to optimize intraocular laser surgery, since it is accompanied by long plasmas and, therefore, by poor spatial precision in the laser effects, while the threshold for optical breakdown becomes higher. A better strategy is to shorten the laser pulse, since then both the optical breakdown threshold and the ratio $E_{\mathrm{mech}}/E_{\mathrm{v}}$ are lowered (cf. Table 4.1). That ratio is about 5 times smaller, on the average, for ps pulses than for ns pulses. Picosecond pulses are, therefore, well suited for all laser applications in which tissue cutting with slight disruptive side effects is desired. $E_{\mathrm{mech}}/E_{\mathrm{v}}$ can be reduced further through the use of femtosecond pulses (Chapter 8).

5 Cavitation bubble dynamics

The plasma expansion creates a radially outward flow in the surrounding fluid, which leads to the formation of a cavitation bubble (Chap. 3). The bubble expands beyond the equilibrium state because of the inertia of the fluid and then collapses because of the static background pressure in the fluid. The bubble collapse concentrates the bubble energy in a very small volume and is, therefore, an important link in the chain of events during intraocular photodisruption. Whereas the events during optical breakdown are strongly influenced by the laser parameters, the bubble dynamics is primarily influenced by the boundary conditions in the neighborhood of the laser focus. In a free fluid, the bubble collapse is largely spherical and takes place at the site of bubble formation. Near material boundaries, the collapse is asymmetric and is associated with the formation of a water jet, which leads to a concentration of energy at some distance from the optical breakdown [Ben66, Vog89]. Jet formation is often encountered during intraocular microsurgery, since the application site is almost always in the neighborhood of one or more interfaces between tissues and ocular fluids. It rarely contributes to the desired surgical effects, but is most often the cause of unwanted side effects in the area surrounding the application site [Vog96].

The details of jet formation depend on the distance between the bubble and a neighboring boundary, as well as on the type of boundary. They vary quite substantially, depending on whether a free surface, a rigid boundary, or a flexible boundary is involved. If the bubble collapses near a rigid boundary, then the jet flows towards the boundary [Nau61, Lau75, Vog89] and if bubble collapse takes place near a free fluid surface, then the jet flows away from the boundary [Bla87a, Bla87b]. When the bubble collapse occurs near a flexible, elastic boundary, e.g., of biological tissue, the bubble dynamics depends in a very complex manner on the elastic properties and the distance from the boundary [Bla87a, Shi91, Cha98, Bru01a,b]. In a large region of the parameter space, the bubble splits and very fast jets flowing both towards and away from the boundary are formed. In order to be able to evaluate the potential side effects from jet formation in intraocular photodisruption, the dynamics of bubbles in the vicinity of corneal and retinal tissue has been studied using high-speed photography and compared with jet formation in front of solid boundaries.

5.1 Theoretical background

5.1.1 Spherical bubble collapse

When the cavitation bubble has expanded to its maximum volume, it is nearly empty. The water vaporized during optical breakdown in the plasma volume is mostly condensed on the bubble walls, since the temperature in the bubble falls to near room temperature within the first few microseconds of bubble expansion [Fuj80]. All that remains within the bubble is an amount of gaseous water corresponding to the vapor pressure of water. Furthermore, a small amount of air is in the bubble which had been dissolved in the surrounding fluid and has diffused into the expanding bubble, once the pressure in the bubble fell below the hydrostatic pressure [Cur84]. The dissociation of water molecules during optical breakdown [Rob96] provides additional small amounts of noncondensable gases.

The expanded bubble collapses because of the pressure difference between the hydrostatic pressure and the pressure inside the bubble. In this manner, the potential energy of the cavity is converted into the kinetic energy of a radially inward fluid flow. Because of the inertia of this flow, the collapse continues after the pressure inside the bubble has reached the hydrostatic pressure. The collapse compresses the gas and water vapor inside the bubble strongly, and very high values of the pressure and temperature will be reached, similar to those during optical breakdown [Fuj80, Vog88a]. The high pressure causes a rebound of the collapsed bubble exhibiting a strength similar to that during the plasma expansion following optical breakdown. It is, therefore, likewise associated with the emission of a shock wave [Ebe78, Vog88a]. The oscillation cycle is repeated many times, until the bubble has lost its energy through acoustic emission, heat conduction, and the viscosity of the surrounding fluid. Acoustic emission is responsible for about 70-90% of the energy loss [Nis79, Vog89]. As the oscillations come to an end, one or more small gas bubbles remain, since air from the water has diffused into the cavitation bubble as it oscillated (cf. 6.1.2) [Cru84, Chu89]. These small bubbles last a few seconds before the gas dissolves again in the fluid.

Experimental studies of the states in the collapsed bubble are extremely difficult, since the actual transition from collapse to rebound lasts only a few nanoseconds, while the time of collapse of laser produced bubbles varies over a few microseconds from pulse to pulse. Reliable measurements of the pressure in the collapsed bubble are, therefore, not yet available. Calculations of the bubble dynamics using the Gilmore model [Ebe78] (cf. Section 3.1.2) and another model [Hic64], together with estimates based on far field measurements [Vog88a], yielded values from 1000 to 6000 MPa. Pressure pulse durations between 10 and 40 ns were obtained [Rad72, Hin76, Ebe78, Vog88a]. The maximum temperature in the bubble interior is on the order of 5000 K [Fuj80, Sus86, Fli91] and is sufficient to produce free radicals [Sus89, Tim97] and to generate the luminosity of the bubble contents known as "sonoluminescence" [Kut62, Ohl98]. The size of the luminous spot gives a minimum radius of the collapsing bubble of 15±6 μm for $R_{max} = 0.8$ mm, which is the bubble size after a 1 mJ, 6 ns pulse [Ohl98].

Because of the strength of spherical bubble collapse, Rayleigh postulated that the high pressures achieved during collapse are responsible for the cavitation erosion first observed on ship propellers and in hydraulic machinery [Ray17, Kna71]. Since the shock pressure falls off within a few hundred micrometers to values well below the dynamic deformation pressure of metals (about 1300 MPa for aluminum [Lus83, Vog89]), however, a bubble must collapse immediately adjacent to a metallic surface in order to cause damage there. In this case, the boundary conditions are no longer symmetric and the collapse will be aspherical.

5.1.2 Aspherical bubble collapse

5.1.2.1 Jet formation

If a solid boundary exists in the vicinity of a collapsing bubble, the fluid flow into the bubble will be impeded on the side next to the boundary and a low pressure region develops between bubble and boundary. (In the following, the boundary is assumed to be under the bubble in order to simplify the description of bubble dynamics). The pressure difference between the upper and lower parts of the bubble implies that the upper bubble wall will be accelerated more strongly that the lower. As a consequence of the pressure gradient normal to the surface, a force F (the so-called Bjerknes force) acts on the bubble and accelerates it in the direction toward the boundary. The Bjerknes force produces the so-called Kelvin impulse [Ben66]

$$I = \int F(t)dt . \tag{5.1}$$

The Kelvin impulse can be interpreted as the linear momentum of the bubble, if one ascribes a virtual mass to the bubble that corresponds to the fluid motion in its vicinity [Ben66]. During collapse, the Bjerknes force vanishes owing to the rapid decrease of the bubble size. The Kelvin impulse thus ceases to increase and remains at a constant value. Since the mass of the fluid displaced by the bubble becomes smaller during collapse, the translational velocity of the bubble center must increase owing to conservation of the Kelvin impulse. For this to happen, the velocity of the upper bubble wall in the direction of the boundary must increase significantly faster than that of the lower bubble wall in the opposite direction. At the same time, the flow at the top of the bubble will be focussed laterally during the collapse. This focusing leads to the formation of a liquid jet in the direction of the solid boundary (cf. Fig. 5.1).

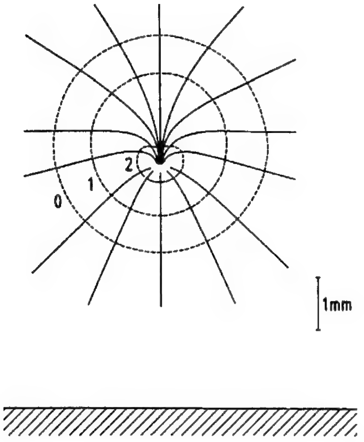

Fig. 5.1 Experimentally obtained streamline pattern of the flow in the neighborhood of a cavitation bubble during its first collapse near a rigid boundary (from [Vog89]). Stage 0 represents the bubble contour at the time of maximum expansion, and stage 2 the bubble shortly before collapse. One can see the motion of the bubble toward the boundary and the focussing of the jet on the upper side of the bubble, which leads to the formation of a liquid jet directed toward the boundary.

Since very high bubble wall velocities are reached owing to the spatial concentration of the flow during collapse, the jet velocity is also correspondingly high: it reaches 80-150 m/s, depending on the distance between bubble and rigid boundary [Lau75, Vog89, Phi98]. The jet velocity near elastic boundaries can even reach values as high as 960 m/s [Bru01a]. With asymmetric bubble collapse, only part of the kinetic energy of the collapsing flow leads to compression of the contents of the bubble. The rest remains kinetic energy of the jet flow. Because of the remaining jet energy, the internal pressure of the bubble and the temperature cannot be as high as for spherical collapse [Cha83, Vog88a].

The above argument based on the Kelvin impulse explains the bubble migration during collapse near a rigid boundary, but cannot yield further details of the bubble dynamics. They depend very strongly on the distance s between the bubble center and the boundary. The distance is customarily scaled by the maximum bubble radius and specified as the dimensionless quantity γ:

$$\gamma = \frac{s}{R_{\max}} . \tag{5.2}$$

The dependence of the bubble dynamics on γ is very complicated and has already been investigated in various experimental [Tom86, Vog89, Phi98] and theoretical [Ple71, Bla87a, Kuc88, Szy93, Bla97, Rog97, Ton97] studies. Therefore, it will only be summarized briefly here. For $\gamma > 1$ the jet impinges on the opposite bubble wall in the end phase of bubble collapse. During rebound, it first creates a protrusion of the bubble wall and then it breaks through this protrusion (Fig. 1.1). After the breakup of the protrusion, a ring vortex forms from the jet flow with the bubble being the hollow core of the annular flow. The motion of the ring vortex in the direction of the boundary conserves the Kelvin impulse of the bubble [Vog89]. Because of the motion of the ring vortex, the second collapse of the now toroidal bubble takes place right at the boundary, if the bubble was not produced too far away ($\gamma \leq 1.8$) [Phi98].

For $\gamma < 1$ the expanded bubble touches the boundary and the jet impinges directly on the boundary without being slowed down in a layer of water lying in front of it. Here the bubble assumes a toroidal shape already during the first collapse, since the jet strikes the boundary and streams radially outward on it before the collapse has ended [Shu65, Vog89, Phi98]. When $\gamma \approx 1$, there is still a thin layer of water between the bubble and the boundary surface at the first collapse, which dampens the impact of the jet and separates the high-pressure region within the collapsed bubble from the boundary.

5.1.2.2 Causes of cavitation damage

The water hammer pressure produced by the jet impact is a possible cause of cavitation damage. The water hammer pressure depends on the shape of the jet tip. For a jet with a flat tip and velocity v, this pressure is [Bru 66]

$$p_{WH} = \frac{\rho_1 c_1 \cdot \rho_2 c_2 \cdot \mathrm{v}}{\rho_1 c_1 + \rho_2 c_2}, \tag{5.3}$$

where ρ_1, c_1 and ρ_2, c_2 are the density and sound speed in the jet and in the impacted material, respectively. When the material is a biological tissue, these parameters are similar for the jet and tissue, since both consist mainly of water. Equation (5.3) can then be approximated by

$$p_{WH} = \frac{\rho_1 c_1 \mathrm{v}}{2}. \tag{5.4}$$

For a jet velocity of 100 m/s the water hammer pressure is about 75 MPa. The pressure can be up to three times higher if the jet tip has a conical shape or is round [Les83]. After the jet impact, the compression of the fluid at its tip will be reduced by stress release waves travelling from the periphery to the middle of the jet tip. For a jet diameter of 30-120 µm (depending on γ), the propagation time of the release wave and thus the duration of the water hammer pressure is 10-40 ns. Afterwards, only the dynamic pressure of the jet flow,

$$p_{dyn} = \frac{\rho_1 \mathrm{v}^2}{2}, \tag{5.5}$$

remains; 5 MPa for v = 100 m/s.

A second possible reason for cavitation damage is the high collapse pressure in the bubble, which can act directly on the material if the bubble collapses right at the material surface. For $\gamma < 1$ this is already the case with the first collapse, but for higher γ it is not so until the second collapse. A measurement of the pressure inside the collapsed toroidal bubble is extraordinarily difficult, as is a direct measurement of the pressure as the jet tip strikes. Tomita and Shima (1986) used the surface of a pressure transducer as a solid boundary in order to measure the impact pressure. They obtained a value of ≈5 MPa. However, this value was far too low, since the 5.5 mm diameter of the pressure sensor was substantially greater than the cross section of the jet and the area on which the collapsed bubble affects the pressure sensor. Besides, the risetime of the pressure sensor (1 μs) was considerably longer than the duration of the water hammer pressure produced by the jet impact and the duration of the maximum collapse pressure in the bubble. The slow rise time of the transducer also results in pressure readings which are too low [Vog88a]. Vogel, et al. (1988a) and Philipp and Lauterborn (1998) estimated the collapse pressure from far field measurements with a fast hydrophone. The far-field pressure data were extrapolated to the bubble wall using the photographically determined size of the collapsed bubble. The peak pressures obtained in this manner were 350 and 1000 MPa, respectively, for $\gamma < 1$.

Studies of the cavitation erosion of metals by Shutler and Mesler (1965) and Philipp and Lauterborn (1998) show that the damage patterns correlate primarily with the sites where the bubble comes into direct contact with the boundary during the first or second bubble collapse. Cavitation erosion of metals is thus mostly attributable to the high pressure inside bubbles as they collapse. Only if a bubble touches the boundary during the whole collapse phase (for $\gamma \leq 0.7$), is additional damage produced by the jet impact [Phi98]. When cavitation bubbles interact with biological tissue, jet formation probably plays a greater role as a possible damage mechanism, since (i) higher jet velocities are reached near elastic boundaries than near rigid boundaries [Bru00a,b], and (ii) the material strength is considerably lower than for metals. This situation is true for connective tissue, but even more so for cellular structures. Besides the water hammer pressure produced by the jet impact, shear forces acting on the tissue surface through the radial flow after the impact are also important. Rooney (1974) has shown that shear forces owing to microscopic streaming near an oscillating gas bubble can cause membrane rupture of red blood cells, and Leverett et al. (1972) have found that shear forces acting for just 25 μs are sufficient to cause hemolysis. These times are of the same order of magnitude as the duration of the radial jet flow during aspherical bubble collapse.

If laser-induced cavitation bubbles are created in the neighborhood of a free fluid surface, the surface is lifted during bubble expansion, and a pressure maximum develops between surface and bubble during the collapse phase. As a consequence, two jets are formed, one directed out of the fluid and the other entering the bubble [Bla87b]. Thus, depending on the mechanical properties of the material forming a boundary in the vicinity of a cavitation bubble, jets flowing towards or away from the boundary can be created, or two jets flowing simultaneously in opposite directions [Bru00a,b, Shi89]. Jet formation near rigid boundaries and biological tissues will be examined below.

5.2 Experimental methods

The cavitation bubble dynamics unfold over a time between 30 µs and 1 ms, depending on the laser pulse energy. High-speed photography of these events, which last about 1000 times longer than shock wave formation, cannot be performed using a time delayed portion of the laser pulse employed for optical breakdown, so an independent light source is required. A spark lamp (High-Speed Photosysteme, Nanolite KL-K) that produces a 10 ns light pulse was used for this purpose.

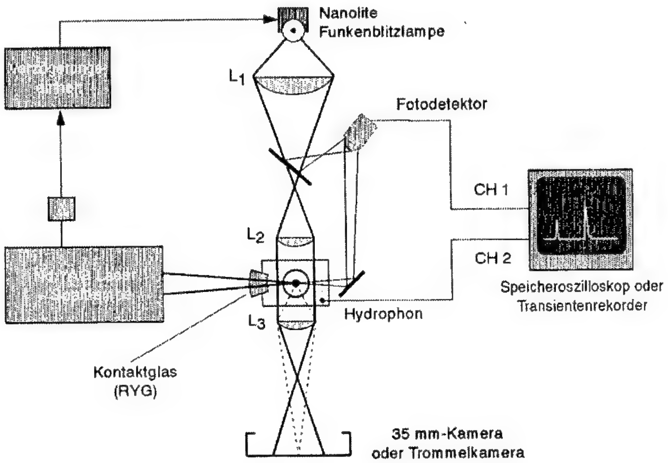

Fig. 5.2 Experimental arrangement for high speed photography to study cavitation bubble dynamics near a rigid boundary and near ocular tissue.

Figure 5.2 shows the arrangement used for studying cavitation bubble dynamics with the Nanolite spark lamp. A clinical Nd:YAG laser (Lasag Mikroruptor II) which emitted 12 ns pulses was used to produce cavitation bubbles. The laser pulses, which leave the laser slit lamp with a convergence angle of 12°, were focussed by an ophthalmologic contact lens (Rodenstock RYG) into a glass cell ($50 \times 50 \times 50$ mm^3). The cell contained distilled water, or, in the experiments with tissue specimens, physiological saline solution. The illumination system for the high-speed photography is based on the principle of a microscope illumination system. The combination of a fast collimation objective L_1 (Canon 1.2/50 mm) and a condenser L_2 (Pentax 1.8/50 mm) makes it possible to collect a large fraction of the light emitted from the spark source and to illuminate a small object volume brightly. The object volume was imaged at low magnification (2.6 to 4.2 times) using a photographic objective in retrofocus configuration (Nikon 1.8/50 mm) or at a 7-fold magnification using a Leitz Photar objective (3.5/40mm). The cavitation bubble was usually illuminated diffusely, a situation in which the liquid jet penetrating the bubble can be observed best.

For high-frequency photography of the bubble dynamics, the spark lamp was used as a stroboscopic light source, and series of pictures with up to 20000 frames per second were recorded with a rotating drum camera (High Speed Photosysteme, Strobodrum). Since the time resolution of the high-frequency photography (50 µs between frames) was not very good, single framing pictures were also taken of the collapse phase and in the time between the first and second bubble collapses. To do this, the rotating drum camera was replaced by a 35 mm camera body. Pictures were taken with increasing times between optical breakdown and the illuminating pulse in 5-10 µs steps. The separation between the laser pulse and the illuminating spark was measured with the aid of a photodetector in every shot. The time of the exposure relative to the cavitation bubble collapse was documented by simultaneously recording the acoustic signal from the oscillating bubble. The pressure pulse from the bubble collapse serves to mark the time of collapse, if the transit time from the bubble center to the hydrophone is taken into account.

For studies of bubble collapse in the neighborhood of a solid boundary, the cell was filled with distilled water and a brass block was placed under the laser focus. The bubble dynamics near tissue was studied using corneal and retinal specimens from bovine eyes. The corneal specimens were attached with surgical needles to a teflon holder which was immersed in the cell filled with physiological saline solution. Bubble dynamics in the neighborhood of the retina were studied by filling the cell with vitreous humor from bovine eyes. A tissue specimen containing sclera, choroid membrane, retina, and the adjoining vitreous humor was prepared from the posterior pole of the cow's eye. It was attached with needles to a piece of polyurethane foam and placed, with the retina upward, in the cell. The distance between laser focus and tissue specimen was 1.0-1.5 mm.

5.3 Results and discussion

5.3.1 Solid boundary

Figure 5.3 illustrates the bubble dynamics in front of a solid boundary for different distances between bubble and boundary.

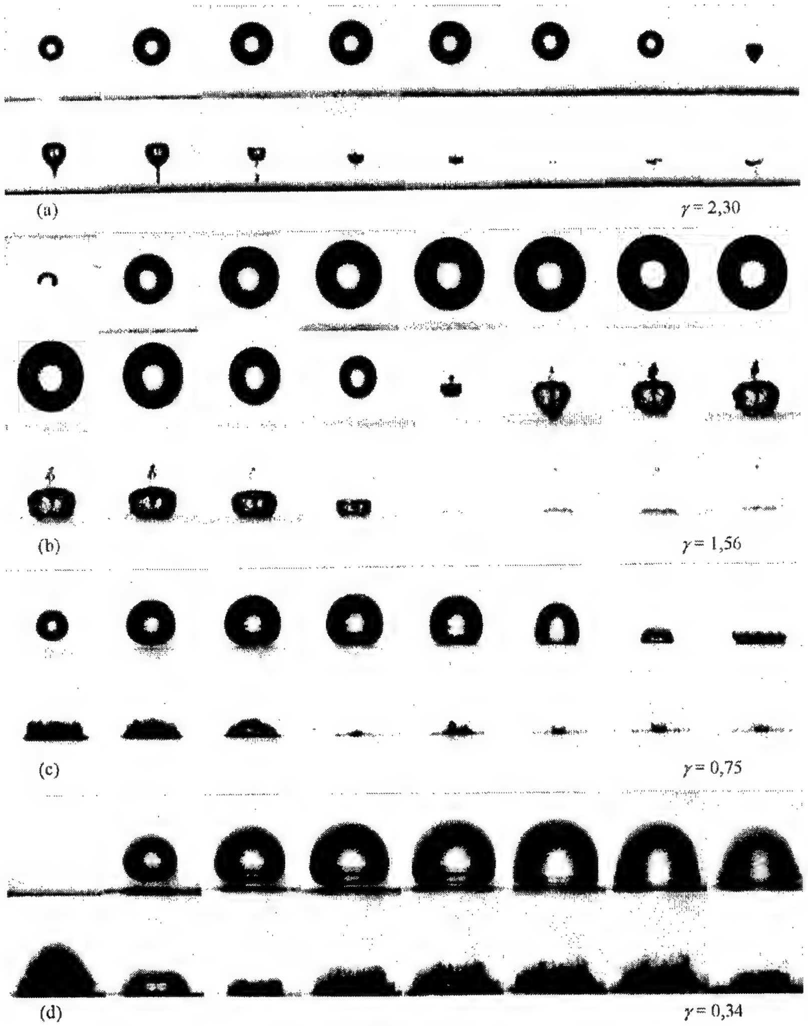

Fig. 5.3 Jet formation in front of a solid boundary for different distances γ between the locations where a bubble is formed and the boundary. The boundary is located at the bottom of each picture. I_{max} is the maximum bubble radius. The pictures were taken with the rotating drum camera at a rate of 20000 frames/s.

If the bubble is produced relatively far from the boundary ($\gamma = 2.3$, Fig. 5.3a), it moves toward the boundary during the collapse phase and a jet is formed, which protrudes the lower bubble wall when the bubble rebounds after the collapse. The jet is clearly visible in the bright center of the bubble images. Because of the jet flow, the bubble acquires a toroidal shape and a ring vortex develops which moves toward the boundary with an approximately constant velocity. In the second series of pictures ($\gamma = 1.56$, Fig. 5.3b), a counterjet appears at the top of the bubble before the actual jet becomes visible. The mechanisms for counterjet formation have been discussed by various authors [Vog89, Ohl95], but are only of secondary importance for the interaction between a bubble and a boundary. As in the previous case, the jet flow produces a toroidal bubble after the first collapse and causes the bubble move toward the boundary. During the second collapse, the bubble sits right on the brass block and the high pressure inside the bubble creates an annular high-pressure zone at the rigid boundary. As γ decreases, the jet becomes thicker and strikes the boundary even before the first bubble collapse ($\gamma = 0.75$, Fig. 5.3c). Thus, a ring vortex has already developed before the collapse, and the bubble collapses as a torus. Because of the early development of the ring vortex, a large part of the fluid flow originally directed toward the bubble center is redirected. The formation of the vortex thus diminishes the pressure attained in the collapsing bubble [Cha83, Vog89]. When the distance between the bubble and boundary surface is reduced further ($\gamma = 0.34$, Fig. 5.3d), the diameter of the jet becomes smaller once again. The bubble collapses as a torus, but, because the mass of fluid in the jet is lower, the ring vortex component of the fluid flow is much less marked than for $\gamma = 0.75$. The bulk of the kinetic energy in the fluid flow goes into a pressure rise in the bubble which is attached to the boundary. Thus, high pressure values can be reached at the boundary during the first bubble collapse.

5.3.2 Tissue boundary

Figure 5.4 illustrates the cavitation bubble dynamics in the neighborhood of a corneal specimen. The bubble moves toward the cornea and a jet develops in the direction of the specimen. Jet formation can be recognized through the protrusion of the bubble. Figure 5.4a gives the impression of a bubble moving into the cornea. This impression, however, is a illusion owing to the curved shape of the tissue specimen.

A comparison with Fig. 5.3 shows that the bubble dynamics in front of the cornea at $\gamma = 1.5$ is more like the dynamics in front of solid boundaries at $\gamma = 2.3$ (Fig. 5.3a) than that at $\gamma = 1.5$ (Fig. 5.3b). This similarity indicates that the effect of a flexible tissue boundary on the bubble dynamics is not as strong as that from a solid metal block. Nevertheless, the maximum velocity of the jet in front of the cornea (between the first and second pictures in Fig. 5.4b) is about 140 m/s (averaged over 3 μs); it is of a

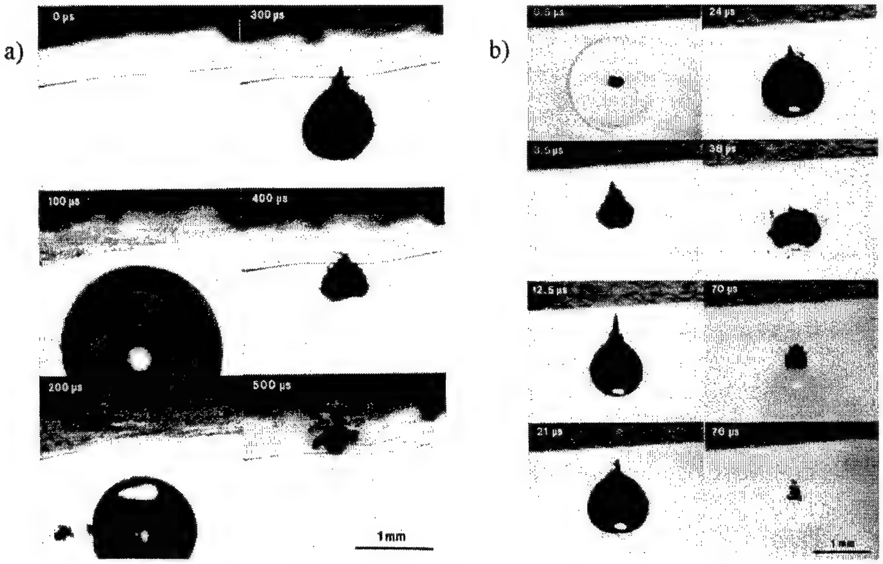

Fig. 5.4 Cavitation bubble collapse with jet formation in front of a corneal specimen (at the top of each frame). (a) Pictures series taken at 10000 frames/s with the rotating drum camera ($\gamma = 1.5$). The first collapse occurs between the third and fourth frame. (b) Single shot pictures of the bubble dynamics between the first and second bubble collapse ($\gamma = 1.45$). The time given refers to the time of the first collapse. In each picture, the plasma light from the optical breakdown can be seen along with the cavitation bubble. It indicates the site where the bubble was formed.

similar order of magnitude as the jet velocity in front of a solid boundary for $\gamma \approx 2$ [Vog89, Phi98]. The velocity would probably be even higher in the bubble splitting region at smaller γ-values [Bru01b].

When a cavitation bubble was created in front of a retina specimen, no jet developed in the direction of the specimen, but the bubble moved away from the tissue (Fig. 5.5). After the first bubble collapse, which occurred about 143 µs after bubble formation, protrusions can be seen emerging from the top of the bubble which could have been produced by a wide (but slow) jet. The observation that the jet is now directed away from the tissue boundary can be explained by the fact that the tissues of the ocular fundus and, especially, the retina, are much softer than the cornea [Shi89]. The flexibility of the retina also explains why it is lifted up during the first bubble collapse. This uplifting resulting from the low pressure between boundary and collapsing bubble is a potential cause of tissue damage, even without jet impact. A similar damage mechanism has been observed in arthroscopic surgery [Gri98] and in laser angioplasty, where the dilatation of a blood vessel during bubble expansion was followed by an invagination of the vessel wall during the collapse phase [Lee93, Vog96b].

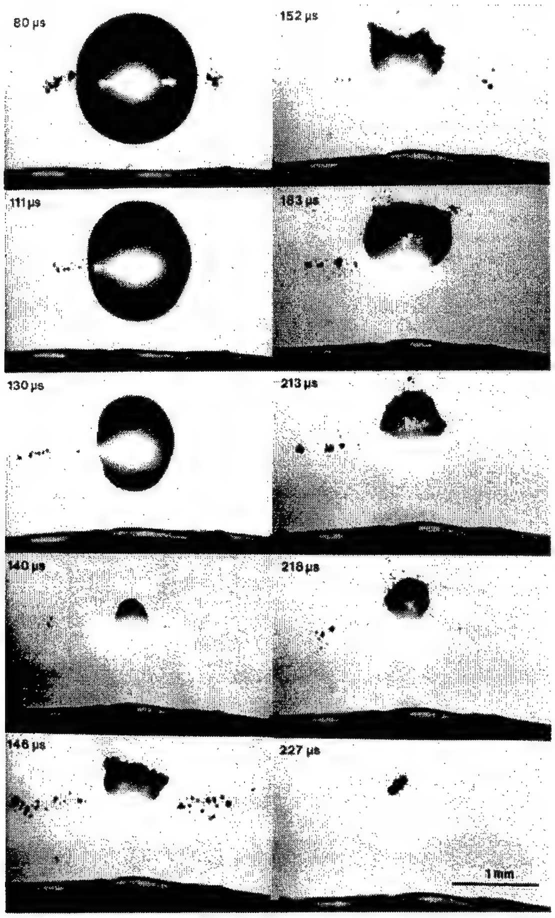
80 µs
152 µs
111 µs
183 µs
130 µs
213 µs
140 µs
218 µs
146 µs
227 µs
1 mm

Fig. 5.5 Cavitation bubble dynamics in front of a retinal specimen (at the bottom of each frame) with $\gamma = 1.4$. The times are given relative to the time of optical breakdown. The first collapse occurs between the fifth and sixth picture, and the second collapse shortly before the twelfth picture.

5.4 Summary and clinical consequences

During bubble collapse in the neighborhood of rigid boundaries and relatively stiff tissue structures, such as the cornea, the bubble moves in the direction of the boundary and a liquid jet directed toward the boundary develops. With softer, more flexible tissue structures, such as the retina, bubble movement and jet formation are suppressed or may even take place in the opposite direction.

Due to the bubble migration, its collapse can take place directly on a boundary even if the bubble creation site is some distance away from the boundary. In the case of solid boundaries, the first collapse takes place right at the boundary when $\gamma < 1$, and the second collapse takes place there when $1 < \gamma \leq 1.8$. The collapse pressure acting on the boundary can reach several hundred MPa up to a GPa. The energy transfer away from the creation site owing to bubble migration is a possible cause of side effects during intraocular photodisruption; its extent scales with the maximum bubble size.

Jet formation is a second mechanism through which the bubble energy can be focussed onto a location remote from the laser application site. It is a potent cause of side effects, especially if the jet impact is not slowed by a liquid layer in front of the tissue, i.e., when $\gamma < 1$. Tissue damage can be caused by the short duration water hammer pressure generated by the jet impact (about 75 MPa, duration 10-40 ns), as well as by the longer lasting dynamic flow pressure at the impact point (up to 5 MPa, lasting several microseconds) and by the shear forces created by the radially outward flow from the impact point [Roo74].

During cavitation bubble collapse in front of the retina, no jet formation in the direction of the retina was observed, but the retinal surface was be drawn into the vitreous humor because of the reduced pressure in the neighborhood of the collapsing bubble (Fig. 5.5). It is conceivable that this effect might lead to local retinal damage during vitreoretinal laser surgery. Perhaps, one might be able to exploit this effect to deliberately detach the membrane surrounding the vitreous from the retina, in order to avoid tractions on the retina in vitreoretinal pathologies that can lead to retinal detachment.

Besides their potential for side effects, the hydrodynamic phenomena associated with the dynamics of cavitation bubbles that lead to high flow velocities at some distance from a laser plasma can also be put to surgical use. Examples include the cleaning of deposits from intraocular lenses [Bra90] or the removal of protein coatings of the posterior lens capsule ("Elschnig pearls") which sometimes develop after cataract surgery [Bra90]. For this purpose, a laser pulse is focussed at some distance from the lens or lens capsule in order to avoid plasma-induced damage and only the flow caused by cavitation is used.

6 Multipulse interactions

Multiple laser pulses are almost always required to obtain the therapeutic goal in intraocular microsurgery. With nanosecond pulses, the individual pulses are separated by times up to many seconds, i.e., the pulse repetition rate is 0.1 to 1 Hz. When picosecond pulses with lower energies are used, the repetition rate must be considerably higher in order to ensure a sufficiently high cutting rate. The clinical picosecond lasers manufactured by the Intelligent Surgical Lasers company emit a series of pulses at a variable repetition rate of up to 2 kHz. Still higher repetition rates are employed in some clinical nanosecond lasers emitting bursts of two or three pulses with a 50-100 kHz repetition rate to increase the energy delivered to a site. Other clinical nanosecond lasers have lower burst repetition rates of 50 Hz to 1 kHz. Extremely high pulse repetition rates of 80-200 MHz are found in mode-locked picosecond pulse trains, which were quite often used in the initial period after intraocular photodisruption had been introduced into clinical practice.

In all these cases, there is an interaction between successive laser pulses which may influence the tissue effect. The details of this interaction depend on the pulse repetition rate, the spatial distance between successive application sites, and the properties of the surrounding medium. Three scenarios can be distinguished.

1. Successor pulses are focussed onto a cavitation bubble produced by a previous pulse. The oscillation periods of cavitation bubbles in aqueous media range between about 30 μs and 350 μs for pulse energies of 30 μJ to 10 mJ. This means that, for high frequency bursts at 50-100 kHz, plasma formation by later pulses is influenced by the previously created bubbles and may be hindered if the 10-20 μs time interval between the pulses is shorter than the oscillation period of the cavitation bubbles [Jun92]. In high viscosity tissues, such as the cornea, bubbles last for a few seconds or minutes [Vog94b, Juh94]. Here plasma formation will be affected even when the pulse repetition rate is low, if the lateral distance between successive application sites does not exceed the bubble radius [Vog97c].

2. If the time between the laser pulses is shorter than the duration of the cavitation bubble oscillations and the creation sites are further apart than the bubble radius, then several bubbles exist simultaneously and their bubble dynamics interact. It is conceivable that jet formation in front of tissue boundaries might be significantly intensified through the interaction of the bubbles, so that the potential for damage owing to the bubble dynamics would be enhanced. Tomita, et al. (1994) and Jungnickel (1995) have shown, however, that this is not the case. An oscillating second bubble can, indeed, lead to earlier jet formation during the collapse of a bubble previously generated near a boundary. However, the resulting jet will only be wider and barely faster, and the pressure rise detected at the boundary surface

will be, at most, 20% higher [Jun95]. Add to this the fact that, during clinical applications of a series of laser pulses, the application sites of the successive laser pulses are so close to one another that they cannot create any separate cavitation bubbles. Thus, this scenario is of little practical significance for intraocular photodisruption.

3. During the oscillations of a cavitation bubble, the gas content of the bubble increases through rectified diffusion [Cru84] and, at the end of the oscillations, one or more small gas bubbles remain. They dissolve into the surrounding fluid within seconds or minutes [Fir91]. If the small gas bubbles linger at an application site, they impede plasma formation by subsequent laser pulses. If the small gas bubbles move away from the application site, as is usually the case, there is an interaction between them and the optical breakdown created by subsequent pulses. The shock wave produced during breakdown and the flow field of the expanding cavitation bubble induce a collapse of the small gas bubbles [Lau72], during which a jet is formed in the propagation direction of the shock [Bir58, Bow65, Vog90]. This jet can, like the cavitation bubble jet, cause side effects at a large distance from the application site if it strikes sensitive tissue [Vog90]. This scenario is of great clinical significance, since, because of the long lifetime of the small gas bubbles, shock-induced bubble collapse plays a role, at high as well as low repetition rates. It can occur either when all laser pulses are focussed onto the same application site or when the focus is moved during a series of pulses.

In the following sections, plasma formation during a series of laser pulses and the effect of optical breakdown on neighboring gas bubbles will be investigated in detail.

6.1 Theoretical background

6.1.1 Plasma formation by a series of laser pulses

The influence of cavitation or gas bubbles from previous pulses on plasma formation during a series of laser pulses depends on the ratio of the breakdown thresholds in the bubble and in the fluid. The breakdown threshold I_{th} in gases is essentially determined by the threshold I_C for cascade ionization, since there are usually enough impurities present to provide the seed electrons for an ionization avalanche [DeM69]; I_C is given by Eq. (2.18). The material dependent parameters in Eq. (2.18) are the average time τ between collisions of free electrons with heavy particles, the band gap ΔE or ionization energy E_{ion}, the rate g of diffusion losses from the focal volume, the refractive index n_0 of the medium, and the mass M of the heavy particles. The differences between gases and liquids are greatest in the collision time τ which is about 10^{-15} s in fluids [Blo74] and about 2×10^{-13} s in gases at standard pressure [Smi76]. The different collision times in Eq. (2.18) imply that the threshold I_C in gases at standard pressure for 1064 nm laser pulses is about 500 times I_C in fluids. The actual breakdown threshold I_{th} in distilled water for a 6 ns pulse is about 50 times I_C because of the need to initiate the cascade by multiphoton ionization (cf. Section 2.3.1.6). Thus, I_{th} in a gas bubble should be about 10 times higher than in water. For 30 ps pulses, I_{th}/I_C is about 6 for breakdown in water (cf. 2.3.1.6), so that I_{th} in a gas bubble is expected to be about 80 times higher than in water.

These crude estimates agree quite well with experimental observations for 6 ns pulses, although only the difference in the collision time τ was taken into account and all the other material dependent parameters were neglected. For 30 ps pulses the experimentally observed threshold in air is about 20 times higher than in water, i.e., the difference is not as large as predicted.

Since τ is inversely proportional to the gas pressure [Smi76], the breakdown threshold inside a cavitation bubble is substantially higher than in a gas bubble, because the pressure inside a cavitation bubble is considerably lower than standard pressure for most of the oscillation period. Therefore, no plasma will be formed in a cavitation bubble even for pulse energies well above the breakdown threshold in water or tissue.

6.1.2 Effect of optical breakdown on gas bubbles from previous pulses

6.1.2.1 Gas bubble formation

At the end of the oscillations of a cavitation bubble, a few long-lived gas bubbles, which essentially contain air, remain. The dissociation of water molecules owing to the high temperature in the laser plasma and in the collapsing cavitation bubble contribute to the formation of the gas bubbles [Rob96], but the main mechanism for their formation is "rectified diffusion" of gas from the fluid into the oscillating cavitation bubble [Apf81, Cru84, Chu89, Lei94]. Several effects contribute to the rectified diffusion: first, the surface area of the bubble in its expanded state, when it has a low internal pressure and gas can diffuse inward, is substantially greater than during the collapse, when the pressure inside the bubble exceeds the hydrostatic pressure and the gas diffuses outward. Second, the pressure gradient is directed toward the interior of the bubble longer than outward because of the long lasting bubble expansion. Third, the gas concentration gradient in the fluid directed toward the bubble is steeper than the gradient directed out of the bubble in the neighborhood of the collapsing bubble. The reason is that, the fluid "shell," within which gas exchange takes place, contracts to a thin layer during expansion and thickens during collapse. The stable gas bubble which remains at the end of the cavitation bubble oscillations owing to directed diffusion is substantially smaller than the maximum radius of the cavitation bubble from which it originates. Because of the small surface area of the gas bubble and the low partial pressure difference to its surroundings, it lasts several seconds, until the gas dissolves again in the fluid.

6.1.2.2 Shock-induced bubble collapse

If a shock wave interacts with a gas bubble in a fluid, the bubble collapses and the acoustic energy in the shock will thus be focussed onto a small volume, where it creates high temperatures and pressures [Eva62, Cha74, San86, Shi88]. The mechanism for the gas bubble collapse depends on the duration of the pressure pulse.

1. If the shock duration is much shorter than the time it takes to cross the bubble, the bubble will never be completely surrounded by a high-pressure region. The shock is reflected at the boundary between the fluid and gas bubble, so the fluid adjacent to the interface will be accelerated to a velocity equal to twice the post-shock particle velocity u_p [Col48]. The shock wave passage at the sides of the bubble will have little additional effect.

2. If the shock duration exceeds the collapse time for the gas bubble, the bubble wall on the side facing the shock will be first accelerated to a velocity of $2u_p$, as in the previous case, but then the entire bubble wall will be further accelerated because of the prolonged pressure difference between the ambient pressure and the pressure inside the bubble. The latter portion of this process resembles cavitation bubble collapse in a free liquid, but the pressure difference is higher.

The interaction of laser induced shock waves with gas bubbles much larger than ≈150 μm falls into the first category, because the shock waves last about 100 ns and traverse a distance of about 150 μm in this time. Bubbles with a diameter smaller than 150 μm will be completely surrounded by a high pressure region for a short time, but the interaction time with the pressure wave is often shorter than their collapse time. As a consequence, effects owing to momentum transfer from the shock front during reflection at the bubble wall will usually predominate even in this case.

Previous theoretical studies of the shock wave-bubble interaction [Lau72, Tom86, Shi88, Vok93, Phi93] usually neglected the momentum transfer during shock wave reflection and the asymmetry in the boundary conditions associated with shock wave impact. They are, therefore, only to a limited extent suitable for the analysis of the interaction between laser-induced shocks and gas bubbles. To improve the analysis, Jungnickel (1995) took the momentum transfer during shock reflection into account. Calculating the bubble dynamics with the Gilmore model (cf. 3.1.2), she let a pressure pulse corresponding to the measured shock wave profile act on the bubble and additionally assumed a bubble wall velocity of 2 u_p as an initial condition for spherical bubble collapse. In this way, she obtained quite good agreement between the calculated collapse times and the experimental observations. A truly satisfactory description of bubble collapse including shock-induced jet formation can, however, only be obtained if both the post-shock particle velocity and the asymmetric boundary conditions are taken into account.

6.1.2.3 Jet formation

If a shock is incident on a curved fluid surface, a jet develops owing to convergence effects. The velocity of this jet can substantially exceed the initial velocity $2u_p$ imparted to a bubble wall during reflection of a normally incident shock [Bir48, Bow65, Tom86, San88, Dea88] (Fig. 6.1).

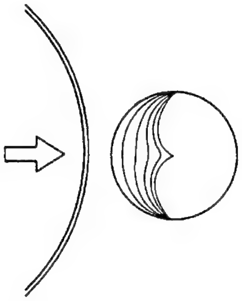

Fig. 6.1 Jet formation by reflection of a shock wave at a gas bubble. The shock, with a particle velocity u_p, is reflected as a rarefaction wave at the fluid-gas interface and, thereby, imparts a velocity $2u_p$ to the bubble wall. Convergence effects then produce a liquid jet with a much higher velocity.

This effect was discovered by the mining engineer Munroe (1888) in experiments with hollow, hemispherical explosive charges. It has been used in military technology where shells are equipped with a metal-coated conical cavity. Shock induced collapse of the cavity forms a metallic jet which can penetrate centimeter thick armor. Birkhoff et al. (1948) developed a theory for this process, but I am unaware of a theoretical analysis of the collapse of a hemispherical cavity upon which a single plane or convex curved shock is incident. Bowden (1966) made an experimental study of the interaction of a shock wave with a nearly hemispherical fluid surface in a nozzle, i.e., with a "half" bubble. He found that the "Munroe jet" produced by convergence effects was roughly three times faster than the main fluid stream used to create it. Philipp, et al. (1993) and Jungnickel (1995) observed jet velocities 6 times the velocity $2u_p$ of the bubble wall immediately after shock reflection in their investigations of the collapse of gas bubbles impacted by shock waves generated with an extracorporeal shock wave lithotriptor (for ESWL). Jet formation during bubble collapse by laser-induced shocks has not been investigated previously.

6.1.2.4 The contributions of shock and flow pressure to gas bubble collapse

If optical breakdown occurs in the neighborhood of a gas bubble, the gas bubble is exposed both to the shock wave produced by the breakdown and to the Bjerknes force created by the flow field of the oscillating cavitation bubble [Bla49, Cru75]. The flow pressure originating from the expansion of the cavitation bubble creates a pressure gradient across the gas bubble which, as described in Section 5.1.2.1, leads to formation of a jet in the direction of the pressure gradient and, thereby, enhances the effect of the shock wave.

It is very difficult to isolate the contributions of the shock impact and cavitation bubble expansion to jet formation during collapse of the gas bubble, especially since the flow during bubble expansion can also be treated as an "afterflow" of the shock wave [Col48]. The total work done as a result of optical breakdown at some point at distance r in the surrounding fluid is given [Col48] by

$$\frac{W(r)}{4\pi r^2} = \frac{1}{\rho_0 c_0} \int_{t(r)}^{\tau} p^2 dt + \frac{1}{\rho_0 r} \int_{t(r)}^{\tau} p(t) \int_{t(r)}^{t} p(t') dt' dt \,. \tag{6.1}$$

Here $t(r)$ is the time at which the shock front reaches r. One can interpret the first term in Eq. (6.1) as the acoustic energy in the shock wave (related to the elastic compression of the liquid) and the second term as describing the change in the kinetic and potential energies of the "afterflow" of the shock [Col48]. This separation is, however, not completely correct. The pressure behind the shock front is at no time exclusively the result of either compressible or incompressible flow, so the terms in Eq. (6.1) cannot be exclusively associated with the shock or the bubble-induced flow. The first term increases very rapidly as the actual shock wave passes, because the pressure p is then very high. Later contributions from the trailing edge of the shock become more and more insignificant. The second term increases considerably more slowly because of the expression $\int p\, dt'$ in the integrand, but since $\int p\, dt'$ increases with time, the second term does make a significant contribution even though the pressure in the trailing edge and afterflow region is much lower than the peak pressure at the shock front. The prefactor $1/r$ means that the afterflow becomes relatively less important with increasing distance from the optical breakdown site. This decreasing importance is a consequence of the rapid drop in the flow velocity with increasing distance from the bubble wall.

The above discussion shows that the relative influence of the cavitation bubble flow on the dynamics of the gas bubble becomes ever smaller compared to that of the shock, the further the gas bubble is from the optical breakdown site and the smaller the gas bubble. If the collapse time of the gas bubble is comparable to the duration of the shock wave (i.e., for small bubbles or for very long shock wave durations), the afterflow behind the shock scarcely plays a role. However, for large gas bubbles with a long collapse time, its contribution to the collapse of the bubble is substantial.

6.2 Experimental methods

6.2.1 Plasma formation by a series of laser pulses

Two clinical Nd:YAG laser systems were used for studying plasma production by a series of successive laser pulses. The time separation of the pulses emitted in burst mode was 20 µs and 20 ms, respectively, corresponding to repetition rates of 50 kHz and 50 Hz. Each burst consisted of three pulses approximately 10 ns in length. The high frequency bursts were produced by a Zeiss Visulas YAG laser (low order mode, focal angle 18° in air) and the low frequency bursts, by a Lasag Mikroruptor II (fundamental mode, focal angle 12° in air). The laser pulse was focussed into a cell filled with physiological saline solution, onto a metal rod inside the cell, or onto the iris of a freshly enucleated bovine eye. The studies of plasma formation in the free liquid and at a rigid boundary provided a better understanding of events in the third case, where optical breakdown was produced at a flexible tissue surface. The laser plasmas were detected by imaging the focal region of the laser with a fast photographic objective onto a photodiode with an built-in amplifier (Opto-Electronics AD110) and the photodiode signal was displayed on a storage oscilloscope. Distortion of the plasma detection by scattered laser light was prevented by using an Nd:YAG blocking filter in front of the diode. The maximum laser output energy was 9.5 mJ per single pulse, i.e., 28.5 mJ per burst; 40 bursts with, respectively, 14 mJ and 28 mJ total energy were produced.

6.2.2 Effect of optical breakdown on gas bubbles from previous pulses

The effect of optical breakdown on gas bubbles from previous laser pulses was studied using the setup described in Section 5.2. First, the formation of gas bubbles from an oscillating cavitation bubble was recorded using the rotating drum camera at a 10 kHz framing rate. The effect of a subsequent laser pulse on the gas bubbles was then studied with higher time resolution using a framing camera that took single shot pictures with increasing time delays between optical breakdown and the illuminating pulse.

In order to analyze the physical mechanisms and resulting tissue effects (cf. Chapter 7), gas bubbles were created under the endothelium of corneal specimens from bovine eyes and a 12 ns, 5 mJ laser pulse was focussed 2.5 mm from the endothelium under the bubble (Fig. 6.2). The gas bubbles were created with a microliter syringe (Hamilton, 10 µL) and had a radius of about 0.35 mm. The gas bubbles remaining after exposure to the laser are smaller. Their maximum radius after a 5 mJ laser pulse is about 75 µm (cf. 6.3.2).

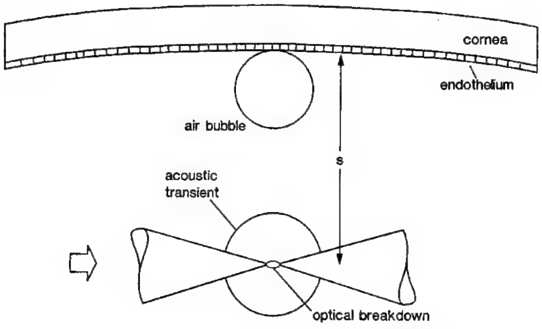

Fig. 6.2 Experimental arrangement for studying the effect of optical breakdown on gas bubbles from previous laser pulses.

The parameter dependence of the shock wave - gas bubble interaction was studied by determining the collapse time of the bubble for different bubble radii (0.3-0.85 mm), pulse energies (20-150 mJ), and distances between the laser focus and bubble (2.5-7.5 mm). The Continuum YG 671 Nd:YAG laser described in Section 2.2.1 was used in this series of measurements to produce the shock waves. The bubble size before collapse and the collapse time yield the average bubble wall velocity during the collapse of the gas bubble and, thereby, a lower bound estimate for the jet velocity. The collapse time was ascertained by visual inspection from the delay time at which the bubble reached its minimum diameter, as the delay time between the optical breakdown and the illumination pulse was increased in 1 μs steps. The corresponding shock pressure was measured with a PVDF hydrophone (CERAM) (cf. 3.2.2) located the same distance from the laser focus as the gas bubble.

6.3 Results and discussion

6.3.1 Plasma formation by series of laser pulses

At a pulse repetition rate of 50 Hz, a plasma is produced during every pulse, regardless of whether the laser is focussed into the free fluid, on a metal rod, or on the iris of a cow's eye, as long as the pulse energy exceeds the breakdown threshold. There is no effect on subsequent pulses, because the cavitation bubble and the residual microbubbles from each individual pulse vanish completely from the focal volume within a millisecond (cf. Fig. 6.4 in the next section) which is much faster than the time separation of 20 ms between the laser pulses. For the same reason, no impairment of plasma formation is to be expected up to a pulse repetition rate of 1-2 kHz.

When high frequency bursts with 50 kHz pulse repetition rate were focussed into the free fluid, only a single laser plasma was created and that by the first pulse in the burst. The second and third pulses were focussed into the center of the cavitation bubble produced by the first pulse (Fig. 6.3). They could not produce a plasma there, since the breakdown threshold in the interior of the bubble is considerably higher than in the fluid (cf. 6.1.1). Bubbles produced, for example, by a 5 mJ pulse have already reached a radius of 0.7 mm after 20 μs (Fig. 6.3a), when the second pulse is generated. This radius is substantially larger than the length of the plasma in the unperturbed fluid (cf. 2.3.2.3), so that no plasma could be produced in the fluid at the edge of the bubble, either.

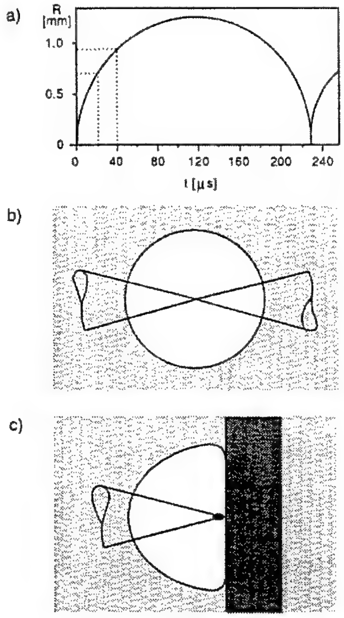

Fig. 6.3 The effect of cavitation bubbles from previous laser pulses on plasma formation. (a) Radius-time plot of the bubble oscillations after a 5 mJ pulse. By the time of the second and third pulses from a burst with a 20 μs pulse separation, the bubble has already reached more than 50% of its maximum radius. (b) Cavitation bubble and laser beam cone at the time of the second and third pulses with focussing into the free liquid. (c) Bubble and laser beam cone with focussing onto the surface of a metal rod in the liquid.

When the laser is focussed onto a metal rod in the fluid (Fig. 6.3c), a plasma is produced by each pulse regardless of the repetition rate of the pulses. The cavitation bubble aquires a hemispherical rather than a spherical shape, owing to the solid boundary. Therefore, the laser focus lies not in the center of the bubble but at the absorbing surface of the metal rod. The breakdown threshold is, hence, low with and without a cavitation bubble.

When high frequency bursts are focussed onto a flexible tissue surface, as is the case during iridotomy, the deformability of the tissue determines whether more plasmas can be produced after the first pulse. Data from experimental iridotomies on bovine eyes are summarized in Table 6.1.

Number of plasmas observed	% of cases with a burst energy of	
	14 mJ	28 mJ
1	40	25
2	45	40
3	15	35

Table 6.1 Probability of creating one, two, or three plasmas during experimental iridotomies with high frequency bursts (50 kHz) of three pulses with different total energies.

The number of plasmas that were created varied between one and three. Even at the maximum burst energy, only one plasma was produced in 25% of the shots and three plasmas were produced only in 35% of all cases. The iris was evidently often so deformed by the cavitation bubble produced by the first pulse that a nearly spherical bubble developed into which the next pulses were focussed. When the tissue is more rigid, it is barely deformed during the bubble expansion and remains near the laser focus. The irradiance at the tissue surface is then sufficiently high in the subsequent laser pulses that optical breakdown can ensue. At higher pulse energies, the probability for multiple plasma formation increases, since the length of the region in which a plasma can be formed increases more rapidly with pulse energy than the cavitation bubble radius.

6.3.2 Effect of optical breakdown on gas bubbles from previous pulses

6.3.2.1 Gas bubble formation

Figure 6.4 shows how small gas bubbles develop from the oscillation of a cavitation bubble generated by a 5 mJ nanosecond pulse. After the collapse of the cavitation bubble, microbubbles remain which move away from the laser focus with an initial velocity of over 10 m/s. Immediately after the

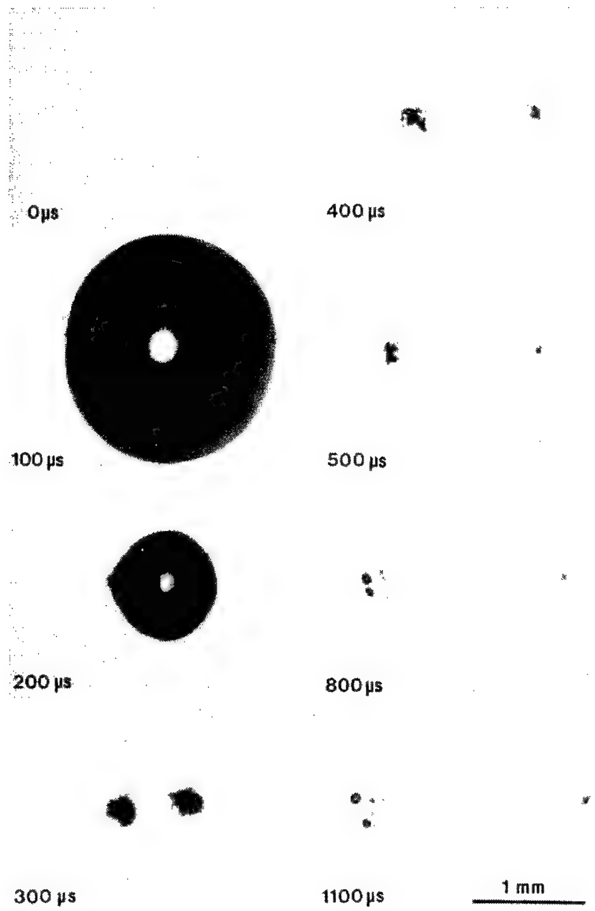

Fig. 6.4 Cavitation bubble dynamics in a free liquid after a 5 mJ laser pulse (10000 frames/s). The second picture shows the bubble shortly before it reaches its maximum radius, the third picture was taken 10 µs before the first collapse, and the fourth picture 9 µs after the second collapse. The microbubbles remaining after the second collapse move away from the laser focus at a velocity exceeding 10 m/s.

collapse, the small bubbles are still oscillating and have an irregular shape, but in the final pictures they already have a constant size and a round shape. The maximum diameter of a single small bubble after a 5 mJ laser pulse is 150 µm. If several of them remain, their diameters are, accordingly, smaller. Because of their long lifetimes of a few seconds, they can be seen with the unaided eye during intraocular microsurgery, unlike the cavitation bubbles which disappear after less than 1 ms.

The cavitation bubble breaks up into several small bubbles, as it is not exactly spherical prior to the collapse. Deviations from a spherical shape become stronger during collapse [Stru71] and lead to the formation of jets [Lau82, Vog89]. Since each jet flow results in the formation of a ring vortex (see Section 5.1.2 and [Vog89]), the bubbles are propelled away from the collapse site. Because of the conservation of momentum, the bubbles move out in opposite directions from one another. The dynamics shown in Fig. 6.4 is often observed with laser-produced cavitation bubbles. Because of the oblong shape of the breakdown plasma, the bubble expansion is greatest in the "equatorial plane" perpendicular to the optical axis. The wall of the expanded bubble is, therefore, especially strongly curved at the equator and the collapse is fastest there [Lau82]. That leads to the formation of an annular fluid flow in the equatorial plane. This flow divides the bubble, and two oppositely directed jets develop along the axis of the laser beam [Lau85, Bru00a]. Because of the jet formation and the ensuing ring vortex flow, the parts of the bubble move away from each other at a high and, over quite long times, relatively constant velocity. They can move several millimeters from the application site. The high velocity of the microbubbles has misled some authors to interpret them as "particles" [Ver86].

6.3.2.2 Bubble collapse and jet formation

Figure 6.5 shows what happens when a laser pulse is focussed near two gas bubbles. The gas bubbles are first struck by a pressure of about 8 MPa lasting about 100 ns from the shock wave produced by the plasma expansion, and are then exposed to the flow created by the expansion of the cavitation bubble. Jets develop that penetrate the gas bubbles in the direction of shock wave propagation, which is the same as the direction of the radial flow produced by the expanding bubble.

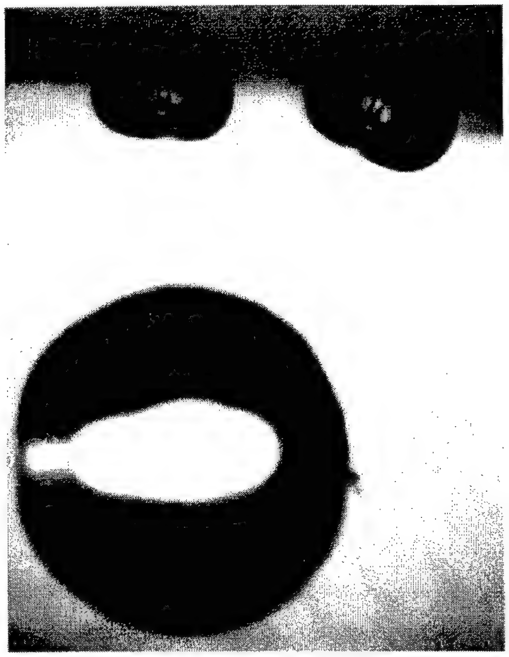

Fig. 6.5 Jet formation in two gas bubbles (at the upper boundary of the picture) 70 µs after optical breakdown created by a 9 mJ laser pulse focussed 2.5 mm from the gas bubbles. The shock wave generated during breakdown has a duration of ≈100 ns and hits the gas bubbles with a pressure of about 8 MPa. The cavitation bubble following breakdown can be seen in the lower part of the picture. Jet formation in the gas bubbles follows the propagation direction of the shock wave and of the flow generated by the bubble expansion.

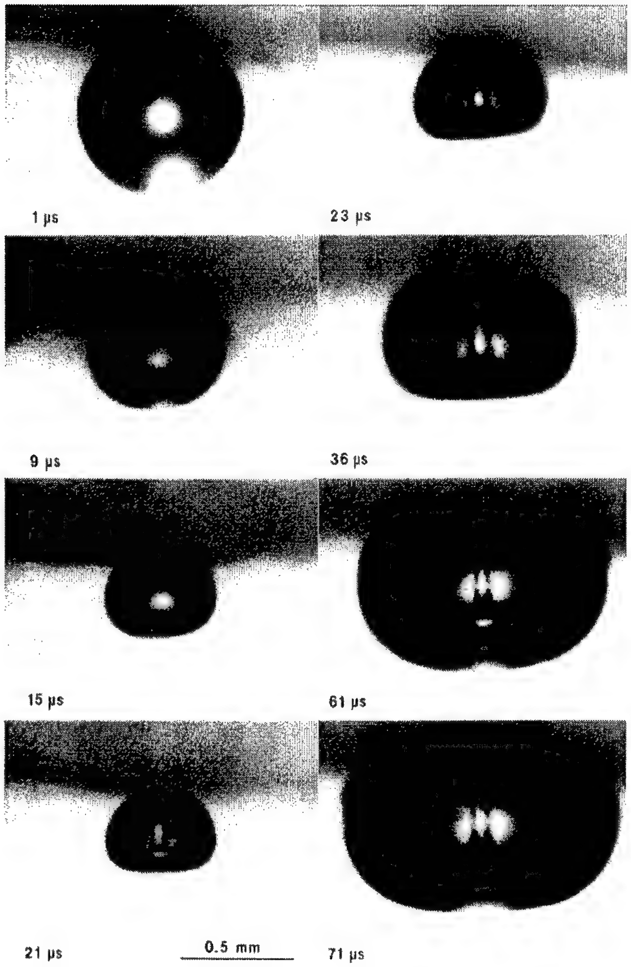

Fig. 6.6 Shock induced jet formation with a gas bubble that has 350 µm initial radius. A shock wave was produced 2.5 mm away from the bubble using a 9 mJ laser pulse.

Figure 6.6 illustrates the jet formation in a series of single shot pictures taken with increasing time delays between the laser pulse and the irradiation pulse. The volume of the gas bubble is compressed by the shock wave and its afterflow within about 15 µs to a third of its initial volume, and then it expands again to more than four times the initial volume. The large increase in the volume of the gas bubble relies partly on the preceding compression of the gas bubble and is partly attributable to the fact that an underpressure develops in the fluid surrounding the laser-induced cavitation bubble within a few microseconds after breakdown. The underpressure in the liquid is a consequence of the fact that the pressure inside the expanding cavitation bubble falls to a level below the hydrostatic pressure.

The jet formed during the gas bubble collapse can first be seen when the bubble rebounds after collapse, and then remains visible for a long time. Fig. 6.6 allows a crude estimate of the jet velocity: We assume that the part of the bubble wall opposite to the boundary that then forms the jet tip touches the boundary between the third and fourth frame of the picture series. This implies a jet velocity of 50-60 m/s. The diameter of the jet is about 80 μm, i.e., roughly a ninth of the initial bubble diameter. The jet velo-city is 10 times the post shock particle velocity u_p (5.4 m/s), i. e., 5 times the initial bubble wall velocity $2u_p$ created by reflection of the shock. That the jet velocity is substantially higher than $2u_p$ is explained by convergence effects during the collapse of the bubble (cf. 6.1.2). If the jet hits the boundary at 55 m/s, it produces a water hammer pressure (cf. Eq. (5.4)) of 40 MPa for a time of about 30 ns and, thereafter, a flow pressure of 1.5 MPa. The water hammer pressure is 5 times the shock pressure of 8 MPa which produced the jet, but its duration is shorter than that of the shock. The dynamic pressure of the jet flow is only a fifth of the shock pressure, but it acts for several microseconds. The jet flow also generates shear forces at the boundary surface which last for a few microseconds.

6.3.2.3 Scaling laws

Figure 6.7 shows the average bubble wall velocity $\bar{v}_B$ during bubble collapse as a function of the laser pulse energy E_L and of the distance d between the laser focus and bubble. The fits to the measurement data yield the scaling laws

$$\bar{v}_B \propto E_L^{0.5} \tag{6.2}$$

and

$$\bar{v}_B \propto d^{-0.9}. \tag{6.3}$$

Since the shock pressure and laser pulse energy at a constant distance from the laser focus are related as $p_s \propto E_L^{0.5}$ [Vog88a, Jun95, Noa97], Eq. (6.2) yields a third scaling law

$$\bar{v}_B \propto p_S. \tag{6.4}$$

The average bubble wall velocity during gas bubble collapse is lower than the maximum jet velocity, but the scaling laws derived from it are probably valid for the jet velocity, as well.

It is noteworthy that the collapse velocity falls off slightly below linearly with increasing distance from the laser focus (Eq. (6.3)), although the shock wave pressure decreases with distance as $p_s \propto d^{-1.06}$ (cf. Fig. 3.7). The reason may be that the convex curvature of the shock wave decreases with increasing distance from the focus, so that a larger fraction of the shock momentum is directed toward the center of the gas bubble.

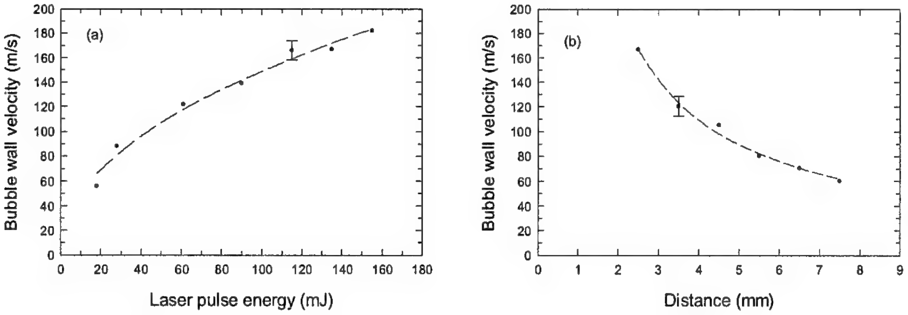

Fig. 6.7 Average bubble wall velocity during breakdown-induced gas bubble collapse as a function of the laser pulse energy (a) and of the distance between laser focus and bubble (b). The initial gas bubble radius was 0.5 mm in both cases. The distance between focus and boundary in (a) was 2.5 mm and the laser energy in (b) was 155 mJ.

In Fig. 6.8 the average bubble wall velocity during gas bubble collapse is plotted as a function of the bubble diameter. The bubble wall velocity has a maximum for a bubble radius of about 0.4 mm. The existence of such a maximum can be explained by the fact that small bubbles collect shock wave and flow energy only from a small cross sectional area. Large bubbles, on the other hand, exhibit only a weak curvature of the bubble wall, which is decisive for the focussing of energy into the jet flow.

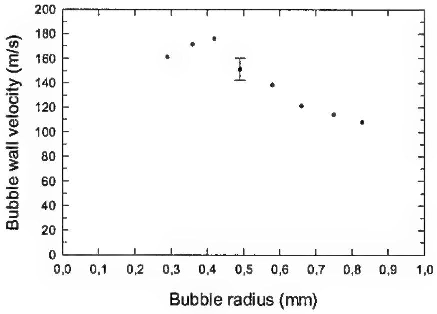

Fig. 6.8 Average bubble wall velocity during shock induced collapse of a gas bubble as a function of the initial bubble radius. A 155 mJ laser pulse was focussed a distance of 2.5 mm from the bubble. The shock pressure upon impact at the gas bubble was 31 MPa.

The duration of the laser-induced shock wave is about 100 ns, significantly shorter than the collapse time for the gas bubbles, which is 18 μs for a pulse energy of 5 mJ and an initial radius of 350 μm (cf. Fig. 6.6). The bubble wall is, hence, no longer accelerated by an elevated pressure during most of the collapse phase. The collapse is started by the shock wave impact, but proceeds only because of the inertia of the fluid surrounding the bubble which has been accelerated by the shock wave reflection at the bubble wall. For longer shock durations of about 1 μs as in extracorporeal shock wave lithotripsy (ESWL), the bubble wall is accelerated during a major part of the collapse phase [Phi93, Jun95]. The bubble collapse is, therefore, substantially more intense than with laser-induced shock waves of equal amplitude. An ESWL shock wave with a pressure of 65 MPa hitting a gas bubble with 0.7 mm radius produces a jet with a velocity of over 500 m/s [Phi93, Jun95] which is more than 12 times higher than the post-shock particle velocity (40 m/s).

6.4 Summary and clinical consequences

6.4.1 Plasma formation by a series of laser pulses

When multiple pulses are applied, plasma production is hindered by the cavitation bubbles from previous pulses when the time between pulses is shorter than the bubble lifetime, because the threshold for optical breakdown is considerably higher in the bubbles than in the fluid or in tissue.

When the application site is surrounded by a low viscosity medium (e.g., aqueous humor), there is no impediment to plasma formation up to a pulse repetition rate of about 2 kHz. For picosecond pulses with energies in the microjoule range, the limit on the rate is about 5 kHz, since here the cavitation bubbles have a shorter lifetime owing to the low pulse energy. When repetition rates below the rate limit are used, plasma production can be impeded only by the small gas bubbles remaining from the cavitation bubbles. The latter is improbable, if the small bubbles can leave the application site unimpeded, but in fistulating operations (e.g., sclerotomies), where the microbubbles are trapped in an already existing channel, they can prevent successful completion of the operation.

With the high frequency burst modes available in many clinical lasers, which have a pulse repetition rate of about 50 kHz, plasma formation is often hindered by cavitation bubbles. In experimental iridotomies on bovine eyes, even with 9.5 mJ pulse energy, a plasma was created in each pulse of a burst in only a third of the cases. This result demonstrates that the efficiency in burst mode is low, and the eye will be exposed to an unnecessarily high light dose. The high-frequency burst mode is, therefore, unsuitable as a means for increasing the laser energy deposited in an application site.

If the application site is in viscous tissue, e. g., in cornea, the maximum cavitation bubble diameter is certainly smaller than in aqueous media, but the lifetime of the bubbles is substantially longer. In this case, a hindrance to plasma production can only be avoided if the laser focus is moved between pulses by a distance larger than the cavitation bubble radius.

6.4.2 Effect of optical breakdown on gas bubbles from previous pulses

At the end of the cavitation bubble oscillations, small gas bubbles remain which can move a few millimeters away from the application site. When subsequent laser pulses are applied, the gas bubbles will be collapsed by the shock wave and by the flow pressure exerted during cavitation bubble expansion. During the gas bubble collapse, a jet develops which penetrates the bubble in the propagation direction of the shock wave. Because of the jet formation, the shock wave and flow energies from the entire gas bubble cross section are concentrated in a much smaller cross section. If the jet strikes sensitive tissue structures, it can produce side effects at a large distance from the application site. The range of potential side effects related to this mechanism is even greater than for cavitation bubble collapse. A 5 mJ laser pulse produces a jet with a velocity of 50-60 m/s, even if the gas bubble is located 2.5 mm away from the laser focus. In addition, shock-induced jet formation does not require any specific boundary conditions, as does jet formation during cavitation bubble collapse, which is most forceful if the bubble is located close to a rigid of flexible boundary.

The average bubble wall velocity $\overline{v}_B$ and, probably, also the jet velocity during gas bubble collapse scale with the laser pulse energy E_L, the distance d between laser focus and gas bubble, and the shock pressure p_S in the following ways: $\overline{v}_B \propto E_L^{0.5}$, $\overline{v}_B \propto d^{-0.9}$, and $\overline{v}_B \propto p_S$. A reduction in the laser pulse energy leads to a drop in the velocity of the jet and, thereby, in the potential for damage. When lower pulse energies are used, the resulting gas bubbles are also smaller, so their potential for damage is reduced even further.

7 Tissue effects

This chapter examines the influence of the various physical mechanisms described in the preceding chapters on the development of tissue effects during intraocular photodisruption and analyzes how these effects are modified when the laser pulse duration is shortened from the nanosecond into the picosecond range.

The tissue effects depend strongly on the boundary conditions: it makes a big difference whether the laser focus is at a tissue surface, in the fluid near a tissue surface, or in the tissue itself.

1. *Laser focus at a tissue surface surrounded with fluid.* This case corresponds to the classical applications of photodisruption, as capsulotomies and iridotomies [Ste85], and it is also of interest for all other laser applications in which intraocular tissue must be cut.

2. *Laser focus in a fluid near a tissue surface.* This configuration is of interest for evaluating possible side effects that may be encountered when the application site is in the vicinity of sensitive structures. Examples include the corneal endothelium during iridotomy, the retina during vitreoretinal laser surgery, and the intraocular lens during posterior capsulotomy [Vog90].

3. *Production of laser effects inside homogeneous tissue.* The third case has acquired great importance in the context of attempts to correct refractive errors of the eye by vaporization of a lenticule in the corneal stroma [Nie93, Hab95, Mar96]. For this application, it is not only important to assess the range of potential side effects, but the question still needs to be answered whether it is at all possible to vaporize enough corneal tissue to obtain the desired change of the corneal topography [Vog97b].

In order to ensure a good comparability of the tissue effects in the different configurations listed above, the studies were performed on a single type of ocular tissue. The cornea was chosen as a model tissue, since it is a good detector of the different physical effects owing to its layered structure. Thermally induced tissue changes can be studied by looking at the collagen denaturation in the corneal stroma, and the corneal endothelium reacts very sensitively to mechanical damage. Lesions in the corneal endothe-lium are, moreover, a clinical complication that is often observed in intraocular photodisruption [Gab85, Ker85, Win88].

The tissue effects in each configuration were studied histologically and morphometrically at various laser pulse durations and energies. For laser effects *inside* tissue, the state immediately after the application of a pulse cannot be documented histologically, because it takes too long until the fixate has reached the lesion by diffusion through the outer tissue layers. In this case, the tissue effects immediately after the laser pulse were documented through high-speed photography [Vog94b,d, Vog97b]. Based on the histological and photographic studies, the physical mechanisms responsible for the tissue effects are identified, and the relationship between the desired surgical effect and undesired side effects with nano- and picosecond pulses are evaluated [Vog90, Vog94b].

7.1 Experimental techniques

7.1.1 Measurements with different irradiation geometries

Figure 7.1 provides an overview of the various irradiation geometries used to study laser induced tissue effects, and Table 7.1 lists the major data on the laser systems employed in those studies (Lasag Mikroruptor II, Continuum YG-617-10, and ISL 2001), along with the corresponding focal parameters.

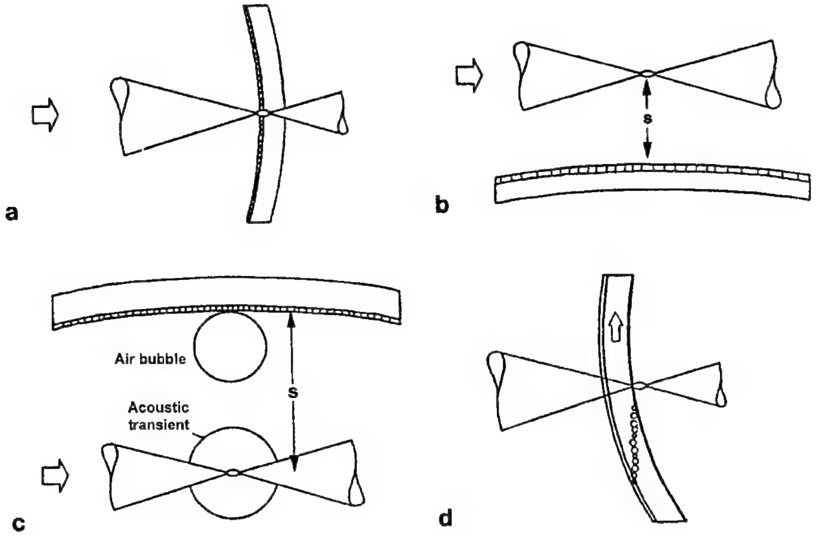

Fig. 7.1 Irradiation geometries for studying the consequences of different physical effects after optical breakdown at the cornea. The laser pulses were focussed (a) perpendicularly and directly onto the corneal endothelium or (b) parallel to the cornea at a distance *s* from the endothelium. (c) Irradiation geometry for studying the damage caused by the interaction of a laser generated acoustic transient with an air bubble attached to the corneal epithelium. (d) To study intrastromal laser effects, an eye was moved laterally across a fixed laser focus. Because of the curvature of the cornea, this movement produces a variable distance between laser focus and corneal endothelium, which is used to determine the range for damage to the endothelium.

Corneal specimens from freshly enucleated bovine or porcine eyes (1-4 hours *post mortem*) were used, after being cut out of the eye with a trephine or a preparation blade. Each specimen was fastened to a holder and immersed in a cell containing physiological saline solution. An XYZ translation stage was used for positioning the sample In some experiments the cell was replaced by a holder in which an entire enucleated eye could be fastened. Aiming was done with a helium-neon laser together with a microscope (Fig. 7.2). Since the cavitation bubble dynamics is the main cause of the disruptive effects in photodisruption, the bubble size in water was determined for each pulse energy used in the tissue experiments. The bubble size was obtained by measuring the time between the shock waves from the optical breakdown and the bubble collapse (cf. 3.2.3).

	Lasag Mikroruptor II		Continuum YG 617-10		ISL 2001
Wavelength (nm)	1064	1064	1064	1064	1053
Pulse duration (ns)	12	12	6	0.03	0.045
Laser mode/ beam profile	fundamental mode	multimode	approximately gaussian	gaussian	approximately gaussian
Test cell wall	glass plate	glass plate	RAK contact lens	RAK contact lens	RYM contact lens
Focusing angle inside the glass cell	9.5°	12.5°	22°	14°	30°
Focal spot diameter (μm)	20	55	8	6	13 (per manufacturer)
Breakdown threshold in distilled water (μJ)	750	6100	140	7	20

Table 7.1 Laser systems and focal parameters for the tissue experiments.

Laser focus at the tissue surface. In order to study the combined effects of plasma, shock wave, and cavitation during tissue cutting, 12 ns laser pulses from the Lasag Mikroruptor II were focussed perpendicular to the Descemet's membrane or into the underlying corneal stroma (Fig. 7.1a) [Vog90].

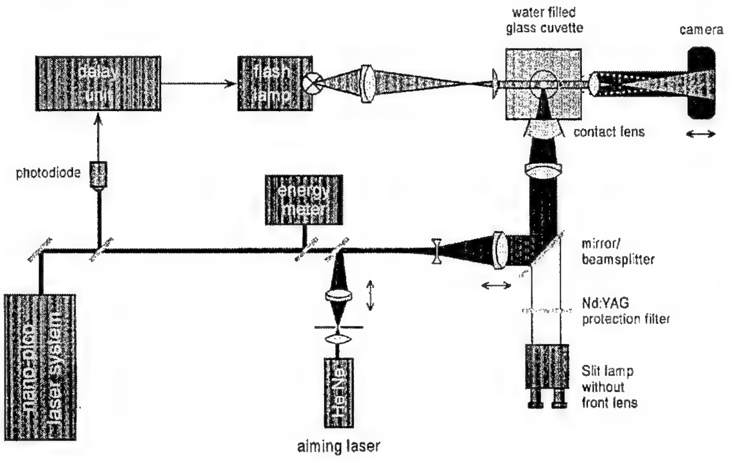
water filled
glass cuvette
camera
delay unit
flash lamp
contact lens
photodiode
energy meter
mirror/
beamsplitter
Nd:YAG
protection filter
Slit lamp
without
front lens
nano-pico laser system
He-Ne
aiming laser

Fig. 7.2 Experimental setup for studying tissue effects with the Continuum laser and for high-speed photography of the resulting cavitation effects.

Laser focus in fluid adjacent to tissue. In order to exclude the direct vaporizing effect of the plasma and permit the mechanical effects of the shock wave and cavitation bubble to work alone, the laser pulses were focussed parallel to the Descemet's membrane (Fig. 7.1b). The distance s between the laser focus and cornea was varied and the effect of single pulses, as well as the cumulated effects of a series of pulses, were studied [Vog90]. The positioning accuracy for s was ±10 µm.

Tissue effects owing to the interaction of optical breakdown with gas bubbles from previous laser pulses (cf. 6.3.2) were studied using the irradiation geometry shown in Fig. 7.1c [Vog90, Fri91]. Small air bubbles with a radius of 350 µm were placed under the cornea with a microliter syringe, or the bubbles remaining after a laser shot, with a maximum radius of 75 µm, were used. Then 4 mJ, 12 ns laser pulses from the Mikroruptor II were focussed at a distance s from the cornea under the air bubble. The transients emitted during optical breakdown, as well as the flow caused by the expanding cavitation bubble, would interact with the air bubble and create a jet in the direction of the endothelium.

The damage range of optical breakdown. For the irradiation geometries shown in Figs. 7.1a and b, the radius r_L of the laser-produced tissue effects was measured as a function of the laser pulse energy [Vog90]. For focussing parallel to the cornea, the damage range was determined . The damage range R is defined as the geometrical distance between the laser plasma and the most distant portion of the corneal lesion, i.e.,

$$R = \sqrt{s^2 + r_L^2} \,. \tag{7.1}$$

A total of 90 specimens were used and 200 lesions evaluated to determine the damage range. The damage range for the shock wave-gas bubble interaction (Fig. 7.1c) was studied by varying the distance s between the laser focus and cornea for a constant laser energy. A total of 17 specimens with laser-generated bubbles and 48 in which the bubble was made with the microsyringe were studied.

Tissue cutting with different laser pulse durations. In order to compare the precision of the tissue effects with picosecond and nanosecond pulses, cuts were made in Descemet's membrane using a series of pulses from the Continuum YG laser. The pulses were applied at a repetition rate of 10 Hz as the corneal preparation was moved laterally with the translation stage (Fig. 7.1a). The effects of 30 ps, 50 µJ and 6 ns, 1 mJ pulses were compared [Vog94b].

Laser focus in tissue. The irradiation geometry of Fig. 7.1d was used to study the morphology and damage range of intrastromal laser effects. Intact bulbi were mounted with a holder onto the translation stage and initially positioned so that the optical axis was coaxial with the laser beam axis and the laser focus was in the plane of the corneal endothelium. Then the eye was slowly moved laterally while 30 ps, 80 µJ pulses from the Continuum YG laser were applied at a repetition rate of 10 Hz (Fig. 7.1d). Because of the curvature of the cornea, this led to effects with a continuously increasing distance from the posterior surface of the cornea. The range for damage to the endothelium was then determined by evaluating a series of histological sections [Vog94d]. The histological study was supplemented with a photographic analysis of the intrastromal cavitation dynamics (cf. 7.1.3).

The possible volume of intrastromal tissue vaporization was analyzed by applying a series of 45 ps pulses from the ISL 2001 laser in a rectangular pattern to the anterior stroma [Vog97c]. The pulses were applied either to a single layer or to several layers lying above one another, beginning with the posteriormost layer. The dependence of tissue vaporization on the laser parameters was established by varying the pulse energy, the lateral pulse separation, and the number and separation of the layers. The thickness of the resulting bubble layer served as a scale for the amount of vaporized tissue. It was documented photographically immediately after application of the pulse in each case. A histological documentation of the thickness of the bubble layer is not possible, since most of the gas diffuses out of the tissue during the fixation process before the fixative has reached the bubble layer and "frozen" the bubble size. In order to be able to photograph the bubble layer from the side, the experiments had to be done with corneal specimens instead of intact eyes. The specimens were irradiated in a cell filled with physiological saline solution. In order to guarantee that the laser focus would be of good quality and to obtain a large focal angle (similar to that with the ISL 4001 system, which is specially constructed for intrastromal refractive surgery), the laser beam was sent through an ophthalmic contact lens built into the wall of the cell.

7.1.2 Microscopic and histological studies

All corneal specimens were fixed in a buffered solution of 4% glutaraldehyde after exposure to the laser, and the lesion size and morphology were studied microscopically in various ways. The size of every lesion was determined with a Zeiss interference contrast microscope (Nomarski type). In this way, the large number of lesions, almost 300, could be evaluated with much less effort than required for histological investigations.

Selected specimens were prepared for electron scanning microscopy by post-fixation in a 2% buffered osmium tetroxide solution, dehydration in ethanol, critical point drying in CO_2, and gold sputtering. The surface morphology of the lesions was studied with a JEOL JSM 35 microscope. Then some of these lesions were again transferred in 100% ethanol and then in propylene oxide and, finally, embedded in Epon 812. Semi-thin sections (1.5 μm) were stained with Tuloidine blue and studied with an optical microscope. Ultra-thin sections (60 nm) were contrasted with uranyl acetate and lead citrate and inspected with a Zeiss EM 9 S-2 transmission electron microscope. It was very difficult to produce good thin sections and, especially, ultra-thin sections, since the gold layer on the surface required for scanning electron microscopy hindered the penetration of the Epon into the tissue. Nevertheless, with this procedure, it was possible for the first time to study both the surface morphology and histological sections of the same corneal lesions [Vog90].

Intact bulbi were used for the histological documentation of intrastromal laser effects and to determine the damage range for damage to the endothelium. Some bulbi were fixed in 4% glutaraldehyde and some in 4% neutral formalin. The whole eye was first prefixed for 2 h and then fixative was injected from the limbus into the anterior chamber. Then the piece of cornea containing the lesion was excised and further fixed overnight at 4 °C. The specimens fixed in glutaraldehyde were post-fixed with osmium tetroxide, dehydrated, and embedded in Epon. Specimens containing laser effects with increasing distance from the corneal endothelium were cut into series of semi-thin sections which were then stained with Tuloidine blue and examined by light microscopy. The specimens fixed in formalin were embedded in paraffin after dehydration; 6 µm thin sections were stained with sirius red [Asi96] and examined with a polarization microscope.

Polarization microscopy is well suited for the analysis of thermal effects in the cornea, since thermal denaturation of corneal tissue leads to changes in the corneal collagen resulting in a reduction or loss of birefringence [Tho89]. Sirius red staining enhances the contrast in the microscopic picture, because Sirius red is an elongated birefringent molecule, which, when bound to a collagen molecule, is oriented parallel to the latter, so that the collagen birefringence is enhanced [Puc73].

7.1.3 Photographic studies

The dynamics of cavitation bubbles inside corneal tissue and the thickness of the bubble layer after the application of a series of pulses were documented in side view using the setup shown in Fig. 7.2 [Vog94b,d]. Top-view photographs of the intrastromal bubble layer were taken with a second camera mounted above a beam splitter on the slit lamp microscope [Vog97c]. The light source was a spark lamp (High Speed Photosysteme, Nanolite K-L) that emits flashes lasting less than 20 ns. The photographs were taken with 7 times magnification (Leitz Photar 3.5/40 mm). The side view pictures show a cross section of the cornea and, thereby, the position of the laser effects relative to the epithelium and endothelium. The bubble dynamics in physiological saline solution was also documented for comparison.

7.2 Results and discussion

7.2.1 Laser focus at the tissue surface

If the laser pulse is focussed directly onto the Descemet's membrane or in the underlying corneal stroma (Figs. 7.3 and 7.4), tissue vaporization owing to the laser plasma is the most important factor in the development of lesions. Acoustic transients and cavitation are secondary mechanisms that enhance the effects already created by the plasma. Figures 7.3a and b present a top view of a lesion created by a 5 mJ, 12 ns laser pulse, and figure 7.3 shows the same lesion in side view. The radius of the lesion is 0.5 mm, i.e., about 1/3 of the maximum cavitation bubble radius. In the center of the lesion there is a deep hole in the Descemet's membrane and in the stroma, around which the Descemet's membrane has been ruptured. Both effects are attributable to the vaporization and disintegration of tissue by the plasma and to the explosive expansion of the plasma an the bubble. In the neighborhood of the crater there is a zone in which the endothelial cell layer is missing and beyond it lies a more extensive region in which the cells are still present but have been damaged. These effects were caused by the acoustic transients and

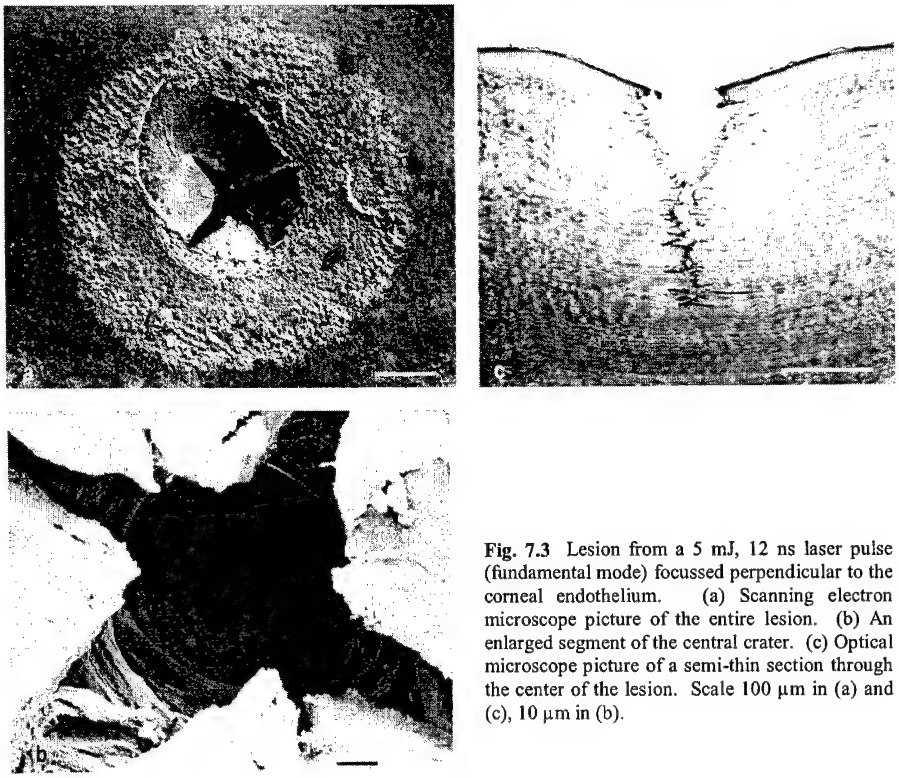

Fig. 7.3 Lesion from a 5 mJ, 12 ns laser pulse (fundamental mode) focussed perpendicular to the corneal endothelium. (a) Scanning electron microscope picture of the entire lesion. (b) An enlarged segment of the central crater. (c) Optical microscope picture of a semi-thin section through the center of the lesion. Scale 100 μm in (a) and (c), 10 μm in (b).

cavitation bubble dynamics. The morphology of the lesion indicates that the shear forces exerted on the corneal surface by the cavitation bubble flow could play an important role in the tissue changes (cf. Chapter 5).

The hole in the stroma has a diameter of about 70 µm and roughly the same depth (Fig. 7.3c). These dimensions are considerably greater than those of the laser focus, but they correspond quite well to the size of the region in which the plasma radiation was observed. (For nanosecond pulses the plasma size near the optical breakdown threshold is substantially greater than the focal volume; cf. Section 2.3.2.3.) The holes under the main crater are presumably caused by multiple optical breakdowns inside the stroma, which might be caused by hot spots due to aberrations in the beam path and by a non-gaussian laser beam profile (cf. Section 2.3.6). The overall length of the bubble filament in the histologic tissue sections is about 200 µm, in good agreement with the length of the plasma that was observed in distilled water for a 5 mJ laser energy (Fig. 2.11).

The morphology of the lesions is highly dependent on whether the plasma was produced at the corneal surface or deep within the stroma. When the plasma was created close to the surface (Fig. 7.3c), the volume of the tissue defect coincided well with the volume within which a plasma was observed upon focussing a pulse with the same energy into saline solution or water. When the plasma was created deep inside the stroma (Fig. 7.4a), a considerably larger hole with a diameter of 230 µm was produced by the expansion of the plasma and cavitation bubble. In this case, a large fraction of the laser energy contributes to the mechanical deformation of the surrounding tissue. The micro-explosion causes a horizontal folding and vertical displacement of the collagen lamellae. When the plasma is created right at the corneal surface (Fig. 7.4b), it can expand unhindered into the surrounding fluid and produces only a small hole in

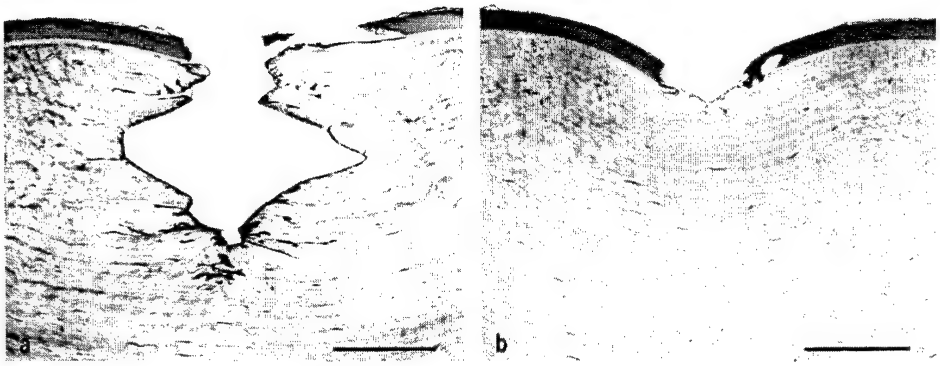

Fig. 7.4 Comparison of laser effects with focussing at different depths. (a) Focussing into the corneal stroma (8.2 mJ, 12 ns, multimode); (b) focussing on Descemet's membrane (9.3 mJ, 12 ns, multimode). The scale is 100 µm.

the tissue. The hole is only slightly greater than the diameter of the laser focus, which was about 50 µm (multimode laser operation). One can see, however, that the corneal surface has been indented as a result of the expansion of the cavitation bubble. Such mechanical tissue deformations are unavoidable during plasma aided laser surgery in a liquid environment. They hardly occur during plasma ablation in air, since the plasma experiences no inertial confinement there. Therefore, in air finer incisions can be made for the same laser parameters and more precise ablation can be achieved [Lud94].

The extent of thermal laser effects can be inferred by inspection of the crater walls of the lesions (Fig. 7.5). Figure 7.5 a shows the wall of the intrastromal lesion from Fig. 7.4a. It is very smooth and no individual collagen fibrils can be identified. The evenness of the crater surface is probably a consequence of the combined action of the high temperature and the high pressure as the plasma expands. At a fissure in the crater wall (presumably an artifact of the preparation) one can see, however, that the changes in the appearance of the collagen fibrils are limited to a superficial layer less than 1 µm thick. This observation

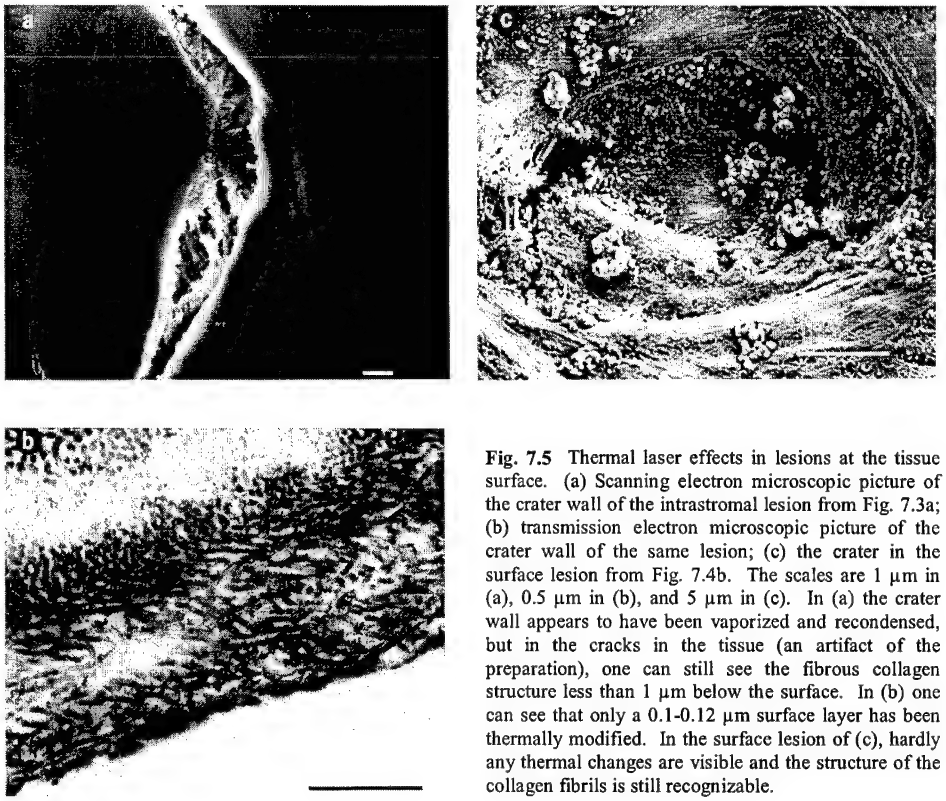

Fig. 7.5 Thermal laser effects in lesions at the tissue surface. (a) Scanning electron microscopic picture of the crater wall of the intrastromal lesion from Fig. 7.3a; (b) transmission electron microscopic picture of the crater wall of the same lesion; (c) the crater in the surface lesion from Fig. 7.4b. The scales are 1 µm in (a), 0.5 µm in (b), and 5 µm in (c). In (a) the crater wall appears to have been vaporized and recondensed, but in the cracks in the tissue (an artifact of the preparation), one can still see the fibrous collagen structure less than 1 µm below the surface. In (b) one can see that only a 0.1-0.12 µm surface layer has been thermally modified. In the surface lesion of (c), hardly any thermal changes are visible and the structure of the collagen fibrils is still recognizable.

was confirmed by the transmission electron microscopic picture of the same crater wall in Fig. 7.5b. Certainly, the regular order of the collagen fibers is disturbed near the wall, probably because of the mechanical forces acting during the plasma expansion, but the periodicity of the collagen fibers is visible here and there even very close to the crater surface. This observation indicates that the fibers are not thermally denatured [Zyp79, Asi96]. The thickness of the dark, thermally modified boundary layer is only about 0.1-0.2 µm. If the laser effects are produced at the tissue surface, as in Fig. 7.4b, the thermal modifications at the crater wall are even weaker (Fig. 7.5c).

The thinness of the thermally modified layer is a consequence of the strong intensity dependence of the optical absorption during optical breakdown that gives rise to a very sharp plasma boundary and thus to an equally sharp border of the region where energy is deposited (cf. Chapter 2). Despite the steep temperature gradient at the plasma boundary, only a small amount of heat diffuses into the surrounding tissue, since the time available for thermal conduction is very short. This is because of the short laser pulse duration and the very rapid adiabatic cooling of the vaporized material during bubble expansion. The temperature inside the bubble drops to a value on the order of room temperature within a few microseconds [Fuj80]. In intrastromal laser effects (Fig. 7.5a), the thermal modifications are somewhat stronger than in superficial lesions (Fig. 7.5c), because bubble expansion and adiabatic cooling are hindered by the surrounding tissue.

7.2.2 Laser focus in fluid near tissue

If the laser is focussed parallel to the cornea at some distance from the corneal surface, a direct interaction between the plasma and tissue is excluded, and the only potential damage mechanisms are the cavitation bubble dynamics and acoustic transients. The possible damage owing to the bubble dynamics depends on the dimensionless distance $\gamma = s / R_{max}$ between the bubble and the boundary (cf. 5.1.2). Figure 7.6 shows two lesions produced for $\gamma = 0.45$ (Fig. 7.6a) and $\gamma = 0.7$. In both cases, a central rupture can be seen in Descemet's membrane which is most likely attributable to the impact of the jet formed during collapse of the cavitation bubble in the neighborhood of the corneal surface. The bubble dynamics for a γ - value similar to that in Fig. 7.6a is illustrated in the series of high-speed photographs in Fig. 5.3d. The picture series indicates that the diameter of the jet is 1/60 of the maximum bubble diameter. Since R_{max} was 1.6 mm in Fig. 7.6a, this corresponds to a jet diameter of 20-30 µm. This is about the same size as the diameter of the hole in the Descemet's membrane. It would be hard for the shock wave generated by optical breakdown to produce such a small, sharply defined hole at a distance of 300 µm from its emission center.

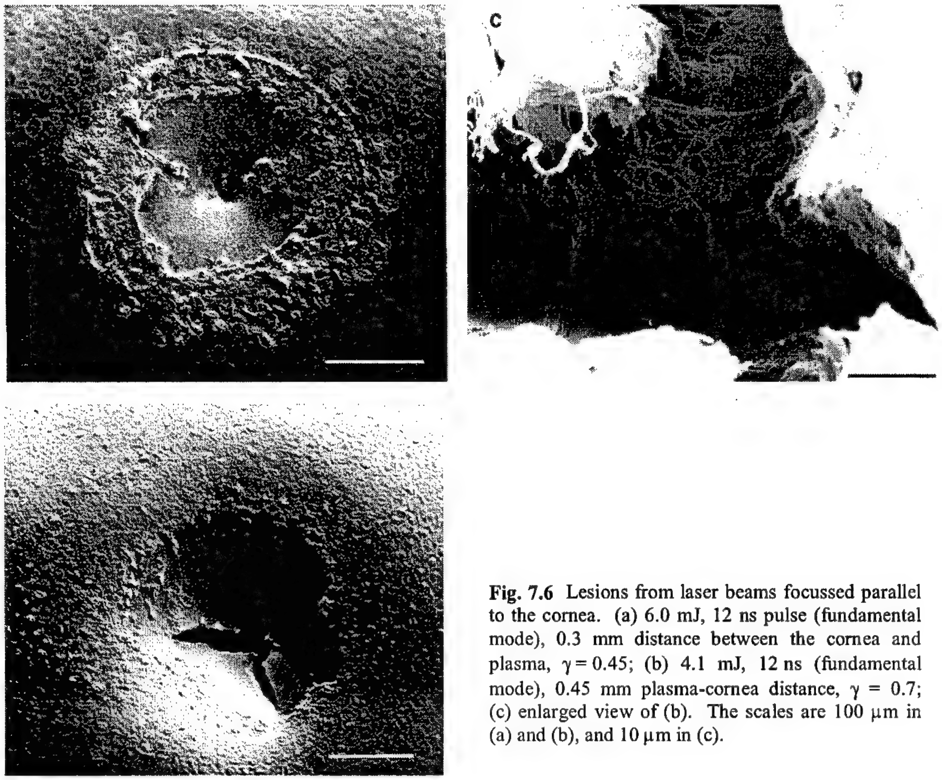

Fig. 7.6 Lesions from laser beams focussed parallel to the cornea. (a) 6.0 mJ, 12 ns pulse (fundamental mode), 0.3 mm distance between the cornea and plasma, $\gamma = 0.45$; (b) 4.1 mJ, 12 ns (fundamental mode), 0.45 mm plasma-cornea distance, $\gamma = 0.7$; (c) enlarged view of (b). The scales are 100 μm in (a) and (b), and 10 μm in (c).

The bubble dynamics for $\gamma \approx 0.7$ (as in Fig. 7.6b) is illustrated in Fig. 5.3c. Here the diameter of the jet is relatively larger, about $R_{max}/10$. The impact of the jet ruptured Descemet's membrane in the neighborhood of the impact point. The shape of the rupture bears a superficial resemblance to that produced by focussing a pulse directly onto the cornea (Fig. 7.3a). At a higher magnification (Fig. 7.6c), however, it becomes obvious that no hole was made in the stroma and one can infer from Fig. 7.6b that, while the Descemet's membrane is torn, no part of the membrane is missing.

For $\gamma > 0.8$ rupture of Descemet's membrane was not observed after single laser pulses. At this bubble-boundary distance, the jet does not strike the corneal surface directly, but a ring vortex, whose toroidal core is the collapsing cavitation bubble, develops because of the jet flow (Section 5.1.2). The ring vortex flow obviously has less damage potential than direct jet impact, but it is still strong enough to cause damage to the sensitive corneal ephithelium. Annular damage patterns, such as those observed on metals by Philipp, et al. (1997) and attributed to the high internal pressure of the toroidal collapsing cavitation bubbles, were not found on the corneal surface.

The denudation of Descemet's membrane near the center of the lesion and the wall of cell debris seen in Fig. 7.6a were probably caused by the radial outward flow on the corneal surface that originates from the impact point of the jet. The damage in the outer part of the lesion, where endothelial cells are still present, may arise from shear forces acting through the radial flow on the endothelial cells.

The effects of the jet flow become even more obvious after multiple laser exposures (Fig. 7.7). Debris from the corneal stroma was swept onto the Descemet's membrane, after the membrane had been ruptured by the first laser pulses (Figs. 7.7a, b). The vertical section through the lesion in Fig. 7.7d shows that the jet flow also caused removal of the Descemet's membrane from the underlying stroma. This sort of removal was never observed after single laser exposures. The enlarged view of the lesion center in Fig. 7.7c reveals that the ground substance normally filling the spaces between the collagen fibrils was washed away and that the regular ordering of the fibrils was destroyed. A further effect of the jet flow is the almost complete removal of endothelial cells up to the edge of the lesion.

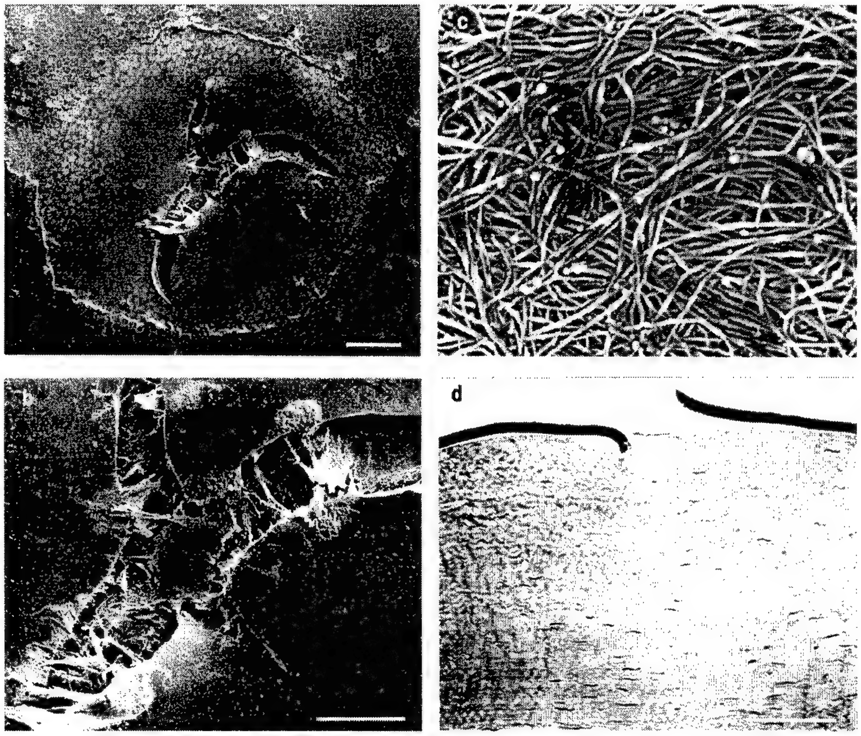

Fig. 7.7 (a) Corneal lesion from 30 successive 4.5 mJ pulses focussed parallel to the cornea at a distance of 0.7 mm from the endothelium ($\gamma = 0.9$). (b) and (c) The central part of the lesion at higher magnifications. (d) A histologic section through the center of the lesion. The scale is 100 μm in (a) and (d), 50 μm in (b) and 1 μm in (c).

7.2.3 Effects of shock-induced gas bubble collapse

Figure 7.8 shows lesions produced by the interaction of optical breakdown with neighboring gas bubbles on the corneal epithelium. In Fig. 7.8a the gas bubble had a diameter of 150 μm and was left by a 4 mJ laser pulse. It was then struck by the shock wave and the radial flow from a 4 mJ pulse focussed at a distance of 2 mm from the gas bubble. In the center of the lesion, the endothelial cells are missing entirely, and in the edge region of the lesion are pieces of cells which have been lifted up from the Descemet's membrane. The diameter of the cell free lesion center is about 1/4 of the gas bubble diameter. The morphological features of the lesion indicate that it has been produced by the impact of the jet formed during shock-induced collapse of the gas bubble (cf. Section 6.3.2). In terms of size and shape, the lesion resembles the endothelial lesions often observed after clinical Nd:YAG laser treatments [Gab85, Ker85, She85].

The diameter of the lesion scales with the size of the gas bubble. Figure 7.8b illustrates the substantially larger endothelial injury produced by collapse of a bubble with a diameter of 700 μm. In this case, the lesion had a size of about 1/7 of the bubble diameter.

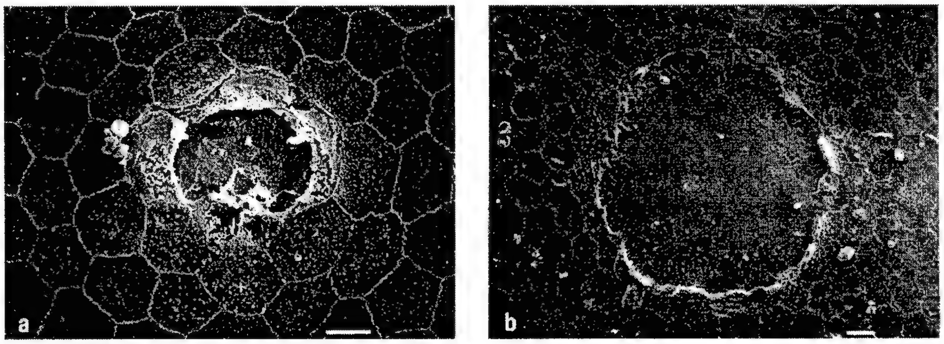

Fig. 7.8 Lesions on the corneal epithelium produced by shock-induced collapse of gas bubbles. (a) Gas bubble diameter 150 μm, laser focus-cornea distance 2.0 mm, 4 mJ, 12 ns laser pulse (fundamental mode); (b) Gas bubble diameter 700 μm, laser focus-cornea distance 3.5 mm, 4 mJ, 12 ns laser pulse (fundamental mode). Scale 10 μm.

7.2.4 Damage range for optical breakdown

The dependence of the damage range for single laser pulses on the absorbed laser energy is plotted in Fig. 7.9 for a parallel irradiation geometry and for direct focussing of the laser on the corneal endothelium. The data for parallel irradiation can be approximated in a log-log plot by a line with a slope of 1/3. The damage range has the same energy dependence as for the cavitation bubble radius, which is

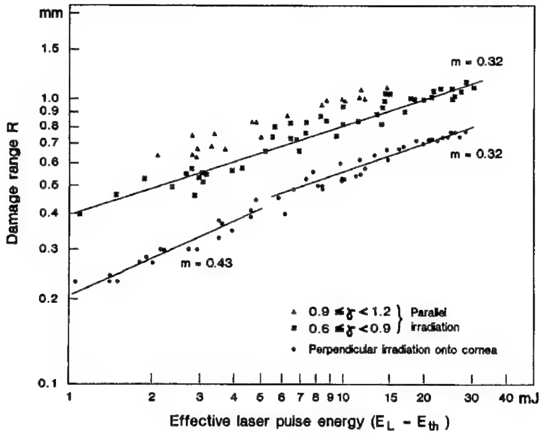

Fig. 7.9 Damage range R as a function of the absorbed laser energy E_{abs} for focussing parallel to the cornea (triangles and crosses) and perpendicular to the cornea (dots). The slope of the line fitted to the data points is 0.32, except for exposure perpendicular to the cornea at pulse energies below 6 mJ, where it is 0.43.

also proportional to $E_{abs}^{1/3}$ [Vog90]. The damage range rose slightly with increasing dimensionless distance γ between the cavitation bubble and cornea. For $\gamma > 1.2$, however, no damage could be observed on the corneal endothelium, since by that distance the jet and annular vortex flows were so buffered by the fluid layer between the bubble and the cornea that they could no longer produce any tissue effect. The maximum damage range for parallel irradiation is, therefore, about 1.2 times the corresponding bubble radius R_{max} for all laser pulse energies. When the laser is focussed directly onto the cornea at high energies (multimode pulses), the same energy dependence holds as for parallel irradiation; at lower energies (fundamental mode), the slope is 0.43.

The values of the damage range observed for single nanosecond pulses with energies of 1-2 mJ are in good agreement with the data of Zysset, et al. (1989a) for 40 ps pulses with the same energy. The energy dependencies of the damage range are also in agreement. They were studied by Zysset, et al. for energies between 10 μJ and 2 mJ.

When multiple laser pulses are used, the radius of the lesion increases slowly until the lesion size has doubled compared to that for a single exposure. After about 20 exposures, saturation occurs [Vog90]. The damage range was significantly extended when the laser-generated shock waves were able to interact with small air bubbles attached to the endothelium. Figure 7.10 shows plots of the radii of the lesions produced by a 4 mJ, 12 ns pulse focused at different distances from the corneal endothelium. For an air bubble diameter of 0.7 mm, endothelial lesions were produced out to distances of 3.5 mm between the focus and the cornea. When the experiment was performed with air bubbles of 0.15 mm diameter which

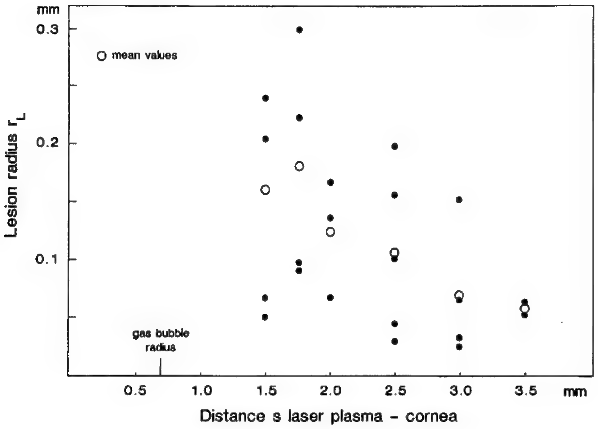

Fig. 7.10 Radius r_L of corneal lesions produced by the interaction of shock waves with a gas bubble at the corneal endothelium. The shock wave was generated by a 4 mJ (fundamental mode) laser pulse focussed at different distances s from the cornea under the bubble. The diameter of the gas bubble was 0.7 mm. The average values of r_L for each distance s are marked with open circles

remain after 4 mJ laser pulses, endothelial lesions occurred when a second 4 mJ pulse was focussed at a distance of up to 2 mm from the cornea (Fig. 7.8a). This distance is substantially greater than the damage range of 0.88 mm from a single 4 mJ pulse (cf. Fig. 7.9).

7.2.5 Comparison of the effects of the different damage mechanisms

The histological studies showed that the plasma-induced tissue vaporization is the main surgical mechanism during photodisruption and that the mechanical effects of the shock and cavitation bubble only have a subsidiary effect. The morphological data imply, on the other hand, that the collateral effects of intraocular microsurgery are mainly caused by the cavitation bubble dynamics, in particular by jet formation. Morphological damage by acoustic transients is undetectable at the level of the light microscopic studies conducted here. The damage range of the acoustic transients for functional cell damage is shorter than the maximum radius of the cavitation bubble (cf. 3.4.3).

Further evidence of the leading role of cavitation bubble dynamics for tissue damage is provided by the fact that the damage range of single laser pulses focussed parallel to the cornea has the same energy dependence as the bubble radius: both are proportional to the cube root of the pulse energy. If the damage range were governed by the pressure amplitude of the acoustic transients, it would scale proportional to the square root of the pulse energy [Vog86, Vog88a, Noa98a]. Interestingly, the damage range for laser exposure directly on the cornea is, at low pulse energies, proportional to $(E_{abs})^{0.43}$, i.e., here the exponent is closer to the value expected for damage by acoustic transients. The reason may be that with these laser parameters deep craters are often created in the stroma (Figs. 7.3c and 7.4a). The crater formation hinders the lateral expansion of cavitation bubbles, but not the propagation of acoustic transients.

The physical parameters in terms of which the damage potential of the shock wave, cavitation bubble expansion, and jet formation can be assessed are the pressure exerted at any given time and the corresponding particle velocity. Table 7.2 lists the distance from the plasma at which similar pressures and particle velocities are encountered and the time intervals over which they operate for a 1 mJ, 6 ns pulse from the Continuum laser. Some of the entries in this table are measurement data from Chapters 3 and 5 and some are calculations from the Gilmore model (cf 3.1). The pressure values given for the bubble expansion do not refer to the fluid pressure at the bubble wall, but to the pressure exerted by the bubble-induced radial flow on a fixed structure in the vicinity of the bubble. They were calculated using Eq. (5.5). The interaction time of the bubble flow with the fixed structure was taken to be the time interval after breakdown necessary for the bubble to expand out to this structure.

The data in Table 7.2 support the results obtained from the morphological studies. They show that the jet can exert a high pressure and a high particle velocity at substantially larger distances from the plasma than the shock wave and the bubble expansion. The remote effects occur because the jet concentrates the bubble energy at some distance from the application site (5.1.2). The jet impact affects the tissue for a short time similar to the shock wave duration, but the effect of the jet continues after the impact through a relatively long lasting flow with lower dynamic pressure. The jet can thus cause coarse tissue effects, including the removal of entire cells, while the shock wave effects are limited to a subcellular level (3.4.3). Shock waves can cause morphological changes at a large distance from the application site only through an interaction with gas bubbles, i.e., mediated by jet formation. Jet formation during gas bubble collapse concentrates the energy of the shock wave and its afterflow onto a small area of about 1/80 times the cross section of the gas bubble (6.3.2).

Physical process	Particle velocity (m/s)	Pressure (Mpa)	Distance from plasma (μm)	Interaction time (ns)
Shock wave	100 45	170 75	160 360	60 60
Bubble expansion	100 45	≈ 5 ≈ 1	180 220	≈ 800 ≈ 2000
Jet impact	100	75	800	10-40
Jet flow	≤ 100	≤ 5	800	> 1000

Table 7.2 Estimates of the distance from the laser plasma at which the shock wave, cavitation bubble expansion, and jet following a 1 mJ, 6 ns pulse yield similar values for the pressure or particle velocity. Also listed are the approximate times during which each process acts on the tissue.

When the laser is focused in the fluid near a tissue surface, the radius of action for the flow induced by cavitation bubble expansion is smaller than the damage range of the jet, because the expansion velocity of the bubble falls rapidly for geometrical reasons. The jet flow, in contrast, concentrates energy at a distance from the laser focus. The creation of tissue effects during optical breakdown within a homogeneous tissue, however, is dominated by the bubble expansion (see below, Section 7.2.7).

The studies reported here are limited to morphological tissue damage, while functional tissue and cell changes have not been analyzed. If shocks rupture cellular membranes, damage cell organelles, and break bonds (3.4.3), these injuries on a subcellular level may lead to serious delayed cell damage owing to biological reinforcement effects. It is, therefore, conceivable that the damage range of the shock waves for functional cell damage is greater than observed with the techniques used here. This point is important, since acoustic transients cross the entire eye, while the effect of a cavitation bubble is limited to a region that does not significantly exceed the maximum bubble radius. However, the thresholds for functional cell damage by laser-induced shock waves reported by other authors [Dou93, Lee96, Dou96] are so high that they are surpassed only in the immediate neighborhood of the plasma, in a region which is considerably smaller than the maximum cavitation bubble radius.

7.2.6 Incision of tissue with different laser pulse durations

Figure 7.11 shows a comparison of the precision of incisions in tissue with nanosecond and picosecond laser pulses. When 30 ps, 50 µJ pulses were used, a clean 30-40 µm wide incision could be produced in Descemet's membrane (Fig. 7.11a, c). The width of the incision is only slightly greater than the plasma diameter. In the neighborhood of the incision the endothelial cells are damaged out to a distance of about 130 µm. Nanosecond pulses with an energy of 1 mJ, on the other hand, ruptured the membrane along the incision and the damage range is about 400 µm (Fig. 7.11b, d).

The ratio of the width of the damage zones for ns- and ps-pulses is about 3, while the ratio of the respective pulse energies is 20. This ratio corresponds to the fact, found in 7.2.4, that the damage range is proportional to the cube root of the laser pulse energy. The damage range is, for both pulse durations, about half as large as the radius of the fully expanded cavitation bubble. Bubble expansion is probably responsible for shearing off of endothelial cells, for denting the stromal lamellae under the incision, and for the rupturing of Descemet's membrane encountered with ns pulses.

The tissue effects with ps pulses are finer than with ns pulses, owing both to the low pulse energy and to the low efficiency with which light energy is converted into mechanical energy (Chapter 4). Figure 7.12 shows that it is possible to produce tissue effects with picosecond pulses in the neighborhood of the breakdown threshold which almost exclusively affect the endothelium cells and have a radius of action of only 50 µm.

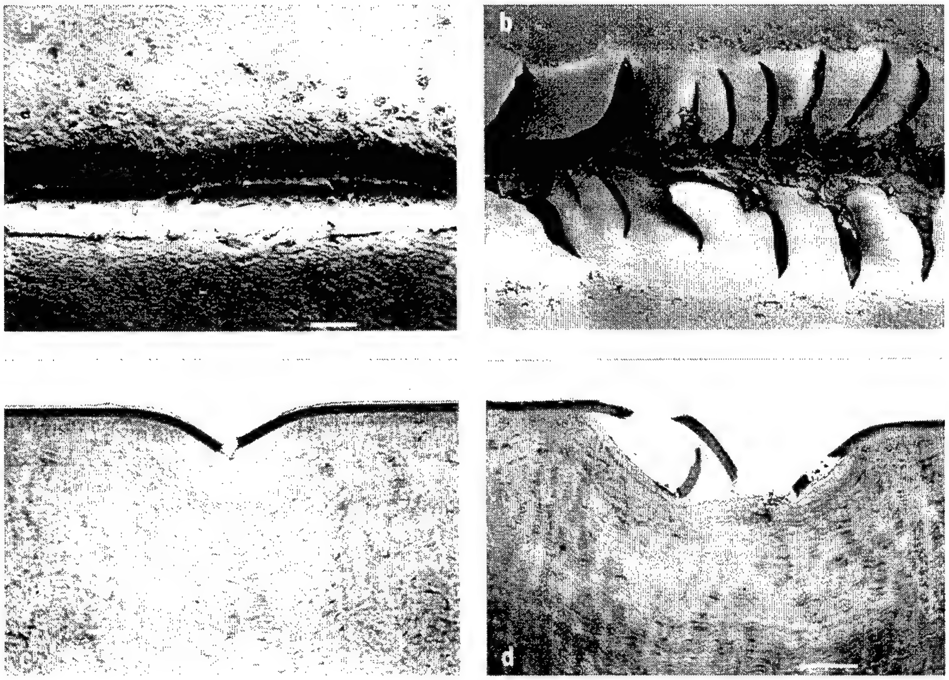

Fig. 7.11 Incisions through Descemet's membrane with pulses of different lengths from the Continuum YG laser. The incision in (a) was produced with 50 μJ, 30 ps pulses and the incision in (b) by 1 mJ, 6 ns pulses. In both cases, about 100 pulses were applied at a repetition rate of 10 Hz. (c, d) Semi-thin histologic sections through the lesions of (a) and (b). The scale is 100 μm.

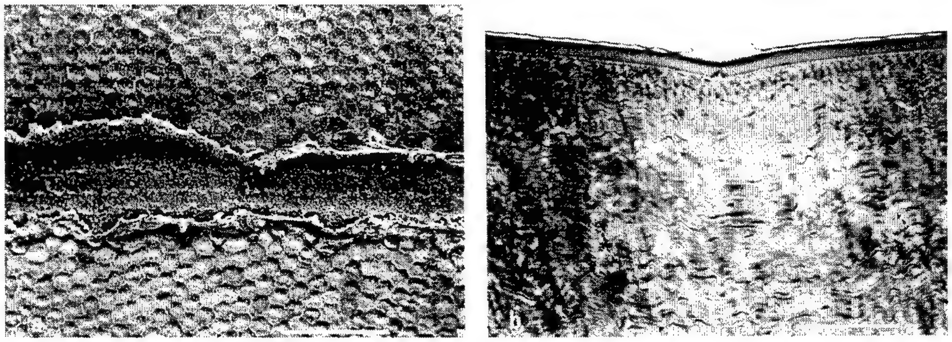

Fig. 7.12 A fine incision in the corneal endothelium produced by a 35 μJ, 30 ps pulse. (a) Scanning electron microscope picture, (b) semi-thin histologic section through the same lesion. The scale is 100 μm.

7.2.7 Laser focus in tissue

7.2.7.1 Acoustic emission and bubble dynamics

When the laser pulses are focussed into corneal tissue, both the acoustic emission (Fig. 7.13) and the cavitation bubble dynamics (Fig. 7.14) change relative to the dynamics in water. The amplitude of the shock wave generated by the plasma expansion is just as high in the cornea as in water; however, the rest of the acoustic signal is sharply different. In corneal tissue a rarefaction pulse follows the shock wave and the pressure peak from the bubble collapse is absent. Both phenomena can be explained by the changes in the bubble dynamics. The expansion of the bubble is strongly damped by the tissue and terminates after 3 µs [Vog94, Vog99a]. The maximum bubble size is, therefore, much smaller than in water and the bubble undergoes no oscillations. The bubble exists for about 30 minutes, and vanishes only through diffusion of its contents into the surrounding tissue. Since the bubble does not collapse, there is also no pressure pulse corresponding to a collapse.

The shock wave produced by breakdown in water is followed by a long underpressure phase, which lasts until the pressure pulse from the bubble collapse (cf. 3.1.1 and [Kna71]). Since the amplitude of the underpressure (≤0.1 MPa at the bubble wall) is much lower than the shock wave amplitude, the underpressure phase cannot be seen in Fig. 7.13. The reduced expansion time of the bubble in corneal tissue implies that the breakdown pulse is followed by a tensile stress wave instead of just an underpressure phase. The impulses $\int p\,\mathrm{d}t$ of the pressure and underpressure phases must always be equal but with opposite signs because of the conservation of momentum. With a reduced bubble oscillation time, this condition can only be fulfilled if the pressure wave is followed by a tensile stress wave. Hence, the acoustic signal acquires a bipolar character (Fig. 7.13). The amplitude of the tensile stress is about 1/3 that of the preceding compression wave. It probably has a greater damage potential that the compression wave, since tissue is much more sensitive to tension than to pressure [Cum93, Par79].

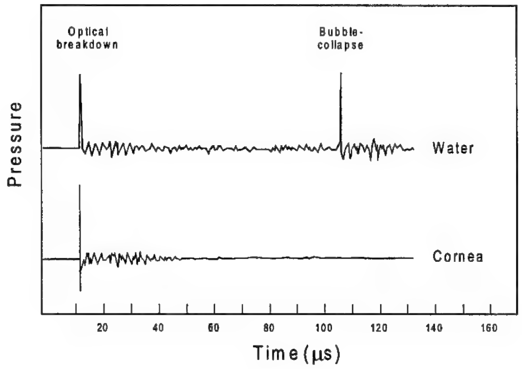

Fig. 7.13 A comparison of the acoustic signals produced by focussing 300 µJ, 30 ps laser pulses in water and in cornea.

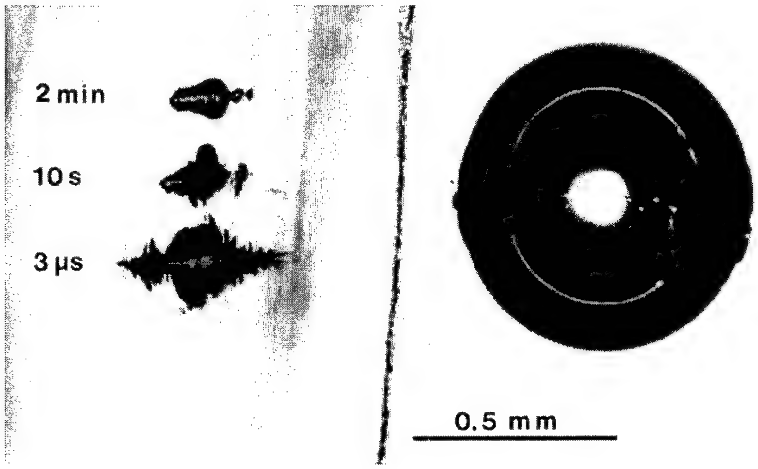

Fig. 7.14 Comparison of the cavitation bubble dynamics in corneal stroma (left) and water (right) following 300 µJ, 30 ps laser pulses. The laser light is incident from the right. The bubble in water was photographed 40 µs after the laser pulse, when it had expanded out to its maximum size.

The damping of the bubble oscillations in cornea implies that, unlike in water, the acoustic signal cannot be heard after optical breakdown. The shock waves from the optical breakdown and from the bubble collapse are inaudible because their frequencies lie in the megahertz range and are, therefore, well above the limits for hearing at about 10 kHz. Only the underpressure or tensile stress wave emitted during the bubble oscillations has frequencies in the audible kilohertz range. In water, the rarefaction (underpressure) wave lasts about 100 µs, which corresponds to frequencies in the audible range of the acoustic spectrum. The tensile stress wave in corneal tissue, on the other hand, has a duration of less than 1 µs, so the lower, audible frequencies are lost.

7.2.7.2 Morphology and damage range

Although the bubble expansion comes to a halt already within 3 µs, the bubble in corneal tissue is substantially larger than the volume of the laser plasma (Fig. 7.14). Even 2 min after optical breakdown, the volume of the bubble is still about 10 times that of the plasma. The irregular lobed shape of the bubble immediately following breakdown suggests a separation of the corneal lamellae owing to the high pressure inside the expanding bubble. The surface of the bubble becomes smooth within a few seconds to minutes following laser exposure. Lobed bubble shapes are not seen in histological sections (Fig. 7.15), since fixation of the tissue requires a longer time.

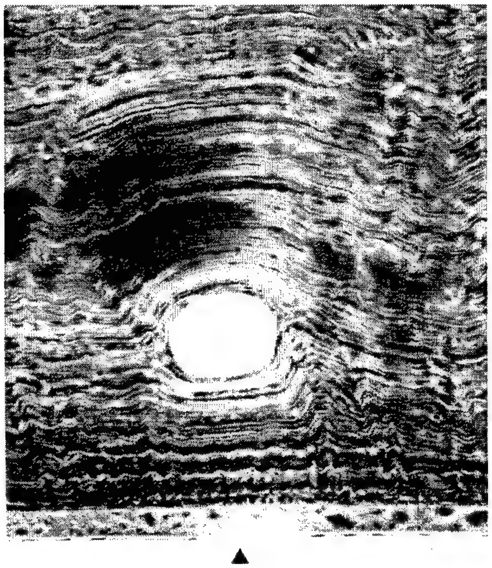

Fig. 7.15 Histological section through an intrastromal bubble produced by an 80 μJ, 30 ps pulse. The collagen lamellae in the neighborhood of the bubble are deformed. The arrow points to endothelial damage. The distance between the laser focus and the endothelium was 130 μm.

Figure 7.15 shows a histological cross section through an intrastromal bubble with a diameter of 60 μm produced by an 80 μJ, 30 ps pulse. The distance between the laser focus and the corneal endothelium was 130 μm. The collagen lamellae in the neighborhood of the bubble are highly deformed and obviously displaced laterally during expansion of the bubble (cf. Fig. 7.4a, as well). The endothelium under the region affected by the laser is damaged and one can see that some cells are missing. For a pulse energy of 80 μJ, endothelial damage sets in when the distance between the laser focus and the endothelium is less than 150 μm. When the laser pulse was focussed in the anterior corneal section or in the middle of the cornea, the endothelium remained intact. The damage to the endothelium was probably caused by stretching of the endothelium during expansion of the bubble. It may also be due to a direct interaction with the laser light (see the long plasma spike in Fig. 7.14 at t = 3 μs) or the partial reflection of the shock wave at the cornea-aqueous humor interface, which would produce a tensile stress wave, since the acoustic impedance of the cornea is greater than that of the aqueous humor.

The laser effects produced when laser beams are focussed into tissue differ substantially from those which occur when the focus is at a thin membrane or at a tissue surface. If breakdown occurs at a tissue surface, tissue is vaporized through the plasma formation, but the cavitation bubble expansion mostly pushes the surrounding fluid away and induces only moderate additional tissue effects. Inside a tissue, on the other hand, the effect of the bubble dynamics predominates and a large cavity is produced which is much more extensive than the volume of vaporized tissue.

As a consequence of the resistance of the tissue against the bubble expansion, the bubble does not grow to the same size as it would in a free liquid or at a tissue surface. Thus, the adiabatic cooling during bubble expansion is not as strong, and this might lead to a thicker thermal damage zone at the edge of the region affected by the laser. The polarization microscopic picture in Fig. 7.16 shows, however, that the thermal damage zone is, still, at most only 2.5 μm thick and that only very slight collagen changes have taken place. This assessment is consistent with the electron microscopic picture in Fig. 7.5.

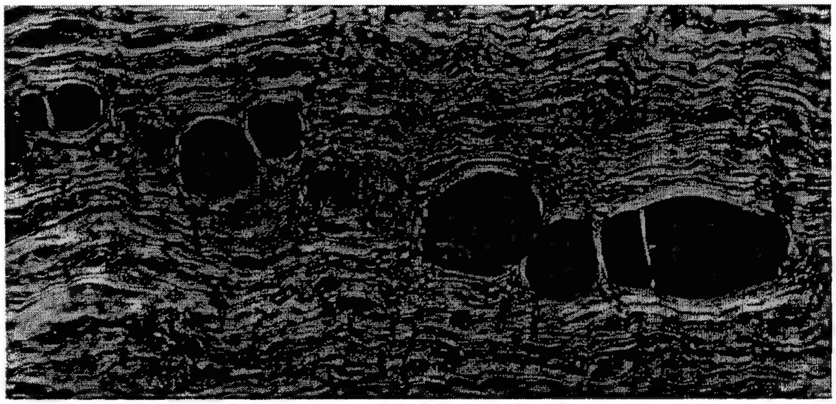

Fig. 7.16 Polarization microscopic picture of a section through an intrastromal corneal lesion produced by a 25 μJ, 45 ps pulse, stained with sirius red. The bright rim of the bubble suggests slight thermal collagen changes, at which more binding sites for the sirius red dye molecules were created, but the fibrous collagen structure is still intact. Tshe birefringence is enhanced, since the dye molecules are aligned parallel to the collagen molecules [Asi96]. The thermally altered zone is, at most, 2.5 μm thick.

7.2.7.3 Vaporization of intrastromal tissue

In order to analyze the possible extent of vaporization of intrastromal tissue for refractive corneal surgery, a series of pulses with a 1000 Hz repetition rate was applied, with the focus being moved laterally from shot to shot. Figure 7.17 shows a top view of the intrastromal bubble layers produced with different lateral displacement of the focus. For small displacements in the range of 5-20 μm, the appearance of the layer is largely independent of the displacement, because plasma formation is affected by the bubbles produced previously. Laser pulses focussed into a bubble cannot produce a plasma and vaporize tissue, because the threshold for optical breakdown in gases is substantially higher than in tissue. (The breakdown threshold for the 45 ps pulses of the ISL 2001 laser is about 20 μJ in cornea and 400 μJ in air). Thus, the laser pulses can contribute to the vaporization of tissue only when the lateral separation of the pulses in the application pattern exceeds the radius of the intrastromal bubbles. The bubble radius

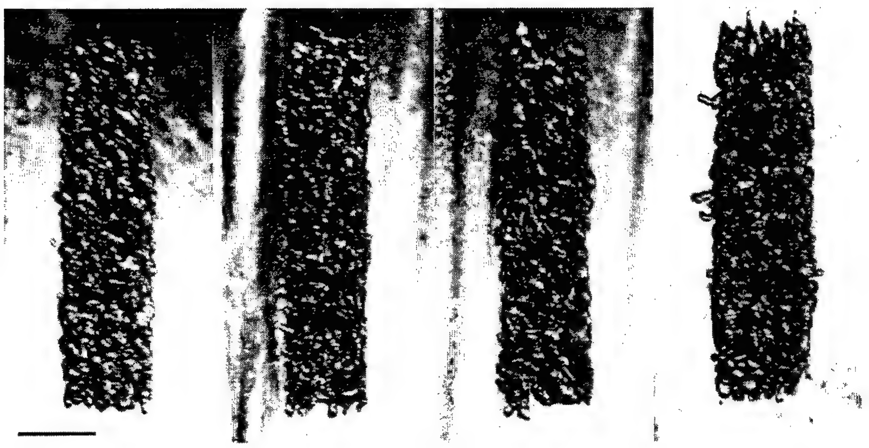

Fig. 7.17 Views of intrastromal bubble layers produced by 25 μJ, 45 ps pulses with 5-20 μm lateral distance between the application sites of subsequent laser pulses. The scale is 250 μm.

for a 25 μJ pulse is, 1 s after the laser pulse, still about 15-20 μm, (not illustrated). After a time interval of only 1 ms corresponding to a 1000 Hz repetition rate, it is even larger [Juh94]. The large bubble radius explains why the laser effects for focal distances of 5, 10, 15, or 20 μm seem to be very similar, since in all cases this distance is smaller than the bubble radius.

With this knowledge, we can estimate how much tissue will be vaporized when a series of picosecond pulses is applied. In order to obtain an upper bound estimate of the amount of vaporized tissue, we assume that every pulse produces a plasma. Photographs of the plasmas show that they are about 30 μm long and have a diameter of 7 μm for 30 μJ pulse energy [Vog97c]. The gaps between the plasmas caused by bubble formation will be taken into account by assuming that the lateral distance between the plasma centers is 15 μm. This assumption implies that only 17.1% of the 30 μm thick layer within which the plasmas will be produced is vaporized. The layer of vaporized tissue is, hence, only 5.1 μm thick.

It might be objected that this calculation underestimates the amount of vaporized tissue, since tissue outside the plasma volume will also be vaporized through heat conduction. Although the appearance of the lesions suggests that heat conduction from the plasma into the surrounding medium plays almost no role (Figs. 7.5 and 7.16), the above result was checked by a second, independent estimate that relies on the energy balance of the ablation process. Figure 2.18 implies that about 10% of the laser light is absorbed in the plasma near the threshold for plasma production. With a separation of 15 μm from pulse to pulse, 4444 pulses/mm^2 are applied to the tissue, and a total energy of 11.1 mJ/mm^2 is deposited if the pulse energy is 25 μJ and 10% of the incident energy are absorbed. Since the vaporization energy of water at body temperature is 2.5 J/mm^3, a 4.4-μm-thick layer can be vaporized by the deposited energy. This estimate is, in fact an upper bound for the amount of vaporized tissue, since it is based on the assumptions that (i) every pulse causes plasma formation and (ii) all the absorbed energy contributes to vaporization. It has been neglected that a portion of the energy is consumed for the mechanical processes of shock wave and bubble formation and is, therefore, unavailable for vaporization. The result of the second estimate (4.4 μm thickness of the vaporized layer) is in good agreement with the outcome of the first calculation (5.1 μm). On the basis of histological studies, other authors have, likewise, concluded that only small amounts of the intrastromal material are vaporized [Bro94, Kru96].

In order to increase the amount of vaporized material, one can either use higher pulse energies or apply the laser pulses in several layers. However, Figs. 7.18 through 7.20 show that both strategies yield only a small increase in the amount of vaporized tissue. Raising the energy by a factor of 10 merely leads to a doubling of the thickness of the bubble layer (Figs. 7.18 and 7.19). If the thickness of the intrastromal bubble layer represents the amount of vaporized tissue, this also means that the volume of vaporized tissue is merely doubled and now corresponds to a layer thickness of 10 μm. The reason for the small increase in the vaporization of the tissue is that the bubbles produced by a single pulse become larger as the pulse energy is raised, so that an increasing number of laser pulses will be focussed into previously created bubbles. Therefore, an increasing fraction of the applied energy is unavailable for vaporization.

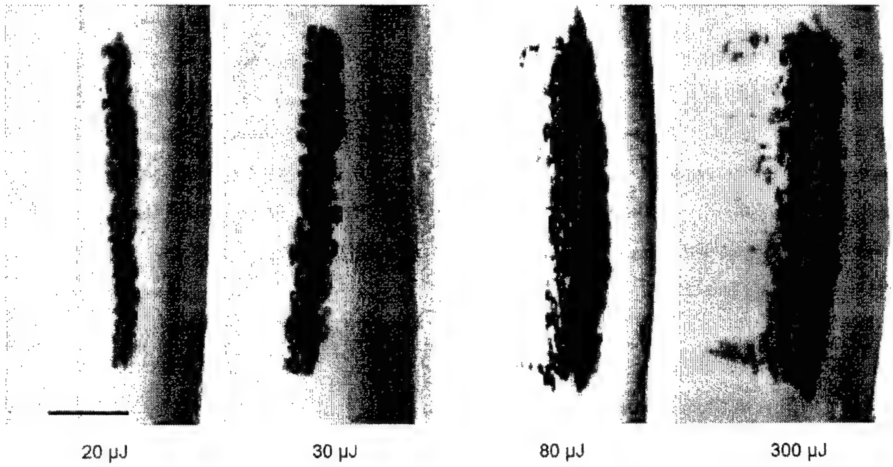

Fig. 7.18 Side view of corneal specimens with intrastromal bubble layers produced by different pulse energies. The laser light is incident from the right. The pulses were applied in a rectangular pattern of 2 mm height and 0.5 mm width. The lateral distance between pulses in the rectangular pattern was 15 μm. The scale length is 250 μm.

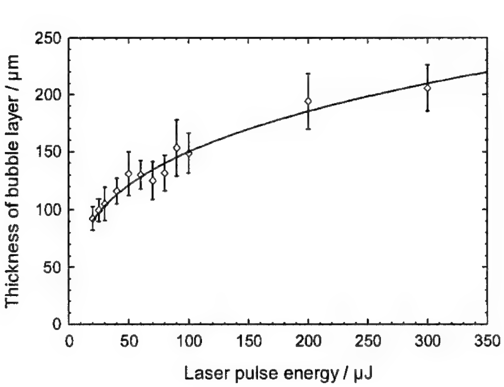

Fig. 7.19 Thickness of the intrastromal bubble layer created by 45 ps pulses as a function of the laser pulse energy.

A similar effect occurred if, instead of a single pulse layer, multiple layers were applied (Fig. 7.20). The bubble layer produced by the first layer of laser pulses with 25µJ pulse energy is already 100 µm thick (see Fig. 7.19). If the distance between the layers is 10 µm (Fig. 7.20a), all the later pulses will thus be focussed into the first bubble layer and produce only slight additional vaporization, even though the laser pulses of the fifth layer are focused 50 µm above the first layer. For 35 µJ pulse energy, the bubble layer thickness increases by a factor of 1.5. A distance between successive layers of 30 µm (Fig. 7.20b), leads to an almost linear dependence of the bubble layer thickness on the number of layers, but this dependence is very weak. Five laser pulse layers only vaporize 1.5 times as much tissue as a single layer. The total thickness of the vaporized tissue layer still amounts to no more than 7.5 µm. More layers cannot be applied without risking damage to the corneal endothelium or epithelium, since, with five layers, the bubbles are already spread over half the thickness of the cornea.

On comparing the maximum possible thickness of a vaporized tissue layer (about 10 µm) with the thickness of the human cornea (about 520 µm on the average [Mau84]), one can see that only a small fraction of the material can be vaporized by plasma-induced effects within the tissue and the laser effects mainly cause mechanical deformations of the tissue structure. This problem is not encountered in plasma-mediated ablation at a tissue surface in air, since there the ablated material can leave the application site without hindrance. The relative amount of vaporized tissue would even be smaller if nanosecond pulses were used instead of the picosecond pulses studied here, since the fraction of the laser energy that is converted into mechanical energy is greater with nanosecond pulses (see Chapter 4). For femtosecond pulses, on the other hand, it is smaller, since a large part of the laser energy is converted into the energy of vaporization (Chapter 8). Femtosecond pulses are, therefore, the best choice for intrastromal tissue vaporization.

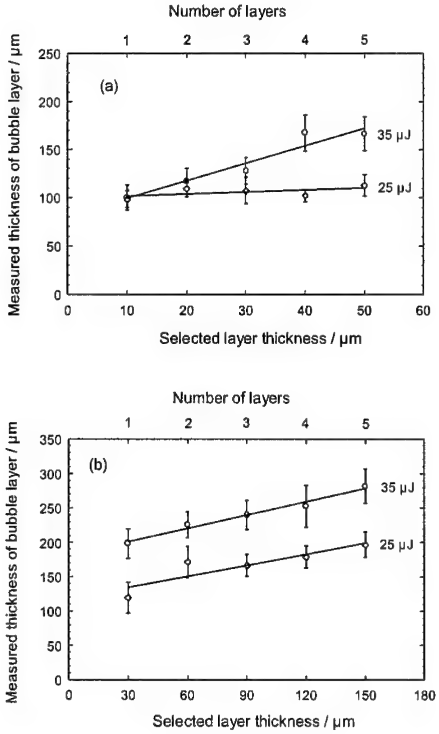

Distance between layers (µm]	Pulse energy (µm)	a	b (µm)
10	25	0.22 ± 0.17	99 ± 6
10	35	1.83 ± 0.30	81 ± 10
30	25	0.54 ± 0.16	118 ± 16
30	35	0.65 ± 0.06	181 ± 6

Fig. 7.20 Thickness of the bubble layer as a function of the number of and distance between layers to which ps pulses with different energies were applied. The pulse duration was 45 ps. The upper axis indicates the number of layers and the lower axis gives the overall depth of ablation set at the control panel of the ISL laser system. (a) Layer separation 10 µm, (b) Layer separation 30 µm. The Table lists the parameters for the line $h=ad+b$ fitted through the measurement data in (a) and (b) (with standard errors).

7.3 Summary and clinical consequences

The *primary cutting mechanism* during photodisruption is the vaporization of tissue owing to the high temperature of the laser plasma. The volume of vaporized material corresponds roughly to the plasma volume.

Because of the explosive expansion of the plasma, *disruptive effects* will occur in addition to the vaporization of tissue. In the immediate vicinity of the plasma, the effects of the shock wave and cavitation bubble expansion can hardly be distinguished, but at a somewhat larger distance the cavitation effects unequivocally predominate in the creation of morphologically identifiable tissue alterations.

The *effects of the plasma and bubble expansion* depend strongly on whether the plasma is produced deep inside or at the surface of a tissue. When the laser pulse is focussed into the corneal stroma, the plasma is entirely surrounded by tissue and all deposited energy above the threshold of vaporization acts to deform the surrounding tissue. As a result, an intrastromal cavity develops with 60 times the volume of the plasma. When the laser pulse is focussed onto the back surface of the cornea, the bulk of the deposited energy is imparted to the surrounding fluid in the anterior chamber during plasma expansion, and the hole created in the tissue is only slightly greater than the diameter of the laser focus. However, the inertial confinement of the vaporized material by the surrounding fluid causes a distinct indentation of the tissue surface during the expansion of the cavitation bubble that is further enlarged by the jet impact during bubble collapse. Neither effect is observed for plasma aided ablation into air, where the plasma is not confined and only the recoil of the ablated material produces a pressure against the tissue surface.

Although the primary laser effect consists of the vaporization of tissue within the plasma volume and is, thereby, thermal in nature, the collateral tissue effects are almost exclusively mechanical. Because of the sharp plasma boundary and the short time available for heat conduction, the *thermally modified zone* is less than 0.2 μm thick when a laser pulse is focussed on a tissue surface. On focussing a pulse into the corneal stroma, slight thermal changes have been observed up to a maximum depth of 2.5 μm.

The *damage range of laser pulses* focussed into the fluid in the neighborhood of the corneal endothelium is proportional to the cube root of the laser pulse energy, i.e., it has the same energy dependence as the cavitation bubble radius. The morphological appearance of laser-induced lesions suggests that they are partially created by the flow during bubble expansion, but primarily by jet formation during bubble collapse, which concentrates a large part of the bubble energy onto a small area. The *damage caused by the jet* is due partly to the high pressure caused by the jet impact on the cornea which can create holes in Descemet's membrane, and partly to the shearing forces acting on the endothelial cells as the jet flows radially outward from the point where it is incident. The jet is especially pronounced when a bubble is produced near a single rigid or elastic boundary. In clinical situations, many boundaries are often present near the bubble. Presence of many boundaries lowers the degree of asymmetry in the surroundings of the bubble and thus reduces the tendency to form jets, because jet formation requires asymmetric boundary conditions. For the strongly asymmetric boundary conditions studied in this work, the maximum damage radius for a single laser pulse was roughly 1.2 times the maximum bubble radius. It was, for example, 0.8 mm after a 4 mJ laser pulse.

The physical mechanism with the longest damage radius is the jet formation occurring when a gas bubble created by a previous laser pulse is hit by a shock wave produced by a later pulse. The damage range of a 4 mJ pulse focussed in the neighborhood of a gas bubble attached to the corneal endothelium was between 2.0 and 3.5 mm, depending on the size of the gas bubble. *Shock-induced jet formation* is much less dependent on the specific boundary conditions than is jet formation at a solid boundary. This damage mechanism is, therefore, of great clinical significance, both for laser surgery in the anterior segment of the eye and for laser applications in the neighborhood of the retina.

The side effects of photodisruption can be considerably reduced by *using shorter laser pulses.* The threshold for optical breakdown is lower for shorter pulse lengths, so that pulses with lower energies can be applied. In addition, the fraction of the laser energy converted into mechanical energy is lower for short pulses. Clean incisions could be made in Descemet's membrane with 30 ps, 50 μJ pulses, while 6 ns, 1 mJ pulses ruptured the tissue along the cut and had three times the damage radius.

Intraocular *photodisruption is better suited to cutting than to vaporizing large volumes of tissue.* Picosecond pulses can certainly produce intrastromal effects without endothelial or epithelial damage, as required for intrastromal photorefractive surgery, but, because of cavitation effects in the corneal stroma, the maximum thickness of the tissue layer that can be vaporized is 10 μm. The removal of a lenticule of this thickness corresponds to a refractive change of only 0.85 diopters for a treatment zone with 6 mm diameter [Vog97c] and that is not enough for refractive surgery.

8 From nano- to femtosecond pulses

In recent years it has become significantly easier to create subpicosecond pulses with energies high enough for microsurgical applications. Prerequisites were new solid-state laser media with large bandwidths (for example, Ti:sapphire), passive mode locking using self-focussing effects in the laser crystal (Kerr-lens mode locking), amplification of pulses after pulse stretching using group velocity dispersion followed by compression of the amplified pulse (chirped pulse amplification), and regenerative amplifiers with gains of up to 10^{11}. State of the art systems permit the generation of energetic (>1 mJ), high repetition rate (>1 kHz) femtosecond pulses with tabletop laser systems [Spi95, Mou98]. Further reductions in the size of these systems are possible with the use of laser diodes as pump sources [Aus98], the development of laser oscillators with dispersive mirrors [Spi95], the development of parametric amplifiers which reach pulse energies of up to 1 mJ in a single pass [Gal98], and the development of compact pulse compression systems [Squ98]. It should, therefore, be possible to employ femtosecond lasers in industrial or clinical applications within the foreseeable future.

The availability of compact femtosecond lasers raises the question of whether the observed trend toward a reduction in the disruptive character of optical breakdown with shorter pulses continues also in the subpicosecond range of pulse durations. For applications in which the disruptive character of the breakdown is used, it is, on the other hand, interesting to know whether the severity of the mechanical effects further increases as the pulse length is increased above 6 ns. In order to address these questions, we review the physical mechanisms for optical breakdown with pulse durations ranging from 80 ns to 100 fs (i. e., over 6 orders of magnitude) [Vog98d].

In order to cover this large parameter range, the experimental procedure used for determining the shock wave pressure was modified. The shock pressure $p_S(r)$ will no longer be determined as a function of distance from the source center from a series of framing photographs with different time delays relative to the laser pulse (as described in Chapter 3.1.7), but rather with the aid of a single streak photograph which records the entire path $r_S(t)$ of the shock wave propagation [Noa98b]. This streak photo, just as the series of framing pictures, is used to determine the shock speed u_S and shock pressure p_S as a function of propagation distance r.

8.1 Experimental techniques

The experimental apparatus for producing and observing laser-induced breakdown with pulse durations between 80 ns and 100 fs is shown in Fig. 8.1. The laser pulses were produced by an alexandrite laser (τ_L = 76 ns, Light Age Inc.), an Nd:YAG laser (τ_L = 6 ns, Continuum YG 671-10), and an Nd:YAG laser pumped dye laser system (τ_L = 60 ps, 3 ps, 300 fs, and 100 fs, Spectra Physics). The laser beam was, as described in Chapter 2.2, expanded, collimated, and focussed into a cell containing distilled water with a contact lens built into its wall in order to avoid spherical aberrations. Since the risk of damage to the contact lens was very high with the 76 ns pulses because of the high pulse energies required for breakdown, the contact lens was replaced for this pulse length by a planoconvex lens (f = 100 mm in air). The use of a planoconvex lens led to increased spherical aberrations and a larger focal diameter.

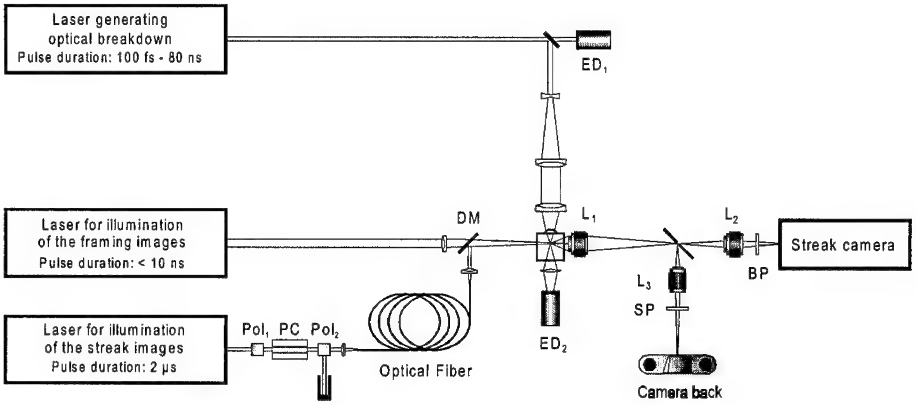
Laser generating optical breakdown Pulse duration: 100 fs - 80 ns
ED₁
Laser for illumination of the framing images Pulse duration: < 10 ns
DM
L₁
L₂
Streak camera
BP
L₃
SP
Laser for illumination of the streak images Pulse duration: 2 µs
Pol₁ PC Pol₂
Optical Fiber
ED₂
Camera back

Fig. 8.1 Experimental apparatus for simultaneous streak and single frame photography of events during optical breakdown [Noa98c].

The focal angles and focal spot diameters were determined using a knife edge technique. They are summarized in Table 8.1 in Section 8.2.1. The pulse energy incident on the cuvette and the energy transmitted within the focal angle were measured with the calibrated pyroelectric detectors ED_1 and ED_2. The optical breakdown threshold for pulse durations ≥ 60 ps was determined using the plasma radiation as a breakdown criterion. For pulse durations of 3 ps or less, no plasma radiation was visible, so that the development of a cavitation bubble in the focal region of the laser served as a criterion for breakdown.

The sequence of events during optical breakdown was recorded simultaneously with streak photography and normal photography [Noa98b, Noa98c]. A two stage optical system was used. First, the object volume was imaged with an objective optimized for a magnification of 8 times (L_1, EL Nikkor

63 mm, $F = 4$) onto an intermediate image plane. There a highly reflecting coated glass substrate with a 20 μm wide slit in the coating was positioned at an angle of 45°. The light transmitted through the slit was imaged by a macro-objective (L_2, Nikon 105/5.6) onto the photocathode of a streak camera (Hadland Photonics, Imacon 792). The reflected picture was imaged onto the film plane of a 35 mm miniature camera with another objective (L_3, Pentax 50/1.8). In the pictures one can see the breakdown region together with the position of the streak slit which appears as a dark line. This allows the position of the streak slit relative to the plasma to be monitored. The overall magnification was varied between 11x and 45x for the framing photographs and between 16x and 73x for the streak photographs. The higher magnifications were used to photograph the breakdown with ultrashort laser pulses and low pulse energies. The time resolution of the streak photographs was better than 200 ps in all cases and the spatial resolution was 6.4 μm for the lowest overall magnification and 3 μm for magnifications exceeding 30 times.

The streak photographs were illuminated by pulses from a flashlamp pumped dye laser (λ = 630 nm), out of which constant-intensity segments lasting 200-400 ns were cut by means of an external Pockels cell. The illumination was coupled into a glass fiber with 300 μm core diameter and a length of several meters whose distal end was imaged onto the object volume. In this way, spatially and temporally uniform illumination could be obtained. The framing pictures were taken with illumination by another dye laser with a pulse duration of < 1 ns. In the experiments with 6 ns and 30 ps pulses, a part of the pulse used to produce the optical breakdown was frequency doubled, optically delayed, and used for illumination (cf. 3.2.1). The two illumination beam paths were combined in front of the cell using a dichroic mirror and separated behind the cell for streak and framing photography by means of a suitable bandpass filter (BP for 630 nm) and a short pass filter (SP).

Digital image processing was used to determine the position r_S of the shock wave as a function of time t from the streak photographs [Noa98a, Noa98b]. The shock velocity was calculated by differentiating the $r_S(t)$ curves and, as described in Section 3.1.7, it was used to determine the shock pressure $p_S(r)$ as a function of distance from the emission center.

Besides the streak photographic studies of shock wave formation in the near field, the shock pressure was measured at a distance of 12 mm from the plasma with a calibrated hydrophone (Ceram) (cf. 3.2.2). The size of the cavitation bubble produced by the breakdown was also determined from the hydrophone signal (cf. 3.2.3).

8.2 Results and Discussion

8.2.1 Plasma formation at the breakdown threshold

During optical breakdown of a medium a large number ($\geq 10^{18}$ cm^{-3}) of free electrons are produced through multiphoton ionization and cascade ionization via inverse bremsstrahlung absorption (cf. Section 2.1). The multiphoton ionization rate has a very strong intensity dependence ($\propto I^K$, where K is the number of photons required for ionization), while the intensity dependence of the cascade ionization rate is much weaker ($\propto I$, if electron losses from the focal volume are neglected). If the laser pulse duration is reduced, a higher intensity is necessary in order for optical breakdown to take place within the shorter time available. Since the rate of multiphoton ionization rises more rapidly with I than that of cascade ionization, multiphoton ionization becomes ever more important for short pulse lengths. For pulse lengths under ≈1 ps, cascade ionization is, furthermore, subject to temporal constraints. Each impact ionization in the cascade must be preceded by a few collisions between electrons and heavy particles, during which the electron energy increases as a result of inverse bremsstrahlung. Multiphoton ionization, in contrast, can take place "instantaneously." The changes in the relationship between multiphoton ionization, cascade ionization, and the recombination of free electrons are the fundamental reason for the changes in optical breakdown as the laser pulse duration is reduced.

The evolution of the free electron density during the laser pulse is described by the rate equation (see Eq. (2.6))

$$\frac{d\rho}{dt} = \eta_{mp} + \eta_{casc}\,\rho - g\rho - \eta_{rec}\,\rho^2 . \tag{8.1}$$

Here the first two terms represent the creation of free electrons by multiphoton and cascade ionization, and the last two the losses of electrons through diffusion out of the focal volume and recombination. Explicit expressions for these terms are given in Section 2.1.4. The threshold for optical breakdown is defined as the minimum irradiance for which a critical electron density ρ_{cr} is exceeded during the laser pulse. It was determined by solving Eq. (8.1) iteratively for different irradiances.

Table 8.1 lists the experimental breakdown thresholds (50% breakdown probability) for different pulse lengths together with the calculated thresholds I_{rate} for two values of the critical electron density ρ_{cr} [Noa98a, Noa99]. There is good agreement between the experimental and calculated threshold values if it is assumed that $\rho_{cr} = 10^{20}\,\mathrm{cm}^{-3}$ for nanosecond pulses and $\rho_{cr} = 10^{21}\,\mathrm{cm}^{-3}$ for pico- and femtosecond pulses.

Pulse duration	Wavelength [nm]	θ °	Measured focal spot diameter [µm]	E_{th} [µJ]	F_{th} [J cm^{-2}]	I_{th} [10^{11} Wcm^{-2}]	I_{rate} $\rho_{cr} = 10^{20}\text{cm}^{-3}$ [10^{11} Wcm^{-2}]	I_{rate} $\rho_{cr} = 10^{21}\text{cm}^{-3}$ [10^{11} Wcm^{-2}]
76 ns	750	19	20	5500	1750	0.23	0.22	1.9
6 ns	532	22	5.3	39	174	0.29	0.40	3.6
60 ps	532	13	5.6	4.1	16.8	2.8	0.60	3.6
30 ps	532	22	3.4	1.0	11.3	3.8	0.93	3.6
3 ps	580	16	5.0	0.51	2.6	8.5	7.10	9.0
300 fs	580	16	5.0	0.29	1.4	47.6	39.0	48
100 fs	580	16	4.4	0.17	1.1	111.0	77.0	98

Table 8.1 Measured breakdown thresholds E_{th}, F_{th} and I_{th} and calculated threshold I_{rate} as functions of the pulse duration for different critical electron densities ρ_{cr}.

Solving Eq. (8.1) numerically yields the time evolution of the electron density and thus provides a deeper understanding of the changes of the breakdown process with pulse duration [Noa99]. For a discussion of these changes, Fig. 8.2 shows the time evolution of the electron density for different pulse lengths and Fig. 8.3 shows the threshold I_{rate} as a function of the pulse duration for two different wavelengths.

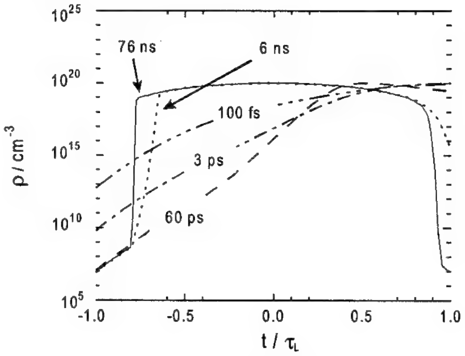

Fig. 8.2 Time evolution of the free electron density at the breakdown threshold for different laser pulse durations τ_L. All the curves were calculated for λ = 580 nm, a 6 µm focal spot diameter, and $\rho_{cr} = 10^{20}\text{cm}^{-3}$. A gaussian laser pulse with a maximum at *t=0* was assumed.

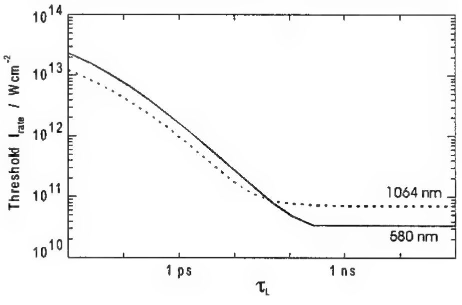

Fig. 8.3 Intensity threshold I_{rate} as a function of the laser pulse duration calculated for λ = 1064 nm and λ = 580 nm (6 µm focal spot diameter, $\rho_{cr} = 10^{20}\text{cm}^{-3}$).

In pure media, such as distilled water, the initial electrons for the breakdown cascade are provided by multiphoton ionization. Therefore, the cascade term in Eq. (8.1) is first taken into account when the probability that a free electron exists in the focal volume has risen to 50% owing to multiphoton ionization. This takes longer for the nanosecond pulses than for the shorter pulses, because the multiphoton ionization rate η_{mp} is here relatively low for the intensity corresponding to the optical breakdown threshold. As soon as the first free electron is created in the focal volume, the electron density rises by almost 11 orders of magnitude within a small fraction of the laser pulse duration as a result of the now active cascade ionization (Fig. 8.2; 76 ns, 6 ns). The cascade ionization rate is very high, since a high irradiance is required to produce the seed electrons by multiphoton ionization. The rise in the free electron density is slowed at high electron densities by the rapidly rising influence of recombination ($\propto \rho^2$). For all pulse durations such that the ionization cascade can take place within a small fraction of the laser pulse duration, the maximum electron density is reached at the intensity peak of the pulse and is determined by the recombination term. Since the recombination rate is independent of pulse duration, I_{rate} is approximately constant within this range of pulse durations (Fig. 8.3).

For a laser pulse length of about 1 ns, the entire pulse duration is required to reach ρ_{cr}. For shorter pulses, the irradiance must therefore be raised for the critical electron density to be reached during the laser pulse. Because of the higher irradiance, the cascade ionization rate is now greater than the recombination losses during most of the laser pulse, i.e. even after the intensity maximum. For a 60 ps pulse, ρ_{cr} is, therefore, first reached in the second half of the laser pulse (Fig. 8.2;60 ps).

While for nanosecond pulses multiphoton ionization provides only seed electrons for the ionization cascade, it becomes ever more important for shorter laser pulse durations where the irradiance required for breakdown is higher. For pulse lengths around 1 ps and below, multiphoton ionization not only produces a large number of seed electrons, but also contributes significantly to the breakdown process afterward. This contribution is especially marked during the first half of the laser pulse [Noa99]. For pulse durations less than about 1 ps, the critical electron density can no longer be reached by cascade ionization alone, because a doubling in the ionization cascade takes at least 6 fs no matter how high the irradiance may be, and may take 30 fs (see Section 2.1.1.2 and [Ken95a,Noa99]). Nevertheless, the majority of the free electrons are produced by cascade ionization for all laser pulse durations studied here, because the cascade starts to dominate once a certain number of free electrons has been produced by multiphoton ionization. Multiphoton ionization predominates only for pulse lengths shorter than 40 fs [Stu96, Fen97, Noa99].

The wavelength dependence of the breakdown threshold (cf. Fig. 8.3) is dominated by the wavelength dependence for multiphoton ionization (Eq. (2.9)) for pulse lengths >100 ps. For long pulse durations the production of seed electrons by multiphoton ionization is the decisive hurdle in the breakdown process ($I_m > I_c$). Therefore, the breakdown threshold is higher for 1064 nm than for 580 nm. For pulses lasting less than 10 ps, in contrast, the wavelength dependence of the breakdown threshold is governed by the wavelength dependence for cascade ionization (Eq. (2.13)) because $I_c > I_m$. Therefore, the threshold is higher for 580 nm.

8.2.2 Plasma formation above the breakdown threshold

If the irradiance exceeds the threshold for optical breakdown, plasma formation is no longer confined to the focal region. With ns- and ps-pulses, plasma formation begins in the beam waist and the plasma then expands toward the incident laser light (cf. 2.1.6). Hardly any plasma develops behind the laser focus, since most of the laser light is already absorbed prior to and in the beam waist. The position of the plasma front at each time is defined by the $I = I_{th}$ iso-intensity contours. The maximum attainable plasma length is proportional to $\sqrt{\beta - 1}$ for ps-pulses, where $\beta = E / E_{th} = I / I_{th}$ (cf. 2.3.2.3). With ns-pulses, the threshold falls to a value $I'_{th} < I_{th}$, as soon as plasma formation has begun, since the UV radiation generated by the plasma creates free electrons which makes the creation of seed electrons by multiphoton ionization superfluous. The position of the plasma front is, therefore, determined by contours with $I = I'_{th}$ and ns-plasmas are substantially longer than ps-plasmas with the same β. This situation holds especially for large focal angles and energies near the breakdown threshold; for θ = 22° and small β, the ns-plasmas are up to 6 times longer than the ps-plasmas (cf. 2.3.2.3).

For fs-plasmas, the plasma length observed above the breakdown threshold is considerably longer than the length of the laser pulse (30 µm for a 100 fs pulse). The long plasma length indicates that plasma formation begins before the pulse reaches the laser focus. The plasma front moves with the laser pulse toward the focus, so that free electrons remain in its wake. This is in contrast to ps- and ns-breakdown where the pulse is much longer than the plasma and the plasma front moves from the focus towards the incoming beam. The plasma length for fs-pulses is proportional to $\sqrt{\beta - 1}$, as for ps-pulses, even though the plasma front moves in opposite direction [Noa98a]. In both cases, the maximum extent of the plasma on the laser side is determined by the distance from the beam waist at which the threshold I_{th} is exceeded for the given β.

For all laser pulse durations, the energy density in the breakdown region is limited by the growth of the plasma during the laser pulse. A higher pulse energy leads to a larger plasma, but not to an increase of the energy density within the plasma. For ns- and ps-pulses, the focal region is shielded by the growth of the plasma in the direction of the incident laser light. For fs-pulses, plasma formation begins in front of the beam waist, and as the laser pulse moves toward the focus, the intensity rise owing to focussing competes with the attenuation of the light by multiphoton absorption and inverse bremsstrahlung absorption. This attenuation limits the average energy density in the focal region, as in the case of long pulses. Only if self-focusing comes into play, can the energy distribution be considerably modified and filaments with higher energy density may be formed (cf. 8.2.5).

8.2.3 Energy deposition and absorption coefficient

It was shown in section 2.3.3 that scattering and reflection on the plasma during optical breakdown in water with 6 ns and 30 ps pulses can be neglected in the first approximation. The absorption is thus given by $A \approx 1 - T$. In the following, it will be assumed that this approximation is also true for shorter laser pulses. Measurements of the transmission are then sufficient to determine the amount of energy absorbed in the breakdown region.

Figure 8.4 shows the transmission for two values of β as a function of the laser pulse duration [Noa99]. The transmission increases by roughly a factor of 10 as the pulse is shortened from the nanosecond to the picosecond range but decreases again in the femtosecond range. A similar observation has been made by Hammer, et al. (1997).

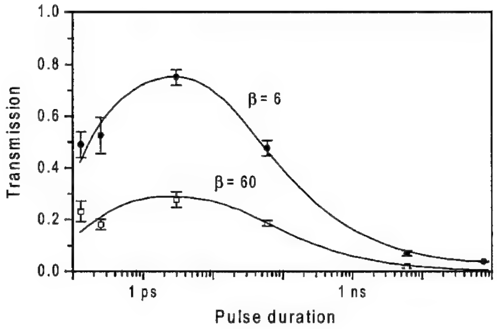

Fig. 8.4 Plasma transmission as a function of laser pulse duration for β = 6 and β = 60. The laser parameters correspond to those from Table 8.1.

The strong dependence of the transmission on the laser pulse duration can be explained by taking into account that the measured values of the transmission are an average over the entire duration of the laser pulse. One must consider the entire time evolution of the electron density during the laser pulse and not just the maximum electron density. The time averaged absorption coefficient α_{LIB} in the neighborhood of the threshold is obtained from the inverse bremsstrahlung scattering cross section σ_a [Fei74] and the time evolution of the free electron density $\rho(t)$ (Eq. (8.1)) with

$$\alpha_{\mathrm{LIB}} = \sigma_a \frac{\int I(t)\rho(t)dt}{\int I(t)dt}. \tag{8.2}$$

The calculated dependence of α_{LIB} on the pulse duration is shown in Fig. 8.5. The absorption coefficient is highest for nanosecond pulses (800 cm^{-1}), since here the electron density is very high thoughout the entire laser pulse (see Fig. 8.2; 76 ns, 6 ns). Since the time evolution is similar for all pulse durations between 1 ns and 100 ns, the absorption coefficient is roughly constant within this interval. For pulse durations <1 ns, a high electron density occurs only in the second half of the laser pulse (Fig. 8.2; 60 ps, 3 ps). As a consequence, the average absorption coefficient decreases until it reaches a minimum of 150 cm^{-1} at pulse lengths around 3 ps. With shorter pulses, the increasing multiphoton ionization leads to a rise in the electron density at the beginning of the laser pulse (Fig. 8.2; 100 fs) and, thereby, also to a rise in the average absorption coefficient.

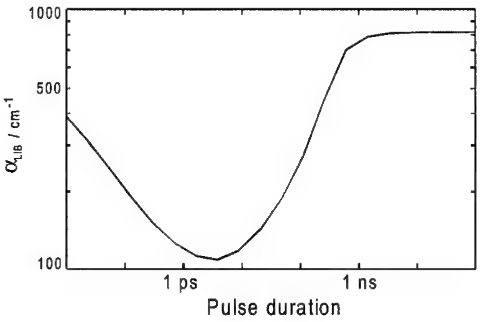

Fig. 8.5 Calculated absorption coefficients of laser induced plasmas at the optical breakdown threshold for a critical electron density of 10^{20} cm^{-3} (6 μm focal spot diameter and 580 nm wavelength).

The dependence of α_{LIB} on pulse duration in Fig. 8.5 is in good qualitative agreement with the variation in the experimentally determined transmission in Fig. 8.4. The absolute magnitudes of the calculated absorption coefficients for ps and ns pulses are, however, about a factor of 3 larger than the experimental values of ≈ 70 cm^{-1} and ≈ 250 cm^{-1}, respectively, determined from the plasma transmission and plasma length at 1064 nm (cf. Section 2.3.3.7). The difference is partly caused by the fact that the experimental values also include light transmitted around the plasma, so they are lower than the actual absorption coefficients of the plasma. The actual electron density in the plasma may also be somewhat lower than that assumed for calculating α_{LIB}.

8.2.4 Mechanical effects

8.2.4.1 Shock waves and cavitation

Figure 8.6 illustrates the appearance of optical breakdown for different laser pulse durations. With the ns pulses, shock wave production and bubble expansion begin in the beam waist and continue toward the incoming laser beam, following the spatial development of plasma formation. With 30 ps pulses, the detachment of the shock from the plasma seems to occur simultaneously everywhere, because the pulse duration is much shorter than the time constants for shock propagation and bubble oscillation. With the 100 fs pulses, no plasma radiation can be seen, as opposed to the case of the longer pulses. The region within which optical breakdown took place becomes visible only through the formation of a cavitation bubble. The shape of the bubble immediately after the end of the laser pulse (a cone with a filamentous tip) suggests that breakdown was accompanied by self-focussing.

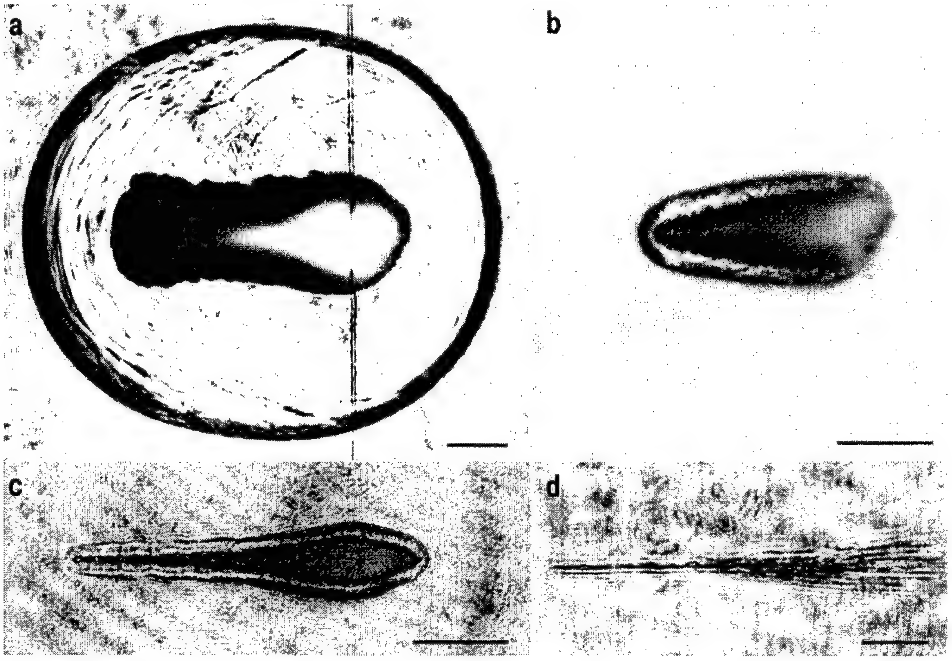

Fig. 8.6 Shock wave formation and cavitation bubble expansion after optical breakdown with different laser pulse durations. (a) Pulse duration τ_L = 76 ns, wavelength λ = 750 nm, focal angle θ = 19°, E = 50 mJ, β = 9. The picture was taken 120 ns after optical breakdown. The black line is from the slit through which part of the light was transmitted for simultaneous streak photography. (b) τ_L = 6 ns, λ = 1064 nm, θ = 22°, E = 8,2 mJ, β = 60, Δt = 10 ns. (c) τ_L = 30 ps, λ = 1064 nm, θ = 14°, E = 740 µJ, β = 150, Δt = 8 ns. (d) τ_L = 100 fs, λ = 580 nm, θ = 16°, E = 35 µJ, β = 200, Δt = 3ns. The light was incident from the right and the scales correspond to 100 µm.

Table 8.2 gives an overview of the pulse duration dependence of the shock pressure and the conversion of laser energy into cavitation bubble energy. The data of Table 8.2 show that the mechanical effects become weaker as the laser pulse duration is reduced; i.e., a smaller percentage of the laser light energy is converted into mechanical energy. This becomes obvious by considering the degree of

Pulse duration	Wavelength (nm)	$\beta = E / E_{th}$	Pressure at plasma boundary (GPa)	Pressure at a distance of 12 mm (MPa)	Degree of conversion of absorbed laser energy into bubble energy (%)
76 ns	750	6	10	4.0	22.0
6 ns	1064	60	30	3.0	22.5
60 ps	532	60	10	0.65	13.5
3 ps	580	60	2.2	0.23	11.0
300 fs	580	60	1.8	0.11	3.0
100 fs	580	60	0.9	0.06	3.0

Table 8.2 Dependence of shock pressure and cavitation bubble energy on laser pulse duration for $\beta = 60$. In the case of the 76 ns pulses, values are given for $\beta = 6$ owing to the limited laser pulse energy. The pressures at the plasma edge were all determined by streak photography and, therefore, differ to some extent from the values given in Chapter 3.

conversion of laser energy into bubble energy. It also shows up as a drop in pressure at the plasma boundary with decreasing pulse duration. The shock pressure in the far field falls off even faster than the pressure at the plasma boundary, because the far-field pressure is determined not only by the pressure in the plasma but also by the plasma size (see Section 3.1.8) which, for constant β, decreases with shorter pulse durations.

8.2.4.2 Energy density in the breakdown region

The intensity of the mechanical effects induced by optical breakdown is related to the average energy density in the breakdown region. The energy density was estimated by comparing the absorbed energy with the photographically determined breakdown volume. With 6 ns pulses at 1064 nm, values of 30-40 kJ/cm^3 were obtained (cf. 2.3.5), well above the vaporization enthalpy of water (2.59 kJ/cm^3 for water at room temperature). The high energy density in the nanosecond plasmas explains both the high efficiency of conversion into bubble energy and the high pressures at the plasma boundary (Table 8.2). For 76 ns pulse duration, the energy density reached in the plasma is no higher than for 6 ns pulses, because a significant expansion of the plasma and the cavitation bubble takes place during the laser pulse. With femtosecond pulses the energy deposition is isochoric, but the average energy density in the breakdown volume is only about 1 kJ/cm^3, i.e., it is lower than the enthalpy of vaporization of water at constant pressure. The liquid in the breakdown volume can, therefore, be only partly vaporized, and the degree of conversion of laser energy into bubble energy is low. The peak pressure at the plasma boundary is thus much smaller than for ns-pulses (≈1 GPa as compared to 30 Gpa, see table 8.2). Because of the vaporization it is, however, still 10 times higher than the pressure rise of about 0.1 GPa owing to thermoelastic effects after the deposition of 1 kJ/cm^3.

Because of the drop in the average plasma energy density with shorter pulse durations, a larger fraction of the laser energy is needed for vaporization of the fluid in the breakdown volume, and a smaller percentage of the laser energy is converted into the mechanical energy of the shock wave and cavitation bubble (cf. Table 8.2). The ratio (E_{mech}/E_v) falls from about 12:1 for 6 ns pulses (cf. Table 4.1) to 1:1 for 100 fs pulses with energies near the breakdown threshold, and even to 0.25:1 for energies well above the threshold. In calculating the above value of (E_{mech}/E_v) for femtosecond pulses, it was assumed that, just as with the longer pulse durations, the shock wave energy is roughly twice the experimentally determined bubble energy. E_V was calculated as $E_V = E_{abs} - E_{mech}$. A direct determination of E_V by photographic determination of the size of the breakdown volume (cf. 4.1.2) is not possible for femtosecond pulses, since the boundaries of the breakdown region are not sharply defined on the side of the incoming laser beam (cf. Fig. 8.6d).

8.2.4.3 Factors controlling the dependence of the energy density on pulse duration

Although the irradiance I is the relevant parameter for the development of the free electron density, the radiant exposure F required for breakdown and the resulting energy density in the breakdown volume are of greater practical interest, since they determine the extent of mechanical effects during plasma-mediated material processing. The pulse duration dependence of the radiant exposure threshold F_{th} (Table 8.1) and of the energy density ε are closely coupled, but they are not necessarily the same, since ε depends not only on F_{th}, but also on the length and the absorption coefficient of the breakdown region. In the following, we shall discuss the factors determining the dependence of the energy density on pulse duration.

Maximum electron density. The energy density in the plasma volume depends, among other things, on the free electron density attained during the laser pulse. Kennedy, et al. (1995a,b) conjectured that a drop in the electron density with shorter pulse durations is the main reason why no plasma light emission is observed with pulses lasting less than 3 ps. For this reason they assumed a critical electron density $\rho_{cr} = 10^{20} cm^{-3}$ when calculating the breakdown threshold for nanosecond and 60 ps pulses and used $\rho_{cr} = 10^{18} cm^{-3}$ for 3 ps and femtosecond pulses. There is, however, as yet no experimental evidence for this sort of dependence of ρ_{cr} on the pulse duration. Experimental data exist only for 30 ns ruby laser pulses, for which Barnes and Rieckhoff (1968) obtained an electron density of about 10^{20} cm^{-3}. Fundamental considerations do, however, allow us to set a limit on the possible range of values for the electron density.

It is unlikely that ρ_{cr} is actually greater than $10^{21} cm^{-3}$, since this is the critical plasma density at $\lambda = 1064$ nm above which the plasma would reflect most of the incident light (cf. 2.1.3). The following arguments will show that during optical breakdown with femtosecond pulses, it is, conversely, unlikely that ρ_{cr} is much less than $10^{21} cm^{-3}$. Up to the end of the pulse, the input energy is primarily stored in the form of free electrons, and hardly any energy has been transferred to the heavy particles. The energy required to produce a free electron is at least 6.5 eV or 1.04×10^{-18} J (cf. 2.1.3). Thus, the energy density of 2.59 kJ/cm^3 required to vaporize water at room temperature and atmospheric pressure corresponds to an electron density of about 2.5×10^{21} cm^{-3} (neglecting the kinetic energy of the free electrons). This means that ρ_{cr} must be about 2.5×10^{21} cm^{-3} in order to create a pure steam bubble. If thermoelastic effects play a role in bubble formation during optical breakdown and only partial vaporization takes place, ρ_{cr} can, indeed, be somewhat lower, but not by 3 orders of magnitude, as Kennedy (1995a) conjectured. With nanosecond pulses, on the other hand, the enthalpy of vaporization can also be reached for the breakdown volume in the case $\rho < 10^{21} cm^{-3}$, since a steady transfer of energy from electrons to heavy particles takes place during a longer laser pulse.

In sum, the above considerations suggest that the average electron density in the plasma will rise with decreasing laser pulse duration. This is confirmed by the results in Section 8.2.1, where good agreement between the experimental and calculated thresholds was obtained if it was assumed that $\rho_{cr} = 10^{20} \mathrm{cm}^{-3}$ for nanosecond pulses and $\rho_{cr} = 10^{21} \mathrm{cm}^{-3}$ for pico- and femtosecond pulses. The observed rapid drop in the energy density as the laser pulse duration is reduced can, therefore, not be explained in terms of changes in the electron density.

Energy transfer from electrons to heavy particles during the laser pulse. With femtosecond pulses, hardly any energy is transferred from the electrons to the water molecules during the laser pulse [Stua96, Chi96; Noa99]. Only after the end of the pulse does an equilibrium temperature develop, and this temperature is substantially lower than the electron temperature, since the specific heat of the electrons is much lower than that of the heavy particles [Chi96]. With nanosecond pulses, on the other hand, the pulse duration is considerably longer than the time for energy transfer from electrons to heavy particles, so that the average temperature in the breakdown volume is raised to the electron temperature during the laser pulse [Chi96]. Energy transfer takes place mainly through collisions between free electrons and heavy particles and through thermalization via recombination events. Some of the recombination events are entirely radiationless [Jon89], and, otherwise, mainly excited electronic states will be populated [Jos95], and radiationless transitions can take place from these states into lower states. It is obvious that, for a constant free electron density, the more energy can be gained through inverse bremsstrahlung and passed on to the molecules the longer the laser pulse is. Figure 8.2 shows that the electron density for nanosecond pulses maintains a high and roughly constant value for quite a long time. Therefore, the equilibrium temperature and energy density in the plasma rise rapidly with increasing laser pulse duration. The energy density is limited only by the fact that the plasma expands during the laser pulse for long pulses (76 ns).

Plasma size. For equal β, nanosecond plasmas are considerably longer than picosecond plasmas, since the optical breakdown threshold falls during the nanosecond pulses due to generation of seed electrons in the plasma vicinity caused by the UV recombination radiation (cf. 2.3.2.3). The enlargement of the plasma size reduces the energy density of the plasma for long pulses.

Energy deposition in the surroundings of the plasma. During optical breakdown with femtosecond pulses the fluid in the beam cone will be heated already in front of the region where the cavitation bubble develops. The heating results in a refractive index change that can be made visible with a schlieren technique (Fig. 8.7). The temperature-induced refractive index variations can be easily distinguished from variations owing to acoustic transients, because they are stationary for several microseconds. Heating to temperatures below the threshold for bubble formation takes place in regions

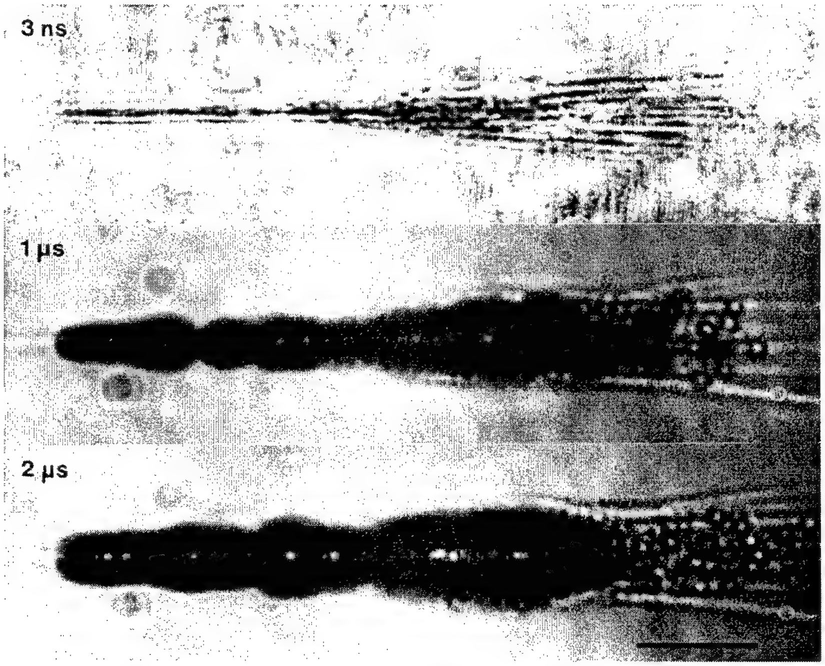

Fig. 8.7 Optical breakdown produced by a 100 fs, 35 μJ pulse (β = 200) photographed at different times after a laser pulse. The pictures taken 1 and 2 μs after breakdown are slightly defocussed in order to make visible the regions outside the cavitation bubble where multiphoton absorption leads to a temperature rise and, thereby, to changes in the refractive index. The laser light was incident from the right and the scale corresponds to 100 μm.

where multiphoton ionization produces a large number of free electrons but the critical electron density is not fully attained. The possibility of such a subthreshold effect is illustrated by the $\rho(t)$ curves in Fig. 8.2, which show that substantially more electrons are available right at the beginning of a 100 fs pulse than for longer pulses and that the free electron density rises very steadily during the fs-laser pulse. A similarly smooth variation of the maximum electron density reached at the end of the laser pulse can be expected when the irradiance is varied around the breakdown threshold. Because of the light absorption in front of the breakdown region, there is a drop in the energy density in the breakdown volume where the cavitation bubble forms. No such effect was observed with the nanosecond or picosecond plasmas. Subthreshold effects are discussed in more detail in [Noa99].

8.2.5 Self-focussing

Thus far, for simplicity we have neglected the fact that all aspects of the breakdown process with ultrashort laser pulses will be influenced by self-focussing. For a gaussian beam, above a critical power

$$P'_{cr} = 3.77\frac{c\lambda^2}{32\pi^2 n_2} \tag{8.3}$$

nonlinearities of the refractive index lead to a beam collapse, i.e., to focussing onto a cross section which is smaller than the diffraction limited focal spot diameter (cf. 2.1.2). Since the irradiance and laser power required for optical breakdown increase as the pulse is shortened, self-focussing plays an ever more important role as the pulse duration is shortened.

Theoretical predictions of the self-focussing dynamics for ultrashort laser pulses are complicated, because the group velocity dispersion, which can be neglected with long pulses, must be taken into account [Lut94, Fib96, Fen97, Ran98].

The experimental results presented here show that self-focussing occurs with 6 ns, 1064 nm pulses only for very small focal angles < 2° (cf. 2.3.1.2). With 30 ps pulses, self-focussing was observed also at larger focal angles such as used in intraocular microsurgery, but only with energies well above the breakdown threshold (cf. 2.3.2.4). With femtosecond pulses, on the other hand, self-focussing plays a role at large focal angles even near the breakdown threshold [Fen97, Ran98]. Self-focussing can be identified by detecting continuum radiation. Continuum radiation develops, like self-focussing, through self phase modulation (cf. 2.1.2) and it is known that it occurs in water only at powers above the threshold for self-focussing [Smi77, Rot92]. A further indication of the presence of self-focussing effects is that the laser power required for breakdown depends only weakly on the focal spot size [Ham97].

At energies above the breakdown threshold, self-focussing causes a deformation of the breakdown region. The result is a filamentary structure at the tip the breakdown region which extends beyond the site of the linear focus (Fig. 8.7). Filaments of this sort produced by ultrashort pulses have previously only been observed in gases [Bra95, Bro97]. There has been some controversy as to whether the filaments are merely the time integrated track of the nonlinear focus which moves along the optical axis during the laser pulse [Bro97, Kos97] or whether a lightguide-like channel, along which part of the laser pulse propagates, develops owing to a combination of self-focussing in the normal medium and self defocussing after the onset of plasma formation [Bra95, Lan98]. The second interpretation is supported by the fact that the elongated breakdown region extends beyond the site of the linear focus. This extension cannot be explained by the first conjecture, since the movement of the nonlinear focus is always from the linear focus in the direction toward the incident laser beam [Mar75, Lan98].

Studies of self-focussing of ultrashort pulses in gases revealed that the filament contains only about 7-10% of the laser pulse energy and that the remaining energy propagates in an intensity "shoulder" surrounding the filament [Bro97, Lan98]. Thus, the energy distribution in the breakdown region is very inhomogeneous. The high energy density in the filament may explain why the shock pressure in femtosecond breakdown is quite high, although the overall degree of conversion of laser energy into mechanical energy is especially low. The low energy density in the "shoulder" region can contribute to the relatively high transmission of the femtosecond plasmas.

8.3 Clinical consequences

The trends discussed in Chapter 4 in a comparison of pico- and nanosecond pulses continue as the laser pulse duration is further reduced into the femtosecond range. The radiant exposure required for optical breakdown with a 100 fs pulse is only 1/160 of that for a 6 ns pulse and the ratio of the mechanical and vaporization energies falls from about 12:1 to 1:1. Thus, the disruptive effect of laser pulses is dramatically reduced and very fine laser effects can be achieved.

The energy density in the plasma is 30-40 kJ/cm^3 for 6 ns pulses and 6-11 kJ/cm^3 for picosecond pulses (cf. 2.3.5). These values are considerably higher than the energy density reached during corneal ablation based on linear absorption - even though the absorption coefficient of the plasma, $\alpha \approx 300$ cm^{-1} (cf. 2.3.3.6), is relatively low. With excimer laser corneal ablation ($\lambda = 193$ nm), the average energy density within the optical penetration depth $1/\alpha$ is only 1.25 kJ/cm^3. An ablation threshold of 0.05 J/cm^2 [Pet95] and an absorption coefficient $\alpha = 39900$ cm^{-1} [Pet96] were assumed in this calculation. At the erbium:YAG laser wavelength $\lambda = 2940$ nm, the ablation threshold is 0.15 J/cm^2 [Ren95] and the average energy density in the cornea within the optical penetration depth is 1.26 kJ/cm^3 (with $\alpha = 11900$ cm^{-1} [Mah78]). The energy density is so much higher in plasma-mediated ablation because the threshold for optical breakdown (453 J/cm^2 for 6 ns pulses and 13.5 J/cm^2 for 30 ps pulses, Table 8.1) is considerably higher than the linear ablation threshold. Only when the pulse length is reduced into the femtosecond range does the threshold for optical breakdown fall to about 1 J/cm^2 and the average energy density reach a value similar to that for pulsed laser ablation based on linear absorption.

Intraocular applications of femtosecond pulses will be impaired by self-focussing effects if the application site lies deep in the eye, where only relatively small focal angles can be used owing to the aperture restrictions given by the diameter of the pupil. Self-focusing decreases the localization of the laser effects because it leads to an elongation of the breakdown region, especially when pulse energies far above the breakdown threshold are used. Laser applications in the cornea, on the other hand, will not be impaired by self-focussing, since here (i) the path length through the nonlinear medium is very short and (ii) it is possible to work with a very large focal angle for which the displacement of the linear focus and the elongation of the breakdown region are particularly small.

9 Strategies for optimizing intraocular photodisruption

In this chapter the results from our studies of the mechanisms of optical breakdown and tissue effects of intraocular photodisruption are summarized with a view to optimizing the parameters of clinical laser applications, and the results of the first clinical tests with ultrashort pulses are reported. In addition, possible new applications of photodisruption with pico- and femtosecond pulses that go beyond the scope of hitherto conventional clinical photodisruption are discussed.

9.1 General considerations for parameter choices

9.1.1 Wavelength

The optimum wavelength for intraocular laser surgery lies in the range from about 800 nm to 1150 nm. In this range, the light is transmitted well in the eye, the linear absorption by melanin and blood in the ocular fundus is low, and the light cannot be seen by the patient (cf. 2.1.1.1). With the Nd:YAG (1064 nm) and Nd:YLF (1053 nm) lasers, there are two compact solid state lasers available in this wavelength range which can provide pulses in the nano- and picosecond range; Ti:sapphire ($660 \text{ nm} < \lambda < 1050 \text{ nm}$) or Nd:Glass (1057 nm) lasers can be used for treatment with femtosecond pulses.

9.1.2 Focal angle

The focal angle must be as large as possible for all intraocular laser applications, but small enough to avoid vignetting in the beam path. Large focal angles reduce the focal spot diameter and, thereby, lower the threshold energy for optical breakdown (at 22° it is about 1/4 of that at 8°; cf. 2.3.1.1). Large focal angles generate short and compact laser plasmas, and they ensure maximum absorption of the laser energy in the plasma, i.e., provide optimum "plasma shielding." Given the large divergence angle, the irradiance of the light on the retina or other structures lying behind the application site will be still further reduced. For every application site in the eye, a contact lens must be used that provides the maximum possible focal angle. Using a contact lens also substitutes the smooth surface of the glass for the sometimes optically irregular surface of the cornea. This substitution improves the focal quality and leads to a corresponding drop in the breakdown energy.

9.1.3 Laser modes and aberration free focussing

Minimization of the breakdown energy requires the use of an optimum laser mode and the avoidance of aberrations in the optical system. One can obtain a gaussian beam cross section at the laser focus with a minimum focal spot diameter and a correspondingly low breakdown energy either by running the laser in its fundamental mode or by using an unstable cavity with mirrors that have a position dependent reflectivity [Mag89]. Aberrations can be minimized by coupling the laser light as directly as possible to the optics of the operation microscope (also referred to as the laser slit lamp). In the first clinical nanosecond lasers (e.g., the Lasag Mikroruptor) and picosecond lasers (ISL 2001), the light was coupled through articulated mirror arms and this reduced the focal quality significantly (cf. Fig. 9.1). The prerequisite for direct coupling to the slit lamp is a compact laser system, which, thus far, is only available for nanosecond lasers.

The choice of a suitable contact lens, whose aplanatic point coincides with the plane of the application site in the eye, is also very important for avoiding aberrations. Focussing the laser light behind the aplanatic point of the contact lens leads to a dramatic rise in spherical aberrations [Rol86] and, thereby, to an increase in the breakdown threshold, as well as to a reduction in plasma absorption and a corresponding deterioration in plasma shielding (2.3.6). Tilting of the contact lens has similar negative consequences owing to coma and astigmatism.

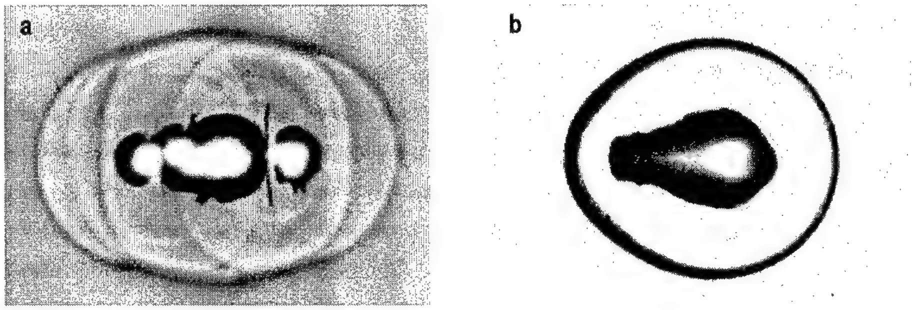

Fig. 9.1 (a) Plasma formation by 12 ns pulses (FM) from the Lasag Mikroruptor II, (b) plasma formation by the 6 ns laser pulses from the laboratory system described in Chapter 2.2. The pulse energy in each case was 5 mJ. In (a) the pulses were transported along an articulated mirror arm system, which impaired the beam quality.

9.1.4 Pulse duration

When the laser pulse duration is reduced from 6 ns to 30 ps, the radiant exposure threshold for optical breakdown is lowered by a factor of about 15, and a further reduction to 100 fs lowers the threshold by an additional factor of about 10 (cf. Section 8.2.1). (These data apply to wavelengths of 532 or 580 nm; no data are yet available for ultrashort pulses in the near IR.) The ratio of mechanical energy to vaporization energy falls from more than 12.5:1 for 6 ns pulses to about 3:1 for 30 ps pulses and (depending on the pulse energy) to between 1:1 and 0.25:1 for 100 fs pulses (cf. 8.2.4). Thus, picosecond and femtosecond pulses are advantageous if fine incisions with little disruptive side effects are desired.

The enhanced fineness of the tissue effects does, however, come at the price of a reduced energy coupling efficiency and inferior plasma shielding. For $\beta = 6$ the transmission rises from 10% for 6 ns pulses to 45% for 60 ps pulses and 50% for 100 fs pulses (cf. 8.2.3; all data are for 532 or 580 nm). Fortunately, this has no negative practical consequences, since the absorption decreases only by about half as the pulse duration is reduced, and the energy transmitted per pulse is - for constant β - always at least 8 times lower with ps- and fs-pulses than for nanosecond pulses (cf. Sections 2.3.3.5 and 8.2.3). Problems may arise when optical breakdown with femtosecond pulses is accompanied by self-focussing, so that the position of the plasma shifts, the plasma becomes longer, and the energy distribution is irregular (cf. 8.2.5).

To maintain a high surgical efficacy while making use of the high precision of ultrashort laser pulses with energies in the microjoule range, a series of pulses with repetition rates of a few hundred Hertz to a few kilohertz must be applied. The scale of single pulse effects is too small to perform surgery with a sequence of individually aimed pulses. The pulses are best applied in a scanning mode with computer controlled patterns (spot, line, circle, spiral, etc.). As the pulse duration is reduced, the single pulse energy and the distance over which mechanically induced side effects occur both decrease, but we observed that the total energy required to fulfill a given surgical task increases [Ger98]. This increase is partly a consequence of the use of pulse series instead of individual aiming, and partly due to the reduction of the disruptive effects which significantly contribute to tissue dissection with nanosecond pulses. The higher total energy has, however, exhibited no clinically significant drawbacks [Ger98].

In certain intraocular laser applications the fineness attainable with ultrashort pulses is greater than the aiming accuracy that a surgeon can achieve with manual aiming. In these cases, somewhat longer pulses are adequate or even advantageous. In each individual case it must be decided which fineness of the individual effect is really required in relation to the overall tissue mass to be removed or cut. Because of the high precision of the laser effects, ultrashort laser pulses are outstandingly suited to microscopic material processing and to the cutting of tissue, but because of the small extent of the effects, they are not effective for ablation of large volumes of tissue. This last point holds especially when the volume to be ablated (or vaporized) is not located at a tissue surface but is surrounded by tissue, because the delivery of the pulses is then further hindered by the cavitation bubbles created by previous pulses.

9.1.5 Repetition rate

The time between laser pulses should always exceed the oscillation period of the cavitation bubbles generated by breakdown. With nanosecond pulses, the maximum useful repetition rate for laser applications at tissue surfaces in aqueous humor or vitreous humor (e.g., in capsulotomies or iridotomies) is limited to about 1 kHz. With picosecond and femtosecond pulses, the repetition rate can be a few kHz because of the shorter lifetime of the bubbles. If the treatment site lies within a tissue (e.g., the cornea), the cavitation bubbles last a few seconds. All that can be done in this case is to separate the application sites spatially by scanning the laser beam in order to avoid interactions between the bubbles and subsequent laser pulses.

The repetition rate should also be low enough that no collateral thermal effects take place as a result of linear absorption in structures behind the laser focus. Linear absorption can play a role, for example, in vitreoretinal laser treatment at locations near the retina. The maximum possible repetition rate without thermal damage depends on the pulse energy, the distance to the retina, and the transmission of the plasma.

9.2 Specific laser applications

In the following the general considerations for choosing the system parameters will be used to set specifications for some already established clinical applications of photodisruption [Ste85, Fan89] and to discuss the question of whether pico- and femtosecond pulses can be used in new applications that require especially precise tissue effects.

9.2.1 Capsulotomies and membranotomies

Surgical treatment of cataracts involves removing the turbid interior of the lens through an opening in the anterior lens capsule and implanting an artificial intraocular lens in the capsular bag. A frequent postoperative complication is that a portion of the lens epithelium that has not been removed during the operation undergoes proliferation, causing clouding and fibrotic alterations of the posterior lens capsule. In order to remove this distortion of the optical path to the retina, the lens capsule is opened by photodisruption in a procedure called posterior capsulotomy.

Nanosecond laser pulses are preferable for posterior capsulotomies, precisely because of their disruptive action. The mechanical laser effects, in combination with the preexisting tension in the fibrotically altered lens capsule, are used to rupture the capsule. A capsulotomy can, therefore, be performed with a few single laser pulses. The capsule ruptures even if the laser is focussed slightly behind the capsule in order to avoid damage to the intraocular lens. If picosecond pulses are used, the capsule does not rupture, but has to be cut by the vaporizing action of the laser plasma. The cutting can be done, for example, by applying a large number of pulses in the form of line patterns whose direction is changed repeatedly during an operation in order to cut a polygon out of the capsule [Ger98]. This technique is relatively time consuming and requires a substantially higher total energy than a capsulotomy using nanosecond pulses. In addition, the application of line patterns involves a higher risk of causing serious damage to the curved surface of the intraocular lens by misaiming than does the application of single, individually aimed nanosecond pulses, even if the energy of the individual picosecond pulses is low [Ger98].

Picosecond pulses have been employed very successfully in pupilloplasty, and anterior capsulotomies were carried out on pseudophacic patients with major fibrotic alterations of the capsule [Ger98]. With nanosecond pulses very high pulse energies would have been required for a capsulotomy in these difficult cases, and the high energies would imply a high risk of side effects through collateral tearing. With a series of picosecond pulses, however, it was possible to cut the capsule smoothly (Fig. 9.2).

One can exploit the cutting ability of picosecond lasers to open the anterior lens capsule prior to a cataract operation. In this way the actual time of the operation would be reduced and the tension on the zonule fibers encountered in capsulorhexis can be avoided. A rapid anterior capsulotomy will require that

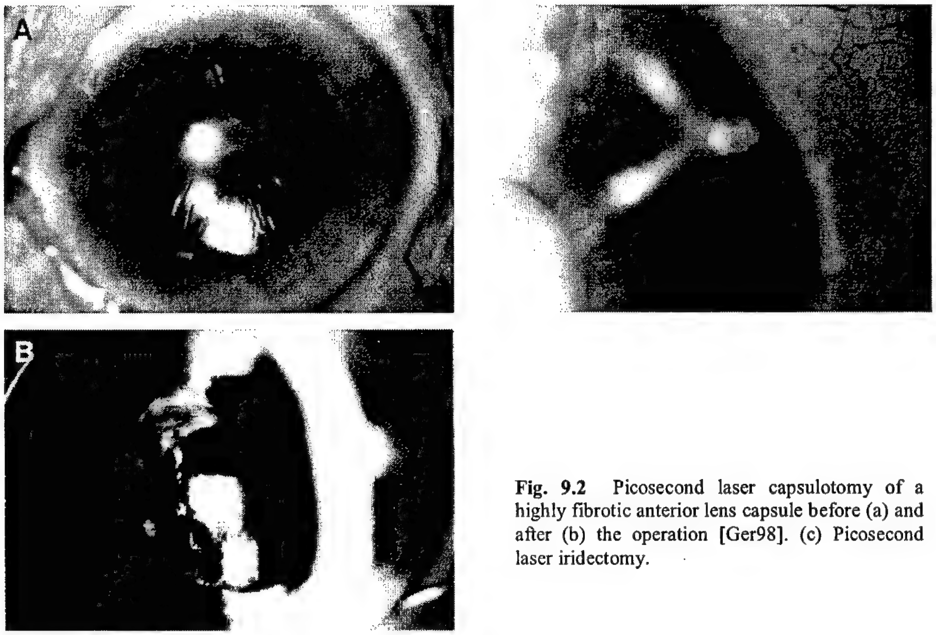

Fig. 9.2 Picosecond laser capsulotomy of a highly fibrotic anterior lens capsule before (a) and after (b) the operation [Ger98]. (c) Picosecond laser iridectomy.

the laser pulses be applied in a circular pattern with a diameter of 5-6 mm, which is not achievable with currently available clinical laser systems. Furthermore, the edge of the cut in a laser capsulotomy is somewhat coarser than the edge of a surgical capsulorhexis, so it may be more easily torn during the implantation of the intraocular lens [Ger98].

9.2.2 Fistulating operations

Fistulating operations serve to regulate the flow of aqueous humor, so as to avoid damaging pressure increases in the eye. Aqueous humor is produced in the ciliary body behind the iris and normally flows through the pupil into the anterior chamber and from there through the trabecula at the junction of the cornea and the sclera into Schlemm's canal, which forms a ring around that junction. In order to regulate the flow of aqueous humor, one creates (i) holes in the iris (iridotomies or iridectomies), (ii) fistulas from the anterior chamber through the sclera, through which the aqueous humor can flow out into the subconjunctival space (sclerostomies), or (iii) holes in the trabecular meshwork which should ease the discharge into Schlemm's canal (trabeculectomies, goniotomies) [Fan89].

Nanosecond iridotomies usually have a relatively small diameter and, especially for strongly pigmented irises, chipping off of part of the pigment sheath is often observed. Because of the disruptive character of the laser-tissue interaction, it is easy to damage the corneal endothelium [Ker85, Gab85, Win88], not only in the immediate vicinity of the application site through the direct action of the oscillating cavitation bubbles, but also at a distance of a few millimeters owing to the interaction between the gas bubble that remains after the oscillations of the cavitation bubble and the optical breakdown of the following laser pulses (cf. Chapter 6). The application of a series of picosecond pulses in a spiral pattern makes it possible to easily create large iridectomies with a diameter of 0.5 to 1 mm (Fig. 9.2c) with very little disruptive side effects [Ger98]. Because of the large diameter of the iridectomies and the lack of disruptive side effects, it was necessary to use about 80 times as much total energy as with ns pulses. The incidence of iris bleeding rose from 50% with nanosecond pulses to 64%, due to the larger diameter of the canal [Ger98]. However, no long-term complications owing to iris bleeding were observed with either pulse length.

Attempts to perform sclerostomies *ab interno* with nanosecond pulses led only to severe mechanical damage in the anterior chamber angle, but not to perforation of the sclera [Köl90]. The reasons for this are: (i) the beam path into the chamber angle through a gonioscopic contact lens is so strongly aberrated that the breakdown threshold is increased to several millijoules. (ii) Vignetting at the mirror aperture of the contact lens and at the opening of the sclerostomy channel prevents deepening it to the required length of several millimeters. (iii) The microscopic gas bubbles remaining after each pulse accumulate in the scleral canal and in the chamber angle and prevent focussing of the laser beam further into the canal. Attempts to perform sclerostomies with picosecond pulses were not very successful for the same reasons, although, because of the low breakdown energy, one can work much further above the threshold than with nanosecond pulses without producing strong disruptive effects. Gross, et al. (1994) have succeeded in performing sclerostomies with picosecond pulses, but they required 5-8 minutes and 92-155 J of laser energy.

The laser pulse can reach the application site most easily if only the trabecular meshwork is ablated to create access to Schlemm's canal. However, when such goniotomies were performed with nanosecond lasers, strong healing reactions were induced by the disruptive laser effects that soon nullified the fistulating action of the laser pulses [Kra77, Fan81]. Goniotomies have not yet been attempted clinically with picosecond pulses, although the prospects for success seem to be much better than with nanosecond pulses owing to their less disruptive mode of action.

9.2.3 Cataract emulsification

It would be desirable if a cataractous lens nucleus could be fragmented by photodisruption, so that the contents of the capsule could be aspirated through a small hole. This procedure would make it possible to fill the capsular bag with a transparent viscoelastic material, so that it might be possible to restore accommodation of the eye [Par86, Het94]. Ultrasonic phacoemulsification is not very well suited for this process, since it requires a 2.5-3 mm long incision [Eme83] and is extremely time consuming in the case of very hard lens nuclei. Studies by Vogel, et al. (1994b) have shown that nanosecond pulses are also not suitable, since, owing to the strong light scattering in a cataractous lens, very high energies of over 20 mJ may be required to produce optical breakdown in the posterior part of the lens. With such high pulse energies, there is a risk of capsule rupture when the scanning laser beam reaches clear parts of the lens, even when the laser pulses are focussed at a relatively large distance from the lens capsule. With picosecond pulses, on the other hand, energies of 3 mJ were sufficient to produce optical breakdown in every part of the lens in all of the lenses that were studied (n = 23, a random selection with different degrees of cataract). Thus far, further studies of this application have been hindered by the absence of suitable viscoelastic lens materials and the lack of a clinical picosecond laser system with sufficiently high pulse energies (the ISL 2001 system can produce pulses with an energy of up to only 0.4 mJ).

9.2.4 Vitreoretinal surgery

Shortly after the clinical introduction of intraocular photodisruption, surgeons began to dissect vitreous strands or membranes using nanosecond pulses [Fan82, Bro85, Gab92] or picosecond pulse trains from mode locked lasers [Tas91]. It turned out that for energies of 3-5 mJ in the pulses or pulse trains, respectively, a safety distance of about 3 mm must be maintained from the retina in order to avoid retinal or choroidal bleeding [Fan82, Bro85, Hie85]. When 200 μJ picosecond pulses were used, the range for retinal damage was, in contrast, only 0.5 mm [Vog94b]. Thus, picosecond pulses allow vitreoretinal surgery to be done closer to the retina than nanosecond pulses. One should, of course, avoid applications in the macular region, since here the risk of damage through inadvertent defocussing is too high. Therefore, attempts were first made to dissect vitreoretinal adhesions in the periphery of the fundus [Ger98]. However, no significant tissue effects could be obtained even with the maximum available pulse energy of 400 μJ per pulse. The reason is probably that the beam path was severely aberrated owing to the use of a Goldmann three-mirror contact lens and the oblique passage through the optical media. Besides that, a large part of the laser light was vignetted at the mirror of the Goldmann lens. Because aberrations increase the breakdown threshold (cf. 2.3.6) and, to make matters worse, the absorption in picosecond plasmas at energies just above the breakdown threshold is low (cf. 2.3.3.5), the surgical efficiency is low. With the currently available pulse energies from clinical picosecond lasers (400 μJ from the ISL 2001), vitreoretinal laser treatments are only possible in the anterior and middle vitreous humor (V. Marchi, personal communication) and in the central fundus region outside the macula.

9.2.5 Intrastromal refractive corneal surgery

One of the shortcomings of photorefractive keratectomy (PRK) with excimer lasers is that the epithelium and Bowman's membrane must be removed in order to ablate a layer of stroma. Haze in the anterior corneal region and a partial regression of the refractive changes are the consequences [Mar96].

An ideal refractive laser would vaporize a lenticule inside the corneal stroma without damage to the outer layers of the cornea. Attempts have been made to achieve such intrastromal photorefractive keratectomies (ISPRK) by means of plasma-mediated vaporization [Höh90, Nie93, Hab95, Mar96, Juh99, Sle99]. Nanosecond pulses proved unsuitable, since they cause excessive tearing in the corneal tissue [Höh90]. With picosecond pulses, it is possible to produce laser effects in the anterior third of the cornea without causing epithelial or endothelial damage [Vog97b] (cf. Fig. 9.3). However, the studies in Chapter 7 showed that, owing to cavitation, the tissue is mainly displaced and only a thin layer of tissue (at most, about 10 µm) can be vaporized. The removal of a lenticule of this thickness would correspond to a refractive change of only 0.85 diopters for a treatment zone with a diameter of 6 mm.

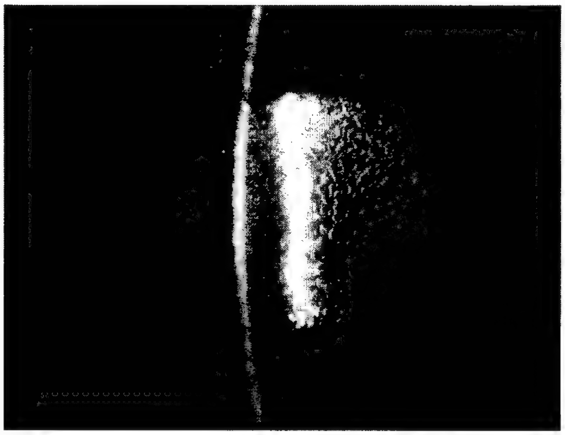

Fig. 9.3 Intrastromal laser effects following the application of a 2-mm-diameter spiral pattern of 40 ps, 40 µJ pulses with a distance of 15 µm between the foci of successive pulses [Vog97b].

It has, therefore, been proposed that the lenticule should not be vaporized, but be cut out of the corneal stroma by applying two layers of laser pulses and then removed mechanically through an incision in the cornea [Bry97, Kru97]. When picosecond pulses are used, the cavitation bubble dynamics again interferes with the cutting process, so that the laser incision acquires a spongy structure with bridges of tissue between the lenticule and the remaining tissue (Fig. 9.4).

For this reason, adjunctive conventional surgical procedures are necessary to detach the lenticule from the remaining corneal tissue, and the area of the incision is relatively coarse. The lenticule must, moreover, have a minimum thickness of about 100 µm if it is to be removed in a single piece (V. Marchi, personal communication), so that this technique is suited only to the correction of very strong myopia. Using femtosecond pulses leads to a distinct improvement in the result, since the breakdown threshold is low and cavitation effects are substantially lower than with picosecond pulses (E_{mech}/E_V falls from 3:1 with ps-pulses to below 0.25:1; cf. Chapter 8.2.4). Since a very large focal angle can be chosen for laser

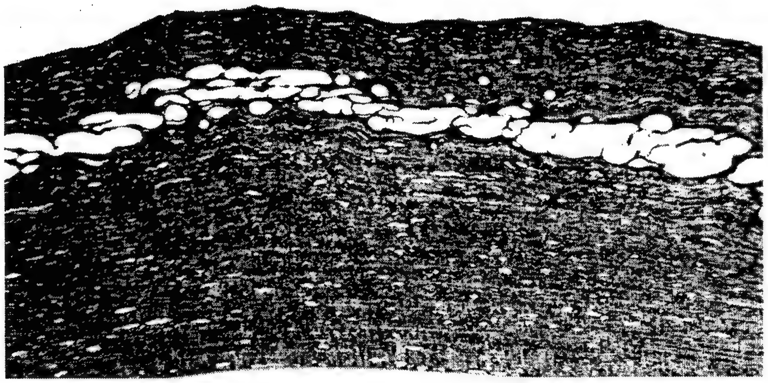

Fig. 9.4 Histological section through a cornea following application of 100 μJ pulses focused into a layer parallel to the corneal surface. The lateral separation between the individual application sites was 15 μm. [Vog97b].

applications in the cornea, self-focussing has no perturbative effect. It has been shown that femtosecond pulses can be used to cut out lenticules with smooth sectional planes in *ex vivo* primate eyes [Kur98, Juh99] and to create corneal thinning by intrastromal vaporization [Sle99].

In summary, the above discussion shows that the use of pico- and femtosecond pulses offer some specific improvements over conventional Nd:YAG surgery with nanosecond pulses, although no fundamentally new treatment possibilities have, as yet, been established. The greatest potential for innovation lies in intrastromal refractive corneal surgery using femtosecond pulses.

10 Summary

Photodisruption by short, intense laser pulses relies on nonlinear absorption of light in the focal region of a laser beam which creates a plasma with a temperature of several thousand Kelvin. This "optical breakdown" makes spatially limited energy deposition possible even inside of structures that are transparent at low light intensities. Noninvasive intraocular microsurgery is an important application. This dissertation is devoted to a study of the physical mechanisms of photodisruption in water and ocular media for the purpose of determining the optimum laser parameters for established laser surgical procedures, as well as for opening up possible new applications that may become possible by shortening the laser pulses from the nanosecond to the pico- and femtosecond range. Laser pulses with durations between 100 ns and 100 fs and wavelengths in the visible and infrared were focussed into water and ocular tissue. The accompanying events (plasma production, shock wave formation, cavitation) were tracked using fast framing and streak photography, as well as acoustic techniques. The resulting tissue effects were documented histologically and correlated with the physical mechanisms. The plasma production, shock wave formation, and cavitation dynamics were modeled theoretically and the results of the models compared with the experimental data.

When the intensity of the light is high, quasi-free electrons are created by multiphoton and cascade ionization, with an avalanche-like increase of the number of free charge carriers. This ionization leads to a rapid rise in the cross section for inverse bremsstrahlung in the focal region of the laser beam and, thus, to an increase in the absorption coefficient by several orders of magnitude bringing about a highly localized energy deposition. The irradiance I_{th} required for optical breakdown increases from $\approx 10^{10}$ W/cm^2 to $\approx 10^{13}$ W/cm^2 when the pulse length is reduced from 100 ns to 100 fs, while the radiant exposure threshold F_{th} decreases by about three orders of magnitude from $\approx 10^3$ J/cm^2 to ≈ 1 J/cm^2. The experimentally determined thresholds are in good agreement with the predictions of a theory for the time evolution of the density of free charge carriers that considers multiphoton and cascade ionization, as well as the losses of free electrons through diffusion, collisions, and recombination.

For pulse energies above the breakdown threshold, nanosecond and picosecond plasmas grow from the beam waist toward the incoming laser light. The movement of the plasma front and the maximum plasma length are determined by the motion of the intensity contour with $I = I_{th}$ during the laser pulse. With femtosecond plasmas, on the other hand, the breakdown front moves in the same direction as the laser pulse. Nevertheless, the plasma length scales in a manner similar to that for the longer pulse durations, as $(E/E_{th}-1)^{1/2}$.

Most of the incident laser energy will be absorbed in the plasma or transmitted through it. Scattering and reflection at the plasma play only a minor role, except when a plasma is formed at a surface. Scattering and reflection are unimportant because the free electron density reached within the breakdown volume is limited by the movement of the breakdown front during the laser pulse. Therefore, the plasma frequency does not exceed the frequency of the light and the reflectivity of the plasma remains low. At the threshold, nanosecond plasmas absorb more than 50% of the incident laser light, while picosecond and femtosecond plasmas absorb only 10%. The corresponding plasma absorption coefficients lie between 1000 cm^{-3} and 100 cm^{-3}. The dependence of the absorption coefficient on the pulse duration can be explained by solving the rate equation for the time evolution of the free carrier density.

The energy density in nanosecond plasmas is 30-40 kJ/cm^3, that is 15 times the enthalpy of vaporization of water. With shorter pulse durations, the energy density decreases continuously and is only about 1 kJ/cm^3 in femtosecond plasmas. The high energy density in nanosecond and picosecond plasmas causes an explosive expansion, which leads to the formation of a shock wave in the surrounding fluid and to the development of a cavitation bubble. In this manner, a large percentage of the absorbed laser energy is converted into mechanical energy (80-90% for nanosecond pulses and 50-70% for picosecond pulses), with about 2/3 going into the energy of the shock wave and 1/3 into the energy of the bubble. Only about 8% of absorbed energy from nanosecond pulses or about 30% of that from picosecond pulses is needed to vaporize the fluid or tissue in the breakdown volume. The high degree of conversion from light energy into mechanical energy explains the disruptive character of plasma-mediated laser surgery. The disruptive character decreases with the use of femtosecond pulses, since then only 10-20% of the absorbed laser energy is converted into mechanical energy.

The shock wave pressure at the plasma boundary and the pressure evolution during shock wave propagation in the surrounding fluid were determined by high-speed framing photography and by streak photography in combination with digital image processing. The pressure at the plasma boundary is about 5-10 GPa for nanosecond pulses and decreases to 0.1 GPa with femtosecond pulses. In the neighborhood of the plasmas, the pressure falls off as $r^{-1.7...-2.5}$ because of the strong energy dissipation at the shock front and, after a few millimeters, it is proportional to $r^{-1.06}$. A model of shock wave production based on the Gilmore model of cavitation bubble dynamics and the Kirkwood-Bethe hypothesis yielded good agreement with the experimental data. The model made it possible to calculate the shock wave energy in the near field of the source. A comparison with far-field hydrophone measurements showed that within the first 10 mm of the shock propagation 85-90% of the shock wave energy is dissipated, mostly in the immediate neighborhood of the plasma ($r < 0.2$ mm).

The cavitation bubbles created by the expansion of the heated plasma region expand in water to a radius ranging from about 100 µm for fs pulses to 2 mm for ns pulses. The bubbles collapse again owing to the static ambient pressure. The maximum bubble wall velocity during the expansion phase was determined by high-speed framing photography. It is 1800-2500 m/s for nanosecond pulses and 400-800 m/s for picosecond pulses. When the bubble collapses in the neighborhood of a rigid boundary, a jet-like fluid flow develops, which streams toward the boundary with a velocity of about 100 m/s. The jet flow leads to a concentration of energy at some distance from the laser focus with the creation of a water hammer pressure of about 75 MPa upon impact at the boundary.

Histological studies showed that macroscopic tissue effects are mostly caused by the expansion and collapse of cavitation bubbles. The range of the mechanical effects from single laser pulses is of the same order of magnitude as the radius of the cavitation bubbles. The shock waves produce tissue effects only at a cellular and subcellular level, because their duration is so short (less than 60 ns in the vicinity of the plasma) that they cannot cause a macroscopic tissue displacement. The shock wave action is restricted to the vicinity of the plasma, within a range of about 1/3 of the maximum bubble radius. Within this range, the shock waves cause a weakening of the tissue matrix, which facilitates the disruptive action of the bubble oscillations.

Cavitation effects lead to displacement and tearing of tissue within a range far greater than the volume of the vaporized tissue, especially with nanosecond and picosecond pulses. Photodisruption is, therefore, better suited for cutting and dissection than for vaporizing a large volume of tissue.

If exceptionally fine laser effects with little disruption are desired, femtosecond pulses give the best results. For them, the energy threshold for optical breakdown is very low (about 0.2 µJ for a 16° focal angle) and a very low fraction of the absorbed laser energy is converted into mechanical energy. One possible new area of application for femtosecond photodisruption is intrastromal refractive corneal surgery. A potential difficulty in the application of femtosecond pulses is that self-focussing has been observed for all focal angles that have been studied. However, self-focusing will not lead to a significant reduction in the surgical prospects if extremely large focal angles and low pulse energies are employed.

11 References

---

1. J. M. Aaron, D. L. M. Ireland, and C. Grey Morgan, Aberration effects in the interaction of focused laser beams with matter, J. Phys. D: Appl. Phys. **7**, 1907-1916 (1974).
2. F. Aitken and Denat A. McCluskey, An energy model for artificially generated bubbles in liquids, J. Fluid. Mech. **327**, 373-392 (1996).
3. A. J. Alcock, C. DeMichelis, K. Hamal, and B. A. Tozer, Expansion mechanism in a laser-produced spark, Phys. Rev. Lett. **20**, 1095-1097 (1968).
4. S. A. Akhmanov, R. V. Khokhlov, and A. P. Sukhorukov, Self-focusing, self-defocusing and self-modulation of laser beams, in: F. T. Arecchi and Schulz-Dubois, eds., *Laser Handbook*, North Holland (1972), Chap. E3, pp. 1151-1228.
5. V. A. Akulichev, Yu. Ya. Boguslavskii, A. I. Ioffe, and K. A. Naugol'nykh, Radiation of finite amplitude spherical waves, Sov. Phys. Acoust. **13**, 281-285 (1968).
6. A. P. Alloncle, D. Dufresne, and M. Autric, Visualisation of laser-induced vapor bubbles and pressure waves, in: J. R. Blake, et al., eds., *Bubble Dynamics and Interface Phenomena*, Kluwer Academic Pressures, Dordrecht, Netherlands (1994), pp. 365-371.
7. A. P. Alloncle, J. Vierne, M. Autric, and D. Dufresne, Laser-induced dielectric breakdown in a transparent liquid, SPIE Proc. **2273**, 98-107 (1994b).
8. R. V. Ambartsumyan, N. G. Basov, V. A. Boiko, V. S. Zuev, O. N. Krokhin, P. G. Kryukov, Yu. V. Senatskii, and Yu. Yu. Stoilov, Heating of matter by focused laser radiation, Sov. Phys. JETP **21**, 1061-1064 (1965).
9. R. E. Apfel, Acoustic Cavitation, in: *Methods of Experimental Physics*, Vol. 19, pp. 355-411 (1981).
10. D. Aron-Rosa, J. Aron, J. Griesemann, and R. Thyzel, Use of the neodymium:YAG laser to open the posterior capsule after lens implant surgery, J. Amer. Interaocul. Implant Soc. **6**, 352-354 (1980).
11. A. B. Arons, Underwater explosion shock wave parameters at large distances from the charge, J. Acoust. Soc. Amer. **26**, 343-346 (1954).
12. M. N. Asiyo-Vogel, R. Brinkmann, H. Norbohm, R. Eggers, H. Lubatschowski, H. Laqua, and A. Vogel, Histological analysis of thermal effects in laser-thermokeratoplasty and corneal ablation using Sirius-Red polarization microscopy, J. Cat. Refract. Surg. **23**, 515-526 (1996).
13. J. Aus der Au, F.H. Loesel, F. Morier-Genoud, M. Moser, and U. Keller, Femtosecond diode-pumped Nd:glass laser with more than 1 W of average output power, Opt. Lett. **23**, 271-173 (1998).
14. P. A. Barnes and K. E. Rieckhoff, Laser induced underwater sparks, Appl. Phys. Lett. **13**, 282-284 (1968).
15. M. Bass and H.H. Barrett, Avalanche breakdown and the probabilistic nature of laser-induced damage, IEEE J. Quantum Electron. **QE-8**, 338-343 (1972).
16. G. Bekefi, *Radiation Processes in Plasmas* , John Wiley & Sons, New York (1966).
17. C.E. Bell and J. A. Landt, Laser-induced high-pressure shock waves in water, Appl. Phys. Lett. **10**, 46-48 (1967).
18. T.B. Benjamin, Pressure Waves from collapsing cavities, in: *Proc. Second Symposium on Naval Hydrodynamics August 25-29, 1958*, Office of Naval Research Report No. ACR, 38, Washington, D.C. (1958), pp. 207-33.
19. T.B. Benjamin and A. T. Ellis, The collapse of cavitation bubbles and the pressures thereby produced against solid boundaries, Philos. Trans. Royal Soc. London **260**, 221-240 (1966).

20. G. Birkhoff, D.P. MacDougall, E.M. Pugh, and G. Taylor, Explosives with lined cavities, J. Appl. Phys. **19**, 563-582 (1948).

21. R. Birngruber and A. Vogel, Untersuchungen des Mechanismus der Laserdisruption in den transparenten Medien des Auges zur Ermittlung optimaler Laserparameter, DFG Project Bi 321/2-1 -- 2-4.

22. R. Birngruber, F. Hillenkamp, F. H. Stefani, and V. P. Gabel, Q-switched ruby laser damage of the rabbit eye lens, Adv. Ophthalmol. **34**, 158-63 (1977).

23. R. Birngruber, C.A. Puliafito, A. Gawande, C. Lin, R. Schoenkin, and J.G. Fujimoto, Femtosecond laser-tissue interactions: retinal injury studies, IEEE J. Quant. Electron. **23**, 1836-1844 (1987).

24. R. Birngruber, Y. Hefetz, J. Roider, U. Schmidt, J. G. Fujimoto, C. A. Puliafito, and A. Vogel, Raumliche Begrenzung von intraokularen Picosekunden-Photodisruptionseffekten, Ophthalmologe, **90**, 387-390 (1993).

25. F. G. Blake, Bjerknes forces in stationary sound fields, J. Acoust. Soc. Am. **21**, 5551 (1949).

26. J. R. Blake, B.B. Taib, and G. Doherty, Transient cavities near boundaries. Part 1. Rigid boundary, J. Fluid Mech. **170**, 479-497 (1986).

27. J. R. Blake and D. C. Gibson, Cavitation bubbles near boundaries, Ann. Rev. Fluid Mech. **19**, 99-123 (1987a).

28. J. R. Blake, B. B. Taib, and G. Doherty, Transient cavities near boundaries, Part 2. Free surface, J. Fluid Mech. **181**, 197-212 (1987b).

29. J. R. Blake, M.C. Hooton, P. B. Robinson, and R. P. Tong, Collapsing cavities, toroidal bubbles and jet impact, Phil. Trans. R. Soc. Lond. A, **355**, 537-550 (1997).

30. N. Bloembergen, Laser-induced electric breakdown in solids, IEEE J. Quantum Electr. **QE-10**, 375-386 (1974).

31. E. A. Boettner and J. R. Wolter, Transmission of the ocular media, Invest Ophthalmol. **1**, 776-783 (1962).

32. S. A. Boppart, C. A. Toth, W.P. Roach, and B.A. Rockwell, Shielding effectiveness of femtosecond laser-induced plasmas in ultrapure water, SPIE Proc. **1882**, 347-354 (1993).

33. F. P. Bowden and M. P. McOnie, Cavities and micro Munroe jets in liquids: Their role in explosion, Nature, **206**, 380-383 (1965).

34. F. P. Bowden, The formation of microjets in liquid under the influence of impact or shock, Phil. Trans. R. Soc. Lond. A, **260**, 94-95 (1966).

35. A. Braun, G. Korn X. Liu, D. Du, J. Squier, and G. Mourou, Self-channeling of high-peak-power femtosecond laser pulses in air, Opt. Lett. **20**, 73-75 (1995).

36. P. Brauweiler and C. Ohrloff, Das Polieren eiweissbeschlagener Intraokularlinsen mit dem Nd:YAG laser, Fortschr. Ophthamol. **87**, 78-79 (1990).

37. R.G. Brewer and K. E. Rieckhoff, Stimulated Brillouin scattering in liquids, Phys. Rev. Lett. **13**, 334-336 (1964).

38. A. Brodeur, C.Y. Chien, F. A. Ilkov, S. L. Chin, O. G. Kosareva, and V. P. Kandidov, Moving focus in the propagation of ultrashort laser pulses in air, Opt. Lett. **22**, 304-306 (1997).

39. G. C. Brown and W. E. Benson, Treatment of diabetic traction retinal detachment with the pulsed Neodymium-YAG laser, Am. J. Ophthalmol. **99**, 258-262 (1985).

40. D. B. Brown, W. J. O'Brien, and R. O. Schultz, The mechanism of ablation of corneal tissue by neodymium doped yttrium-lithium-flouride picosecond laser, Cornea **13**, 479-486 (1994).

41. E. A. Brujan, K. Nahen, P. Schmidt, and A. Vogel, Dynamics of laser-induced cavitation bubbles near an elastic boundary, J. Fluid Mech. **433**, 251-281 (2001).

42. E. A. Brujan, K. Nahen, P. Schmidt, and A. Vogel, Dynamics of laser-induced cavitation bubbles near elastic boundaries: Influence of the elastic modulus, J. Fluid Mech. **433**, 283-314 (2001).

43. J. H. Brunton, High speed liquid impact, Phil. Trans. R. Soc. Lond. A, **260**, 79-85 (1966).

44. M. R. Bryant and T. Juhasz, Predictability of picosecond laser keratomileusis (PLK) for high myopia, J. Refract. Surg. **13;** (1998).

45. M. R. C. Capon and J. Mellerio, Nd:YAG Lasers: Plasma characteristics and damage mechanisms, Lasers Ophthalmol. **1**, 95-106 (1986).

46. M. R. C. Capon, F. Docchio, and J. Mellerio, Investigations of multiple plasmas from ophthalmic Nd:YAG lasers, **1**, 95-106 (1986).

47. M. R. C. Capon, F. Docchio, and J. Mellerio, Nd:YAG laser photodisruption: an experimental investigation on shielding and multiple plasma formation, Graefe's Arch. Clin. Exp. Ophthalmol. **226**, 362-366 (1988).

48. E. F. Carome, C. E. Moiller, and N. A. Clark, Intense ruby-laser-induced acoustic impulse in liquids, J. Acoust. Soc. Am. **40**, 1462-1466 (1966).

49. E. F. Carome, E. M. Carreira, and C. J. Prochaska, Photographic studies of laser-induced pressure impulse in liquids, Appl. Phys. Lett. **11**, 64-66 (1967).

50. G. Cerrullo, S. De Silvestri, and V. Magni, Self-starting Kerr-lens mode locking of a Ti:sapphire laser, Opt. Lett. **19**, 1040-1042 (1994).

51. G. L. Chahine and P. F. Genoux, Collapse of a cavitating vortex ring, Trans ASME I: J. Fluids Eng. **105**, 400-405 (1983).

52. E. J. Chapyak, R. P. Godwin, and A. Vogel, A comparison of numerical simulations and laboratory studies of shock waves and cavitation bubble growth produced by optical breakdown in water, in: Steve Jacques, ed., Laser Tissue Interactions VIII, Proc. SPIE **2975**, 335-342 (1997).

53. E. J. Chapyak and R. P. Godwin, Physcal mechanisms of importance to laser thrombolysis. Proc. SPIE **3245**, 12-18, (1998).

54. M. Chaudri and J. Field, The role of rapidly compressed gas pockets in the initiation of condensed explosives, proc. R. Soc. Lond. A, **340**, 113-128 (1989).

55. C. C. Church, A theoretical study of cavitation generated by an extracorporeal shock wave lithotripter, J. Acoust. Soc. Am. **86**, 215-227 (1989).

56. S. F. Cleary, Laser pulses and the generation of acoustic transients in biological material, in: M. L. Wolbarsht, ed., *Laser Applications in Medicine and Biology, Vol. 3*, Plenum, New York (1977), pp. 175-219.

57. R. H. Cole, *Underwater Explosions,* Princeton University Press, Princeton, NJ (1948).

58. J. A. Cook, A. M. Gleeson, R. M. Roberts, and R. L. Rogers, A spark generated bubble model with semi-empirical mass transport, J. Acoust. Soc. Am. **101**, 1908-1920 (1997).

59. M. Cowperthwaite and R. Shaw, $C_v(T)$ equation of state for liquids, Calculation of the shock temperature of carbon tetrachloride, nitromethane, and water in the 100-kbar region, J. Chem. Phys. **53**, 555-560 (1970).

60. L. A. Crum, Bjerknes forces on bubbles in a stationary sound field, J. Acoust. Soc. Am. **57**, 1363-1370 (1975).

61. L. A. Crum, Rectified diffusion, Ultrasonics **22**, 215-223 (1984).

62. J. P. Cummings and J. T. Walsh, Tissue tearing caused by pulsed laser-induced ablation pressure, Appl. Opt. **32**, 494-503 (1993).

63. J. W. Daiber and H. M. Thompson, Laser-driven detonation waves in gases, Phys. Fluids **10**, 1162-1169 (1967).

64. G. P. Davidson and D. C. Emmony, A schlieren probe method for the measurement of the refractive index profile of a shock wave in a fluid, J. Phys. E: Sci Instrum. **13**, 92-97 (1980).

65. J. P. Dear, J. E. Field, and A. J. Walton, Gas compression and jet formation in cavities collapsed by a shock wave, Nature **322**, 505-508 ((1988).

66. M. Delius, Medical applications and bioeffects of extracorporeal shock waves, Shock Waves **4**, 55-72 (1994).

67. C. DeMichelis, Laser induced gas breakdown: a bibliographical review, IEEE J. Quantum Electron. **QE5**, 188-202 (1969).

68. F. Docchio, L. Dossi, and C. A. Sacchi, Q-switched Nd:YAG laser irradiation of the eye and related phenomena: An experimental study I. Optical breakdown determination for liquids and membranes, Lasers Life Sci. **1**, 87-103 (1986a).

69. F. Docchio, C. A. Sacchi, and J. Marshall, Experimental investigation of optical breakdown thresholds in ocular media under single pulse irradiation with different pulse durations, Lasers Ophthalmol. **1**, 83-93 (1986b).

70. F. Docchio, P. Regondi, M. R. C. Capon, and J. Mellerio, Study of the temporal and spatial dynamics of plasmas induced in liquids by nanosecond Nd:YAG laser pulses. 1: Analysis of the plasma starting times, Appl. Opt. **27**, 3661-3674 (1988a).

71. F. Docchio, P. Regondi, M. R. C. Capon, and J. Mellerio, Study of the temporal and spatial dynamics of plasmas induced in liquids by nanosecond Nd:YAG laser pulses. 2: Plasma luminescence and shielding, Appl. Opt. **27**, 3669-3674 (1988b).

72. F. Docchio and C. A. Sacchi, Shielding properties of laser-induced plasmas in ocular media irradiated by single Nd:YAG pulses of different durations, Invest. Ophthalmol. Vis Sci. **29**, 437-443 (1988c).

73. F. Docchio, Lifetimes of plasmas induced in liquids and ocular media by single Nd:YAG pulses of different duration, Europhys. Lett. **6**, 407=412 (1988d).

74. F. Docchio, Spatial and temporal dynamics of light attenuation and transmission by plasmas induced in liquids by nanosecond Nd:YAG laser pulses, Nuovo Cimento **13**, 87-98 (1991).

75. A. G. Doukas, A. D. Zweig, J. K. Frisoli, R. Birngruber, and T. Deutsch, Non-invasive determination of shock wave pressure generated by optical breakdown, Appl. Phys. B **53**, 237-245 (1991).

76. A. G. Doukas, D. J. McAucliff, and T. J. Flotte, Biological effects of laser-induced shock waves: Structural and functional cell damage in vitro, Ultrasound Med. Biol. **19**, 137-146 (1993).

77. A. G. Doukas, D. McAucliffe, S. Lee, V. Venugopalan, and T. Flotte, Physical factors involved in stress-wave-induced cell injury: the effect of the stress gradient, Ultrasound Med. Biol. **21**, 961-967 (1995).

78. T. Douki, S. Lee, K. Dorey, T. J. Flotte, T. F. Deutsch, and A. Doukas, Stress-wave-induced injury to retinal pigment epithelium cells in vitro, Lasers Surg. Med. **19**, 249-259 (1996).

79. T. A. Dunina, S. V. Egerev, L. M. Lyamshev, K. A. Naugol'nykh, and A. E. Pashin, Hydrodynamic effects in the optical breakdown of a liquid, Sov. Phys. Acoust. **28**, 116-121 (1982).

80. G. E. Duvall and G. R. Fowles, Shock waves, in: R. S. Bradley, ed., *High Pressure Physics and Chemistry*, Academic Press, New York (1963), pp. 209-291.

81. K. J. Ebeling, Zum Verhalten kugelformiger, lasererzeugter Kavitationsblasen in Wasser, Acustica **40**, 229-239 (1978).

82. W. Eisenmenger, Experimentelle Bestimmung der Stossfrontdicke aus dem akustischen Frequenzspekrum elektromagnetisch erzeugter Stosswellen in flussigkeiten bei einem Stossdruckbereich von 10 atm bis 100 atm, Acustica **14**, 187-204 (1964).

83. J. M. Emery and D. J. McIntyre, *Extracapsular Cataract Surgery*, CV Mosby, St. Louis (1983).

84. L. R. Evans and Morgan C. Grey, Lens aberration effects in optical-frequency breakdown of gases, Phys. Rev. Lett. **22**, 1099-1102 (1969).

85. M. W. Evans, H. Harlow, and B. D. Meixner, Interaction of shock or rarefaction with a bubble, Phys. Fluids **5**, 651-656 (1962).

86. F. Fankhauser, P. Roussel, J. Steffen, E. van der Zypen, and A. Chrenkova, Clinical studies on the efficiency of high power laser radiation of some structures of the anterior segment of the eye, Int. Ophthalmol. **3**, 129-139 (1981).

87. F. Fankhauser, H. P. Loertscher, and E. van der Zypen, Clinical studies on high and low laser power radiation upon some structures of the anterior and posterior segments of the eye, Int. Ophthalmol. **5**, 15-32 (1982).

88. F. Fankhauser and S. Kwasniewska, Neodymium:yttrium-aluminum-garnet laser, in: F. A. L'Esperance. ed., *Ophthalmic Lasers*, Third Edition, Mosby, St. Louis, MO (1989), pp. 781-886.

89. M. D. Feit and J. A. Fleck, Effect of refraction on spot size dependence of laser-induced breakdown, Appl. Phys. Lett. **24**, 169-172 (1974).

90. M. P. Felix and A. T. Ellis, Laser-induced liquid breakdown -- a step by step account, Appl. Phys. Lett. **19**, 484-486 (1971).

91. Q. Feng, J. V. Moloney, A. C. Newell, E. M. Wright, K. Cook, P. K. Kennedy, D. X. Hammer, B. A. Rockwell, and C. R. Thompson, Theory and simulation on the threshold of water breakdown induced by ultrashort laser pulses, IEEE J. Quantum Electron. **33**, 127-137 (1997).

92. E. B. Flint and K. S. Suslick, The temperature of cavitation, Science **253**, 1397-1399 (1991).

93. W. M. Flook and D. F. Hornig, Experimental determination of the thickness of weak shock fronts in liquids, J. Chem. Phys. **23**, 816-821 (1955).

94. A. Frieser, Experimentelle Untersuchungen des stosswelleninduzierten Gasblasenkollapses --- ein Nebenwirkungsmechanismus bei der intraokularen Fotodisruption, thesis, Fachbereich Physikalische Technik der Fachhochschule München (1991).

95. S. Fujikawa and T. Akamatsu, Effects of the non-equilibrium condensation of vapour on the pressure wave produced by the collapse of a bubble in a liquid, J. Fluid Mech. **97**, 481-512 (1980).

96. S. Fujikawa and T. Akamatsu, Effects of heat and mass transfer on the impulsive pressure developed by the bubble collapse, Bulletin JSME **28**, 267-273 (1985).

97. J. G. Fujimoto, W. Z. Lin, E. P. Ippen, C. A. Puliafito, and R. F. Steinert, Time-resolved studies of Nd:YAG laser-induced breakdown, Invest. Ophthalmol. Vis. Sci. **26**, 1771-1777 (1985).

98. V. P. Gabel, R. Birngruber, and F. Hillenkamp, Visible and near infrared light absorption in pigment epithelium and choroid, *Excerpta Medica, International Congress Series No. 450 XXIII Concilium Ophthalmologicum, Kyoto*, Elsevier, Amsterdam and Oxford (1978), pp. 659-662.

99. V. P. Gabel, L. Neubauer, H. Zink, and R. Birngruber, Ocular side effects following Neodymium:YAG laser irradiation, Int. Ophthalmol. Clin. **25**, 137-149 (1985).

100. V. P. Gabel, Lasers in vitreoretinal therapy, Ann. Ophthalmic Laser Surg. **1**, 75-89 (1992).

101. A. Galvanauskas, A. Hariharan, D. Harter, M. A. Arbore, and M. M. Fejer, High-energy femtosecond pulse amplification in a quasi-phase-matched parametric amplifier, Opt. Lett. **23**, 210-212 (1989).

102. G. Geerling, J. Roider, U. Schmidt-Erfurth, K. Nahen, E. S. el-Hifnawi, H. Laqua, and A. Vogel, Initial clinical experience with the picosecond Nd:YAG laser for intraocular therapeutic applications, Brit. J. Ophthalmol. **82**, 504-509 (1998).

103. F. R. Gilmore, The growth or collapse of a spherical bubble in a viscous compressible fluid, Calif. Inst. Techn. Rep. **26-4** (1952).

104. S. J. Gitomer and R. D. Jones, Laser-produced plasmas in medicine, IEEE Trans. Plasma Sci. **19**, 1209-1219 (1991).

105. M. E. Glinsky, P. A. Amendt, D. S. Bailey, R. A. London, A. M. Rubenchik, and M. Strauss, Extended Rayleigh model of bubble evolution with material strength compared to detailed dynamic simulations, in: Steve Jacques, ed., Laser Tissue Interactions VIII, SPIE Proc. **2975**, 318-334 (1997).

106. R. P. Godwin, C. G. M. van Kessel, J. N. Olsen, P. Sachsenmaier and R. Sigel, Reflection losses from laser-produced plasmas, Z. Naturforsch. **32a**, 1100-1107 (1977).

107. R. P. Godwin, Multilayer optics provides laser-plasma-coupling insight, Appl. Opt. **34**, 572-580 (1995).

108. R. A. Graham, Shock-induced electrical activity in polymeric solids. A mechanically induced bond scission model, J. Chem. Phys. **83**, 3048-3056 (1979).

109.D. Grand, A. Bernas, and E. Amouyal, Photoionisation of aqueous indole; conducting band edge and energy gap in liquid water, Chem Phys. **44**, 73-79 (1979).

110.C. Grey Morgan, Laser induced breakdown in gases, Rep. Prog. Phys. **38**, 621-665 (1975).

111.M. C. M. Grimbergen, R. M. Verdaasdonk, and C. F. P. van Swol, Correlation of thermal and mechanical effects of the holmium laser for various clinical applications, SPIE Proc. 3254, 69-79 (1998).

112.R. L. Gross, O. Oram, T. D. Severin, and S. Orengo-Nania, Gonioscopic ab interno Nd:YAG Laser sclerostomy in human cadaver eyes, Invest. Ophthalmol. Vis. Sci. **35(4)**, 2171 (1994).

113.L. Haar, J. S. Gallagher, and G. S. Kell, A thermodynamic surface for water: The formulation and computer programs, Laboratory Report NRCC 19178, National Research Council Canada (1981).

114.M. S. Habib, M. G. Speaker, R. Kaiser, and T. Juhasz, Myopic intrastromal photorefractive keratectomy with the neodymium-yttrium lithium fluoride picosecond laser in the cat cornea, Arch. Ophthalmol. **113**, 499-505 (1995).

115.D. X. Hammer, R. J. Thomas, G. D. Noojin, B. A. Rockwell, P. A. Kennedy, and W. P. Roach, Experimental investigation of ultrashort pulse laser-induced breakdown thresholds in aqueous media, IEEE J. Quantum Electr. **QE-3**, 670-678 (1996).

116.D. X. Hammer, E. D. Jansen, M. Renz, G. D. Noojin, R. J. Thomas, J. Noack, A. Vogel, B. A. Rockwell, and A. J. Welch, Shielding properties of laser-induced breakdown in water for pulse durations from 5 ns to 125 fs, Appl. Opt. **36**, 5630-5640 (1997a).

117.D. X. Hammer, G. D. Noojin, R. J. Thomas, R. A. Hopkins, P. K. Kennedy, J. J. Druessel, B. A. Rockwell, A. J. Welch, and C. P. Cain, Measurement of the self-focussing threshold in aqueous media by ultrashort laser pulses, SPIE Proc. **2975**, 163-172 (1997b).

118.P. E. Hamrick and S. F. Cleary, Breakage of tobacco mosaic virus by acoustic transients: a hydrodynamic model, J. Acoust. Soc. Am. **45**, 1-6 (1969).

119.P. Harris and H. N. Presles, The shock induced electrical polarization of water, J. Chem. Phys. **74**, 6864-6866 (1981).

120.P. Harris and H. N. Presles, Reflectivity of a 5.8 kbar shock front in water, J. Chem. Phys. **77**, 5157-5164 (1982).

121.R. W. Hellwarth, *Advances in Quantum Electronics*, Columbia University Press, New York (1961), p. 334.

122.H. J. Hettlich, K. Lucke, M. N. Asiyo-Vogel, M. Schulte, and A. Vogel, Lens refilling and endocapsular polymerization of an injectable intraocular lens: In vitro and in vivo studies of potential risks and benefits. J. Cataract Refract. Surgery **20**, 115-123 (1994).

123.R. Hickling and M.S. Plesset, Collapse and rebound of a spherical bubble in water, Phys. Fluids **7**, 7-14 (1964).

124.H. Hiemer, H. Hutter, V. P. Gabel, and Birngruber, Netzhautschäden bei der Neodym:YAG Laserchirurgie im Glaskörperbereich, Fortschr. Ophthalmol. **82**, 447-449 (1985).

125.F. Hillenkamp, Interaction between laser radiation and biological tissue, in: F. Hillenkamp, R. Pratesi, and C. A. Sacchi, eds., *Lasers in Biology and Medicine. NATO Advanced Study Institutes Series A34,* Plenum Press, New York and London (1980), pp. 37-68.

126.K. Hinsch and E. Brinkmeyer, Investigation of very short cavitation shock waves by coherent methods, SPIE Proc. **97**, 166-171 ((1976).

127.P. P. Ho and R. R. Alfano, Optical Kerr effect in liquids, Phys. Rev. A **20**, 2170-2187 (1979).

128.H. Höh and K. K. W. Becker, Intrastromale Keratorhexis mit dem Nd:YAG laser: Ein möglicher Weg der refraktiven Chirurgie? Klin. Mbl. Augenheilk. **197**, 480487 (1990).

129.N. C. Holmes, W. J. Nellis, W. B. Graham, and G. E. Walrafen, Raman spectroscopy of shocked water, in: Y. M. Gupta, ed., *Shock Waves in Condensed Matter,* Plenum Press, New York and London (1986), pp. 191-200.

130.T. P. Hughes, *Plasmas and Laser Light*, Adam Hilger, Bristol (1975), 606 pp.

131. S. C. Jones, P. Bräunlich, R. T Casper, X. A. Shen, and P. Kelly, Recent progress on laser-induced modifications and intrinsic bulk damage of wide-gap optical materials, Opt. Eng. **28**, 1039-1068 (1989).

132. C. Joshi and P. Corkum, Interaction of ultra-intense light with matter, Phys. Today, Jan. 1995, 36-43.

133. T. Juhasz, X. H. Hu, L Turi, and Z. Bor, Dynamics of shock waves and cavitation bubbles generated by picosecond laser pulses in corneal tissue and water, Lasers Surg. Med. **15**, 91-98 (1994).

134. T. Juhasz, G. A. Kastis, C. Suárez, Z. Bor, and W. E. Bron, Time-resolved observations on shock waves and cavitation bubbles generated by femtosecond laser pulses in corneal tissue and water, Lasers Surg. Med. **19**, 32-31 (1996).

135. T. Juhasz, F. H. Loesel, R. M. Kurtz, C. Horvath, J. F. Bille, G. and Mourou; Corneal refractive surgery with femtosecond lasers. IEEE J. Sel. Top. Quantum Electron. **5**:902-910 (1999).

136. K. Jungnickel and A. Vogel, Efficiency of bursts in intraocular Nd:YAG laser surgery, Lasers Light Ophthalmol. **5**, 95-99 (1992).

137. K. Jungnickel, Experimentelle Untersuchungen zur Kavitationsblasendynamik und ihrer rolle bei der Disruption und Fragmentatierung von biologischem Material, Dissertation, Technisch-Naturwissenschaftliche Fakultät der Medizinischen Universität zu Lübeck (1995).

138. B. L. Justus, A. L. Huston, and A. J. Campillo, Flourescence thermometry of shocked water, App. Phys. Lett. **47**, 1159-1161 (1985).

139. L. V. Keldysh, Ionization in the field of a strong electromagnetic field, Sov. Phys. JETP **20**, 1307-1314 (1965).

140. P. K. Kennedy, A first-order model for computation of laser-induced breakdown thresholds in ocular and aqueous media: Part I - Theory, IEEE J. Quantum Electron. **QE-31**, 2241-2249 (1995a).

141. P. K. Kennedy, S. A. Boppart, D. X. Hammer, B. A. Rockwell, G. D. Noojin, and W. P. Roach, A first-order model for computation of laser-induced breakdown thresholds in ocular and aqueous media: Part II -- Comparison to experiment, IEEE J. Quantum Electron. **QE-31**, 2250-2257 (1995b).

142. P. K. Kennedy, D. X. Hammer, and B. A. Rockwell, Laser-induced breakdown in aqueous media, Progr. Quantum Electron. **21**, 155-248 (1997).

143. M. G. Muir Kerr and E. S. Sherrard, Damage to the corneal endothelium during Nd:YAG photodisruption, Br. J. Ophthalmol. **69**, 77-85 (1985)

144. B. M. Kim, M. D. Feit, A. M. Rubenchik, D. M. Gold, B. C. Stuart, and L. B. Da Silva, ultrashort pulse laser ablation of biological tissue, SPIE Proc. 3254, 203-210 (1998).

145. J. G. Kirkwood, H. A. Bethe, Progess report on "The pressure wave produced by an underwater explosion I," (1942) in: W. W. Wood, ed., *John Gamble Kirkwood Collected Works, Shock and Detonation Waves,* Gordon and Breach, New York (1967), pp. 1-34.

146. R. T. Knapp, J. W. Daily, and F. G. Hammitt, *Cavitation*, McGraw-Hill, New York (1971), pp. 117-131.

147. T. Kodama, M. R. Hamblin, and A. Doukas, Cytoplasmic molecular delivery with shock waves: Importance of impulse. Biophys. J. **79**, 1821-1832 (2000).

148. W. Koechner, *Solid State Laser Engineering*, Springer, Berlin (1988), 606 pp.

149. R. Köll, Experimentelle Untersuchungen zur Sklerostomie mittels Nd:YAG Laser, Dissertation, Medizinische Fakultät der Ludwig-Maximilians-Universität München (1990).

150. O. G. Kosareva, V. P. Kandidov, A. Brodeur, C. Y. Chien, and S. L. Chin, Conical emission from laser-plasma interactions in the filamentation of powerful ultrashort laser pulses in air, Opt. Lett. **22**, 1332-1334 (1997).

151. M. M. Krasnov, Q-switched laser iridectomy and Q-switched laser goniopuncture, Adv. Ophthalmol. **34**, 192-196 (1977).

152. R. R. Krueger, A. J. Quantock, T. Juhasz, M. Ito, K. K. Assil, and D. J. Schanzlin, Ultrastructure of picosecond laser intrastromal photodisruption, J. Refract. Surg. **12**, 607-612 (1996).

153.R. R. Krueger, T. Juhasz, and V. Marchi, The picosecond laser as a nonmechanical microkeratome for LASIK and picosecond laser keratomileusis (PLK), J. Refract. Surg. **13**, (1998).

154.A. Kucera and J. R. Blake, Computational modelling of cavitation bubbles near boundaries, in: J. Noyce and C. Fletcher, *Computational Techniques and Applications CTAC-87*, North Holland (1988), pp. 391-400.

155.R. M. Kurtz, C. Horvath, H.H. Liu, and T. Juhasz, Optimal laser parameters for intrastromal corneal surgery, SPIE Proc. **3255**, 56-66 (1998).

156.H. Kuttruf, Über den Zusammenhang zwischen der Sonoluminsrenz und der Schwingungskavitation in Flussigkeiten, Acustica **12**, 230-254 (1962).

157.L. D. Landau and E. M. Lifschitz, *Hydrodynamik*, Akademie Verlang, Berlin, 5. Auflage (1991).

158.H. R. Lange, G. Grillon, J. F. Ripoche, M. A. Franco, B. Lamouroux, B. A. Prade, A. Mysyrowicz, E. T. J. Nibbering, and A. Chiron, Anomalous long-range propagation of femtosecond laser pulses through air: moving focus or pulse self guiding?, Opt. Lett. **23**, 120-122 (1998).

159.W. Lauterborn, High-speed photography of laser-induced breakdown in liquids, Appl. Phys. Lett. **21**, 27-29 (1972).

160.W. Lauterborn, Kavitation durch Laserlicht, Acustica **31**, 51-78 (1974).

161.W. Lauterborn and H. Bolle, Experimental investigations of cavitation bubble collapse in the neighborhood of a solid boundary, J. Fluid Mech. **72**, 391-399 (1975).

162.W. Lauterborn and K. Ebeling, High-speed holography of laser-induced breakdown in liquids, Appl. Phys. Lett. **31**, 663-664 (1977).

163.W. Lauterborn, Cavitation bubble dynamics -- new tools for an intricate problem, Appl. Sci. Res. **38**, 165-178 (1982).

164.W. Lauterborn and A. Vogel, Modern optical techniques in fluid mechanics, Ann. Rev. Fluid Mech. **16**, 223-244 (1984).

165.W. Lauterborn and W. Hentschel, Cavitation bubble dynamics studied by high speed photography and holography: part one, Ultrasonics **23**, 260-267 (1985).

166.S. Lee, T. Anderson. H. Zhang, T. J. Flotte, and A. Doukas, Alteration of cell membrane by stress waves in vitro, Ultrasound Med. Biol. **22**, 1285-1293 (1996).

167.T. G. Leighton, *The Acoustic Bubble*, Academic Press, London (1994).

168.M. B. Lesser and J. E. Field, The impact of compressible liquids, Ann. Rev. Fluid Mech. **15**, 97-122 (1983).

169.T. G. van Leeuwen, J. H. Meertens, E. Velema, M. J. Post, and C. Borst, Intraluminal vapor bubble induced by excimer laser pulse causes microsecond arterial dilatation and invagination leading to extensive wall damage in the rabbit, Circulation **87**, 1258-1263 (1993).

170.L. B. Leverett, J. D. Hellums, C. P. Alfrey, and E. C. Lynch, Red blood cell damage by shear stress, Biophys. J. **12**, 257-273 (1972).

171.A. Lezzi and A. Prosperetti, Bubble dynamics in a compressible liquid. Part 2. Second-order theory. J. Fluid Mech. **185**, 289-321 (1987).

172.J. Lighthill, *Waves in Fluids*, Cambridge University Press, Cambridge, UK (1978).

173.C. P. Lin, Y. K. Weaver, R. Birngruber, J. G. Fujimoto, and C. A. Puliafito, Intraocular microsurgery with a picosecond Nd:YAG laser, Laser Light Ophthalmol. **15**, 44-53 (1994).

174.H.P. Loertscher, Laser-induced breakdown for ophthalmic applications, in: S. L. Trokel, ed., *YAG Laser Opthalmic Microsurgery*, Appleton-Century-Crofts, Norwalk, Conn. (1983), pp. 39-66.

175.E. Y. Lo, H. Peschek, and D. I. Rosen, A hydrodynamic model for the laser-induced fragmentation of calculi, Lasers Life Sci. **3**, 233-244 (1990).

176.M. T. Loy and Y. R. Shen, Study of self-focusing and small-scale filaments of light, IEEE J. Quantum Electron. **QE-9**, 409-422 (1973).

177.M. Ludwig, L. C. Busch, K. Jungnickel, and A. Vogel, Präparation critical-point-getrockneter Mausenembryonen mit einem Laserskalpell, Ann. Anat. **176**, 559-563 (1994).

178.P. A. Lush, R. J. Wood, and L. J. Carpanini, Pitting in soft aluminum produced by spark-induced cavitation bubbles, in: J. E. Field, ed., *Proc. 6th Int. Conf. on Erosion by Liquid and Solid Impact* Cavendish Laboratory, Cambridge, paper 5 (1983).

179.G. G. Luther, J. V. Moloney, A. C. Newell, and E. M. Wright, Self-focusing threshold in normally dispersive media, Opt. Lett. **19**, 862-864 (1994).

180.L. M. Lyamshev, Optoacoustic sources of sound, Sov. Phys. Usp. **24**, 977-995 (1981).

181.S. P. Lyon, J. D. Johnson, ed., SESAME: The Los Alamos National Laboratory EOS Data, Report LA-UR-92-3407 (1992).

182.M. Ludwig, L. C. Busch, K. Jungnickel, and A. Vogel, Präparation critical-point-getrockneter Mausenembryonen mit einem Laserskalpell, Ann. Anat. **176**, 559-563 (1994).

183.J. J. Machat, ed., *Excimer Laser Refractive Surgery. Practice and Principles.* Slack, Thorofare, NJ (1996).

184.V. Magni, S. DeSilvestri, and A. Cybo-ottone, Resonators with variable reflectivity mirrors, in: D. R. Hall and P. E. Jackson, ed., *The Physics and Technology of Laser Resonators*, Adam Hilger, Bristol and New York (1989), pp. 94-105.

185.E. F. Maher, Transmission and absorption coefficients for ocular media of the rhesus monkey. *Report SAM-TR-78-32,* USAF School of Aerospace Medicine, Brooks Air Force Base, Texas, USA (1978).

186.M. A. Mainster, D. H. Sliney, C. D. Belcher, and S. M. Buzney, Laser photodisruptors. Damage mechanisms, instrument design and safety, Ophthalmology **90**, 973-991 (1983).

187.P. D. Maker, R. W. Terhune, and C. M. Savage, Optical third harmonic generation, in: E. Grivet and N. Bloembergen, eds., *Proc. 3rd Int. Conf. Quantum Electron,* Dunod, Paris (1964), pp. 1559-1576.

188.J. H. Marburger, Self-focusing: Theory, Progr. Quantum Electron. **4**, 35-110 (1975).

189.V. Marchi, A. Gualano, G. Zumbo, and S. Marchi, Intrastromal photorefractive keratectomy for myopia by Nd:YLF picosecond laser, J. Refract. Surg. **12**, S284-S287 (1996).

190.D. Maurice, The Cornea and Sclera, in: H. Davison, ed., *The Eye, Vol. 1b*, Academic Press, Orlando (1984), pp. 1-158.

191.J. Mellerio, M. R. C. Capon, and F. Docchio, Nd:YAG lasers: a potential hazard from cavitation bubble behaviour in anterior chamber procedures?, Lasers Ophthalmol. **1**, 185-190 (1987).

192.R. G. Meyerandt and A. F. Haught, Gas breakdown at optical frequencies, Phys. Rev. Lett. **11**, 401-403 (1963).

193.R. G. Meyerandt and A. F. Haught, Optical-energy absorption and high-density plasma production, Phys. Rev. Lett. **13**, 7-9 (1964).

194.G. A. Mourou, C. P. J. Barty, and M. D. Perry, Ultrahigh-intensity lasers: Physics of the extreme on a tabletop, Phys. Today Jan. 1998, 22-28 (1998).

195.M. Müller, Stosswellenfokussierung in Wasser, PhD. thesis, Rheinisch-Westfälisch Technische Hochschule, Aachen (1987).

196.C. E. Munroe, Modern explosives, Scribners Mag. **3**, 563 (1888).

197.K. Nahen and A. Vogel, Plasma formation in water by picosecond and nanosecond Nd:YAG laser pulses -- Part II: Plasma transmission, scattering and reflection, IEEE J. Selected Topics Quantum Electron. **2**, 861-871 (1996).

198.C. F. Naudé and A. T. Ellis, On the mechanism of cavitation damage by nonhemispherical cavities collapsing in contact with a solid boundary, Trans. ASME D: J. Basic Eng. **83**, 648-656 (1961).

199.E. T. J. Nibbering, M. A. Franco, B. S. Prade, G. Grillon, C. Le Blanc, and A. Mysyrowicz, Measurement of the nonlinear refractive index of transparent materials by spectral analysis after nonlinear propagation, Opt. Comm. **119**, 479-484 (1993).

200.H. Niedrig, ed., *Bergmann Schaefer: Lehrbuch der Experimentalphysik, Band 3 Optik,* Walter der Gruyter, Berlin and New York (1993).

201.M. H. Niemz, E. G. Klancnik, and J. F. Bille, Plasma-mediated ablation of corneal tissue at 1053 nm using a Nd:YLF oscillator/regenerative amplifier laser, Lasers Surg. Med. **11**, 426-431 (1991).

202.M. H. Niemz, T. P. Hoppeler, T. Juhasz, and J. F. Bille, Intrastromal ablations for refractive corneal surgery using picosecond infrared laser pulses, Lasers Light Ophthalmol. **5**, 149-155 (1993).

203.M. H. Niemz, Threshold dependence of laser-induced optical breakdown on pulse duration, Appl. Phys. Lett. **66**, 1181-1183 (1995).

204.T. Nishiyama and M. Akaizawa, Pressure waves produced by the collapse of a spherical bubble, Technol. Rep. Tohoku Univ. **44**, 579-602 (1979).

205.J. Noack and A. Vogel, Streak photographic investigation of shock-wave emission after laser-induced plasma formation in water, SPIE Proc. **2391A**, 284-293 (1995).

206.J. Noack, Optischer Durchbruch in Wasser mit Laserpulsedauern zwischen 100 ns and 100 fs. Dissertation, Technisch-Naturwissenschaftliche Fakultät der Medizinischen Universität zu Lübeck (1998a).

207.J. Noack and A. Vogel, Single-shot spatially resolved characterization of laser-induced shock waves in water, Appl. Opt. **37**, 4092-2099 (1998b).

208.J. Noack, D. X. Hammer, G. D. Noojin, B.A. Rockwell, and A. Vogel, Influence of pulse duration on mechanical effects after laser-induced breakdown in water, J. Appl. Phys. **83**, 7488-7495 (1998c).

209.J. Noack and A. Vogel, Laser-induced plasma formation in water at nanosecond to femtosecond time scales: Calculation of thresholds, absorption coefficients, and energy density. IEEE J. Quantum Electron. **35**, 1156-1167 (1999).

210.C. D. Ohl, A. Phillip, and W. Lauterborn, Cavitation bubble collapse studied at 20 million frames per second, Ann. Physik **4**, 26-34 (1995).

211.K. D. Ohl, O. Lindau, and W. Lauterborn, Luminescence from spherically and aspherically collapsing laser induced bubbles, Phys. Rev. Lett. **80**, 393-396 (1998).

212.R. Painter, R. D. Birkhoff, E. T. Arakawa, Optical measurements of liquid water in the vacuum ultraviolet, J. Chem. Phys. **51**, 243-251 (1969).

213.M. Paillette, Ann. Phys. (Paris) **4**, 671 (1969).

214.J. M. Parel, H. Gelender, W. F. Tefers, and E. W. D. Norton, Phaco-Ersatz: Cataract surgery designed to preserve accommodation, Graefes Arch. Clin. Exp. Ophthalmol. **24**, 165-173 (1986).

215.J. B. Park, *Biomaterials, An Introduction,* Plenum Press, New York (1979).

216.A. Penzkofer and W. Kaiser, Generation of picosecond light continua by parametric four-photon interactions in liquids and solids, Opt. Quant. Electron. **9**, 315-349 (1977).

217.G. H. Pettit, M. N. Ediger, and R. P. Weiblinger, Excimer laser ablation of the cornea, Opt. Eng. **34**, 661-667 (1995).

218.G. H. Pettit and M. N. Ediger, Corneal tissue absorption coefficients for 193- and 213-nm ultraviolet radiation, Appl. Opt. **35**, 3386-3391 (1996).

219.Y. V. Petukhov, Modified Kirkwood-Bethe approximation suitable for calculating the complete profile of a detonation wave and its spectrum near the source, Sov. Phys. Acoust. **33**, 185-188 (1987).

220.A. Phillip, M. Delius, C. Scheffczyk, A. Vogel, and W. Lauterborn, Interaction of lithotripter-generated shock waves with air bubbles, J. Acoustic. Soc. Am. **93**, 2496-2509 (1993).

221.A. Phillip and W. Lauterborn, Cavitation erosion by single laser-produced bubbles, J. Fluid Mech. **361**, 75-116 (1998).

222.M. S. Plesset, The dynamics of cavitation bubbles, Trans. ASME J. Appl. Mech. **16**, 228-231 (1949).

223.M. S. Plesset and R. B. Chapman, Collapse of an initially spherical vapor cavity in the neighborhood of a solid boundary, J. Fluid Mech. **47**, 283-290 (1971).

224.L. b. Poché, Underwater shock-wave pressures from small detonators, J. Acoust. Soc. Am. **51**, 1733-1737 (1971).

225.M. R. Prince, G. M. LaMuraglia, P. Teng, T. F. Deutsch, and R. R. Anderson, Preferential ablation of calcified arterial plaque with laser-induced plasmas, IEEE J. Quantum Electro. **QE-23**, 1783-1786 (1987).

226.A. Prosperetti and A. Lezzi, Bubble dynamics in a compressible liquid. Part I. First order theory, J. Fluid Mech. **168**, 457-478 (1986).

227.H. Puchtler, F. Waldrop Sweat, and L. S. Valentine, Polarisation microscopic studies of connective tissue stained with picro-sirius red FBA, Beitr. Pathol. **150**, 174-187 (1973).

228.C. A. Puliafito and R. F. Steinert, Short-pulsed Nd:YAG laser microsurgery of the eye: biophysical considerations, IEEE J. Quantum Electron. **QE-20**, 1442-1448 (1984).

229.Yu. P. Raizer, Heating of a gas by a powerful light pulse, Sov. Phys. JETP **48**, 1508-1519 (1965).

230.Yu. P. Raizer, Breakdown and heating of gases under the influence of a laser beam, Sov. Phys. Usp. **8**, 650-673 (1966).

231.S. A. Ramsden and W. E. R. Davies, Radiation scattered from the plasma produced by a focused ruby laser beam, Phys. Rev. Lett. **13**, 227-229 (1964a).

232.S. A. Ramsden and P. Savic, A radiative detonation model for the development of a laser-induced spark in air, Nature **302**, 1217-1219 (1964b).

233.J. K. Ranka and A. L. Gaeta, Breakdown of the slowly-varying envelope approximation in the self-focusing of ultrashort pulses, Opt. Lett. **23**, 534-536 (1998).

234.Lord Rayleigh, On the pressure developed in a liquid during the collapse of a spherical cavity, Philos. Mag. **34**, 94-98 (1917).

235.U. Radek, Kavitationserzeugte Druckimpulse und Materialzerstörung, Acustica **26**, 270-283 (1972).

236.J. F. Ready, *Effects of High Power Laser Radiation,* Academic Press, Orlando (1971).

237.J. F. Reintjes, Nonlinear optical processes, in: *Encyclopedia of Physical Science and Technology, Vol. 9* , Academic Press, Orlando (1987), pp. 103-156.

238.Q. Ren, V. Venugopalan, K. Schomacker, T. Deutsch, T. Flotte, C. Puliafito, and R. Birngruber, Mid-infrared laser ablation of the cornea: a comparative study, Lasers Surg. Med. **12**, 274-281 (1992).

239.M. H. Rice and J. M. Walsh, Equation of state of water to 250 kilobars, J. Chem. Phys. **26**, 824-830 (1957).

240.S. Ridah, Shock waves in water, J. Appl. Phys. **64**, 152-158 (1988).

241.K. Rink, G. Delacrétaz, R. P. Salathé, Fragmentation process induced by microsecond laser pulses during lithotripsy, Appl. Phys. Lett. **61**, 258-260 (1992).

242.R. M. Roberts, J. A. Cook, R. L. Rogers, A. M. Gleeson, and T. A. Griffy, The energy partition of underwater sparks, J. Acoust. Soc. Am. **99**, 3465-3475 (1996).

243.B. A. Rockwell, W. P. Roach, M. E. Rogers. M. W. Mayo, C. A. Toth, C. P. Cain, and G. D. Noojin, Nonlinear refraction in vitreous humor, Opt. Lett. **18**, 1792-1794 (1993).

244.B. A. Rockwell, personal communication, 1997.

245.P. H. Rogers, Weak-shock solution for underwater explosive shock waves, J. Acoust. Soc. Am. **62**, 1412-1419 (1977).

246.J. C. W. Rogers and W. G. Szymczak, Computations of violent surface motions: comparisons with theory and experiment, Phil. Trans. R. Soc. Lond. A **355**, 649-663 (1997).

247.P. Rol, F. Fankhauser, and S. Kwasniewska, Evaluation of contact lenses for laser therapy, Part I, Lasers Ophthalmol. **1**, 1-20 (1986).

248.J. A. Rooney, Hydrodynamic shearing of biological cells, J. Biol. Phys. **2**, 26-40 (1974).

249.J. E. Rothenberg, Space-time focusing: breakdown of the slowly varying envelope approximation in the self-focusing of femtosecond pulses, Opt. Lett. **17**, 1340-1342 (1992).

250.C. A. Sacchi, Laser-induced electric breakdown in water, J. Opt. Soc. Am. B. **8**, 337-345 (1991).

251.N. Sanada, J. Ikeuchi, K. Takayama, and O. Onodera, Interaction of an air bubble with a shock wave generated with a microexplosion in water, in: Proc. Int. Symp. Cavitation, Sendai, 67-92 (1986).

252.N. Sanada, O. Asano, J. Ikeuchi, K. Takayama, and O. Onodera, Interaction of a gas bubble with an underwater shock wave, pit formation on the metal surface, in: *Proc. Int. Symp. Shock Tubes and Waves*, Aachen, 311-317 (1988).

253.N. W. Sasnett, Propagation of multimode laser beans -- the M^2 factor, in: D. R. Hall and P. E. Jackson, eds., *The Physics and Technology of Laser Resonators*, Adam Hilger, Bristol and New York (1989), pp. 94-105.

254.R. J. Scammon, El J. Chapyak, R. P. Godwin, and A. Vogel, Simulations of shock waves and cavitation bubbles produced in water by picosecond and nanosecond pulses, in: Steve Jacques, ed., Laser Tissue Interactions IX, SPIE Proc. **3254A**, 264-275 (1998).

255.U. Schmidt-Erfurth, A. Vogel, and R. Birngruber, The influence of wavelengths on the laser power required for retinal photocoagulation in cataractous human eyes, Lasers Light Ophthalmol. **5**, 69078 (1992).

256.H. Schmidt-Kloiber, G. Paltauf, and E. Reichl, Investigation of the probabilistic behavior of laser-induced breakdown in pure water and in aqueous solutions of different concentrations, J. Appl. Phys. **66**, 4149-4153 (1989).

257.H. Schoeffmann, H. Schmidt-Kloiber, and E. Reichl, Time-resolved investigations of laser-induced shock waves in water by use of polyvinylidene flouride hydrophones, J. Appl. Phys. **63**, 46-51 (1987).

258.L. F. Shampine and M. K. Gordon, *Computer Solution of Ordinary Differential Equations. The Initial Value Problem,* Freeman and Company, San Francisco, CA (1975). O. V. Rudenko and S. I. Soluyan, *Theoretical Foundations of Nonlinear Acoustics,* Consultants Bureau, Plenum Publishing Corp., New York (1975).

259.Y. R. Shen, Self-focusing: Experimental, Progr. Quant. Electr. **4**, 1-34 (1975).

260.Y. R. Shen, *The Principles of Nonlinear Optics*, Wiley, New York (1984).

261.Y. R. Shen and G. Z. Yang, Theory of self-phase modulation and spectral broadening, in: R. R. Alfano, ed., *The Supercontinuum Laser Source*, Springer, New York (1989), pp. 1-32.

262.E. S. Sherrard and M. G. Kerr Muir, Damage to the corneal endothelium by Q-switched Nd:YAG laser posterior capsulotomy, Trans. Ophthalmol. Soc. UK **104**, 524-528 (1985).

263.A. Shima, Y. Tomita, and T. Sugui, Impulsive pressure generation by bubble/pressure wave interaction, AIAA Journal **26**, 434-437 (1988).

264.A. Shima, Y. Tomita, D. C. Gibson, and J. R. Blake, The growth and collapse of cavitation bubbles near composite surfaces, J. Fluid Mech. **203**, 199-214 (1989).

265.N. D. Shutler and R. B. Mesler, A photographic study of the dynamics and damage capabilities of bubbles collapsing near solid boundaries, Trans. ASME D: J. Basic Eng. **87**, 511-517 (1965).

266.A. E. Siegman, M. W. Sasnett, and T. F. Johnson, Choice of clip levels for beam width measurements using knife-edged techniques, IEEE J. Quantum Electron. **QE-27**, 1098-1104 (1991).

267.M. W. Sigrist, Laser generation of acoustic waves in liquids and gases, J. Appl. Phys. **60**, R83-R121 (1986).

268.K. R. Sletten, K. G. Yen, S. Sayegh, F. Loesel, C. Eckhoff, C. Horvath, M. Meunier, T. Juhasz, and R. M. Kurtz; An in vivo model of femtosecond laser intrastromal refractive surgery. Ophthalmic Surg. Lasers 30; 742-749 (1999)

269.R. J. Smith and S. F. Cleary, Investigation of structural bonding forces in bacteriophage T2, J. Acoust. Soc. Am. **56**, 1883-1889 (1975).

270.D. C. Smith and R. G. Meyerand, Laser radiation induced gas breakdown, in: G. Bekefi, ed., *Principles of Laser Plasma*, Wiley, New York (1976), pp.457-507.

271.W. L. Smith, P. Liu, and N. Bloembergen, Superbroadening in H_2O and D_2O by self-focused picosecond pulses from a YAlG:Nd laser, Phys. Rev. Lett. A **15**, 2396-2403 (1977).

272.M. J. Soileau, W. F. Williams, N. Mansour, and E. W. Van Stryland, Laser-induced damage and the role of self-focusing, Opt. Eng. **28**, 1133-1144 (1989).

273.M. Sparks, D. L. Mills, R. Warren, T. Holstein, A. A. Maradudin, L. J. Sham, E. Loh, and D. F. King, Theory of electron-avalanche breakdown in solids, Phys. Rev. B **24**, 3519-3536 (1981).

274.C. Spielmann, M. Lenzner, A. Stingl, R. Szipöcs, and F. Krausz, Femtosekundenlaser: Sind die Grenzen schon erreicht? Phys. Bl. **51**, 289-292 (1995).

275.J. A. Squier, Compact ultrafast sources for biomedical applications, Vortrag auf der BIOS 98 *Applications of Ultrashort-Pulse Lasers in Medicine and Biology* (1988).

276.R. F. Steinert and C. A. Puliafito, Plasma formation and shielding by three ophthalmic neodymium-YAG lasers, Am. J. Ophthalmol. **96**, 427-434 (1983a).

277.R. F. Steinert, C. A. Puliafito, and C. Kittrell, Plasma shielding by Q-switched and mode-locked Nd:YAG lasers, Ophthalmology **90**, 1003-1006 (1983b).

278.R. F. Steinert and C. A. Puliafito, *The Nd:YAG Laser in Ophthalmology*, Saunders, Philadelphia (1985).

279.D. Stern, C. A. Puliafito, E. T. Dobei, and W. T. Reidy, Corneal ablation by nanosecond, picosecond and femtosecond laser pulses at 532 nm and 625 nm, Arch. Opthalmol. **107**, 587-592 (1989).

280.D. J. Stolarski, J. Hardman, C. G. Bramlette, G. D. Noojin, R. J. Thomas, B. A. Rockwell, and W. P. Roach, Integrated light spectroscopy of laser-induced breakdown in aqueous media, SPIE Proc. **2391**, 100-109 (1995).

281.H. W. Strube, Numerische Untersuchung zur Stabilität nichtsphärisch schwingender Blasen, Acustica **25**, 289-303 (1971).

282.E. W. van Stryland. M. J. Soileau, A. L. Smirl, and W. E. Williams, Pulsewidth and focal-volume dependence of laser-induced breakdown, Phys. Rev. B **23**, 2144-2151 (1981).

283.B. C. Stuart, M. D. Feit, S. Hermann, A. M. Rubenchik, B. W. Shore, and M. D. Perry, Nanosecond to femtosecond laser-induced breakdown in dielectrics, Phys. Rev. B **53**, 1749-1761 (1996).

284.B. Sullivan and A. C. Tam, Profile of laser-produced acoustic pulse in a liquid, J. Acoust. Soc. Am. **75**, 437-441 (1984).

285.K. S. Suslick, D. A. Hammerton, and R. E. Cline, The sonochemical hotspot, J. Am. Chem. Soc. **108**, 5641-5642 (1986).

286.K. S. Suslick, ed., *Ultrasound: its chemical, physical and biological effects,* VCH Verlag, New York, Weinheim (1988).

287.K. S. Suslick, The chemical effects of ultrasound, Scient. Amer. **260**, 62-68 (1989).

288.W. G. Szymczak, J. W. C. Rogers, J. M. Solomon and A. E. Berger, A numerical algorithm for hydrodynamic free boundary problems, J. Comp. Phys. **106**, 319-336 (1993).

289.J. Taboada, Interaction of short laser pulses with ocular tissue, in: S. L. Trokel, ed., *YAG Laser Ophthalmic Microsurgery*, Appleton-Century-Crofts, Norwalk, Conn. (1983), pp. 15-38.

290.M. J. Tassignon, I. Kreissig, N. Strempels, and M. Brihave, Indications for Q-switched and mode-locked Nd:YAG lasers in vitreoretinal pathology, Eur. J. Ophthalmol. **1**, 123-130 (1991).

291.P. Teng, N. S. Nishioka, R. R. Anderson, and T. F. Deutsch, Acoustic studies of the role of immersion in plasma-mediated laser ablation, IEEE J. Quant. Electr. **QE-23**, 1845-1852 (1987).

292.K. Teshima, T. Ohshima, S. Tanaka, and T. Nagai, Biomechanical effects of shock waves on Escherichia coli and λphage DNA, Shock Waves **4**, 293-297 (1995).

293.V. S. Teslenko, Investigation of photoacoustic and photohydrodynamic parameters of laser breakdown in liquids, Sov. J Quant. Electron. **7**, 981-984 (1977).

294.R. J. Thomas, D. X. Hammer, G. D. Noojin, D. J. Stolarski, B. A. Rockwell, and W. P. Roach, Time-resolved spectroscopy of laser-induced breakdown in water, SPIE Proc. **2681**, 402-410 (1996).

295.S. Thomsen, J. A. Pearce, and W. F. Cheong, Changes in birefringence as markers of thermal damage in tissue, IEEE Trans. Biomed. Eng. **36**, 1174-1179 (1989).

296.I. Thormählen, J. Straub, and U. Grigull, Refractive index of water and its dependence on wavelength, temperature, and density, J. Phys. Chem. Ref. Data **14**, 933-945 (1985).

297.G. T. Timberlake, A. W. Gemperli, C. K. Larive, K. A. Warren, and M. A. Mainster, Free radical production by Nd:YAG laser photodisruption, Ophthalmic Surg. Lasers **28**, 582-589 (1997).

298.K. Tödheide, Water at high temperatures and pressures, in: Franks, ed., *Water. A Comprehensive Treatise. Vol. I. The Physics and Physical Chemistry of Water* , Plenum Press, New York (1972), pp. 463-514.

299.Y. Tomita and A. Shima, Mechanisms of impulsive pressure generation and damage pit formation by bubble collapse, J. Fluid Mech. **169**, 535-564 (1986).

300.Y. Tomita, K. Sato, and A. Shima, Interaction of two laser-produced cavitation bubbles near boundaries, in: J. R. Blake et al., eds., *Bubble Dynamics and Interface Phenomena*, Kluwer Academic Publishers, Dordrecht, the Netherlands (1994), pp. 33-45.

301.R. P. Tong, W. P. Schiffers, S. J. Shaw, J. R. Blake, and D. C. Emmony, The role of "splashing" in the collapse of a laser-generated cavity near a rigid boundary, submitted to J. Fluid Mech. (1997).

302.S. L. Trokel, ed., *YAG Laser Opthalmic Microsurgery,* Appleton-Century-Crofts, Norwalk, Conn. (1983).

303.S. A. Vernon and H. Cheng, Freeze frame analysis on high speed cinematography of Nd:YAG laser explosions in ocular tissue, Brit. J. Ophthalmol. **70**, 321-325 (1986).

304.A. Vogel, W. Hentschel, J. Holzfuss, and W. Lauterborn, Cavitation bubble dynamics and acoustic transient generation in ocular surgery with pulsed neodymium: YAG lasers, Opthalmology **93**, 1259-1269 (1986).

305.A. Vogel and W. Lauterborn, Acoustic transient generation by laser-produced cavitation bubbles near solid boundaries, J. Acoust. Soc. Am. **84**, 719-731 (1988a).

306.A. Vogel, Prinzipien der Laserdisruption, in: J. Wollensak, ed., *Laser in der Ophthalmologie,* Ferdinand Enke Verlag, Stuttgart (1988b), pp. 44-55.

307.A. Vogel, W. Lauterborn, and R. Timm, Optical and acoustic investigation of the dynamics of laser-produced cavitation bubbles near a solid boundary, J. Fluid Mech. **206**, 299-338 (1989).

308.A. Vogel, R. Schweiger, A. Frieser, M. Asiyo, and R. Birngruber, Intraocular Nd:YAG laser surgery: Light-tissue interaction, damage range, and reduction of collateral effects, IEEE J. Quantum Electr. **QE-26**, 2240-2260 (1990).

309.A. Vogel and R. Birngruber, Temperature profiles in human retina and choroid during laser coagulation with different wavelengths ranging from 514 to 810 nm, Lasers Light Ophthalmol. **5**, 9-16 (1992).

310.A. Vogel, S. Busch, K. Jungnickel, and R. Birngruber, Mechanisms of intraocular photodisruption with picosecond and nanosecond laser pulses, Laser Surg. Med. **15**, 32-43 (1994a).

311.A. Vogel, M. R. C. Capon, M. N. Asiyo, and R. Birngruber, Intraocular photodisruption with picosecond and nanosecond laser pulses: tissue effects in cornea, lens and retina, Invest. Ophthalmol. Vis. Sci. **35**, 3033-3044 (1994b).

312.A. Vogel and S. Busch, Time-resolved measurements of shock-wave emission and cavitation-bubble generation in intraocular laser surgery with ps- and ns-pulses, In. J. R. Blake et al., eds., *Bubble Dynamics and Interface Phenomena* , Kluwer Academic Publishers, Dordrecht, the Netherlands (1994c), pp. 105-117.

313.A. Vogel, M. N. Asiyo-Vogel, and R. Birngruber, Untersuchungen zur intrastromalen refraktiven Hornhautchirurgie mit Picosekunden-Nd:YAG Laser-Pulsen, Fortschr. Ophthalmol. **91**, 655-662 (1994d).

314.A. Vogel, S. Busch, and U. Parlitz, Shock wave emission and cavitation bubble generation by picosecond and nanosecond optical breakdown in water, J. Acoust. Soc. Am. **100**, 148-165 (1996a).

315.A. Vogel, R. Engelhardt, U. Behnle, and U. Parlitz, Minimization of cavitation effects in pulsed laser ablation -- illustrated on laser angioplasty, Appl. Phys. B **62**, 173-182 (1996b).

316.A. Vogel, K. Nahen, and D. Theisen, Plasma formation in water by picosecond and nanosecond Nd:YAG laser pulses - Part I: Optical breakdown at threshold and superthreshold irradiance, IEEE J. Selected Topics Quantum Electron. **2**(4), 847-860 (1996c).

317.A. Vogel, Nonlinear absorption: Intraocular microsurgery and laser lithotripsy, Phys. Med. Biol. **42**, 895-912 (1997a).

318.A. Vogel, T. Günther, M. N. Asiyo-Vogel, and R. Birngruber, Factors determining the refractive effects of intrastromal photorefractive keratectomy with the picosecond laser, J. Cataract Refract. Surg. **23**, 1301-1310 (1997b).

319.A. Vogel, K. Nahen, D. Theisen, R. Birngruber, R. J. Thomas, and B. A. Rockwell, Influence of optical aberrations on plasma formation in water, and their consequences for intraocular photodisruption, in: P. O. Rol, K. M. Joos, and F. Manns, eds., Ophthalmic Technologies VIII, SPIE Proc. **3246**, 120-131 (1998a).

320.A. Vogel, J. Noack, K. Nahen, D. Theisen, S. Busch, U. Parlitz, D. X. Hammer, G. D. Noojin, B. A. Rockwell, and R. Birngruber, Energy balance of optical breakdown in water, in: S. Jacques, ed., Laser Tissue Interactions IX, SPIE Proc. **3254**, 168-179 (1998b).

321.A. Vogel and J. Noack, Shock wave energy and acoustic energy dissipation after laser-induced breakdown, in: S. Jacques, ed., Laser Tissue Interactions IX, SPIE Proc. **3254**, 180-189 (1998c).

322.A. Vogel, J. Noack, K. Nahen, D. Theisen, R. Birngruber, D. X. Hammer, G. D. Noojin, and B. A. Rockwell, Laser induced breakdown in the eye at pulse durations from 80 ns to 100 fs, in: J. Neev, ed., Applications of Ultrashort-Pulse Lasers in Medicine and Biology, SPIE Proc. **3255**, 34-48 (1998d).

323.A. Vogel, R. Scammon, and R. P. Godwin, Tensile stress generation by optical breakdown in tissue: experimental investigation and numerical simulations. SPIE Proc. **3601**, 191-206 (1999a).

324.A. Vogel, J. Noack, K. Nahen, D. Theisen, S. Busch, U. Parlitz, D. X. Hammer, G. D. Nojin, B. A. Rockwell, and R. Birngruber, Energy balance of optical breakdown in water at nanosecond to femtosecond time scales. Appl. Phys. B **68**, 271-280 (1999b).

325.A. Vogel, K. Nahen, D. Theisen, R. Birngruber, R. J. Thomas, and B. A. Rockwell, Influence of optical aberrations on laser-induced plasma formation in water and their consequences for intraocular protodisruption. Appl. Opt. **38**, 3636-3643 (1999c)

326.K. Vokurka, Excitation of gas bubbles for free oscillations by changing the ambient pressure, Acustica **78**, 84-92 (1993).

327.Q. Z. Wang, P. P. Ho, and R. R. Alfano, Supercontinuum generation in condensed matter, in: R. R. Alfano, ed., *The Supercontinuum Laser Source*, Springer, New York (1989), pp. 33-90.

328.B. Ward and D. C. Emmony, Interferometric studies of the pressures developed in a liquid during infrared-laser-induced cavitation-bubble oscillation, Infrared phys. **32**, 489-515 (1991).

329.G. M. Watson, S. Murray, S. P. Dretler, and J. A. Parrish, The pulsed dye laser for fragmenting urinary calculi, J. Urol. **138**, 195-198 (1987).

330.A. J. Welch, M. J. C. van Gemert, eds, *Optical-Thermal Response of Laser-Irradiated Tissue*, Plenum Press, New York, (1995).

331.H. Welsch, Spektrale Lichtabsorption in Blut unter Berücksichtigung der Streuung, Dissertation, Ludwig Maximilians-Universität München (1984).

332.G. M. Weyl, Physics of laser-induced breakdown: An update, in: L. J. Radziemski and D. A. Cremers, *Laser-Induced Plasmas and Applications*, Marcel Dekker, New York (1989a), pp. 1-67.

333.G. M. Weyl and T. Tucker, Penetration of plasma radiation in tissue, Laser Life Sci. **3**, 125-138 (1989b).

334.B. S. Wherret, Scaling rules for multiphoton interband absorption in semiconductors, JOSA B **1**, 67-72 (1984).

335.F. Williams, S. P., Varama, and S. Hillenius, Liquid water as a lone-pair amorphous semiconductor, J. Chem. Phys. **64**, 1549-1554 (1976).

336.R. Winter, M. Böhnke, M. Lojewski, and H. zur Nieden, Nebenwirkungen von YAG Laserbehandlungen am vorderen Augenabschnitt -- Experimentelle Untersuchungen am Hornhautendothel, in: J. Wollensak, ed., *Laser in der Ophthalmologie*, Enke, Stuttgart (1988), pp.116-120.

337.E. Yablonovitch and N. Bloembergen, Avalanche ionization and the limiting diameter of filaments induced by light pulses in transparent media, Phys. Rev. Lett. **29**, 907-910 (1972).

338.Y. B. Zeldovich and Y. P. Raizer, Physics of Shock Waves and High Temperature Hydrodynamic Phenomena, Academic Press, New York and London (1966), Vols. I and II, 916 pp.

339.L. V. Zhigilei and B. J. Garrison, Microscopic simulation of short pulse laser damage of melanin particles, in: S. Jacques, ed., Laser Tissue Interactions IX, SPIE Proc. **3254**, 135-145 (1998).

340.E. van der Zypen, F. Fankhauser, H. Bebie, and J. Marshall, Changes in the ultrastructure of the iris after irradiation with intense light, Adv. Ophthal. **39**, 59-180 (1979).

341.B. Zysset, J. G. Fujimoto, C. A. Puliafito, R. Birngruber, and T. F. Deutsch, Picosecond optical breakdown: tissue effects and reduction of collateral damage, Lasers Surg. Med. **9**, 183-204 (1989a).

342.B. Zysset, J. G. Fujimoto, and T. F. Deutsch, Time-resolved measurements of picosecond optical breakdown, Appl. Phys. B **48**, 139-147 (1989b).

Acknowledgments

I sincerely thank the following:

Professor Reginald Birngruber for making this work possible, first, in the Hermann Wacker Laboratory of the Eye Clinic at the Ludwig-Maximilian University, Munich and, later, at the Medical Laser Center Lübeck; for enabling me to engage in international exchanges with other researchers, and for many fruitful discussions.

Professor Werner Lauterborn, who introduced me to the fascinating realm of laser-produced plasmas and cavitation.

Professor Veit-Peter Gabel and Professor Horst Laqua, who ensured that the clinical aspects of intraocular photodisruption were kept in sight while investigating the underlying physical mechanisms.

Professor Otto-Erich Lund, who lent considerable support to the research in its initial stages at the Eye Clinic of Ludwig-Maximilian University, Munich.

My friend, PD Dr. Ulrich Parlitz, for a fruitful collaboration on mathematical models of shock wave emission and cavitation bubble formation during optical breakdown.

Dr. Malcolm R. C. Capon for the joint research on laser-induced tissue effects.

Dr. Gerd Geerling for his dedicated work during the clinical trials of picosecond lasers.

Many graduate and postgraduate students contributed with their work and ideas to the completion of this thesis: Stefan Busch, Alex Frieser, Dr. Thomas Günther, Dr. Kerstin Jungnickel, Dr. Kester Nahen, Dr. Joachim Noack, Stefan Rein, Dr. Peter Schweiger, Dirk Theisen. I thank them all for their involvement and for pleasant collaborations.

The research with ultrashort laser pulses was done in collaboration with the Air Force Research Laboratory, Brooks Air Force Base, San Antonio, Texas. I particularly thank Professor William P. Roach, Dr. Paul K. Kennedy, and Dr. Benjamin A. Rockwell.

For stimulating discussions, I thank Professor Franco Docchio, Professor Apostulos Doukas, Professor Franz Fankhauser, Dr. Robert Godwin, and Professor Franz Hillenkamp.

Without the help of Ms. Barbara Flucke, Mr. C. Grosse, Mr. Harald Kröhn, Mr. Rene Kube, Ms. Lisa Merz, Ms. Sabine Reidinger, Ms. Monika Volkholz and Ms. Ursula Weinrich in the areas of histology, photography, and graphics, this work could not have been realized in its present form.

Very special thanks go to my wife, Dr. Mary Nyamasi Asiyo-Vogel, who opened my eyes not only to many scientific details but also to many other things in life.

The research was supported by the German Research Council (DFG), grants BI-321/2-1,2,3,4. The Hermann Wacker Foundation provided funds for some of the experimental apparatus.

The English translation of this work has been made possible through the support of Dr. Benjamin A. Rockwell and the American Institute of Physics. I would like to express my thanks to the translator Dr. Donald McNeill, and to Dr. Robert P. Godwin for his careful reading and final polishing of the manuscript.

Printing of the manuscript was funded by the EOARD (European Office of Aerospace Research and Development), grant F61775-01-WE016.

Curriculum Vitae

Name: Dr. Alfred Otto Heinrich Vogel
Birth date and place: 31 Dec. 1953, in Lilienthal, Lower Saxony
Nationality: German
Marital status: married to Dr. Mary Asiyo-Vogel, ophthalmologist

School Education

1960-1964 -- Elementary school in Lilienthal
1964-1972 -- Secondary school: Gymnasium Am Barkhof, Bremen
May 1972 -- Abitur

Alternative Service

July 1973 - Oct. 1974 -- Ev. Luth. Wichernstift, Delmenhorst

University Education and Degrees

Oct. 1972 - July 1973 -- Physics at Georg-August University, Göttingen, interrupted by Alternative Service

Oct. 1974 - Dec. 1980 -- Secondary school teachers education in physics (major) and political science at Georg-August University, Göttingen, qualified as secondary school teacher.

July 1987 -- Ph.D. in physics, Georg-August University, Göttingen; title of dissertation: "Optical and Acoustic Investigations on Laser Induced Cavitation Bubble Dynamics near Solid Boundaries."

Professional Experience

1981-1987 -- Graduate Assistant at the Third Physics Institute, Göttingen University.

1988-1992 -- Staff member at the Hermann Wacker Laboratory for Medical Laser Applications, Eye Clinic, Ludwig-Maximilians University, Munich; from the end of 1988 to the end of 1991, Acting Head of the Hermann Wacker Laboratory.

Since 1992 -- Group leader at the Medical Laser Center, Lübeck.

Teaching Experience

1981- 87 -- Supervision and teaching in practical studies and in semi-annual two-week courses, "Laser Physics and Holography," at the Third Physics Institute, Göttingen University.

1988 -1992 -- Supervision of diploma theses at the Polytechnical of Munich, and of a medical dissertation at the Ludwig-Maximilians University, Munich.

Since 1992 -- Supervision of physical and medical dissertations at the Medical University of Lübeck, diploma theses in masters degree programs at the University of Hamburg and diploma theses at the Polytechnical of Lübeck.

Lectures in the Series "Lasers in Medicine" at the Medical University of Lübeck; instructor at the "Essen Training Courses for Ophthalmologists," lectures at the Edgar-Lüscher Seminars for Teachers of Physics, courses in laser safety at the Medical Laser Center Lübeck, and for the Berufsgenossenschaft der Feinmechanik und Elektrotechik.

Memberships

German Physical Society, Optical Society of America, Acoustical Society of America, Association for Research and Vision in Ophthalmology

Publications

Total number of publications: 89

Peer reviewed: 48